Proposal to Perform a High-Statistics

Neutrino Scattering Experiment

Using a Fine-grained Detector

in the NuMI Beam

December 3, 2003

Abstract

The NuMI facility at Fermilab will provide an extremely intense beam of neutrinos for the MINOS neutrino-oscillation experiment. The spacious and fully-outfitted MINOS near detector hall will be the ideal venue for a high-statistics, high-resolution ν and $\bar{\nu}$–nucleon/nucleus scattering experiment. The experiment described here will measure neutrino cross-sections and probe nuclear effects essential to present and future neutrino-oscillation experiments. Moreover, with the high NuMI beam intensity, the experiment will either initially address or significantly improve our knowledge of a wide variety of neutrino physics topics of interest and importance to the elementary-particle and nuclear-physics communities.

The MINERνA Collaboration

D. Drakoulakos, P. Stamoulis, G. Tzanakos, M. Zois
University of Athens; Athens, Greece

D. Casper
University of California, Irvine; Irvine, California, USA

E. Paschos
University of Dortmund, Dortmund, Germany

D. Harris, M. Kostin, J.G. Morfín*, P. Shanahan
Fermi National Accelerator Laboratory; Batavia, Illinois, USA

M.E. Christy, W. Hinton, C.E. Keppel[1]
Hampton University; Hampton, Virginia, USA

R. Burnstein, A. Chakravorty[2], O. Kamaev, N. Solomey
Illinois Institute of Technology; Chicago, Illinois, USA

W.K. Brooks, A. Bruell, R. Ent, D. Gaskell, W. Melnitchouk, S.A. Wood
Thomas Jefferson National Accelerator Facility; Newport News, Virginia, USA

I. Niculescu, G. Niculescu
James Madison University, Harrisonburg, Virginia, USA

M.A.C. Cummings, V. Rykalin
Northern Illinois University; DeKalb, Illinois, USA

S. Boyd, D. Naples, V. Paolone
University of Pittsburgh; Pittsburgh, Pennsylvania, USA

A. Bodek, H. Budd, J. Chvojka, P. deBarbaro, S. Manly, K. McFarland*, I. Park, W. Sakumoto, R. Teng
University of Rochester; Rochester, New York, USA

R. Gilman, C. Glashausser, X. Jiang, G. Kumbartzki, K. McCormick, R. Ransome
Rutgers, The State University of New Jersey; Piscataway, New Jersey, USA

H. Gallagher, T. Kafka, W.A. Mann, W. Oliver
Tufts University; Boston, Massachusetts, USA

[1] Also at Thomas Jefferson National Accelerator Facility
[2] Also at Saint Xavier College, Chicago, Illinois, USA
* Co-spokespersons

Contents

List of Figures

List of Tables

Part I
Introduction

1 Executive Summary

The imminent completion of the NuMI beamline, which will be the highest intensity neutrino beamline in the world for many years after its completion, offers the particle and nuclear physics community a new opportunity. By constructing a fully active neutrino detector to run for the first time in a high rate neutrino beam, the MINERνA experiment, a collaboration between the high energy physics community already working at Fermilab and groups of new users from the medium energy nuclear physics community, proposes to exploit this opportunity to access a broad and rich program in neutrino scattering physics.

MINERνA will be able to complete a physics program of high rate studies of exclusive final states in neutrino scattering, as described in Chapters 6–8, of elucidation of the connection between pQCD and QCD in non-perturbative regime, as described in Chapter 10, and of studies of the axial current in the elastic (Chapter 6), DIS (Chapter 10) and off-forward (Chapter 11) regimes, as well as inside the nucleus (Chapter 12). MINERνA then seeks the application of its data to aid present and future neutrino oscillation experiments (Chapter 13), where understanding the details of neutrino cross-sections and final states is essential for separating backgrounds to oscillation from signal.

MINERνA can address all these topics, and can bring a new physics focus to the Fermilab program with a simple, low-risk detector of modest cost, as detailed in Chapters 14 and 16–17. The performance of this detector is expected to be excellent for resolving individual final states as well as measuring kinematics in inclusive reactions as documented in Chapter 15.

As we submit this proposal to Fermilab, we are also preparing to request funding from sources outside Fermilab to pursue this interdisciplinary experiment at the intersection of particle and nuclear physics. We request that the lab and its Physics Advisory Committee support this physics and our efforts to seek outside funding by granting stage one approval to MINERνA in time for this approval to enter into funding deliberations this spring and summer.

2 Overview of the MINERνA Experiment

Upcoming neutrino oscillation experiments in the United States, Europe and Japan are driving the construction of new, very intense neutrino beamlines required to achieve reasonable event rates at detectors located hundreds of kilometers away. These new beamlines will allow us to initiate a vigorous research program at a detector, located close to the production target, where event rates are much higher than at the previous generation of neutrino beam facilities. In addition, it is neutrino oscillation experiments, with their low-energy neutrinos and massive nuclear targets, which highlight the need for much improved knowledge of low-energy neutrino–Nucleus interactions, the overall goal of this experiment.

At Fermilab, the new neutrino facility NuMI, designed for the MINOS neutrino oscillation experiment, will be based on the Main Injector (MI) accelerator. The neutrino beams from the MI yield several orders of magnitude more events per kg of detector per year of exposure than the higher-energy Tevatron neutrino beam. This highlights the major improvement of this next generation of neutrino experiments. One can now perform statistically-significant experiments with much lighter targets than the massive iron, marble and other high-A detector materials used in the past. That these facilities are designed to study neutrino oscillations points out the second advantage of these neutrino experiments: An excellent knowledge of the neutrino beam will be required to reduce the beam-associated systematic uncertainties of the oscillation result. This knowledge of the neutrino spectrum will also reduce the beam systematics in the measurement of neutrino-scattering phenomena.

To take advantage of these major improvements in experimental neutrino physics possible with the NuMI beam and facility, a collaboration of elementary particle and nuclear physics groups and institutions named "MINERνA" (Main INjector ExpeRiment: ν–A) has been formed. This collaboration represents the combined efforts of two earlier groups that submitted Expressions of Interest (EOI) [1] to the Fermilab PAC in December, 2002. The goal of the MINERνA experiment is to perform a high-statistics neutrino-nucleus scattering experiment using a fine-grained detector located on-axis, upstream of the MINOS near detector.

2.1 The Fermilab NuMI Facility

The Fermilab NuMI on-site facility is made up of the beamline components, the underground facilities to contain these components and a large, on-site experimental detector hall to contain the MINOS near detector, located just over 1 km downstream of the target and $\sim$ 100 meters underground.

2.1.1 The NuMI near experimental hall

This experimental hall is being constructed and completely outfitted for the MINOS near detector. The hall is 45 m long, 9.5 m wide and 9.6 m high. There is a space upstream of the MINOS near detector amounting to, roughly, a cylindrical volume 26 m long and 3 m in radius for additional detector(s) which, were it desired, could use the MINOS near detector as an external muon-identifier and spectrometer.

2.1.2 The NuMI neutrino beam

The neutrino energy distribution of the NuMI beam can be chosen by changing the distance of the target and second horn from the first horn, as in a zoom lens. The energy of the beamline can also be varied, essentially continuously, by simply changing the target's distance from the first horn and leaving the

second horn in a fixed position. There is a loss of event rate with this procedure compared to also moving the second horn, and the most efficient energy tunes will always require moving the second horn. However, moving the target and second horn involves considerably more time and expense then simply moving the target. It is now expected that the Main Injector will deliver 2.5×10^{20} POT/year at the start of MINOS running, and will ramp up to to higher proton intensities if the required funds can be obtained. The charged-current neutrino event rates per ton (of detector) per year at startup of MINOS would then range from just under 200 K to over 1200 K depending on the position of the target.

For the MINOS experiment the beamline will be operating mainly in its lowest possible neutrino energy configuration to probe the desired low values of Δm^2. However, to minimize systematics, there will also be running in higher-energy configurations that will significantly increase the event rates and kinematic reach of MINERνA.

The ν_e content of the low-energy beam is estimated at just over 1% of the flux. An important function of MINERνA will be to provide a far more accurate measurement of the ν_e flux and energy spectrum within the NuMI beam than is possible with the much coarser MINOS near detector. This important figure-of-merit is needed for the design of next-generation neutrino-oscillation experiments using the NuMI beam, as well as ν_e studies in the MINOS experiment.

2.2 Neutrino Scattering Physics

A neutrino scattering experiment in the NuMI near experimental hall offers a unique opportunity to study a broad spectrum of physics topics with measurement precision heretofore unachievable. Several of these topics have not yet been studied in any systematic, dedicated way. For other topics, the few results that do exist are compromised by large statistical and systematic errors. Topics particularly open to rapid progress upon exposure of MINERνA in the NuMI beam include:

- Precision measurement of the quasi-elastic neutrino–nucleus cross-section, including its E_ν and q^2 dependence, and study of the nucleon axial form factors.

- Determination of single- and double-pion production cross-sections in the resonance production region for both neutral-current and charged-current interactions, including a study of isospin amplitudes, measurement of pion angular distributions, isolation of dominant form factors, and measurement of the effective axial-vector mass.

- Clarification of the W ($\equiv$ mass of the hadronic system) transition region wherein resonance production merges with deep-inelastic scattering, including tests of phenomenological characterizations of this transition such as quark/hadron duality.

- Precision measurement of coherent single-pion production cross-sections, with particular attention to target A dependence. Coherent π^0 production, especially via neutral-currents, is a significant background for next-generation neutrino oscillation experiments seeking to observe $\nu_\mu \rightarrow \nu_e$ oscillation.

- Examination of nuclear effects in neutrino-induced interactions including energy loss and final-state modifications in heavy nuclei. With sufficient $\bar{\nu}$ running, a study of quark flavor-dependent nuclear effects can also be performed.

- Clarification of the role of nuclear effects as they influence the determination of $\sin^2 \theta_W$ via measurement of the ratio of neutral-current to charged-current cross-sections off different nuclei.

6

- With sufficient $\bar{\nu}$ running, much-improved measurement of the parton distribution functions will be possible using a measurement of all six ν and $\bar{\nu}$ structure functions.

- Examination of the leading exponential contributions of perturbative QCD.

- Precision measurement of exclusive strange-particle production channels near threshold, thereby improving knowledge of backgrounds in nucleon-decay searches, determination of V_{us}, and enabling searches for strangeness-changing neutral-currents and candidate pentaquark resonances. Measurement of hyperon-production cross-sections, including hyperon polarization, is feasible with exposure of MINERνA to $\bar{\nu}$ beams.

- Improved determination of the effective charm-quark mass (m_c) near threshold, and new measurements of V_{cd}, $s(x)$ and, independently, $\bar{s}(x)$.

- Studies of nuclear physics for which neutrino reactions provide information complementary to JLab studies in the same kinematic range.

In addition to being significant fields of study in their own right, **improved knowledge of many of these topics is essential to minimizing systematic uncertainties in neutrino-oscillation experiments.**

2.2.1 Low-energy neutrino cross-sections

This is a topic of considerable importance to both present and proposed future (off-axis) neutrino oscillation experiments. Available measurements of both total and exclusive cross-sections from early experiments at ANL, BNL, CERN and FNAL all have considerable uncertainties due to low statistics and large systematic errors, including poor knowledge of the incoming neutrino flux[2]. A working group[3] to assemble all available data on ν and $\bar{\nu}$ cross-sections and to determine quantitative requirements for new experiments has been established by members of this collaboration. MINERνA will be able to measure these cross-sections with negligible statistical errors and with the well-controlled beam systematic errors needed for the MINOS experiment

2.2.2 Quasi-elastic scattering

Charged-current quasi-elastic reactions play a crucial role in both non-accelerator and accelerator neutrino oscillation studies, and cross-section uncertainties - often expressed as uncertainty in the value of the axial-vector mass - are a significant component in error budgets of these experiments. There have been recent advances in the measurement of the vector component of elastic scattering from SLAC and Jefferson Lab. Measurement of the neutrino quasi-elastic channel is the most direct way to improve our knowledge of the axial-vector component to this channel. MINERνA's ability to carefully measure $d\sigma/dQ^2$ to high Q^2 allows investigation of the non-dipole component of the axial-vector form factor to an unprecedented accuracy. Combining these MINERνA measurements with present and future Jefferson Lab data will permit precision extraction of all form factors needed to improve and test models of the nucleon. In addition, due to the well-constrained kinematics of this channel, a careful study of the muon and proton momentum vectors allows an important probe of nuclear effects.

·2.2.3 Resonances and transition to deep-inelastic scattering

Existing data on neutrino resonance-production is insufficient for the task of specifying the complex overlapping Δ and N^* resonance amplitudes and related form-factors which characterize the 1–5 GeV E_ν regime. Neutrino Monte-Carlo programs trying to simulate this kinematic region have used early theoretical predictions by Rein and Sehgal[4] or results from electro-production experiments. Recently Lee and Sato[5] have developed a new model for weak production of the Δ resonance. Paschos and collaborators[6] have also contributed to this effort. It is noteworthy that the theoretical and experimental picture of the resonance region is far more obscure than the quasi-elastic and deep-inelastic scattering (DIS) regions which border it and that much of the relevant MINOS event sample falls inside this poorly-understood resonance region.

Recent work at Jefferson Lab[7] shows strong support for quark/hadron duality, which relates the average resonance production cross-section to the DIS F_2 structure function. How to incorporate this new paradigm into neutrino Monte Carlos is currently being studied. An analysis by Bodek and Yang[8] offers a very promising procedure for fitting F_2 in the low-Q^2/high-x region. Extrapolating their results through the resonance region yields values of F_2 consistent with duality arguments and the Jefferson Lab results mentioned above. The resonance and transition region will be carefully examined by MINERνA.

2.2.4 Coherent pion production

Both charged- and neutral-current coherent production of pions result in a single forward-going pion with little energy transfer to the target nucleus. In the neutral-current case, the single forward-going π^0 can mimic an electron and be misinterpreted as a ν_e event. Existing cross-section measurements for this reaction are only accurate to $\sim 35\%$ and are only available for a limited number of target nuclei.

2.2.5 Studying nuclear effects with neutrinos

The study of nuclear effects with neutrinos can be broadly divided into two areas. The first area involves the kinematics of the initial interaction (spectral function of the struck nucleon within the nucleus and Pauli-excluded interactions) and the evolution of the hadronic cascade as it proceeds through the nucleus. This aspect has direct and important application to the MINOS neutrino oscillation experiment since it can drastically distort the initial neutrino energy by mixing final states to such an extent that the visible energy observed in the detector is much different than the initial energy.

The second area involves modification of the structure functions, F_i and, consequently, the cross-section of ν–A scattering compared to ν–nucleon scattering. Nuclear effects in DIS have been studied extensively using muon and electron beams, but only superficially for neutrinos (in low-statistics bubble-chamber experiments). High-statistics neutrino experiments have, to date, only been possible using heavy nuclear targets such as iron-dominated target-calorimeters. For these experiments, results from e/μ–A analyses have been applied to the results. However, there are strong indications that the nuclear corrections for e/μ–A and ν–A are different. Among these differences is growing evidence for quark-flavor dependent nuclear effects. A neutrino-scattering program at NuMI would permit a systematic, precision study of these effects, by using a variety of heavy nuclear targets and both ν and $\bar{\nu}$ beams.

2.2.6 Strangeness and charm production

MINERνA will allow precise measurement of cross-sections for exclusive-channel strangeness associated-production ($\Delta S = 0$) and Cabbibo-suppressed ($\Delta S = 1$) reactions. Detailed studies of the hadronic systems will be carried out, including q^2 dependence, resonant structure, and polarization states for produced lambda hyperons. A detailed study of coupling strengths and form-factors characterizing the ΔS weak hadronic current is envisaged, which will hopefully reawaken efforts at detailed modelling of these reactions[9]. MINERνA observations of strangeness production near threshold will have ramifications in other areas of particle physics, as for example with estimation of atmospheric-neutrino ΔS backgrounds for nucleon decay searches with megaton-year exposure. Searches for new resonant states and new physics will of course be possible: we envisage a dedicated search for strangeness-changing neutral-current reactions and investigation of unusual baryon resonances such as the recently reported candidate pentaquark state (in $K^+ n$ and $K^0 p$ systems). Clean measurement of V_{us} should be feasible; it may be possible to address long-standing discrepancies between theory and experiment concerning hyperon beta-decay by exploring the related inverse reactions obtained via $\Delta S = 1$ single-hyperon production by antineutrinos[10]. The production of hyperons by neutrinos and antineutrinos would provide new information in the form of hyperon polarization which would reduce ambiguities which currently compromise the analysis of hyperon beta-decay processes.

Although the neutrino energy spectrum is relatively low for a high-statistics charm study, it does cover the important threshold region where production rates are highly dependent on the mass of the charm quark. Depending on the value of m_c, the expected number of charm events could change by as much as 50% in this sensitive region.

2.2.7 Extracting parton distribution functions

Neutrinos have long been a particularly sensitive probe of nucleon structure. One obvious reason is the neutrino's ability to directly resolve the flavor of the nucleon's constituents: ν interacts with d, s, $\bar{u}$ and $\bar{c}$ while the $\bar{\nu}$ interacts with u, c, $\bar{d}$ and $\bar{s}$. This unique ability of the neutrino to "taste" only particular flavors of quarks enhances any study of parton distribution functions. Study of the partonic structure of the nucleon, using the neutrino's weak probe, would complement the on-going study of this subject with electromagnetic probes at Jefferson Lab as well as earlier studies at SLAC, CERN and FNAL. With the high statistics foreseen for MINERνA, as well as the special attention to minimizing neutrino beam systematics, it should be possible for the first time to determine the separate structure functions $2xF_1^{\nu N}(x, Q^2)$, $2xF_1^{\bar{\nu} N}(x, Q^2)$, $F_3^{\nu N}(x, Q^2)$ and $F_3^{\bar{\nu} N}(x, Q^2)$. This in turn would allow much-improved knowledge of the individual sea-quark distributions.

2.3 The MINERνA Detector

To perform the full spectrum of physics outlined in this proposal, the MINERνA target/detector must be able to:

- Identify muons and measure their momentum with high precision,

- identify individual hadrons and π^0 and measure their momentum,

- measure the energy of both hadronic and electromagnetic showers with reasonable precision,

- minimize confusion of neutral-current and charged-current event classifications, and

- accommodate other nuclear targets.

These goals can be met by a relatively compact and active target/detector consisting of a central section of essentially solid scintillator bars (Figure 1). This central detector is surrounded on all sides by an electromagnetic calorimeter, a hadronic calorimeter and a magnetized muon-identifier/spectrometer. The detector has the approximate overall shape of a hexagon (to permit three stereo views) with a cross-section of 3.55 m minor and 4.10 m major axis. The length is up to 5.9 m depending on how close MINERνA can be placed to the MINOS near detector. The active plastic scintillator volume is 4.2 tons allowing variable sized fiducial volumes depending on the channel being studied. At the upstream end of the detector are nuclear targets consisting of 1 ton of Fe and Pb. Significant granularity and vertex-reconstruction accuracy can be achieved by the use of triangular-shaped extruded plastic scintillator(CH) bars with 3.3 cm base, 1.7 cm height and length up to 4.0 m, with an optical fiber placed in a groove at the base of the bar for readout. A second triangular shape with base 1.65 cm and height 1.7 cm (1/2 of the larger triangles) will be used in the barrel and downstream calorimeter detectors. Recent work at the Fermilab Scintillator R&D Facility has shown that using light division across triangularly shaped scintillator strips of this size can yield coordinate resolutions of a few millimeters. The orientation of the scintillator strips are alternated so that efficient pattern recognition and tracking can be performed.

Following the downstream end of the central detector are electromagnetic and hadronic calorimeters. MINERνA should be placed as close as possible to the upstream face of the MINOS near detector
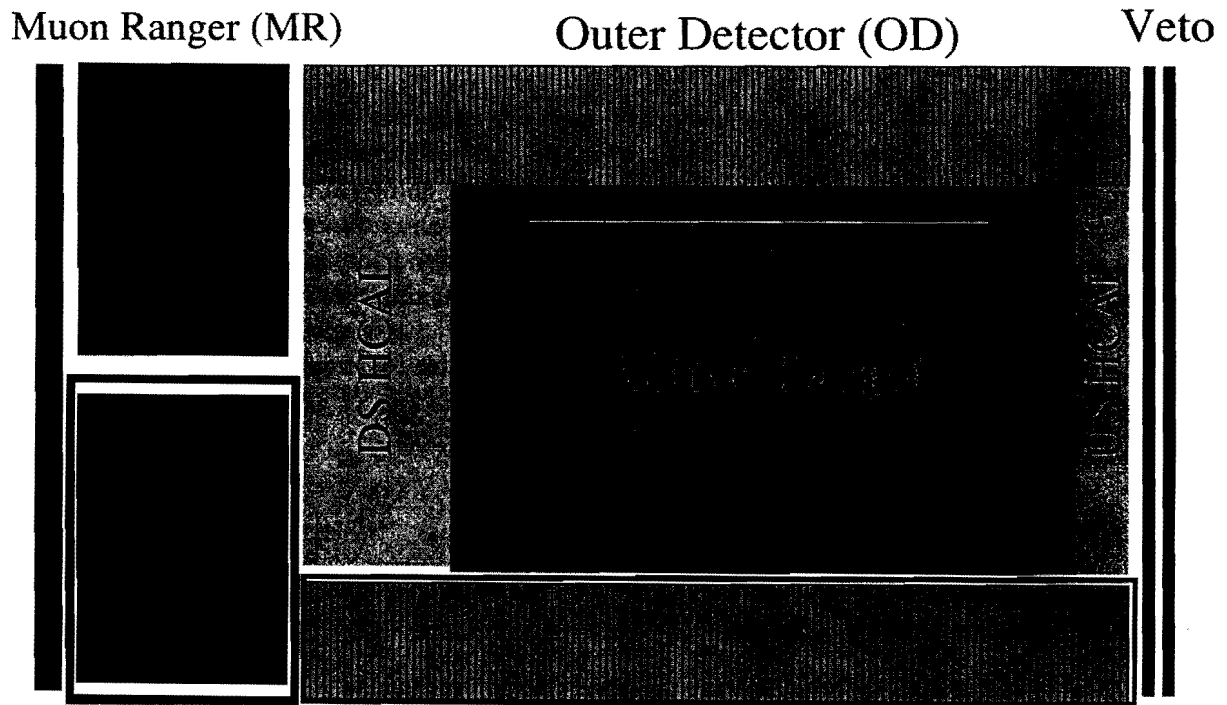
Figure 1: A schematic side view of the MINERνA detector with sub-detectors labeled. The neutrino beam enters from the right.

10

in order to use that detector's magnetic field and steel as an external muon-identifier and spectrometer for the forward-going muons, and as a calorimeter for any hadronic energy exiting MINERνA itself. Moving the MINERνA detector further upstream from the MINOS detector will decrease the acceptance for muons in the MINOS detector. If necessary a "muon ranger", consisting of 1.2 m of segmented and magnetised iron, will be added to help identify and measure the momentum of low-energy muons. For high-energy muons, the MINOS near detector will provide much better momentum resolution than the muon ranger.

With this design, even at the lowest beam-energy setting, MINERνA will collect more than 580 K events per 2.5×10^{20} POT in a 3 ton active target fiducial volume and just under 200 K events in each of the nuclear targets.

The statistics from a several-year MINOS run will suffice to study all the physics topics listed above, although some measurements would be limited in kinematic reach by the beam energies used for MINOS. In addition, all studies involving $\overline{\nu}$ channels would be somewhat limited with the currently-planned MINOS exposure, which includes relatively little $\overline{\nu}$ running.

3 Low-Energy Neutrino Scattering Overview

3.1 Form Factors and Structure Functions

Several formalisms are used to discuss electron-nucleon and neutrino-nucleon scattering, and the corresponding reactions on nuclear targets.

Inclusive lepton scattering can be described in the language of structure functions or in terms of form factors for the production of resonant final states. The two descriptions are equivalent and there are expressions relating form-factors to structure functions. In electron scattering, the vector form factors can be related to the two structure functions W_1 and W_2 (which are different for neutrons and protons), or equivalently F_2 and R.

In neutrino scattering, there are three structure functions W_1, W_2 and W_3 (or F_2, R and xF_3), different for neutrons and protons, and containing both vector and axial-vector components. There are also two other structure functions (important only at very low energies) whose contributions depend on the final-state lepton mass; these can be related to the dominant structure functions within the framework of theoretical models.

3.2 Electron versus Neutrino Scattering

From the conservation of the vector current (CVC), the vector structure functions (or form-factors) measured in electron scattering can be related to their counterparts in neutrino scattering for specific isospin final states. For elastic scattering from spin-$\frac{1}{2}$ quarks or nucleons, these relationships between vector form factors are simple. For production of higher spin resonances, the relations are more complicated and involve Clebsch-Gordon coefficients.

In contrast, the axial structure functions in neutrino scattering cannot be related to those from electron scattering, except in certain limiting cases (for example, within the quark/parton model at high energies with V=A). At low Q^2, the axial and vector form factors are different, e.g. because of the different interactions with the pion cloud around the nucleon.

Another difference arises from nuclear effects in inclusive neutrino vs. electron scattering. Nuclear effects on the axial and vector components of the cross-section can differ due to shadowing, and can also affect valence and sea quarks differently.

3.3 Sum Rules and Constraints

Several theoretical constraints and sum rules can be tested in electron and neutrino reactions (or applied in the analysis of data). Some of the sum rules and constraints are valid at all values of Q^2, and some are valid only in certain limits.

The Adler sum rules apply separately to the axial and vector parts of W_1, W_2, and W_3 and are valid for all values of Q^2 (since they are based on current algebra considerations). At high Q^2, these sum rules are equivalent to the statement that the number of u valence quarks in the proton minus the number of d valence quarks is equal to 1.

Other sum rules, such as the momentum sum rule (sum of the momentum carried by quarks and gluons is 1) and the Gross/Llewelyn-Smith sum rule (number of valence quarks is equal to 3), have QCD corrections and break down at very low Q^2.

As $Q^2 \to 0$, the vector structure functions are further constrained by the measured photoproduction cross-section. Conversely, as $Q^2 \to \infty$ it is expected that the structure functions are described by QCD

13

and satisfy QCD sum rules.

3.4 Final States

Quasi-elastic[1] reactions, resonance production, and deep-inelastic scattering are all important components of neutrino scattering at low energies.

To describe specific final states, one can use the language of structure functions, combined with fragmentation functions, at high values of Q^2. At low values of Q^2, many experiments describe the cross-sections for specific exclusive final states. Both of these pictures need to be modified when the scattering takes place on a complex nucleus.

Figure 2 shows the total neutrino and anti-neutrino cross-sections (per nucleon for an isoscalar target) versus energy (at low energies) compared to the sum of quasi-elastic, resonant, and inelastic contributions. These two figures also show the various contributions to the neutrino and anti-neutrino total cross-sections that will be investigated in this experiment.

---

[1]We should clarify that the neutrino community uses the term 'quasi-elastic' to describe a charged-current process in which a neutrino interacts with a nucleon to produce a charged lepton in the final state. The nucleon can be a free nucleon or a nucleon bound in the nucleus. The term 'quasi-elastic' refers to the fact that the initial state neutrino changes into a different lepton, and there is a single recoil nucleon in the final state (which changes its charge state). In contrast, the electron scattering community refers to electron-nucleon scattering with a single recoil nucleon as 'elastic' scattering. The term 'quasi-elastic' scattering is used by the electron scattering community to describe elastic electron-nucleon scattering from bound nucleons in a nucleus. Here the term 'quasi-elastic' refers to the fact that the bound nucleon is quasi-free. Both nomenclatures are used in the literature.
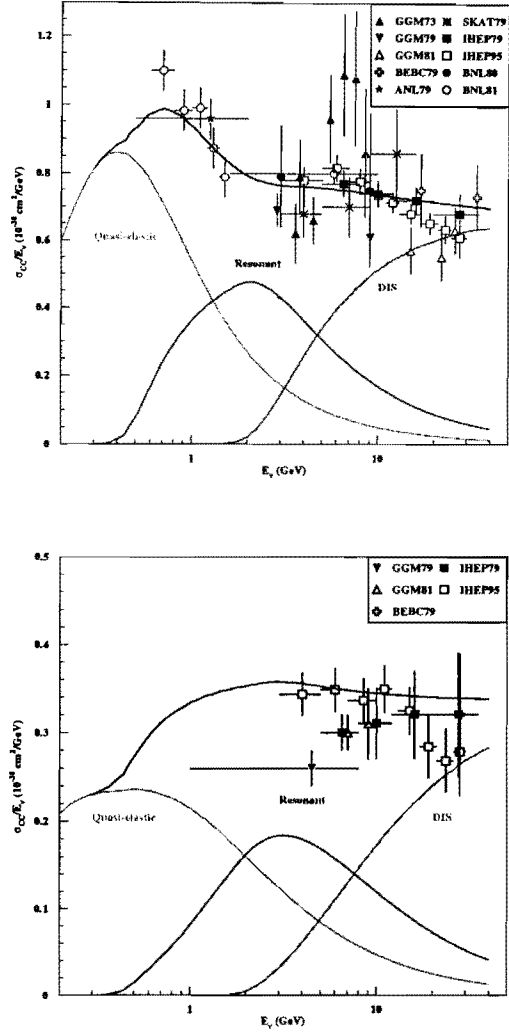
Figure 2: Total neutrino (top) and anti-neutrino (bottom) cross-sections divided by energy versus energy compared to the sum of quasi-elastic, resonant, and inelastic contributions from the NUANCE model. The sum is constructed to be continuous in W ($\equiv$ mass of the hadronic system) as follows. For $W > 2$ GeV the Bodek-Yang model is used. The Rein-Sehgal model is used for $W < 2$ GeV. In addition, a fraction of the Bodek-Yang cross-section is added to the Rein-Sehgal cross-section between $W = 1.7$ GeV and $W = 2$ GeV. The fraction increases linearly with W from 0 to 0.38 between $W = 1.7$ and $W = 2$ GeV.

15

4 Existing Neutrino Scattering Data

Neutrino experiments dating back to the 1960's have played an important role in particle physics, including discovery of neutral currents, electroweak measurements, determination of the flavor composition of the nucleon, measurements of the weak hadronic current, and QCD studies based on scaling violations in structure and fragmentation functions.

In the 1–10 GeV energy range of interest to the current and future generation of neutrino-oscillation studies, relevant data comes from bubble-chamber experiments that ran from the 1960's through the 1980's. Gargamelle, the 12-foot bubble chamber at the Argonne ZGS, the 7-foot bubble chamber at the AGS at Brookhaven, the Big European Bubble Chamber (BEBC) at CERN, the Serpukhov bubble chamber SKAT, and the FNAL 15-foot bubble chamber all studied neutrino and anti-neutrino interactions off free nucleons and heavy liquid targets. Spark-chamber and emulsion experiments from this era played a less prominent role but did make crucial measurements in a number of areas.

Despite limited statistics, the excellent imaging capabilities of bubble chambers made a wide range of physics topics accessible. It is primarily this data that is used to tune our Monte Carlo simulations and provides the basis for our present understanding of low-energy neutrino cross-sections. While adequate for validating the models at some level, most of the bubble-chamber data-sets are limited in size and do not cover the full range of neutrino energy, nuclear targets and neutrino species ($\nu/\bar{\nu}$) required for a complete understanding of neutrino interactions. Some of the main topics of interest for experiments of this era are described below. For each topic, an approximate count of the number of SPIRES publication references for is included.

4.1 Quasi-elastic Scattering

(**8 pubs**) Studies of quasi-elastic charged-current (CC) interactions were among the first results from bubble-chamber neutrino exposures, and are the primary tool for studying the axial component of the weak nucleon current. While data were taken on both light (H_2/D_2) and heavy (Neon/propane/freon) targets, no attempts were made to extract measurements related to the nuclear system. Rather, the nuclear system was treated as a complication needing corrections. In many instances even this correction was not done, and the published data are for interactions on nucleons in a particular nucleus. This helps account for the large spread in data points between different experiments in Figure 9.

4.2 Other Exclusive Charged-current Channels

(**19 pubs**) Total cross-section measurements and studies of differential distributions were made for both light and heavy targets in each of the three charged-current single-pion channels. In nearly all cases cuts were placed on the hadronic invariant mass (*e.g.* $W < 1.4 \, \text{GeV}/c^2$) to limit the analysis to the resonant region. The results are shown in Figure 4. Fewer experiments published cross-sections for two- and three-pion channels.

4.3 Neutral-current Measurements

(**22 pubs**) Neutral-current (NC) measurements fall into three categories: elastic measurements in dedicated experiments, single-pion exclusive final-state measurements, or NC/CC ratio measurements in the deep-inelastic scattering (DIS) regime. NC/CC ratio measurements were made at high energies and applied cuts on the energy transfer ν to isolate the DIS regime. Single-pion studies of the NC electroweak

17

couplings and the isospin characteristics of the hadronic current in the rsonance region suffered from lack of statistics. Table 1 summarizes the published data. These processes are of particular interest, as they constitute one of the primary backgrounds to ν_e appearance in oscillation experiments.

4.4 Hadronic Final States

(32 pubs) A number of publications were devoted to inclusive measurements of the hadronic system produced in neutrino interactions. Multiplicity measurements, transverse momentum distributions, inclusive particle production, fragmentation functions, and evaluation of the universality of hadron dynamics were studied. In this area, hadronic mass cuts (*e.g.* $W > 2$ GeV) were applied to limit the analysis to the DIS region.

4.5 Strange and Charmed Particle Production

(27 pubs) Because of their clear signatures in photographic quality bubble chambers, exclusive and inclusive measurements of strange and charm particle production were popular topics. A survey of these results is given in Section 9.3.

4.6 Total Cross-sections

(19 pubs) Total charged-current cross-section measurements were a staple of bubble-chamber experiments. Their data is shown in Figure 3. The large errors are due to a combination of low statistics and poor knowledge of the ν beam.

4.7 Structure Functions

(18 pubs) Numerous experiments, particulary those at higher energies (and of course all the large calorimetric neutrino detectors like CDHS, CCFR, NuTeV, etc that followed) measured structure functions. Neutrino experiments are complementary to studies with electron and muon beams as they allow extraction of the valence quark distributions through measurement of xF_3 as well as independent analysis of the strange quark content via di-muon production. These experiments made possible precision electroweak and QCD measurements with the NC/CC ratio and scaling violation in the structure functions.

4.8 Summary

Viewed from a historical perspective, the results from these experiments clearly reflected the topics of interest (and the theoretical tools available) *at the time they were performed.* A general trend is clear. These experiments focused on two regimes. First, low Q^2 scattering: the non-perturbative regime where the scattering takes place from a single nucleon. By measuring total and differential cross-sections for exclusive channels (like quasi-elastic and Δ production), these experiments studied in detail the weak hadronic current of the nucleon. Parton-model studies form a second, complementary class of experiments, studying scaling phemonena like total cross-sections, structure functions, scaling-variable distributions, and inclusive final-state dynamics, and applying kinematic cuts to remove resonant and quasi-elastic contributions.

This dichotomy reflects the fact that decent models only existed for the extreme perturbative and non-perturbative limiting cases. The resonant/DIS transition region, where perturbative QCD breaks

Experiment	Year	Reaction	Measurement	Events	Ref
Gargamelle	1977	$\nu/\bar{\nu}$ - propane/freon	semi-inclusive	ν: 1061	[25]
	1977	$\nu/\bar{\nu}$ - propane/freon	π production	$\bar{\nu}$: 1200	
Gargamelle	1978	$\bar{\nu}$-propane/freon	$\bar{\nu}(\pi^o)$	139	[26]
	1978	$\bar{\nu}$-propane/freon	$\bar{\nu}(\pi^-)$	73	
Gargamelle	1978	ν-propane/freon	$\nu\,p \rightarrow \nu\,p\,\pi^o$	240	[27]
	1978	ν-propane/freon	$\nu\,p \rightarrow \nu\,n\,\pi^+$	104	
	1978	ν-propane/freon	$\nu\,n \rightarrow \nu\,n\,\pi^o$	31	
	1978	ν-propane/freon	$\nu\,n \rightarrow \nu\,p\,\pi^-$	94	
Gargamelle	1979	$\nu/\bar{\nu}$ - propane/freon	$\nu(1\pi^o)$	178	[28]
	1979	$\nu/\bar{\nu}$ - propane/freon	$\bar{\nu}(1\pi^o)$	139	
BNL - Counter	1977	$\nu/\bar{\nu}$ - Al/C	$\nu(1\pi^o)$	204	[29]
	1977	$\nu/\bar{\nu}$ - Al/C	$\bar{\nu}(1\pi^o)$	22	
ANL - 12'	1974	ν-D_2/ν-H_2	$\nu\,p \rightarrow \nu\,n\,\pi^+$	8	[30]
	1974	ν-D_2/ν-H_2	$\nu\,p \rightarrow \nu\,p\,\pi^o$	18	
ANL - 12'	1980	ν-D_2	$\nu\,n \rightarrow \nu\,p\,\pi^-$	?	[31]
ANL - 12'	1981	ν-D_2	$\nu\,n \rightarrow \nu\,p\,\pi^-$	?	[32]
	1981	ν-D_2	$\nu\,p \rightarrow \nu\,p\,\pi^o$	8	
	1981	ν-D_2	$\nu\,p \rightarrow \nu\,n\,\pi^+$	22	
BNL 7'	1981	ν-D_2	$\nu\,n \rightarrow \nu\,p\,\pi^-$	200	[33]

Table 1: Neutral-current measurements

down, was avoided because a clear theoretical framework for it was not available. With the current generation of duality studies at JLab and elsewhere, this complex but fundamental region is just now being fruitfully probed.

Another area of difficulty was treatment of nuclear effects. While heavy targets gave bubble chambers increased target mass, the confounding effects of the nuclear environment on the target kinematics and observed final states were a topic which was largely ignored. Very few nuclear physics studies were ever carried out with neutrinos, and these had only the most naïve models available for comparison. These studies focused on nuclear rescattering of produced pions, shadowing and EMC effects, formation-zone studies, and inclusive production of slow particles. Neither the small samples nor the models available allowed neutrinos to probe the nuclear environment in detail.

These "holes" in existing neutrino data and related phenomenology are now becoming increasingly evident. The MINOS experiment, for instance, will see a wide-band beam of 1–50 GeV neutrinos. Since a significant fraction of the interactions in MINOS are in the "transition" region, and nearly all take place on Iron nuclei, the areas of study neglected during the bubble-chamber era begin to loom large. MINOS, and the neutrino-oscillation experiments that will follow it, will be forced to confront them to achieve maximum sensitivity. Part II of this proposal explains in detail how MINERνA will not only address fundamental topics in nuclear and neutrino physics, which are compelling in their own right, but also substantially improve the quality of results from future oscillation experiments.
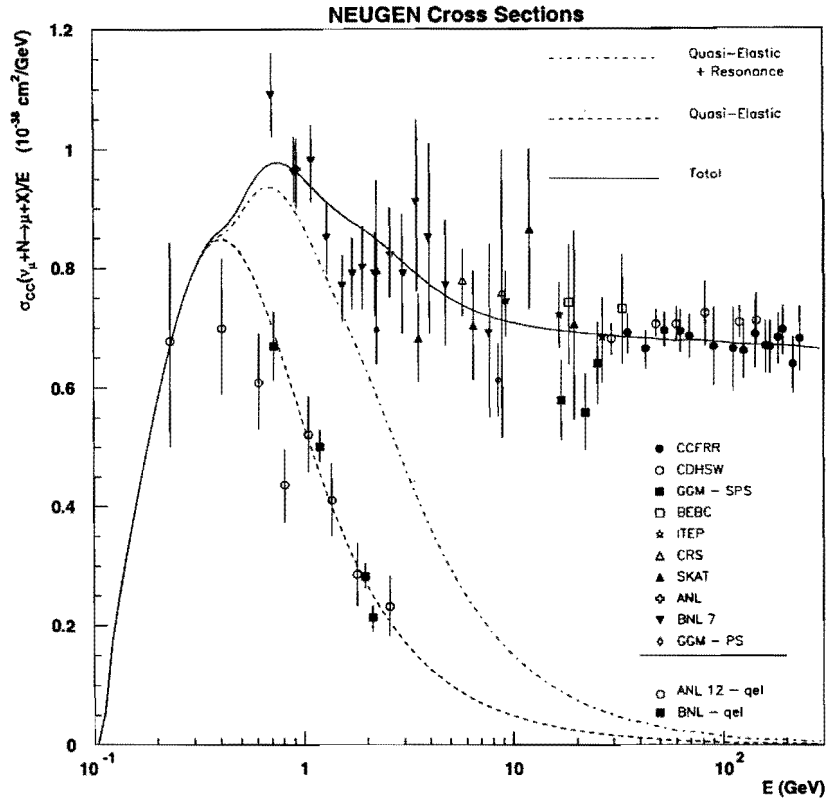
Figure 3: The NEUGEN prediction for the ν_μ charged-current cross-section (σ/E_ν) from an isoscalar target compared with data from a number of experiments. Quasi-elastic and single-pion contributions are also shown. Data are from: CCFRR [13], CDHSW [14], GGM-SPS [15], BEBC [16], ITEP [17], SKAT [18], CRS [19], ANL [20], BNL [21], GGM-PS [22], ANL-QEL [23], BNL-QEL [24].
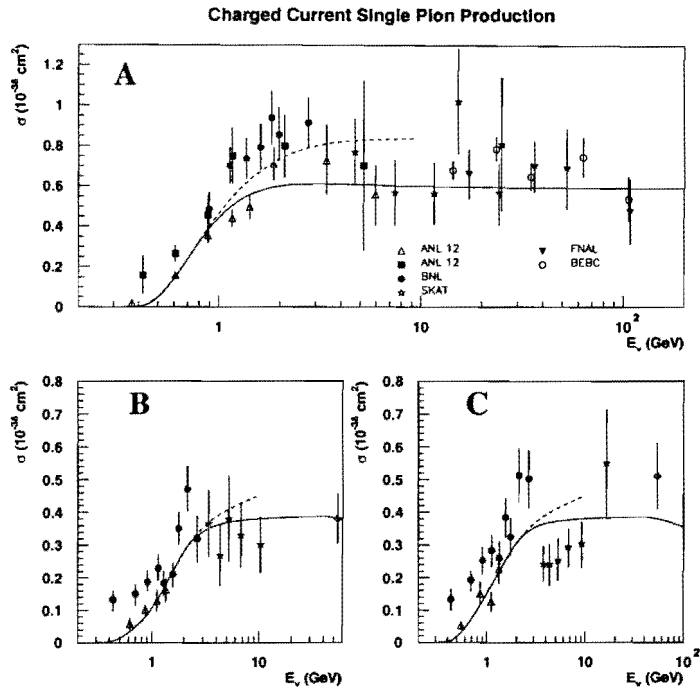
Figure 4: Cross-sections for charged-current single-pion production. Plot A: $\nu_\mu + p \to \mu^- + p + \pi^+$, Plot B: $\nu_\mu + n \to \mu^- + n + \pi^+$, Plot C: $\nu_\mu + n \to \mu^- + p + \pi^0$. Solid lines are the NEUGEN predictions for W<1.4 GeV (plot A) and W<2.0 GeV (plots B and C). The dashed curve is the NEUGEN prediction with no invariant mass cut, for comparison with the BNL data. Data are from: ANL [34, 20], BNL [35], FNAL [36], BEBC [37]

5   The NuMI Beam and MINERνA Event Sample

The NuMI neutrino beam is produced from π- and K-decay in a 675 m decay pipe beginning 50 m downstream of a double horn focusing system. At the end of the decay pipe a 10 m long hadron absorber stops the undecayed secondaries and non-interacting primary protons. Just downstream of the absorber, 240 m Dolomite is used to range out muons before the ν beam enters the near detector hall. Figure 5 shows the beam component and near detector hall layout.
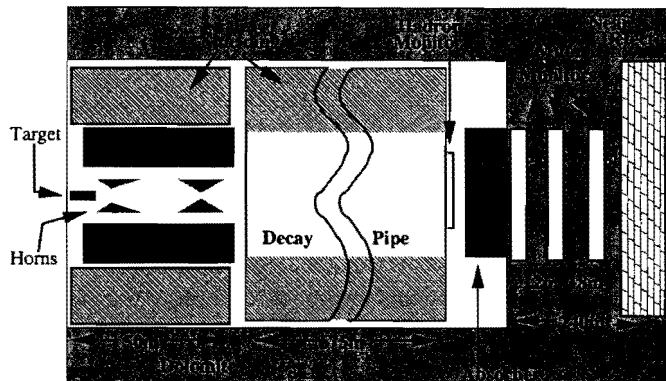
Figure 5: Layout of NuMI beamline components and near detector hall.

5.1   Energy Options

The neutrino energy distribution of the NuMI beam can be chosen by changing the distance of the target and second horn with respect to the first horn, as in a zoom lens. These three configurations result in three beam energy tunes for the low (LE), medium (ME), and high (HE) energy ranges respectively. However, to switch from one the beam mode into an alternate configuration will require down time to reconfigure the target hall and a loss of beam time. An alternative to this which allows the peak energy to be varied is to change the distance of target from the first horn and leave the second horn fixed in the LE position. This can be accomplished remotely with maximum transit of -2.5 m motion of the target upstream of the first horn from its nominal low energy position. The configurations corresponding to target -1.0 m from nominal results in a "semi-medium" energy beam tune (sME) and target -2.5 m from nominal will produce "semi-high" energy beam (sHE). These semi-beam configurations are less efficient and result in lower event rates than the ME and HE beams. A considerably more efficient sHE beam is possible with three-day downtime to allow the target to be moved back to its nominal HE position of -4.0 m. This more efficient sHE(-4.0) beam would yield over 50% more events than the sHE(-2.5) beam. For the MINOS experiment the beamline will be operating mainly in its lowest possible neutrino energy configuration to be able to reach desired low values of Δm^2. However, to minimize systematics, there will also be running in the sME and sHE configurations described above. The neutrino energy distributions for the LE, sME, and sHE running modes are shown in Figure 6. Figure 7 shows the event energy distributions for the ME and HE beam configurations for comparison.
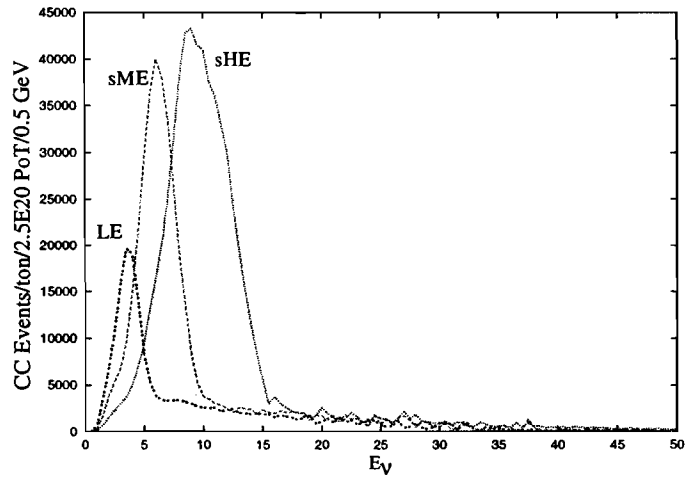
Figure 6: The neutrino charged-current event energy distribution for the three configurations of the NuMI beam corresponding to low-energy (LE), medium-energy (sME) and high-energy (sHE).
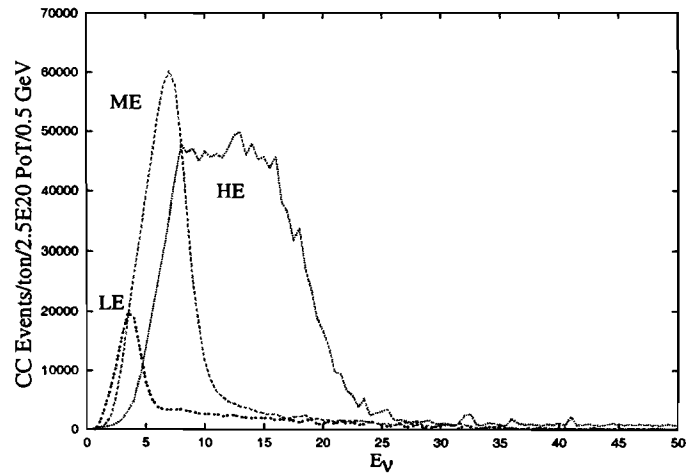
Figure 7: The neutrino charged-current event energy distribution for the high-rate medium and high-energy beam configurations (ME and HE) which involve movement of the second horn as well as target position.

24

5.2 MINERνA Event Rates

Table 2 shows the charged-current event rates per 10^{20} protons on target (PoT) per ton for the three beam configurations discussed above. In addition, the same configurations but with horn-current reversed provide anti-neutrino beams. Event rates for $\bar{\nu}_\mu$ charged-current events using anti-neutrino beam configurations (LErev, MErev, and HErev) are also shown along with their ν_μ background components. Running in these modes would be highly desirable for MINERνA physics.

CC Events/10^{20} PoT/ton		
Beam	CC ν_μ	CC ν_e
LE	78 K	1.1 K
sME	158 K	1.8 K
sHE	257 K	2 K
	CC $\bar{\nu}_\mu$	CC ν_μ
LErev	26 K	34 K
MErev	56 K	10 K
HErev	75 K	13 K

Table 2: MINERνA event rates for different beam configurations.

5.3 Baseline MINOS Run Plan

Table 3 shows a scenario for predicted PoT over a conservative hypothetical four-year MINOS run. From this table the total integrated charged-current event samples for a four-year MINERνA run would be 940 K ν_μ charged-current events per ton and 275 K $\bar{\nu}_\mu$ charged-current events per ton.

Scenario for PoT per year ($\times 10^{20}$)						
year	total PoT	LE	sME	sHE	LErev	MErev	HErev
2006	3.0	3.0	0.0	0.0	0.0	0.0	0.0
2007	4.0	3.0	0.7	0.3	0.0	0.0	0.0
2008	4.0	1.0	0.5	0.5	1.0	0.5	0.5
2009	4.0	1.0	0.5	0.5	0.0	0.5	1.0
total	15.0	7.0	1.2	0.8	3.0	1.5	1.5

Table 3: Hypothetical proton luminosity scenario for a four-year run.

5.4 MINERνA Data Samples

The event rates for physics processes of interest to MINERνA for the four-year scenario discussed in the previous section are summarized in the Table 4.

The distribution of the number of interactions expected for different x_{Bj} and Q^2 values are shown for the quasi-elastic, resonant and deep-inelastic channels in Tables 5, 6 and 7, respectively. The spread

25

of the quasi-elastic events in x is due to the smearing from the Fermi motion of the target nucleon. For clarity the x_{Bj} and Q^2 distributions of the total and deep-inelastic event samples are shown in Figure 8. These tables are based on the four-year scenario outlined in Table 3.

The number of interactions expected during the full four-year exposure of the detector in the NuMI beam eclipses the number of events recorded in the bubble-chamber experiments described in Section 4 by several orders of magnitude. The implications of this unprecedented event sample for physics are described in later sections. It would not be an exaggeration to observe that this large sample of neutrino interactions will reduce many of the systematic errors currently limiting the sensitivity of neutrino oscillation experiments and allow detailed study of kinematic regions that are presently rather poorly understood.

Were MINERνA the prime user of NuMI, the beamline would be run in the high-energy configuration with energies in the 5–25 GeV range. This configuration offers the ability to study neutrino interactions across an appreciable fraction of the x_{Bj} range at reasonable Q^2. In HE beam mode expected event rates would be 580 K charged-current ν_μ events per 10^{20} PoT per ton, over twice as many as the sHE(-2.5) beam.

5.5 Accuracy of Predicted Neutrino Flux

As mentioned earlier, one of the significant advantages of MINERνA over previous wide-band neutrino experiments is the expected accuracy with which the neutrino absolute and energy dependent flux is known. Since the NuMI beamline has been designed for the MINOS neutrino oscillation experiment, particular attention has been paid to control and knowledge of the beam of neutrinos being used in the experiment.

The biggest uncertainty in the predicted energy spectrum of the neutrinos comes directly from the uncertainty of hadron prodution spectrum of the π and K parents of the neutrinos. To help reduce this uncertainty, there is an approved Fermilab experiment E-907[11, 192] which has as it's main goal the measurement of hadron production spectra off various nuclear targets. One of the measurements that will be made by E-907 is an exposure of the NuMI target to the 120 GeV Main Injector proton beam. By using the NuMI target material and shape, E-907 will be able to provide the spectra coming off the target including all of the secondary and tertiary interactions which can significantly modify the produced spectra. It is expected that with the input from E-907, the absolute and energy dependent shape of neutrinos per POT will be known to $\approx 3\%$.

For the absolute flux of ν's there is a second uncertainty which must be considered and that is the accuracy with which we know the number of protons on target. With the planned NuMI primary proton beamline instrumentation[12], the number of protons on target will be known to between (1 - 3)%, the range being determined by the calibration techniques used to control drift of the primary beam toroid devices.

To summarize, the energy shape of the NuMI beam should be known to 3% while the absolute flux should be known to between (3 - 5)%.

Event Rates per ton		
Process	CC	NC
Elastic	103 K	42 K
Resonance	196 K	70 K
Transition	210 K	65 K
DIS	420 K	125 K
Coherent	8.3 K	4.2 K
Total	940 K	288 K

Table 4: Total event rates for different reaction types, per ton, for the four-year scenario outlined in Table 3.
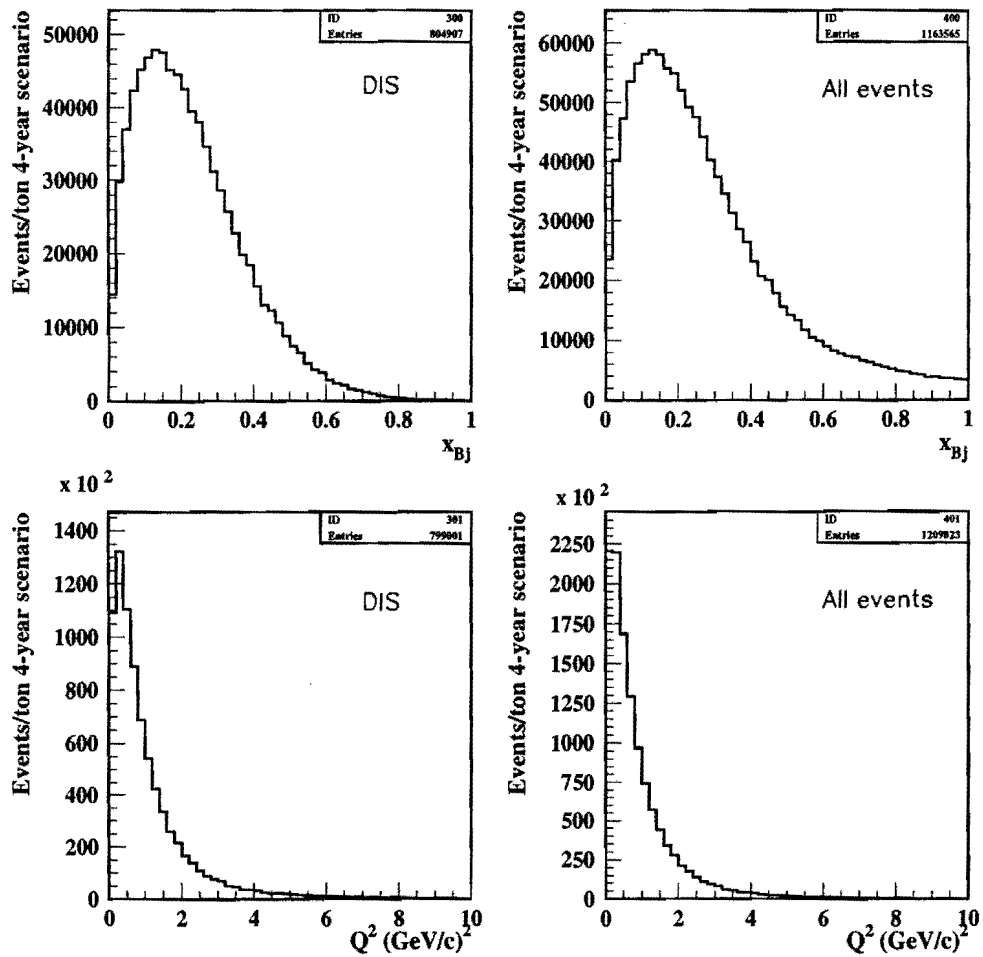
Figure 8: Kinematic distributions (x_{Bj} and Q^2) expected for deep-inelastic (top left and bottom left) and all event types (top right and bottom right).

Quasi-elastic events per ton vs. (x_{Bj}, Q^2) for four-year scenario								

	Q^2 (GeV/c)^2								
x_{Bj}	0.0-0.5	0.5-1.0	1.0-1.5	1.5-2.0	2.0-2.5	2.5-3.0	3.0-3.5	3.5-4.0	4.0+
0.0-0.1	1305	0	0	0	0	0	0	0	0
0.1-0.2	2287	0	0	0	0	0	0	0	0
0.2-0.3	3413	14	0	0	0	0	0	0	0
0.3-0.4	5127	136	12	1	0	0	0	0	0
0.4-0.5	7330	360	96	14	7	1	1	0	0
0.5-0.6	9573	1077	161	42	22	7	3	3	1
0.6-0.7	9902	3274	808	245	70	38	14	6	5
0.7-0.8	8871	4492	1740	737	345	133	70	51	36
0.8-0.9	7514	4396	2140	960	461	268	145	113	87
0.9-1.0	6872	4192	1979	1015	555	365	231	116	111

Table 5: Quasi-elastic interactions expected per ton for the four-year scenario of Table 3.

Resonant events per ton vs. (x_{Bj}, Q^2) for four-year scenario								

	Q^2 (GeV/c)^2								
x_{Bj}	0.0-0.5	0.5-1.0	1.0-1.5	1.5-2.0	2.0-2.5	2.5-3.0	3.0-3.5	3.5-4.0	4.0+
0.0-0.1	51011	98	0	0	0	0	0	0	0
0.1-0.2	44651	6786	197	0	0	0	0	0	0
0.2-0.3	26286	14782	2782	290	24	3	0	0	0
0.3-0.4	14877	14335	6049	1875	378	88	13	3	11
0.4-0.5	5400	12832	5844	3088	1282	460	128	56	24
0.5-0.6	1003	8645	5200	3173	1647	830	386	194	149
0.6-0.7	160	3737	4344	2495	1490	971	644	335	138
0.7-0.8	19	1160	2266	1934	1216	883	537	293	410
0.8-0.9	3	197	833	915	726	535	431	258	293
0.9-1.0	0	43	215	325	317	237	194	154	215

Table 6: Resonant interactions expected per ton for the four-year scenario of Table 3.

Deep-inelastic events per ton vs. (x_{Bj}, Q^2) for four-year scenario								
	Q^2 (GeV/c)^2							
x_{Bj}	0-2	2-4	4-6	6-8	8-10	10-12	12-16	16-20
0.0-0.1	25182	7190	1007	139	35	0	0	0
0.1-0.2	122542	43974	10281	3161	590	347	278	0
0.2-0.3	189545	65092	18687	7086	3994	1528	1563	70
0.3-0.4	60229	76519	19069	8996	4446	2397	2536	556
0.4-0.5	4133	45537	13755	7225	3994	2258	2535	1107
0.5-0.6	104	11254	9205	4863	2362	1667	1536	868
0.6-0.7	0	1077	2918	1910	1250	521	1042	208
0.7-0.8	0	104	486	695	521	382	521	224
0.8-0.9	0	35	69	0	35	104	173	35
0.9-1.0	0	0	0	0	0	30	35	20

Table 7: Deep-inelastic interactions expected per ton for the four-year scenario of Table 3.

Part II
Physics Motivation and Goals

6 Quasi-Elastic Scattering

6.1 Quasi-elastic Cross-sections

Quasi-elastic scattering makes up the largest single component of the total ν–N interaction rate in the threshold regime $E_\nu \leq 2$ GeV. Precision measurement of the cross-section for this reaction, including its energy dependence and variation with target nuclei, is essential to current and future neutrino-oscillation experiments. Figures 9 and 10 summarize current knowledge of neutrino and anti-neutrino quasi-elastic cross-sections. Among the results shown, there are typically 10–20% normalization uncertainties from knowledge of the fluxes. These plots show that existing measurements have large errors throughout the E_ν range accessible to MINERνA (Figure 9, upper plot), and especially in the threshold regime which is crucial to future oscillation experiments (Figure 9, lower plot). Figure 10 shows these large uncertainties extend to anti-neutrino measurements as well.

MINERνA will measure these quasi-elastic cross-sections with samples exceeding earlier (mostly) bubble-chamber experiments by two orders of magnitude. MINERνA will also perform the first precision measurement of nucleon form-factors for $Q^2 > 1$ (GeV/c)^2 using neutrinos.

Consistent and up-to-date treatment of the vector and axial-vector form-factors which characterize the nucleon weak current is essential to a realistic cross-section calculation. MINERνA collaborators have been active in this area for some time[39]. Recent parameterizations and fits published by Budd, Bodek and Arrington are hereafter referred to as "BBA-2003" results. The curves in Figures 9 and 10 are based on BBA-2003 form-factors, with the axial form-factor mass parameter set to $M_A = 1.00$ GeV$/c^2$. The solid curves are calculated without nuclear corrections, while the dashed curves include a Fermi gas model. The dotted curves are calculations for Carbon nuclei and include Fermi motion, Pauli blocking, and the effect of nuclear binding on the nucleon form-factors as modeled by Tsushima et $al.$[59].

Nuclear effects reduce the calculated cross-sections by $\geq 10\%$; this sensitivity to the details of nuclear physics shows that an understanding of final-state nuclear effects is essential to interpretation of quasi-elastic neutrino data. As as fine-grained tracking calorimeter, MINERνA is designed to facilitate systematic comparison of quasi-elastic scattering (and other exclusive channels) on a variety of nuclear targets, providing a vastly improved empirical foundation for theoretical models of these important effects.

6.2 Form-factors in Quasi-elastic Scattering

MINERνA's large quasi-elastic samples will probe the Q^2 response of the weak nucleon current with unprecedented accuracy. The underlying V-A structure of this current include vector and axial-vector form-factors whose Q^2 response is approximately described by dipole forms. The essential formalism is given by[40]

$$
< p(p_2)|J_\lambda^+|n(p_1) > =
$$
$$
\bar{u}(p_2)\left[\gamma_\lambda F_V^1(q^2) + \frac{i\sigma_{\lambda\nu}q^\nu \xi F_V^2(q^2)}{2M} + \gamma_\lambda\gamma_5 F_A(q^2) + \frac{q_\lambda\gamma_5 F_P(q^2)}{M}\right]u(p_1),
$$

where $q = k_\nu - k_\mu$, $\xi = (\mu_p - 1) - \mu_n$, and $M = (m_p + m_n)/2$. Here, μ_p and μ_n are the proton and neutron magnetic moments. It is assumed that second-class currents are absent, hence the scalar (F_V^3) and tensor (F_A^3) form-factors do not appear.
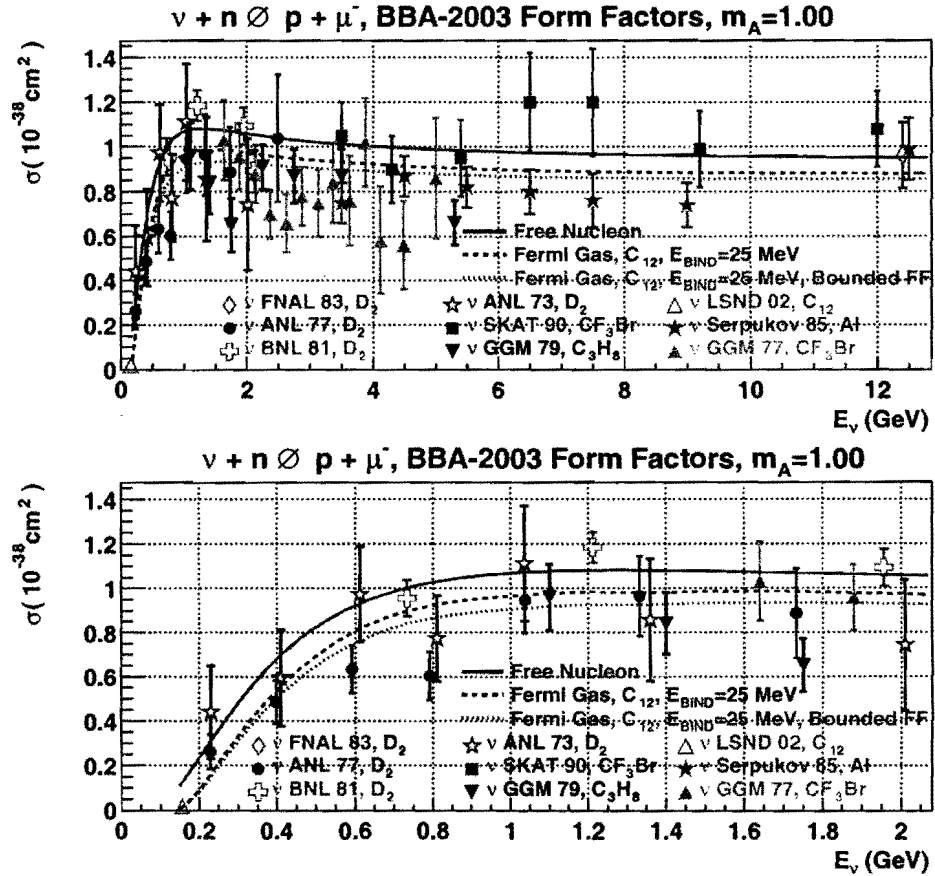
Figure 9: Compilation of neutrino quasi-elastic cross-section data. The data have large errors and are only marginally consistent throughout the E_ν range accessible to MINERνA (upper plot), and particularly in the threshold region (lower plot). Representative calculations are shown using BBA-2003 form factors with M_A=1.00 GeV. The solid curve is without nuclear corrections, the dashed curve includes a Fermi gas model [56], and the dotted curve includes Pauli blocking and nuclear binding. The data shown are from FNAL 1983 [47], ANL 1977 [23], BNL 1981 [24], ANL 1973 [49], SKAT 1990 [50], GGM 1979 [51], LSND 2002 [52], Serpukov 1985 [53], and GGM 1977 [54].

34

ν̄ + p ∅ n + μ⁺, BBA-2003 Form Factors, m$_A$=1.00
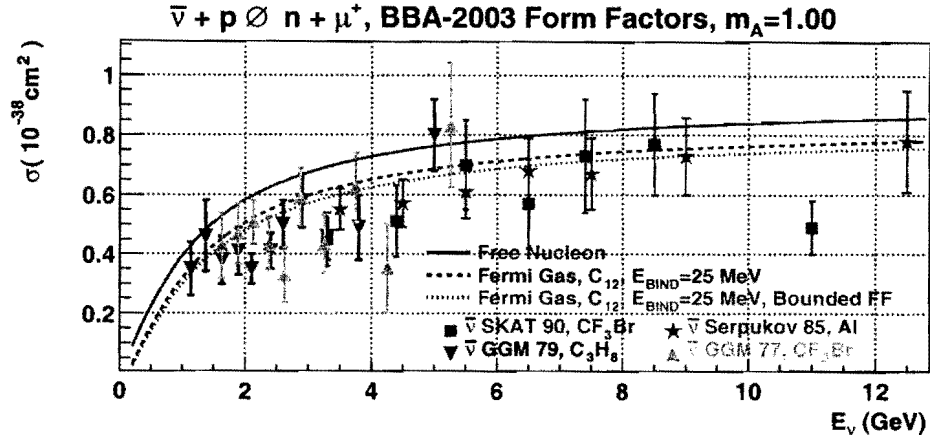
Figure 10: Compilation of anti-neutrino quasi-elastic cross-section data. As in Figure 9, the data have large errors, and considerable scatter among the different experiments. Theoretical predictions without (solid curve) and including nuclear corrections (dashed, dotted curves) are shown for comparison. The data shown are from SKAT 1990 [50], GGM 1979 [55], Serpukov 1985 [53], and GGM 1977 [54].

The form-factors $F_V^1(q^2)$ and $\xi F_V^2(q^2)$ are given by:

$$F_V^1(q^2) = \frac{G_E^V(q^2) - \frac{q^2}{4M^2} G_M^V(q^2)}{1 - \frac{q^2}{4M^2}}, \quad \xi F_V^2(q^2) = \frac{G_M^V(q^2) - G_E^V(q^2)}{1 - \frac{q^2}{4M^2}}.$$

According to the conserved vector current (CVC) hypothesis, $G_E^V(q^2)$ and $G_M^V(q^2)$ are directly related to form-factors determined from electron scattering $G_E^p(q^2)$, $G_E^n(q^2)$, $G_M^p(q^2)$, and $G_M^n(q^2)$:

$$G_E^V(q^2) = G_E^p(q^2) - G_E^n(q^2), \quad G_M^V(q^2) = G_M^p(q^2) - G_M^n(q^2).$$

The axial (F_A) and pseudoscalar (F_P) form-factors are

$$F_A(q^2) = \frac{g_A}{\left(1 - \frac{q^2}{M_A^2}\right)^2}, \quad F_P(q^2) = \frac{2M^2 F_A(q^2)}{M_\pi^2 - q^2}.$$

In the differential cross-section, $F_P(q^2)$ is multiplied by $(m_l/M)^2$, consequently its contribution to muon neutrino interactions is very small, except below 0.2 GeV. In general, the axial form-factor $F_A(q^2)$ can only be extracted from quasi-elastic neutrino scattering; at low q^2, however, its behavior can also be inferred from pion electroproduction data.

Until recently, it has been universally assumed that the form-factors' q^2 dependence is described by the dipole approximation. For example, the vector form factors are normally expressed:

$$G_D(q^2) = \frac{1}{\left(1 - \frac{q^2}{M_V^2}\right)^2}, \quad M_V^2 = 0.71 \ GeV^2$$

35

$$G_E^p = G_D(q^2), \quad G_E^n = 0, \quad G_M^p = \mu_p G_D(q^2), \quad G_M^n = \mu_n G_D(q^2).$$

As discussed below, the dipole parameterization is far from perfect, and MINERνA will be able to measure deviations from this form.

6.2.1 Vector form-factor discrepancy at high Q^2

Electron scattering experiments at SLAC and Jefferson Lab (JLab) have measured the proton and neutron electromagnetic (vector) form-factors with high precision. The vector form-factors can be determined from electron scattering cross-sections using the standard Rosenbluth separation technique[42], which is sensitive to radiative corrections, or from polarization measurements using the newer polarization transfer technique[44]. Polarization measurements do not directly measure form-factors, but rather the ratio G_E/G_M. These form-factors can be related to their counterparts in quasi-elastic neutrino scattering by the CVC hypothesis. Naturally, more accurate form-factors translate directly to improved calculations of neutrino quasi-elastic cross-sections.

Recently, discrepancies in electron scattering measurements of some vector form-factors have appeared; study of quasi-elastic reactions in MINERνA may help reveal the origin these discrepacies. Figure 11 shows the BBA-2003 fits to $\mu_p G_E^p/G_M^p$. There appears to be a difference between the two different methods of measuring this ratio. The fit including only cross-section data (*i.e.* Rosenbluth separation) is roughly flat in Q^2 and is consistent with form-factor scaling. This is expected if the electric charge and magnetization distributions in the proton are the same. However, the newer polarization transfer technique yields a much lower ratio at high Q^2, and indicates a difference between the electric charge and magnetization distributions. The polarization transfer technique is believed to be more reliable and less sensitive to radiative effects from two-photon corrections.
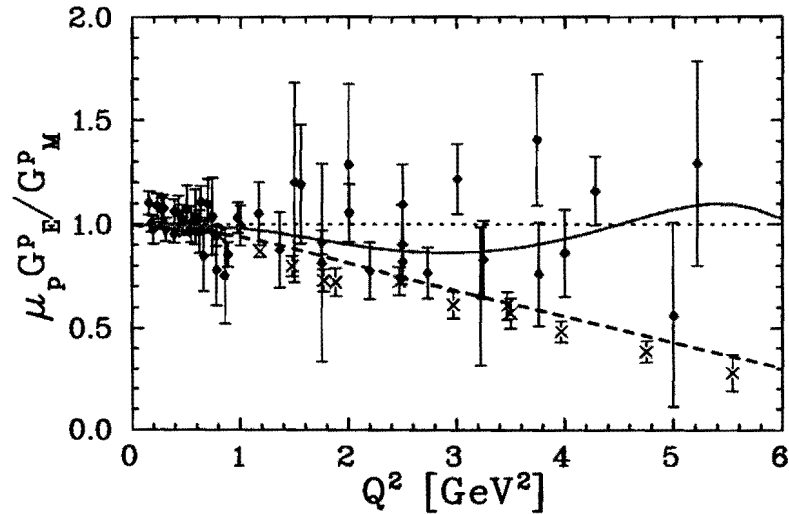
Figure 11: Ratio of G_E^p to G_M^p as extracted by Rosenbluth separation measurements (diamonds) and polarization measurements(crosses). The data are in clear disagreement at high Q^2.

If the electric charge and magnetization distributions of the proton are indeed different, a test of the axial form-factor's high-Q^2 shape can provide important new input to help resolve differences between

36

electron scattering measurements. As discussed below, MINERνA will be able to accurately measure the high-Q^2 behavior of F_A.

6.2.2 Form-factor deviations from dipole behavior

Electron scattering shows that dipole amplitudes provide only a first-order description of form-factor behavior at high Q^2. Figure 12 shows the deviation of G_M^p from dipolar Q^2 dependence. In general, these deviations are different for each of the form factors.
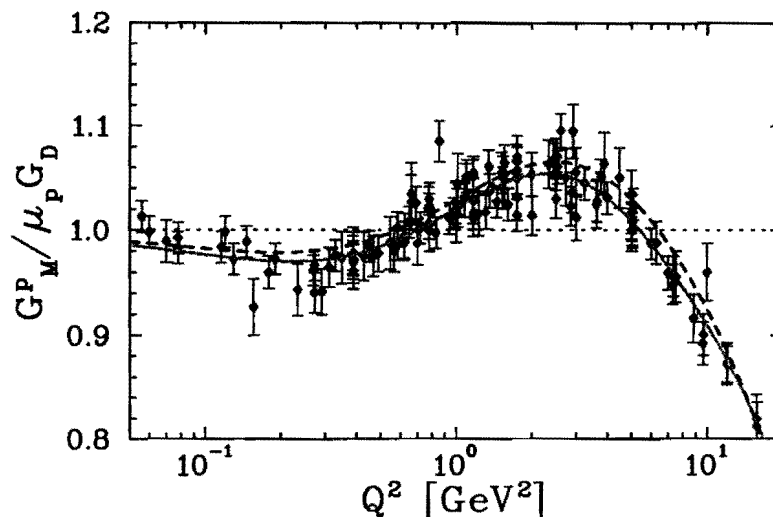
Figure 12: BBA-2003 fits to $G_M^p/\mu_p G_D$. The departure from 1.0 indicates deviation from a pure dipole form; the deviation is quite pronounced for $Q^2 > 1$ (GeV/c)^2.

Figure 13 shows the ratio of the BPA-2003 neutrino and anti-neutrino quasi-elastic cross-sections to the prediction using dipole vector form-factors (with $G_E^n = 0$ and M_A kept fixed). This plot shows that the importance accurately parameterizing the form-factors. In MINERνA, it will be possible to study the Q^2 dependence of the form-factors beyond the simple dipole dipole approximation which has been assumed by all previous neutrino experiments.

6.3 Axial Form-factor of the Nucleon

Electron scattering experiments continue to provide increasingly precise measurements of the nucleon vector form-factors. Neutrino scattering, however, remains the only practical route to comparable precision for the axial form-factors, in particular $F_A(Q^2)$. The fall-off of the form-factor strength with increasing Q^2 is traditionally parameterized using an effective axial-vector mass M_A. Its value is known to be ≈ 1.00 GeV/c^2 to an accuracy of perhaps 5%. This value agrees with the theoretically-corrected value from pion electroproduction[41], 1.014 ± 0.016 GeV/c^2. Uncertainty in the value of M_A contributes directly to uncertainty in the total quasi-elastic cross-section.

The fractional contributions of F_A, G_M^p,G_M^n,G_E^p, and G_E^n to the Q^2 distribution for quasi-elastic neutrino and anti-neutrino scattering with the NuMI beam are shown in Figure 14. The contributions are determined by comparing the BBA-2003 cross-sections with and without each of the form-factors
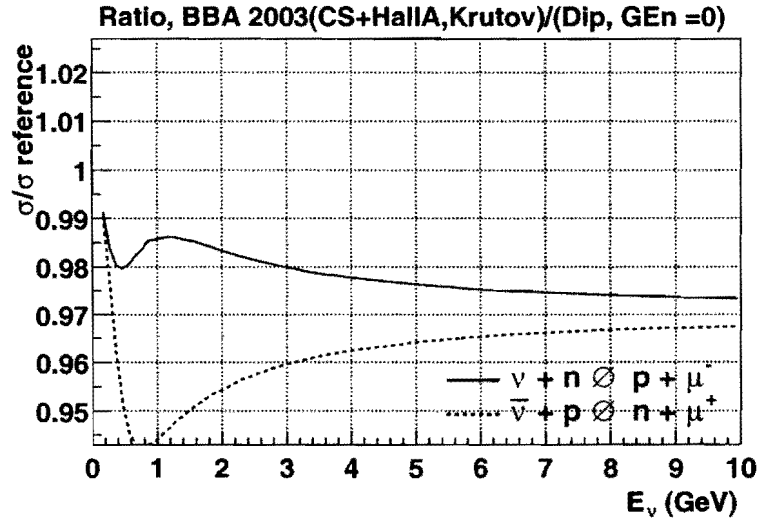
Figure 13: Ratio of the neutrino and anti-neutrino quasi-elastic cross-sections calculated with BBA-2003 form-factors to the simple dipole approximation with $G_E^n = 0$.

included. MINERνA will be the first systematic study of F_A, which accounts for roughly half of the quasi-elastic cross-section, over the entire range of Q^2 shown in the figure.
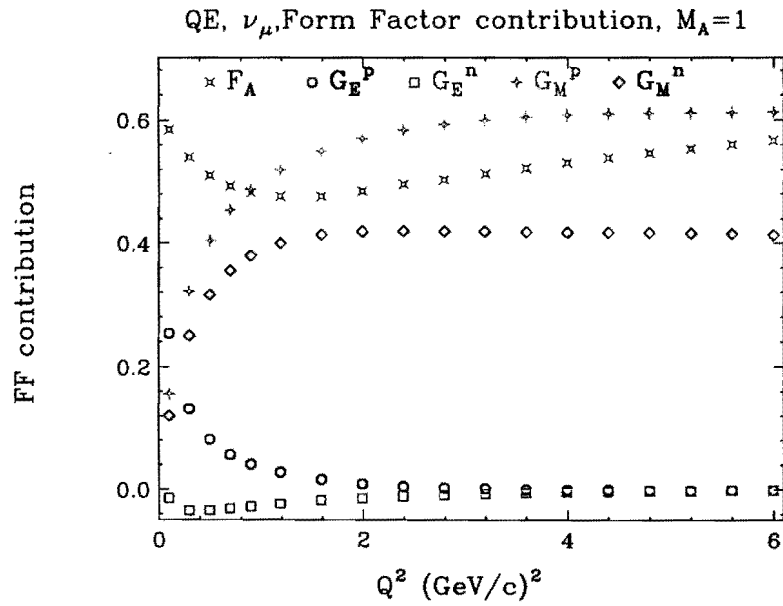
Figure 14: Fractional contributions of $G_M^p, G_M^n, G_E^p, G_E^n$ and F_A to the Q^2 distributions for quasi-elastic neutrino (top) and anti-neutrino (bottom) samples with the NuMI beam. Because of interference terms, the sum of the fractions does not necessarily add up to 100%.

6.3.1 Vector form-factors and M_A

Earlier neutrino measurements, mostly bubble-chamber experiments on Deuterium, extracted M_A using the best inputs and models available at the time. Changing these assumptions changes the extracted value of M_A. Hence, precision measurement of M_A requires starting with the best possible vector form-factors, coupling constants, and other parameters.
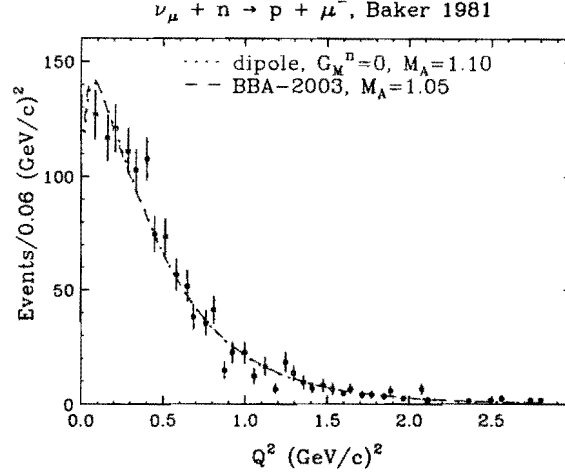
Figure 15: Comparison of Q^2 distributions using two different sets of form-factors. The data are from Baker et al.[24]. The dotted curve uses dipole form-factors with $G_E^n = 0$ and $M_A = 1.10$ GeV/c^2. The dashed curve uses more recent BBA-2003 form-factors and $M_A = 1.05$ GeV/c^2. It is essential to use the best possible information on vector form-factors from electron scattering experiments when extracting the axial form-factor from neutrino data.

Figure 15 shows the Q^2 distribution from the Baker et al.[24] neutrino experiment compared to the dipole form-factor approximation with $G_E^n = 0$ and $M_A = 1.100$ GeV/c^2. Also shown are BBA-2003 predictions with $M_A = 1.050$ GeV/c^2. Use of more accurate electromagnetic form-factors requires a different M_A value to describe the same Q^2 distribution. Thus, with the same value of g_A, adopting the dipole approximation (and $G_E^n = 0$) instead of the BBA-2003 form-factors may lead to an error in M_A of 0.050 GeV/c^2.

6.3.2 Measurement of the axial form-factor in MINERνA

Current and future high-statistics neutrino experiments at low energies (e.g. K2K, MiniBooNE, J-PARCnu and MINERνA) use an active nuclear target such as scintillator (mostly Carbon) or water (mostly Oxygen). The maximum Q^2 values that can be achieved with incident neutrino energies of 0.5, 1.0, 1.5 and 2 GeV are 0.5, 1.2, 2.1 and 2.9 (GeV/c)^2, respectively. Since K2K, MiniBooNE and J-PARCnu energies are in the 0.7–1.0 GeV range, these experiments probe the low $Q^2 < 1$ (GeV/c)^2 region where nuclear effects are large (see Figures 19 and 21) and where the free-nucleon axial form-factor is known rather well from neutrino data on Deuterium (see Figure 15). The low Q^2 ($Q^2 < 1$ (GeV/c)^2) MiniBooNE and K2K experiments have begun to investigate the various nuclear effects in Carbon and Oxygen.

At higher Q^2, as shown by the BBA-2003 fits, the dipole approximation for vector form-factors can
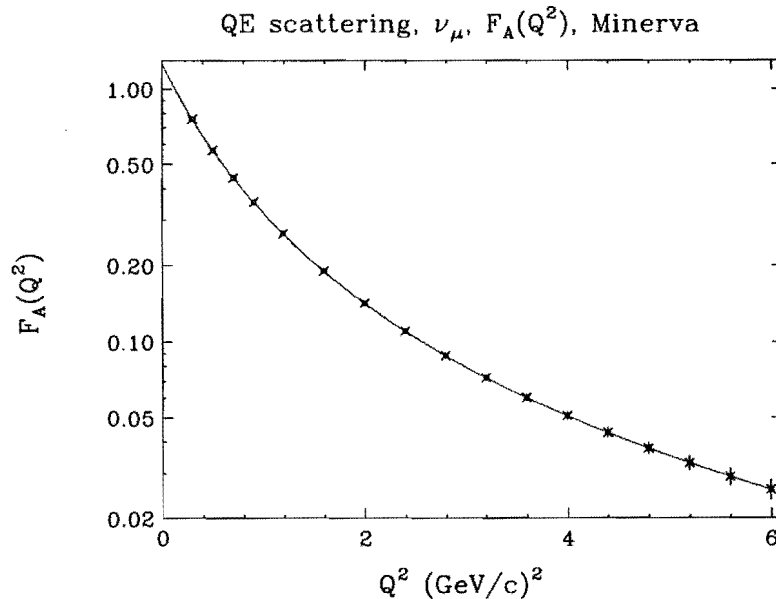
Figure 16: Estimation of F_A from a sample of Monte Carlo neutrino quasi-elastic events recorded in the MINERνA active Carbon target. Here, a pure dipole form for F_A is assumed, with $M_A = 1$ GeV/c^2. The simulated sample and error bars correspond to four years of NuMI running.

be in error by a factor of two when $Q^2 > 2$ (GeV/c)^2. There is clearly no reason to assume the dipole form will be any better for the axial form-factor. As shown in Figure 15 there is very little data for the axial form-factor in the high-Q^2 region (where nuclear effects are smaller). Both the low-Q^2 ($Q^2 <$ 1 (GeV/c)^2) and high-Q^2 ($Q^2 > 2$ (GeV/c)^2) regions are accessible in higher-energy experiments like MINERνA, which can span the 2–8 GeV neutrino energy range. MINERνA's measurement of the axial form-factor at high Q^2 will be essential to a complete understanding of the vector and axial structure of the neutron and proton.

Figure 16 shows the extracted values and errors of F_A in bins of Q^2 from a sample of simulated quasi-elastic interactions in the MINERνA active Carbon target, for a four-year exposure in the NuMI beam. Clearly the high-Q^2 regime, which is inaccessible to K2K, MinibooNE and J-PARCnu, will be well-resolved in MINERνA. Figure 17 shows the these results as a ratio of F_A/F_A(Dipole), demonstrating MINERνA's ability to distinguish between different models of F_A. MINERνA will be able to measure the axial nucleon form-factor with precision comparable to vector form-factor measurements at JLab.

Figure 18 shows a typical quasi-elastic event, as simulated in MINERνA.

6.4 Nuclear Effects in Quasi-elastic Scattering

6.4.1 Fermi gas model

There are three important nuclear effects in quasi-elastic scattering from nuclear targets: Fermi motion, Pauli blocking, and corrections to the nucleon form factors due to distortion of the nucleon's size and its pion cloud in the nucleus. Figure 19 shows the nuclear suppression versus E_ν from a NUANCE[58]
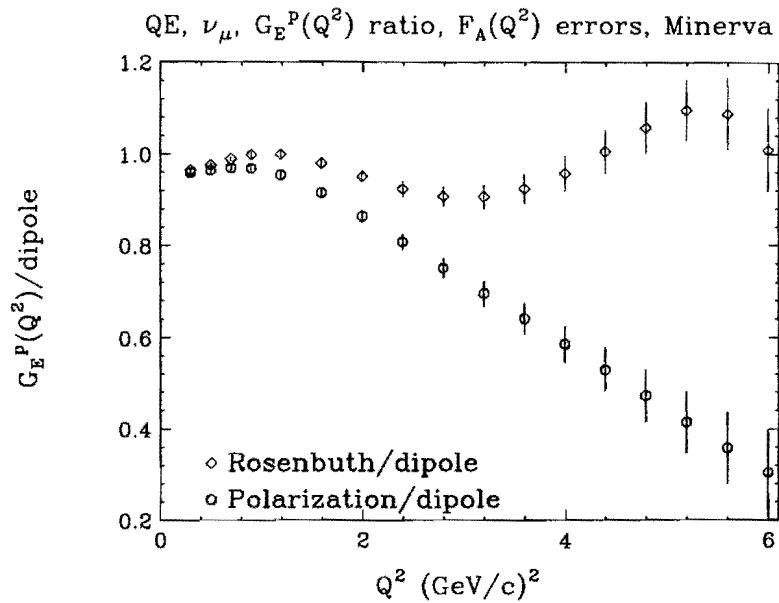
Figure 17: Extracted ratio F_A/F_A(Dipole) from a sample of Monte Carlo quasi-elastic interactions recorded in the MINERνA active Carbon target, from a four-year exposure in the NuMI beam. The lower points assume this ratio is described by the ratio of G_E^p(Cross-Section)/G_E^p(dipole), which was the the accepted result for G_E^p before new polarization transfer measurements. The upper points assumes a ratio of 1.0, which is expected if the axial form factor is described exactly by the dipole form.

MINERVA SIDE VIEW

Run   0 Event   20 Int Type QE
CC/NC   1 Mech. nu—n
Vertex (0.0,   0.0,1336.3)
PNEU 14 (0.0000,0.0000,2.2266,2.2266)
PLEP 13 (−.6252,−.4796,1.5804,1.7691)
x 0.952 q2 0.817 y 0.205 w2 0.9383
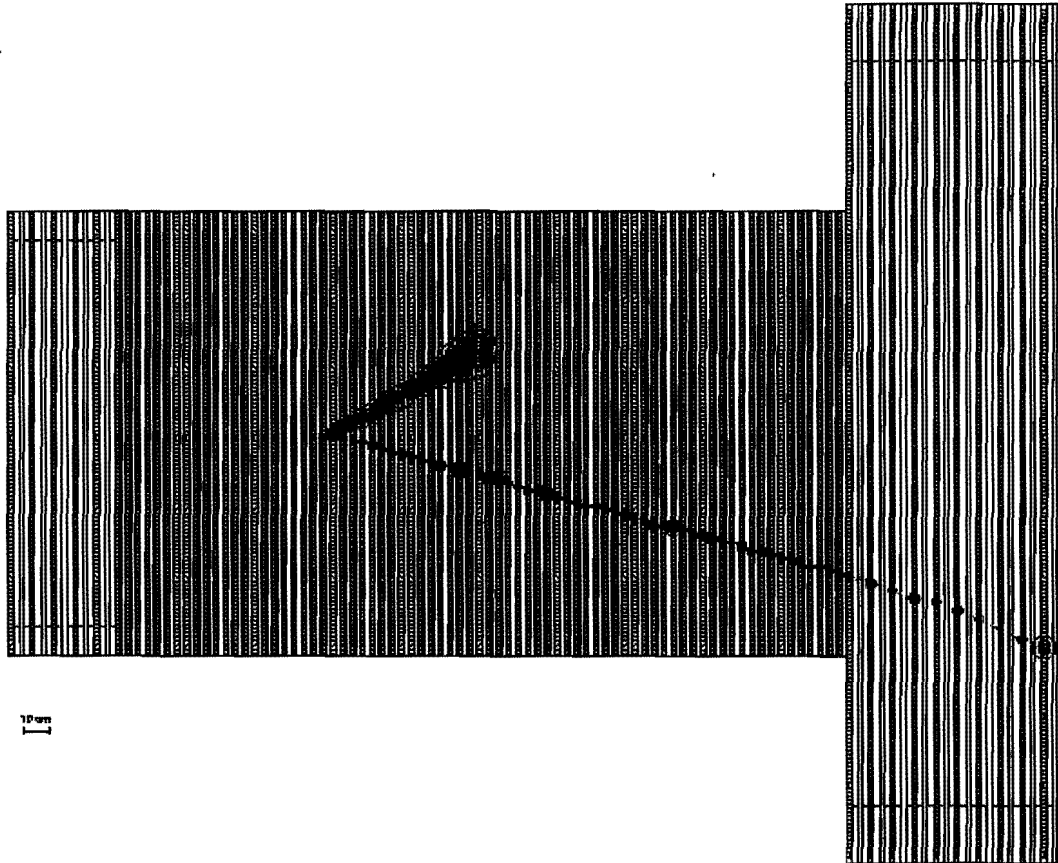
Figure 18: A simulated charged-current quasi-elastic interaction in MINERνA. The proton (upper) and muon (lower) tracks are well resolved. In this display, hit size is proportional to energy loss within a strip. The increased energy loss of the proton as it slows and stops is clear. Note that for clarity the outer detector has not been drawn.

calculation[56] using the Smith and Moniz[57] Fermi gas model for Carbon. This nuclear model includes Pauli blocking and Fermi motion but not final state interactions. The Fermi gas model uses a nuclear binding energy $\epsilon = 25$ MeV and Fermi momentum $k_f = 220$ MeV/c. Figure 20 from Moniz et. al.[57] shows how the effective k_f and nuclear potential binding energy ϵ (within a Fermi-gas model) for various nuclei is determined from electron scattering data. The effective k_f is extracted from the

42

width of the scattered electron energy distribution, and the binding energy ϵ from the shifted location of the quasi-elastic peak.
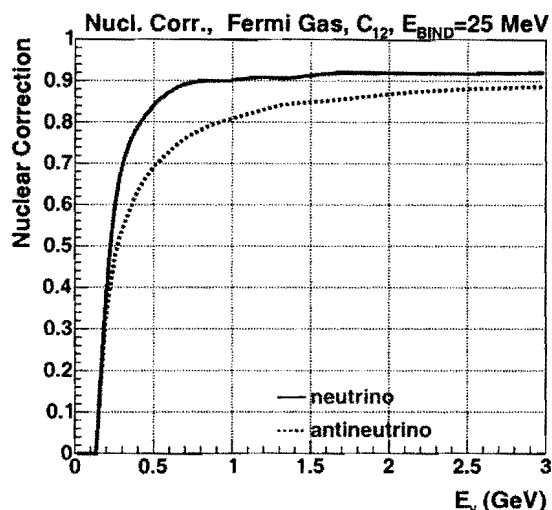
Figure 19: Pauli suppression in a Fermi gas model for Carbon with binding energy $\epsilon = 25$ MeV and Fermi momentum $k_f = 220$ MeV/c. A similar suppression is expected for quasi-elastic reactions in MINERνA.

6.4.2 Bound nucleon form-factors

The predicted distortions of nucleon form-factors due to nuclear binding are shown in Figure 21 as the ratios of F_1, F_2, and F_A for bound and free nucleons. With a variety of nuclear targets, MINERνA will be able to compare measured form-factors for a range of light to heavy nuclei.

6.4.3 Intra-nuclear rescattering

In neutrino experiments, detection of the recoil nucleon helps distinguish quasi-elastic scattering from inelastic reactions. Knowledge of the probability for outgoing protons to reinteract with the target remnant is therefore highly desirable. Similarly, quasi-elastic scattering with nucleons in the high-momentum tail of the nuclear spectral function needs to be understood. More sophisticated treatments than the simple Fermi gas model are required. Conversely, inelastic reactions may be misidentified as quasi-elastic if a final-state pion is absorbed in the nucleus. Because of its constrained kinematics, low-energy neutrino-oscillation experiments use the quasi-elastic channel to measure the (oscillated) neutrino energy spectrum at the far detector; the uncertainty in estimation of this background due to proton intra-nuclear rescattering is currently an important source of systematic error in the K2K experiment.

The best way to study these effects is to analyze electron scattering on nuclear targets (including the hadronic final states) and test the effects of the experimental cuts on the final-state nucleons. MINERνA can address proton intra-nuclear rescattering by comparing nuclear binding effects in neutrino scattering on Carbon to electron data in similar kinematic regions. Indeed, MINERνA members will be working
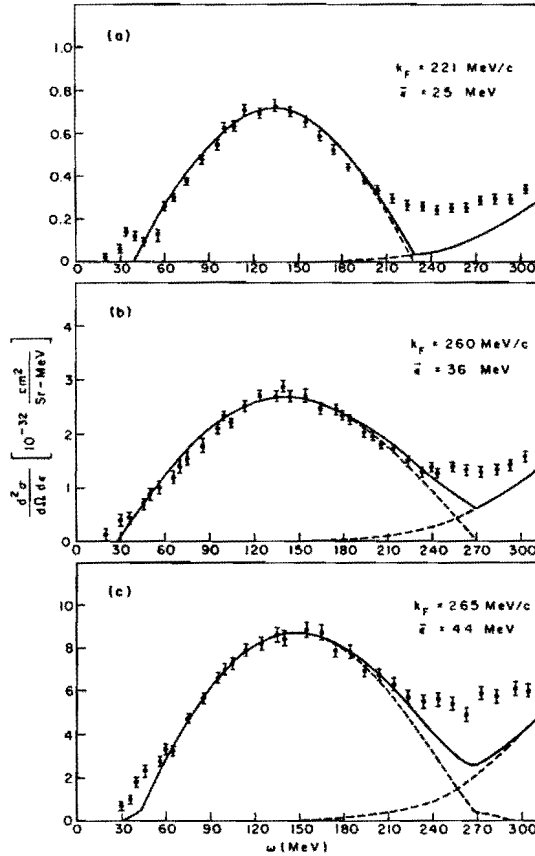
Figure 20: Extraction of Fermi gas model parameters, the effective Fermi momentum k_f and nuclear binding energy ϵ, from 500 MeV electron scattering data[57]. Distributions shown correspond to scattering from (a) Carbon, (b) Nickel, and (c) Lead.

with the CLAS collaboration to study hadronic final states in electron scattering on nuclear targets using existing JLab Hall B data. This analysis will allow theoretical models used in both electron and neutrino experiments to be tested. Other work in progress, with the Ghent[60] nuclear physics group, will develop the theoretical tools needed to extract the axial form-factor of the nucleon using MINERνA quasi-elastic data on Carbon. The ultimate aim is to perform nearly identical analyses on both neutrino and electron scattering data in the same range of Q^2.

Ratios of Bounded to Free Form Factors
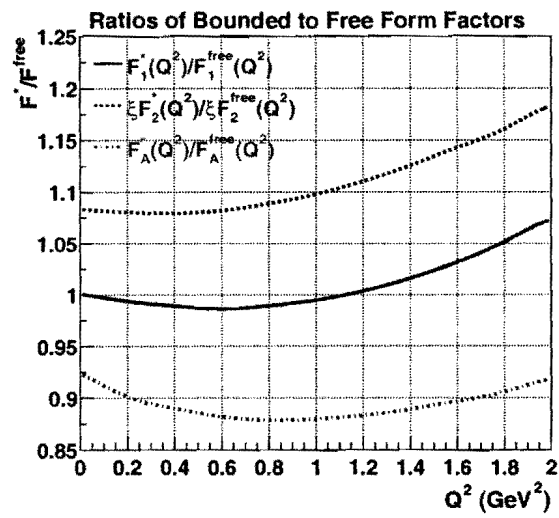
Figure 21: The ratio of bound (in Carbon) to free nucleon form-factors for F_1, F_2, and F_A from ref [59]. Binding effects on the form factors are expected to be small at higher Q^2 (therefore, this model is not valid for $Q^2 > 1$ (GeV/c)^2).

7 Resonance-Mediated Processes

Inclusive electron scattering cross-sections with hadronic mass $W < 2$ GeV/c^2 exhibit peaks corresponding to the $\Delta(1232)$ and higher resonances at low Q^2 (see Figure 22). This resonant structure is also present in neutrino scattering, although there is little data in this region. In addition to the natural interest in probing the nucleon weak current and axial structure via neutrino-induced resonance production, a better understanding of this process is essential for interpreting modern neutrino-oscillation and nucleon-decay experiments. This is particularly true for neutrinos in the region around 1 GeV, where single-pion production comprises about 30% of the total charged-current cross-section.
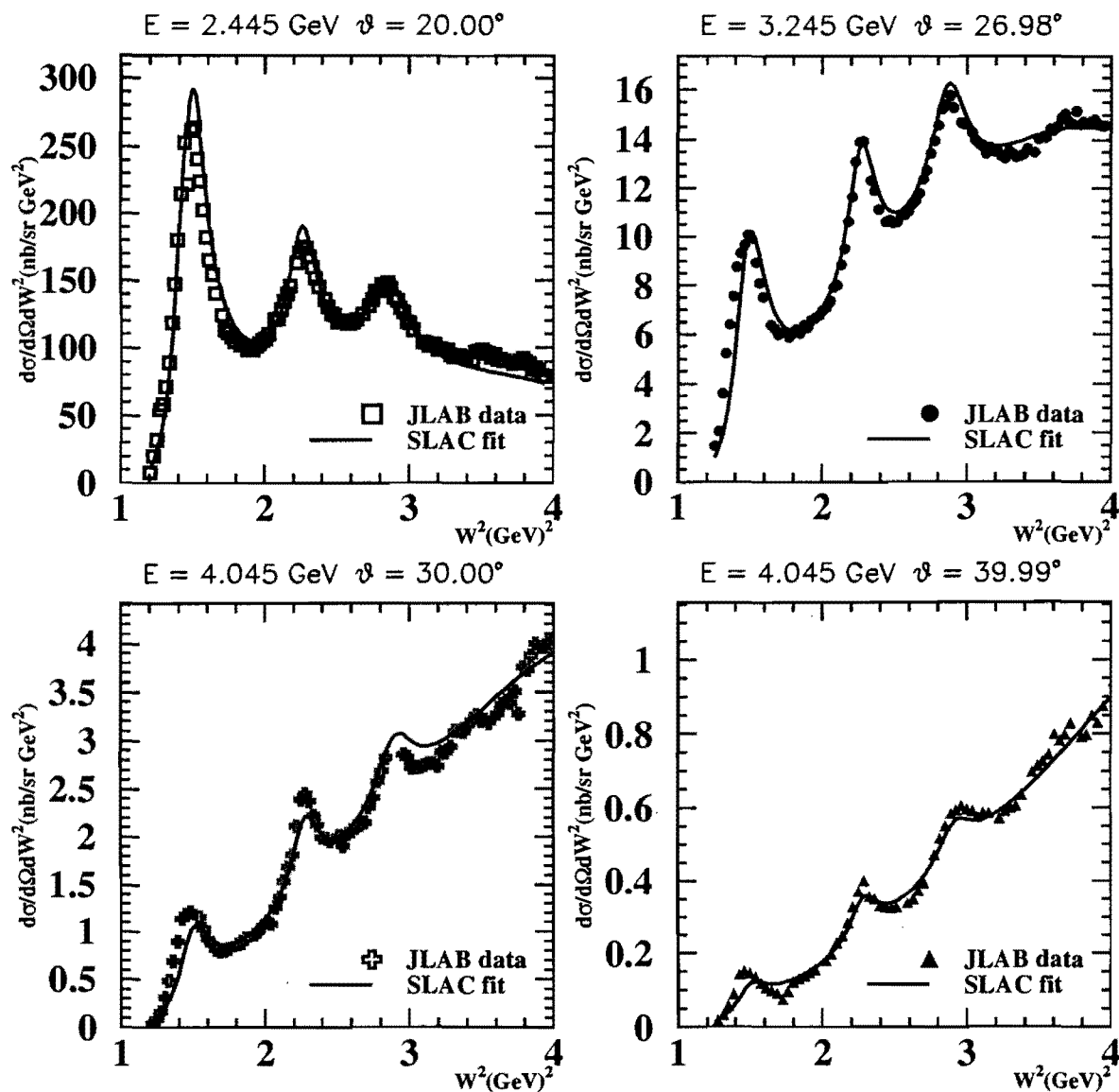
Figure 22: Inclusive electron scattering showing the Δ and higher resonances. Q^2 at the Δ peak is approximately 0.5, 1.5, 2.5 and 3.5 (GeV/c)^2 for the four spectra, respectively

47

In this kinematic region, neutrino Monte Carlo programs have relied on early theoretical predictions by Rein and Sehgal[70]. Recently Sato, Uno and Lee[68] have extended a model of Δ-mediated pion electroproduction to neutrino reactions. Also, Paschos and collaborators, using the formalism of Schreiner and von Hippel[69] have included the effects of pion rescattering and absorption for resonance production in nuclei.

7.1 Overview of Resonant Electroproduction

In electron scattering, the behavior of the $\Delta(1232)$ transition form-factor is considered to be a primary indicator of the onset of perturbative QCD (pQCD). The Q^2 behavior expected for a resonant spin-flip transition is dramatically different from the helicity conservation characteristic of perturbative descriptions. Comparison of the measured elastic and resonant form-factors reveals[71, 72, 73, 74, 75, 84] that while the nucleon and higher-mass resonant form-factors appear to approach the predicted Q^{-4} leading-order pQCD behavior around $Q^2 = 2$ (GeV/c)^2, the $\Delta(1232)$ transition form-factor decreases more rapidly with Q^2. One possible explanation[71] is that helicity-nonconserving processes are dominating. The Δ excitation is primarily a spin-flip transition at low momentum transfer, in which the helicity-nonconserving $A_{\frac{3}{2}}$ amplitude is dominant[76]. If the leading order $A_{\frac{1}{2}}$ helicity-conserving amplitude were also supressed at large momentum transfers, the quantity $Q^4 F$ would decrease as a function of Q^2.

Electromagnetic helicity matrix-elements correspond to transitions in which the initial state has helicity λ and the final states have helicity λ'. Transitions between a nucleon state $|N>$ and a resonant state $|R>$ can be expressed in terms of dimensionless helicity matrix-elements[71]:

$$G_\lambda = \frac{1}{2M} < R, \lambda' | \epsilon^\mu J_\mu | N, \lambda > \tag{1}$$

In this equation, the polarization vectors $\epsilon^{+,-,0}$ correspond to right- and left-circularly polarized photons, and longitudinally polarized photons, respectively. Following the formalism used by Stoler[72] and others, the differential cross-section may be written in terms of longitudinal and transverse form-factors G_E and G_T, as follows:

$$\frac{d^2\sigma}{d\Omega dE'} = \sigma_m f_{rec} \left[\frac{|G_E|^2 + \tau^* |G_T|^2}{1 + \tau*} + 2\tau^* |G_T|^2 \tan^2 \left(\frac{\theta}{2} \right) \right] R(W) \tag{2}$$

G_E and G_T are analogous to the Sachs form-factors for elastic scattering. In terms of the dimensionless helicity elements above,

$$G_E = G_0 \tag{3}$$

and

$$\tau^* |G_T|^2 = \frac{1}{2}(|G_+|^2 + |G_-|^2) \tag{4}$$

where

$$\tau^* = \frac{\nu^2}{Q^2} \tag{5}$$

The recoil factor f_{rec} is given by

$$f_{rec} = \frac{E'}{E_o} \tag{6}$$

48

$R(W)$ is the familiar Breit-Wigner expression[77] for the line-shape as a function of energy:

$$R(W) = \frac{2\pi^{-1}W_R M \Gamma_R}{(W^2 - W_R^2)^2 + W_R^2 \Gamma_R^2} \qquad (7)$$

The mass and width of the resonance are W_R and Γ_R.

Helicity is conserved in vector interactions of free, relativistic fermions. In the limit that a spin-$\frac{1}{2}$ parton is massless and free, its helicity must be conserved in interactions with a vector gluon or photon. At sufficient momentum transfer, the constituent quarks within a hadron can indeed be treated as massless and free, and the hadron helicity can be replaced by the sum of its constituent quark helicities[78, 79]. Therefore, at high Q^2, hadron helicity should also be conserved.

For resonant electroproduction, the scattering can be analyzed in the Breit frame of the $\lambda = 3/2$ Δ resonance. The incoming virtual photon can have positive, zero, or negative helicity. The outgoing resonance helicity can be calculated from angular momentum conservation[80]:

$$\lambda_\Delta = \lambda_\gamma - \lambda_N \qquad (8)$$

Hadron helicity is conserved when the incoming photon helicity is positive, and the Δ excitation emerges with the same helicity (1/2) as the initial nucleon state. This is described by the helicity amplitude $A_{\frac{1}{2}}$ given by:

$$A_{\frac{1}{2}} = \sqrt{\frac{2\pi\alpha}{\kappa}} G_+ \qquad (9)$$

κ is the energy of an equivalent on-mass-shell (real) photon producing a final mass state W:

$$\kappa = (W^2 - M^2)/2M \qquad (10)$$

Helicity is not conserved when $A_{\frac{3}{2}}$, given by

$$A_{\frac{3}{2}} = \sqrt{\frac{2\pi\alpha}{\kappa}} G_- \qquad (11)$$

is the dominant amplitude.

In terms of helicity amplitudes a dimensionless form-factor F may be defined where:

$$F^2 = |G_T(Q^2)|^2 = \frac{1}{4\pi\alpha} \frac{2M}{Q^2} (W_R^2 - M_N^2)|A_H(Q^2)|^2 \qquad (12)$$

Here,

$$|A_H(Q^2)|^2 = |A_{\frac{1}{2}}(Q^2)|^2 + |A_{\frac{3}{2}}(Q^2)|^2 \qquad (13)$$

At high Q^2, the helicity conserving amplitude should dominate the helicity-nonconserving amplitude. $A_{\frac{3}{2}}$ should be small compared to $A_{\frac{1}{2}}$ according to pQCD.

In leading-order pQCD, two gluons are exchanged among the three pointlike quarks. These gluon exchanges ensure that the final quarks, like the initial ones, have low relative momenta, so that no powers of Q^2 come from the wave functions. Form-factors calculated in the light-cone frame take the form [72]:

$$F(Q^2) = \int_0^1 \int_0^1 dx dy \Phi(x)^* T_H \Phi(y) \qquad (14)$$

49

where x and y are the initial and final longitudinal momentum fractions. $\Phi(x)$ and $\Phi(y)$ are the corresponding quark distribution amplitudes and T_H is the transition operator which is evaluated over all possible leading-order diagrams. This leads to the dimensional scaling rule[81]

$$G_+ \propto A_{\frac{1}{2}} \propto Q^{-3}, \tag{15}$$

or

$$F \propto Q^{-4} \tag{16}$$

This Q^2 dependence of the helicity amplitudes may be established up to factors involving $\ln(Q^2)$[82]. At high Q^2, where the quark helicities are conserved,

$$G_+ \propto Q^{-3} \tag{17}$$

$$G_0 \propto (\frac{m}{Q})G_+ \tag{18}$$

and

$$G_- \propto (\frac{m^2}{Q^2})G_+ \tag{19}$$

The prediction that $F(Q^2) \propto 1/Q^4$ if G_+ is dominant can be understood by combining the above with the definitions of $A_{\frac{3}{2}}$ and $A_{\frac{1}{2}}$ in the dimensionless form-factor expression.

In addition to this Q^2 dependence of the transition form-factors, pQCD makes definite predictions about the relative contributions of the magnetic dipole M_{1+}, electric quadrupole E_{1+}, and Coulomb quadrupole S_{1+} amplitudes. In quark models at low Q^2, the N $-$ Δ transition is primarily due to a single quark spin-flip, requiring the M_{1+} to be the dominant contribution[83]. At very low Q^2, near zero, experiments have confirmed this prediction, evaluating E_{1+} and M_{1+} at the resonance position. However, as noted, only helicity-conserving amplitudes should contribute at high Q^2, which leads to the prediction that the ratio $E_{1+}/M_{1+} = 1$. Results from Jefferson Lab[84] indicate that hadron helicity is not yet conserved at $Q^2 = 4$ GeV^2, finding the transition form-factor F to be decreasing faster than Q^{-4} and continued M_{1+} dominance. However, while pQCD apparently does not yet describe resonant excitation at these momentum transfers, it is not clear how constituent quark models can be appropriate at such high Q^2 values, and regardless, no single model describes all of the data well. The Delta resonance, then, remains an object of intense study at facilities like Jefferson Lab and Mainz, with future experiments planned.

7.2 Weak Resonance Excitation

Sato and Lee[67] have developed a dynamical model for pion photo- and electroproduction near the Δ resonance which is used to extract N $-$ Δ transition form-factors. Through this work, the aforementioned discrepenacy between the Δ transiton form-factor as calculated from a constituent quark model and the measured transition form-factor (a difference of about 35%) has been understood by including a dynamical pion cloud effect. Recently this work has been extended by Sato, Uno and Lee to weak pion production[68]. They show that the renormalized axial N $-$ Δ form-factor contains large dynamical pion cloud effects which are crucial in obtaining agreement with the available data (in this case, on Hydrogen and Deuterium). Contrary to previous observations, they conclude that the N $-$ Δ transitions predicted by the constituent quark model are consistent with existing neutrino-induced pion

50

production data in the Δ region. It is interesting to note that the pion cloud effect on the axial $N - \Delta$ form-factor is mainly to increase the magnitude. On the other hand, both the magnitude and the slope of the M_{1+} are significanlty changed by including pion cloud effects. The authors cite the need for more extensive and precise data on neutrino-induced pion-production reactions to test their model and to pin down the Q^2-dependence of the axial-vector $N - \Delta$ transition form-factor - data which MINERνA can certainly provide.

MINERνA will measure scattering on nuclei, at least in the first years without a hydrogen target, and comparison to improved data on a free proton target will not be possible. Still, as discussed in Section 10, the average Q^2 dependence of the cross-sections (and, hence, structure functions and form-factors) will be magnified by the Fermi smearing of the resonant enhancements. It should be possible to map out the Q^2-dependence of the axial-vector $N - \Delta$ form-factor. The work of Sato, Uno and Lee can be used as Monte Carlo input for MINERνA, and should be essential to predictions of Δ excitation in nuclei which can be compared directly with MINERνA data.

7.3 Nuclear Effects

Neutrino experiments rely heavily on detailed Monte Carlos to simulate the response of the rather complicated target / detector systems involved. The MINERνA simulation will be greatly enhanced by accurate descriptions of the nuclear effects involved. The majority of hadrons produced in inelastic scattering are pions, and so the nuclear attenuation of these must be taken into account. In considering hadron attentuation results from HERMES, Gaskell[91] suggests that a good first step is the one time scale parameterization, which goes as $(1 - z)\nu$. The A-dependence could then be taken into account via a simple $A^{2/3}$ scaling in $(1 - R_A)$, where R_A is the ratio of cross-section on nucleus A to deuterium.

Another relevant nuclear effect, currently being applied in neutrino event generators for protons but not pions, is termed color transparency (CT). Color transparency, first conjectured by Mueller and Brodsky [85] refers to the suppression of final (and initial) state interactions of hadrons with the nuclear medium in exclusive processes at high momentum transfers. CT is an effect of QCD, related to the presence of non-abelian color degrees of freedom underlying strongly interacting matter. The basic idea is that, under the right conditions, three quarks (in the case of the proton), each of which would normally interact strongly with the nuclear medium, can form an object that passes undisturbed through the nuclear medium. This small object would be color neutral outside of a small radius in order not to radiate gluons. Unambiguous observation of CT would provide a new means to study the strong interaction in nuclei.

Several measurements of the transparency of the nuclear medium to high energy protons have been carried out in the last decade. At Jefferson Lab, CT searches have concentrated on the quasi-elastic $A(e, e'p)$ reaction which has several advantages in the search for CT. To date, A(e,e'p) experiments at SLAC [86] and JLab [87] have found no evidence for the onset of CT at momentum transfers up to 8.1 $(GeV/c)^2$. However, there is some potential evidence for CT in $A(p, 2p)$ data from Brookhaven [88, 89].

It has been suggested that the onset of CT will be sooner in a $q\bar{q}$ system than in a three-quark system. Thus, the next best reaction in the expectation of CT is the $A(e, e'\pi)$ reaction. Current theoretical calculations suggest that most of this CT effect should be seen around $Q^2 = 10$ $(GeV/c)^2$, well within the MINERνA kinematic range. This effect has not yet been considered in neutrino Monte Carlos, nor has it been well studied in other processes. However, it will be well-measured in the Jefferson Lab kinematic regime prior to MINERνA[90], and should then be incorporable into the Monte Carlo.

51

7.4 Exclusive Channels

While there is a large body of inclusive (e, e') scattering data in the resonance region on hydrogen, deuterium and nuclei, more exclusive measurements have been rare until recently. With JLab $p(e, e'p)\pi^0$ spectrometer measurements[72, 84], the CLAS N^* program[65] and CLAS $^{12}C(e, e'X)$ data, more exclusive reactions are becoming available. This data will help to "calibrate" the vector current part of weak resonance/meson production models and to extend Delta resonance models such as that of Sato, Uno and Lee to higher resonances. These exlusive measurements are also naturally of interest because even to make inclusive measurements with neutrinos, the full final state must be observed and reconstructed. With the expected statistics and resolution of MINERνA, it should thus be possible to extract much more information about resonances than what is available in the inclusive channel.

Figure 23 from the CLAS[64] is an illustration of the type of just part of the information available when one or more reaction fragments are detected in resonance region electron scattering. One item of interest in this data is a peak observed near $W = 1.72\,\mathrm{GeV}/c^2$ in the spectrum for the $p\pi^+\pi^-$ final state. While an analysis of the angular distribution of this peak gives quantum numbers that agree with the PDG $N^*_{3/2+}(1720)$ state, the observed hadronic properties (coupling amplitudes) of this resonance are quite different from what is predicted from the PDG state. This illustrates that electro-weak excitiation of baryon resonances is an active field and that MINERνA measurements are timely.

7.5 Expected Results

Resonance production measurements in MINERνA can be grouped into several categories:

1. Measurement of inclusive (ν_μ, μ^-) and (ν, ν) spectra in the resonance region: As is done in the deep-inelastic region, this implies extraction of structure functions which can be compared to structure functions and form-factors from electron scattering. The experimental method is the same as for DIS events. For each event, we sum up the energies and momenta of the muon and all final state hadrons (either pions and nucleons, or all nucleons if the pions from resonance decay get absorbed on their way out of the nucleus) to get the total neutrino energy, and calculate Q^2 and W, y etc. This kind of analysis will be done as a function of W for the entire resonance region.

   Although these measurements are done on a nucleus, we will be able to compare results to resonance production predictions (such as Rein Seghal[70]) on nucleons, with some guidance from electron scattering. Because inclusive measurements are a sum over all final states, nuclear effects should be primarily limited to Fermi motion and some Pauli Blocking. Despite the Fermi motion and resolution of MINERνA, the Delta resonance will still be clear so it's form factor as a function of Q^2 can be measured. The higher resonances will be smeared out, but still can be compared to "smoothed" behaviour of resonance models and to predictions from duality. One practical result of measurements above the Delta resonanance may be to modify the amount of non-resonant background in the resonance region models used in neutrino event generators.

2. Examination of specific final state reaction products (single pion production, inclusive pion spectra): Specific final states, through the reactions: $(\nu_\mu, \mu^- p\pi^+)$, $(\nu_\mu, \mu^- n\pi^+)$, $(\nu_\mu, \mu^- p\pi^0)$, $(\nu_\mu, \nu_\mu^- n\pi^0)$, $(\nu_\mu, \nu_\mu^- p\pi^0)$, and $(\nu_\mu, \nu_\mu^- n\pi^+)$, are useful in selection of a specific final state isospin.

   These final state measurements will rely on an improved understanding of final state interactions and will benefit from electron scattering hadron transparency studies and CLAS $^{12}C(e, e'X)$ data

52
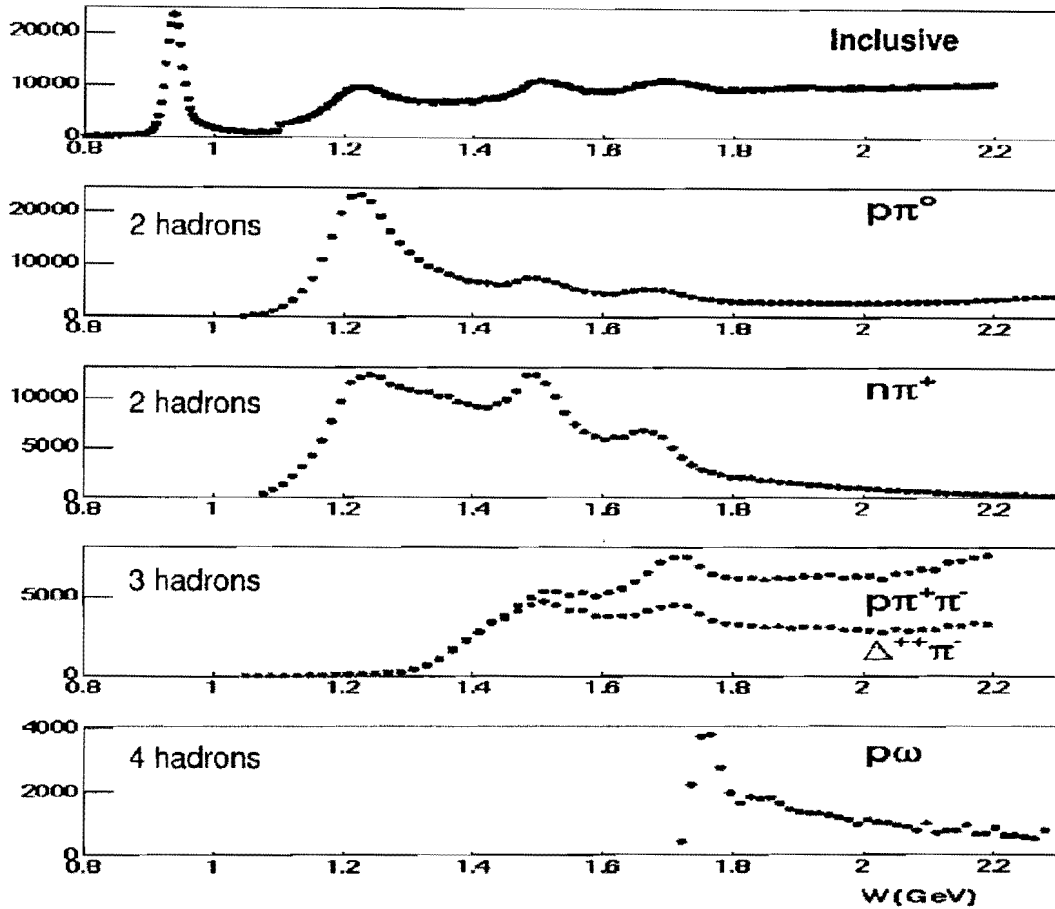
Figure 23: Invariant mass spectra from $p(e, e'X)$ demonstrating the multi-hadron reconstruction capability in the JLab CLAS spectrometer.[64]

(which includes $(e, e'p\pi^0)$, and $(e, e'n\pi^+)$, and which are equivalent to two of the above neutrino reactions). With these inputs, we will be able to map out the Q^2 dependence of the Axial vector $N - \Delta$ form factor. But even without this better understanding, angular distributions should be less affected by final state interactions than overall cross sections. Thus, we will be able to extract ratios of weak transition amplitudes to compare to similar electron scattering amplitudes

As measurement of detailed angular distributions of these final states is possible, the data on nuclear targets can also be used to study the feasibility of doing a phase shift analysis of the data if a hydrogen target is used in later phases of this experiment. This phase shift analysis, recommended by Sato, Uno and Lee[68], like the JLab CLAS N^* program, would be aimed at extracting the $N - \Delta$ form factor model independently and providing a better understanding of low-lying nucleon resonances.

3. Using resonance production as a tool to study final state interactions: Having a selection of nuclear targets helps here as the A dependence of the various reactions channels listed above can be studied. Another analysis that can be done along these lines is to measure inclusive pion spectra.

53
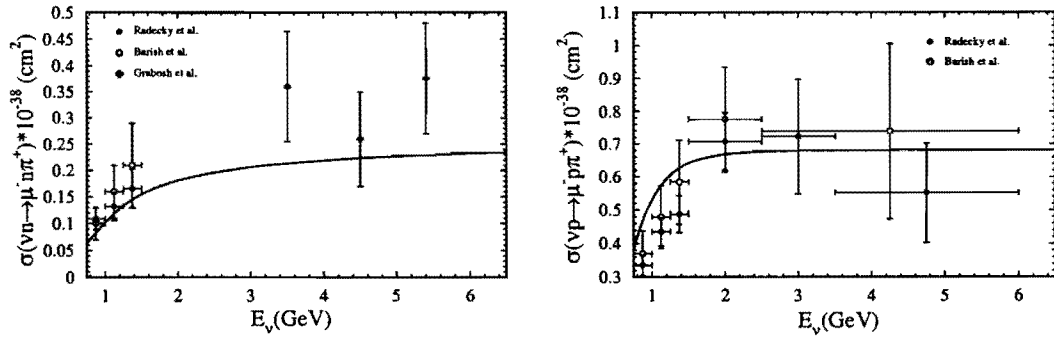
Figure 24: Total pion production cross-sections.

Paschos et.al.[6] combine resonance production and final state interactions to make predictions of pion spectra from neutrino scattering on nuclei. These spectra (Fig. 25 can be easily convoluted with neutrino beam energy distributions to produce pion energy distributions that can be directly compared with our data.

7.5.1 Complementary studies at JLab

The analysis of the above types of measurements will be closely coordinated with complementary experiments at Jefferson Laboratory (which are led by members of the MINERνA collaboration). The following are the Jefferson Laboratory electron scattering experiments in Hall C that are connected with measurments of inclusive scattering in the resonance region at MINERνA.

1. JLab hydrogen experiment E94-110 (investigates inclusive F_2 and R in the resonance region). C.E. Keppel spokesperson (data already taken).

2. JLab deuterium experiment E02-109, investigates inclusive F_2 and R in the resonance region. C.E. Keppel, M. E. Christy, spokespersons (approved to run in 2004).

3. JLab experiment E99-118 investigates nuclear the dependence of F_2 and R at low Q^2 for high values of W. A. Brull, C.E. Keppel spokespersons (data already taken).

4. Jlab experiment E02-103 hydrogen and deuterium resonance F_2 data at high Q^2 approved by Jlab PAC24 to run in 2004 (J. Arrington, spokesperon)

5. Jlab Proposal PR03-110 to investigate F_2 and R in the resonance region with nuclear targets. A. Bodek and C. E. Keppel, spokespersons (proposed to run in Hall C together with E02-109 in 2004) to provide vector resonance form factors and R on the same nuclear targets that are used in neutrino experiments (e.g. Carbon, Iron, Lead).

The following are collaborative programs between the electron scattering community that are connected with measurements of final states in the quasielastic region and in the region of the first resonance at MINERνA.

54
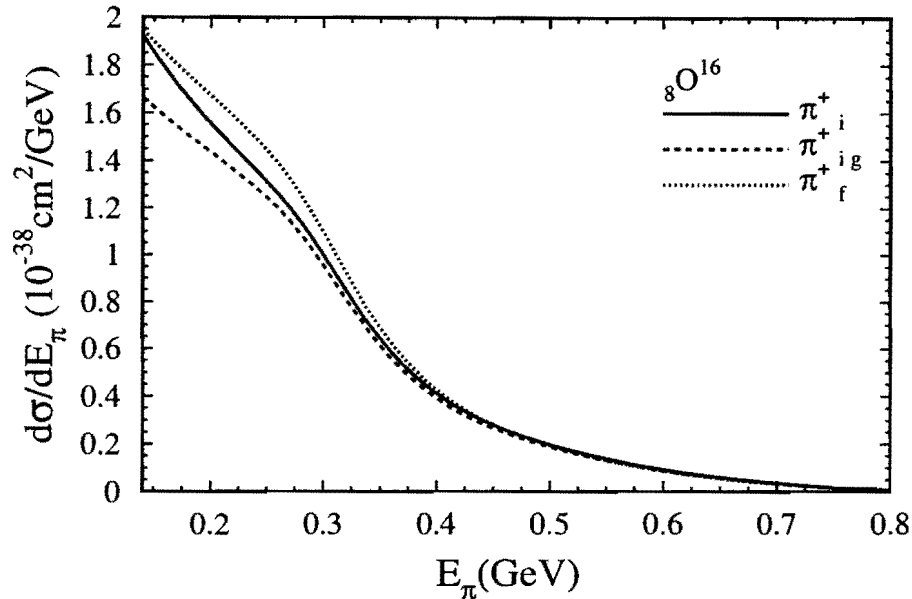
Figure 25: Predicted π^+ energy distribution for ν_μ scattering on ^{16}O of Paschos et. al.[6].

1. Steve Manly (Rochester) and Will Brooks (Jlab) program to use existing Hall B CLAS data at Jefferson Laboratory to study hadronic final states in electron scattering on nuclear targets (e.g. Carbon).

2. Work with the Argonne group of Lee to model first resonance production in the region of the first resonance and also Ghent nuclear physics group in Belgium [60], to model both electron and neutrino induced final states. In addition, there are other theoretical efforts (e.g. Sakuda and Paschos[6]) on nuclear effects for the hadronic final states in the region of the first resonance.

3. Comparison of electron scattering data (primarily proton and pion transparency measurements) to final state interaction models used in neutrino event generators such as NUANCE and NEUGEN[66].

7.5.2 Resonant form-factors and structure functions

The analysis of inclusive data in the resonance region with MINERνA will be done using the standard structure function analysis techniques. The sum of neutrino and antinuetrino differential cross-sections is used to do a Rosenbluth separation and extract F_2 and R for a Carbon target. The difference between neutrino and anti-neutrino differential cross-sections is used to extract the structure function xF_3. The nuclear effects in the resonance region at low values of Q^2 are not well understood. Electron scattering

data show that duality works at Q^2 greater than 1 $(\text{GeV}/c)^2$ for hydrogen and deutrium targets. In addition, there are indications that the nuclear effects also scale with the Nachtman scaling variable. However, these observations have not been tested in neutrino scattering, nor have they been tested in neutrino or electron scattering at lower values of Q^2. The information from Jefferson Laboratory proposal E03-110 will provide this information for nuclear targets for the vector structure functions. MINERνA in turn will be able to extend these duality studies to the axial vector structure functions.

At present, the axial form-factor for the first resonance is not very well known. MINERνA will have a very high statistics sample in this region, which is equivalent to the sample for quasilelastic scattering described earlier. However, since MINERνA data is on a Carbon target, nuclear effects must be understood. The theoretical tools used to model the nuclear effects in Carbon for the final state particles in the region of the first resonance in neutrino scattering, will be tested with CLAS Hall B electron scattering Jefferson Lab data on Carbon and other electron scattering data.

7.5.3 Single-pion final states

Using the angular distribution in the exclusive final states $\nu_\mu p \rightarrow \mu^- \pi^+ p$, we plan to fit for the resonant and non-resonant amplitudes. The extracted non-resonant amplitude should be consistent with the measured value of R in this region (extracted from the inclusive scattering sample).

By using both neutrino and anti-neutrino data MINERνA can investigate transitions into isospin 3/2 states Δ^{++} and Δ^-. An analysis of the ratios of various final states. $p\pi^+$, $n\pi^+$ and $p\pi_0$ will provide additional information. As mentioned ealrier, we plan to do a comparison of resonance production with electron scattering on free nucleons to Hall B CLAS data with bound nucleons in Carbon. Within MINERνA itself, we can compare the reactions $\nu p \rightarrow \nu n\pi^+$ and $\nu n \rightarrow \nu p\pi^-$ on bound nucleons directly, and investigate additional channels in order to better understand the effects of pion and nucleon rescattering.

MINERνA is expected to have good resolution for single pion events in the resonance region ($W < 2$ GeV/c). Figure 26 shows Q^2 and W distributions of single pion events from CH_2 in the MINERνA Monte Carlo along with reconstructed distributions that take into account MINERνA's energy resolution for hadrons (Figure 28). While the Fermi motion in nuclei washes out higher resonances, it is clear that Delta events can be readily identified and separated from higher resonances. This expected resolution implies that a differential cross-section $d\sigma/dQ^2$ for Delta production on Carbon equivalent to that for Hydrogen (Figure 29) can be obtained with high statistics. Figure 27 shows an example of a charged-current neutrino interaction producing a Δ^{++} which decays to a pion and proton. Distinct muon, proton and pion tracks are all visible showing that the resonance can be well reconstructed.
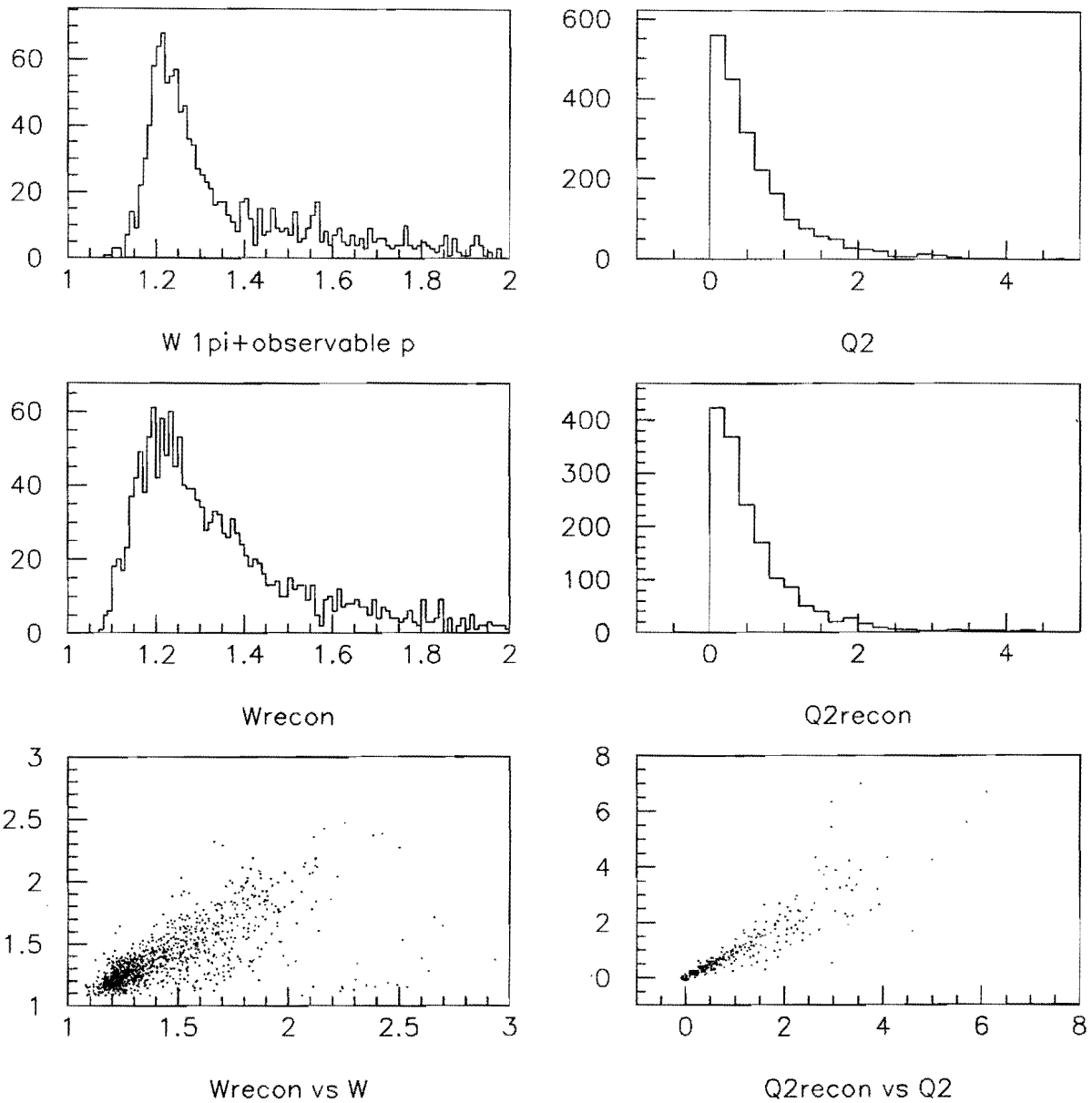
Figure 26: W and Q^2 reconstruction for events with a single π^+. Top row are "true" W and Q^2 distributions from the MINERνA Monte Carlo. The second row are the reconstructed distributions assuming hadron energy resolutions from Figure 28. The invariant mass of the pion and highest energy proton give W which along with the muon energy and direction gives sufficient information to reconstruct Q^2. Bottom row shows the correlation between the "true" and reconstructed quantities.

MINERVA TOP VIEW   Run   0 Event   11 Int Type RES
                                                     CC/NC   1 Mech. nu—p
                                                     Vertex (0.0,
                                            PNEU 14 (0.0000,0.00   8)
                                            PLEP 13 (0.5777,−.30   5)
                                                 x 0.362 q2 0.795 y
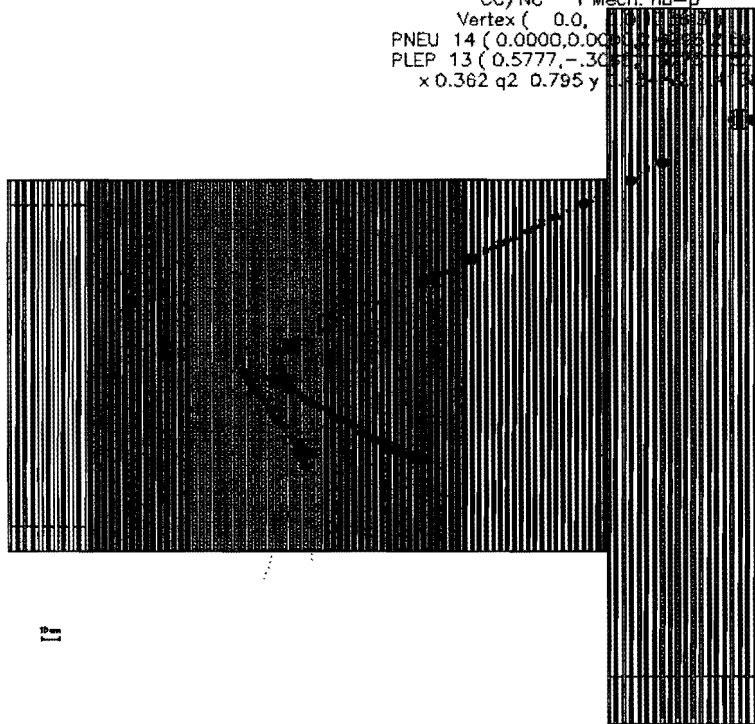
Figure 27: Δ^{++} production and decay in a charged-current neutrino interaction in the MINERνA detector. Shown are (top track) the muon and (middle and bottom track) the pion and proton produced in the decay. Energy deposition is shown by hit size. For clarity the outer barrel is not shown.
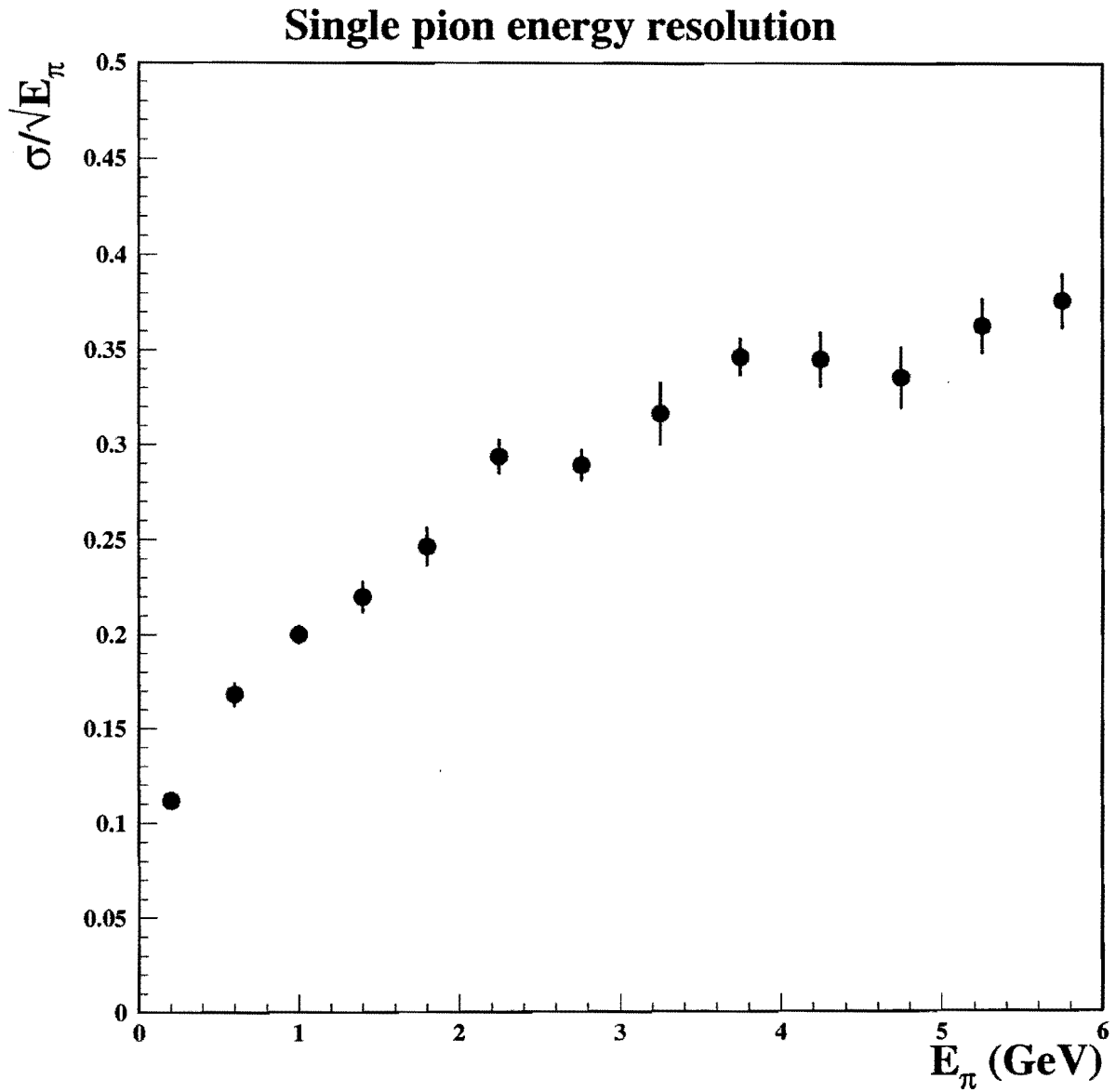
Figure 28: Single charged pion resolution derived from MINERνA Monte Carlo.
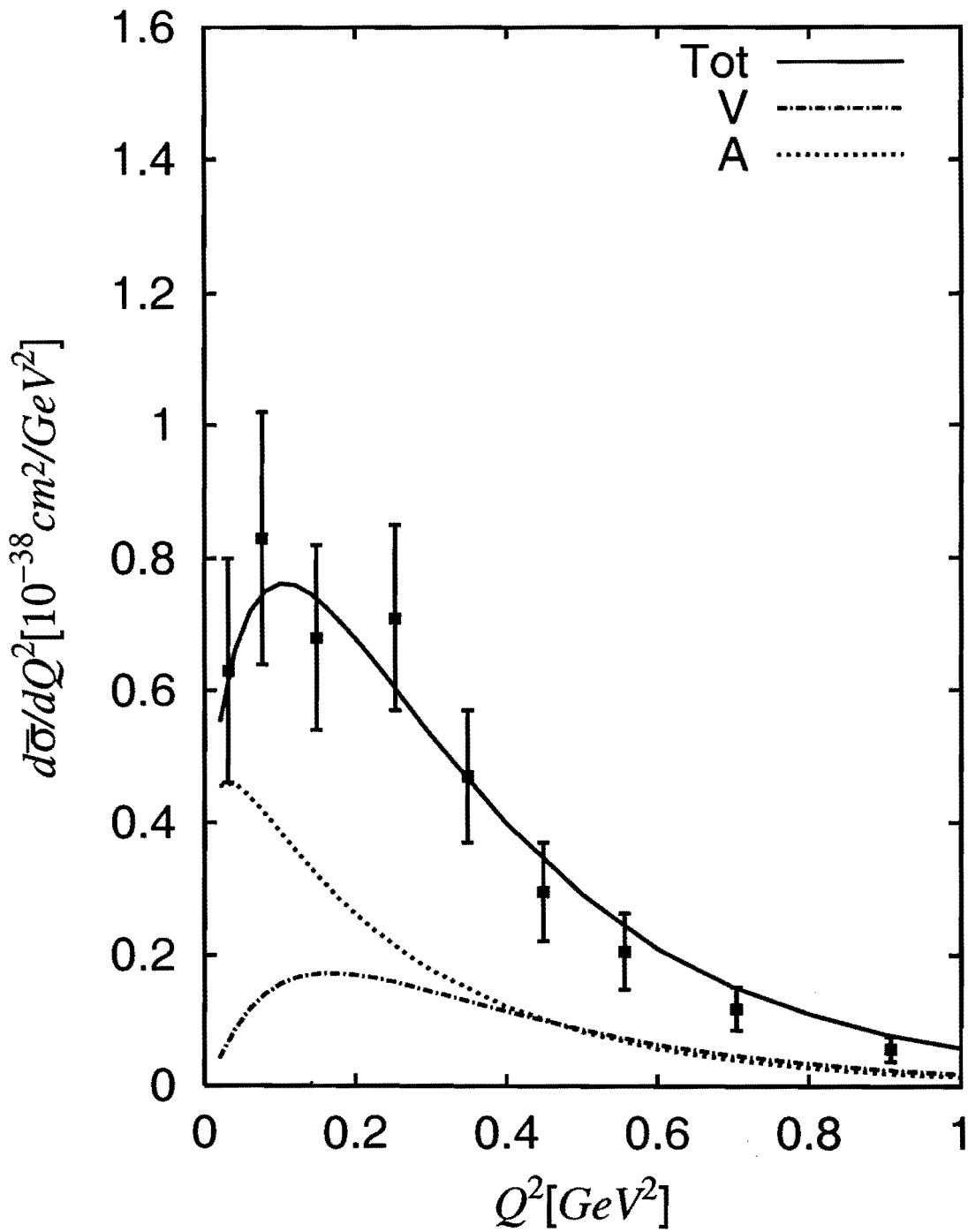
Figure 29: Differential cross-section $d\sigma/dQ^2$ (10^{-38}cm^2/GeV^2) of $p(\nu_\mu, \mu^- \pi^+)p$ averaged over neutrino energies. Calculations from Ref. [68], data from Ref. [20].

8 Coherent Neutrino-Nucleus Scattering

The MINERνA experiment has the potential to dramatically improve our knowledge of the dynamics of coherent neutrino-nucleus scattering. This process, in which the neutrino scatters coherently from the entire nucleus with small energy transfer, leaves a relatively clean experimental signature and has been studied in both charged-current $(\nu_\mu + A \rightarrow \mu^- + \pi^+)$ and neutral-current $(\nu_\mu + A \rightarrow \nu + \pi^o)$ interactions of neutrinos and anti-neutrinos. Although the interaction rates are typically an order of magnitude or more lower than other single-pion production mechanisms, the distinct kinematic characteristics of these events allow them to be identified. Because the outgoing pion generally follows the incoming neutrino direction closely, this reaction is an important background to searches for $\nu_\mu \rightarrow \nu_e$ oscillation, as these events can easily mimic the oscillation signature of a single energetic electron shower. Neutral-current coherent production will be discussed in more detail in Section 13.5; here we limit our attention to the charged-current channel where the kinematics can be fully measured and the underlying dynamics explored.
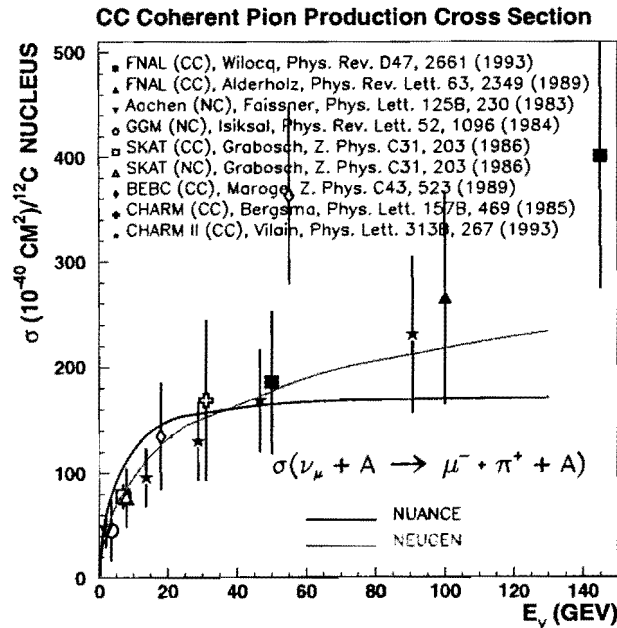
Figure 30: Charged-current neutrino–carbon coherent cross-sections. Results have all been scaled to carbon assuming an $A^{1/3}$ dependence, and $\sigma(CC) = 2\sigma(NC)$ [108].

8.1 Theory

It is well known from electron scattering that at low Q^2 and high ν, vector mesons are abundantly produced through diffractive mechanisms. These interactions are interpreted as fluctuation of the virtual photon intermediary into a virtual meson with the same quantum numbers, which by the uncertainty principle can travel a length

61

$$l \sim \frac{\nu}{Q^2 + m^2} \tag{20}$$

where m is the mass of the meson in question. For the weak current, similar fluctuations can occur, into both vector- and axial-vector mesons. From the Adler relation and "partially-conserved axial current" (PCAC) hypothesis, it is known that the hadronic current at low Q^2 is proportional to the pion field. The hadronic properties of the weak current in these kinematic regions have been investigated through the study of nuclear shadowing at low x and the coherent production of π, ρ, and a_1 mesons. Coherent scattering therefore allows investigation of the PCAC hypothesis and hadron dominance models of the weak current in detail [92].

A number of calculations of coherent scattering, involving substantially different procedures and assumptions, have been made over the past thirty years[93, 94, 95, 96]. These calculations factorize the problem in terms of the hadron-like component of the weak current and the scattering of this hadron with the nucleus. The calculations assume PCAC as a starting point but quickly diverge when it comes to the number of hadronic states required to describe the weak current and how the hadron–nucleus scattering should be treated. The Rein-Sehgal model, used by both NUANCE and NEUGEN, describes the weak current only in terms of the pion field; the Q^2 dependence of the cross-section is assumed to have a dipole form. Other calculations rely on meson-dominance models[95] which include the dominant contributions from the ρ and a_1 mesons. Figure 30 shows the coherent charged-current cross-section as a function of energy, compared to the model by Rein and Sehgal as implemented in NEUGEN and the calculation in [96].

8.2 Experimental Signatures

The kinematics of coherent scattering are quite distinct compared to the more common deep-inelastic and resonant interactions. Because the coherence condition requires that the nucleus remain intact, low-energy transfers to the nuclear system, $|t|$, are needed. Events are generally defined as coherent by making cuts on the number of prongs emerging from the event vertex followed by an examination of the t distribution, where t is approximated by:

$$-|t| = -(q - p_\pi)^2 = (\Sigma_i(E_i - p_i^{||}))^2 - (\Sigma_i(p_i^\perp))^2 \tag{21}$$

With its excellent tracking capabilities, the MINERνA inner detector can measure this kinematic variable well.

Figure 31 shows an event display of a coherent charged-current interaction in the MINERνA inner tracking detector. Distinct muon and pion tracks are clearly visible and the vertex location is well defined. An analysis designed to isolate a charged-current coherent scattering sample in MINERνA would likely be based on the following cuts:

- Require positive identification of a muon track. Since these events have small Q^2, the muon ranges out in either the downstream hadron calorimeter or the MINOS near detector.

- Require identification of the second track as a pion, by presence of a hadronic interaction along the track and/or dE/dx. Some number of interacting protons from quasi-elastic events will also pass these first cuts, but can be identified by their kinematics.

MINERVA SIDE VIEW

Run   0 Event   8 Int Type COH
CC/NC   2 Mech. nu-p
Vertex (15.2, 19.2,1322.0)
PNEU 14 (0.0000,0.0000,5.7188,5.7188)
PLEP *** (-.0091,0.0351,0.1042,******)
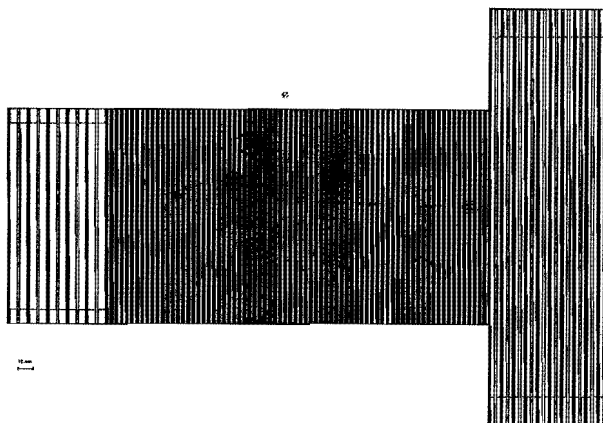
Figure 31: A charged-current coherent event in the inner tracking detector of MINERνA. For clarity the outer barrel detector is not shown.

- Require that the two tracks clearly emerge from a common vertex with no other activity in nearby upstream and downstream planes. Since hadronic activity, slow nucleons, and nuclear fragments should be absent, an energy cut on the vertex cells could also be effective.

- Calculate $|t|$ for these events and extract the coherent signal.

8.3   Expected Results

The low-energy NuMI beam will produce ≈ 760 coherent charged-current events/ton/10^{20} protons on target. For a three-ton fiducial volume and the assumed four-year run, the expected sample would be about 25,000 events in the fiducial volume. Bubble-chamber analyses typically achieved $\approx 60\%$ signal efficiency[106]. Conservatively estimating MINERνA efficiency to be 30% gives a total yield of 7,500 charged-current events in carbon. As Table 8.3 indicates, this would more than double the world's total for this reaction and represents an order of magnitude improvement in statistics for energies below 10 GeV.

Another task for MINERνA will be comparison of reaction rates for lead and carbon. The expected yield from lead will be ≈ 1800 charged-current events, assuming the same efficiency. The A dependence of the cross-section depends mainly on the model assumed for the hadron–nucleus interaction, and serves as a crucial test for that component of the predictions. No experiment to date has been able to perform this comparison. For reference, the predicted ratio of carbon to lead NC cross-sections at 10 GeV in the Rein-Sehgal and Paschos models are 0.223 and 0.259, respectively [107]. Figure 32 shows the predicted A-dependence according to the model of Rein and Sehgal.

63

Experiment	Reaction	Energy (GeV)	A	Signal	Ref
Aachen-Padova	NC	2	27	360	[97]
Gargamelle	NC	2	30	101	[98]
CHARM	NC	20-30	20	715	[99]
CHARM II	CC	20-30	20	1379	[100]
BEBC (WA59)	CC	5-100	20	158	[101, 102]
SKAT	CC (NC)	3-20	30	71 (14)	[103]
FNAL 15'	NC	2-100	20	28	[104]
FNAL 15' E180	CC	10-100	20	61	[105]
FNAL 15' E632	CC	10-100	20	52	[106]

Table 8: Existing measurements on coherent pion production[92].
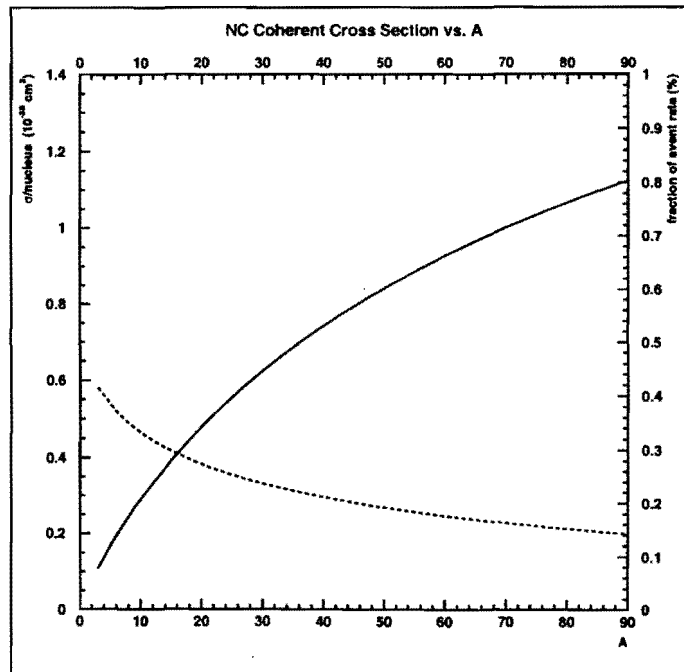
Figure 32: Coherent cross-sections as a function of atomic number.

64

9 Strangeness and Charm Production

9.1 Overview

The MINERνA experiment in the NuMI near hall will allow high-statistics studies of the rich complexion of exclusive-channel strange-particle production reactions accessible in the $1 \leq E_\nu \leq 8$ GeV energy regime. We propose precision measurement of cross sections $\sigma(E_\nu)$ of exclusive associated-production reactions ($\Delta S = 0$) and Cabbibo-suppressed $\Delta S = 1$ reactions. The ΔS weak hadronic current will be mapped out in detail, including its q^2 dependence, resonant structure, and polarizations of produced hyperons, to elucidate its coupling strengths and form-factors. A panoramic experimental delineation of all near-threshold ν_μ-N strangeness production processes is envisaged which will motivate renewed efforts to formulate detailed models of these reactions. The resulting picture will have ramifications in other areas of particle physics, for example in estimation of atmospheric neutrino ΔS backgrounds for nucleon-decay searches at megaton-year sensitivities. A MINERνA exposure will also enable searches for new processes, e.g. unusual baryon resonances such as the recently reported candidate pentaquark state in K^+n and $K^0_s p$ systems, and neutral-current strangeness-changing reactions. Extended running of the NuMI beam will allow $\bar{\nu}_\mu$ exposures that will provide valuable complementary data for many neutrino topics. Anti-neutrino exposure will facilitate study of $\Delta S = 1$ single-hyperon production (Λ, Σ, Y^*). Study of hyperon reactions will greatly extend the q^2 range over which the weak interaction form-factors which govern hyperon beta-decay can be examined. Thus a much better determination of the form-factors - especially of the three axial form-factors - will be possible. Hyperon polarization will provide additional analyzing power here, and the analysis will be free of the 'missing neutrino' problem which has hindered examination of the underlying V-A structure using semi-leptonic hyperon decays. As a natural extension of strange-particle production studies, we will search for strangeness production which accompanies dilepton processes. Such reactions have, in previous neutrino experiments, served as gateways to the study of charmed baryon production.

The NOMAD experiment[114] has studied inclusive strange-particle production extensively. MINERνA will not improve significantly on those results, and the physics motivation for attempting to do so is unclear. MINERνA will focus instead on exclusive channels; this is relatively unexplored territory, with the potential for high impact on future physics.

9.2 Neutrino Strangeness Production Near Threshold

In the threshold regime $1 \leq E_\nu \leq 8$ GeV, neutrino interactions involving strangeness production yield final states containing either one or two strange particles. Exclusive ν-N channels comprise three categories, distinguished by reaction type (charged-current (CC) or neutral-current (NC)) and the net change in strangeness $\Delta S = S_f - S_i$ of the hadronic system (either $\Delta S = 0$ or $\Delta S = 1$).

The first category comprises charged-current $\Delta S = 0$ reactions initiated by ν_μ. These are associated-production reactions where a strangeness +1 meson (K^+ or K^0) is produced together with a strangeness -1 hyperon (Λ or $\Sigma^{\pm,0}$) or meson (K^- or $\overline{K}^0$). Reactions of this category include:

$$\nu_\mu n \;\rightarrow\; \mu^- K^+ \Lambda^0 \tag{22}$$

$$\nu_\mu n \;\rightarrow\; \mu^- \pi^0 K^+ \Lambda^0 \tag{23}$$

$$\nu_\mu n \;\rightarrow\; \mu^- \pi^+ K^0 \Lambda^0 \tag{24}$$

$$\nu_\mu n \;\rightarrow\; \mu^- K^- K^+ p \tag{25}$$

$$\nu_\mu p \quad \rightarrow \quad \mu^- K^+ \overline{K}^0 \pi^0 p \tag{26}$$

Among charged-current $\Delta S = 0$ reactions, reaction (22) has the largest cross-section. This reaction, and reactions (23) and (24) as well, may proceed predominantly via N^* production followed by strong decay into $K\Lambda$.

Charged-current $\Delta S = 1$ reactions make up a second category. For ν_μ reactions, the resulting final states contain single strange K-mesons. The reaction cross-sections are Cabbibo-suppressed relative to $\Delta S = 0$ reactions involving similar hadronic masses. Additionally the $\Delta S = \Delta Q$ selection rule applies, and so the produced mesons are necessarily (K^+, K^0) and not $(K^-, \overline{K}^0)$. Reactions of this category include

$$\nu_\mu p \quad \rightarrow \quad \mu^- K^+ p \tag{27}$$

$$\nu_\mu n \quad \rightarrow \quad \mu^- K^0 p \tag{28}$$

$$\nu_\mu n \quad \rightarrow \quad \mu^- \pi^+ K^0 n. \tag{29}$$

Reaction (27) has the largest cross-section among $\Delta S = 1$ exclusive ν_μ–N reactions.

Note that $\Delta S = \Delta Q$ selection restricts $\Delta S = 1$ single-hyperon production to $\overline{\nu}$ rather than ν reactions, e.g.

$$\overline{\nu}_\mu N \rightarrow \mu^+ + (\Lambda, \Sigma, Y^*). \tag{30}$$

Strange-particle $\Delta S = 0$ associated production can also proceed via neutral-current reactions. Observed channels include

$$\nu_\mu p \quad \rightarrow \quad \nu K^+ \Lambda^0 \tag{31}$$

$$\nu_\mu n \quad \rightarrow \quad \nu K^0 \Lambda^0 \tag{32}$$

$$\nu_\mu n \quad \rightarrow \quad \nu \pi^- K^+ \Lambda^0 \tag{33}$$

As with final states of (22) - (24), it is similarly plausible that the hadronic systems of (31) through (33) are dominated by intermediate N^* states.

9.3 Strangeness Production Measurements at Bubble Chambers

Cross-sections for many associated-production and $\Delta S = 1$ reactions were obtained during the 1970's and '80s in experiments using large-volume bubble chambers exposed to accelerator neutrino beams. Principal experimental programs were the ν_μ and $\overline{\nu}_\mu$ exposures of the Gargamelle heavy-liquid (CF_3Br) bubble chamber at CERN [109, 110] and the ν_μ–D_2 exposures of the 12-foot diameter bubble chamber at Argonne [111] and of the 7-foot diameter bubble chamber at Brookhaven [112]. Typical samples involved less than ten observed events per channel, and cross-sections thereby inferred relate to one or a few bins in E_ν. Contemporaneous theoretical/phenomenological treatments of reactions (22), (28), (29), (31), and (32) can be found in [9, 115, 116].

Cross-section ratios obtained by the bubble-chamber experiments provide rough characterizations of relative rates of occurrence among the strangeness reaction categories. For example, the frequency of strange versus non-strange hadronic final states in charged-current reactions is indicated by [111]:

$$\frac{\sigma(\nu N \rightarrow \mu^- \Lambda K^+ + \mu^- p\, K)}{\sigma(\nu N \rightarrow \mu^- N + \text{pion(s)})} = 0.07 \pm 0.04 \tag{34}$$

The relative contribution of neutral-current versus charged-current reaction to threshold strangeness production is indicated by [24]:

$$\frac{\sigma(\nu_\mu N \rightarrow \nu_\mu V^0 + \text{anything})}{\sigma(\nu_\mu N \rightarrow \mu^- V^0 + \text{anything})} = 0.22 \pm 0.14 \tag{35}$$

and

$$\frac{\sigma(\nu K^+ \Lambda^0)}{\sigma(\mu^- K^+ \Lambda) + \sigma(\mu^- K^+ \Lambda X^0)} = 0.18 \pm 0.13 \tag{36}$$

Perhaps the most significant "find" arising from bubble-chamber survey experiments was the first observation of CC charmed-baryon production in a $\Delta S = 1$ final state at BNL[113]:

$$\nu_\mu p \rightarrow \mu^- \quad \Sigma_c^{++} \tag{37}$$

$$\Sigma_c^{++} \quad \rightarrow \Lambda_c^+ \pi^+ \rightarrow \Lambda^0 \pi^+ \pi^+ \pi^- \pi^+ \tag{38}$$

That excellent spatial resolution is a prerequisite for study of neutrino strangeness-production reactions is illustrated by the bubble-chamber event in Figure 33. The figure shows the tracing of a photographic image recorded by one of four separate camera views of this ν_μ–n interaction. The event shown was the first example of NC associated strangeness production via reaction (32) obtained using the deuterium-filled 12-ft diameter bubble chamber at ANL. Within the final state, the flight paths of the K_s^0 and and Λ^0 from the primary vertex to their respective "vee" decay points are 8.0 cm and 5.5 cm respectively [111]. Fortunately it should be possible, with the lattice of triangular-cell scintillator tracking elements of a fine-grained detector, to achieve spatial resolutions near bubble-chamber quality (studies currently predict vertex resolutions of less than 1 centimeter in MINERνA; see Section 15.5.4). This capability, together with dE/dx ionization imaging and momentum determination by ranging and external magnetic tracking, will allow MINERνA to explore exclusive strangeness-production processes.

9.4 Expected Results

The paragraphs below summarize some specific topics involving neutrino strangeness-production processes that can be investigated using MINERνA.

9.4.1 Backgrounds to nucleon decay

Current lifetime lower limits for nucleon decay ($\tau/\beta \geq 10^{33}$ years) have not diminished hopes for the eventual success of supersymmetric grand unification (SUSY GUTs). Indeed, there is strong motivation to proceed with more ambitious experimental searches. For the near future, improved searches will be carried out by Super–Kamiokande. Eventually these will be taken up by a next generation of underground detectors, e.g. by megaton-scale water Cherenkov experiments such as Hyper–Kamiokande and/or UNO[117].

Continued progress, either by improving limits to 10^{34} year lifetimes or discovery of nucleon decay, hinges upon improved knowledge of certain neutrino interactions which, when initiated by atmospheric neutrinos, can imitate nucleon-decay signals. The most problematic backgrounds to SUSY GUT modes arise via neutral-current associated production of strangeness at threshold energies.
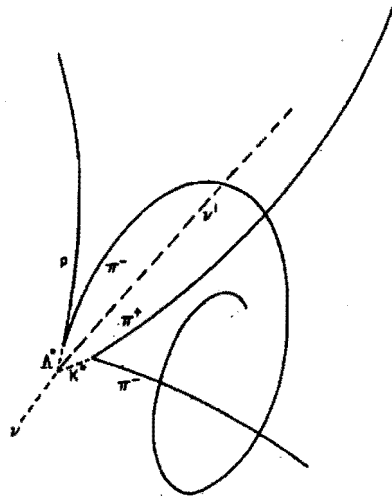
Figure 33: Trace of photograph from the ANL 12-ft diameter bubble chamber, of a neutrino neutral-current interaction in liquid Deuterium yielding NC associated production $\nu K \Lambda$. Flight paths to the vee decays of the two strange particles in the event are 8.0 cm and 5.5 cm in real space.

SUSY GUTs predict that nucleon-decay modes proceeding via virtual transitions involving inter-generational mixing are favored. Such modes yield final states containing strangeness $+1$ mesons, e.g.

$$p \rightarrow \nu K^+ \tag{39}$$
$$n \rightarrow \nu K^0 \tag{40}$$

and possibly

$$p \rightarrow \mu^+ K^0 \tag{41}$$
$$p \rightarrow e^+ K^0 \tag{42}$$

Decays (39) and (40) are thought to hold particular promise for first observation of baryon instability.

Search for $p \rightarrow \nu K^+$ The leading nucleon-decay search experiment for the next decade (and perhaps longer) will be Super–Kamiokande. Its successor is also likely to be an underground water Cherenkov detector with similar resolutions but a fiducial volume approaching megaton scale. In Super–Kamiokande, the search for proton decay mode (39) is currently carried out using three different methods, each motivated by the particulars of the final-state sequence being sought:

$$^{16}O(7p + p + 8n) \rightarrow {}^{15}N + \gamma(6.3 \text{ MeV})$$

$$\mathrel{\rule[-1ex]{0.01pt}{2.5ex}\!\!\rule{1.5ex}{0.01pt}} \nu K^+$$

68

$$\longrightarrow \begin{cases} \mu^+\nu_\mu, \quad \mu^+ \rightarrow e^+\nu\bar{\nu} \\ \pi^+ + \pi^0 \\ \quad \quad \rightarrow \gamma\gamma \\ \rightarrow \mu^+\nu_\mu, \quad \mu^+ \rightarrow e^+\nu\bar{\nu} \end{cases}$$
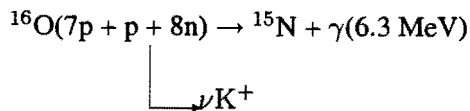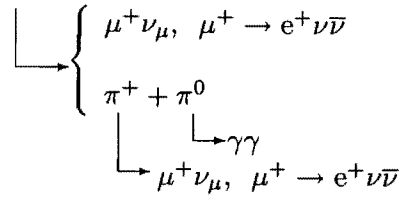
The three Super–Kamiokande approaches to finding proton decay (39) are:

i) $K^+ \rightarrow \mu^+\nu$ spectrum search: Looks for an excess of single μ-like ring events for which the reconstructed momentum p_μ matches that of two-body K^+ decay at rest and the delayed rings accompanied by subsequent $\mu \rightarrow e$ decay showers. This technique is already background limited.

ii) $K^+ \rightarrow \mu^+\nu$ gamma search: A candidate event has a signature 6.3 MeV gamma emitted by the parent nucleus together with a single μ-like ring having p_μ for a stopped K^+ and accompanied by $\mu \rightarrow e$ decay.

iii) $K^+ \rightarrow \pi^+\pi^0$ search: Candidates have three rings compatible with $\pi^+\pi^0$ with $\pi^0 \rightarrow \gamma\gamma$ from a stopped K^+ and with a subsequent $\mu \rightarrow e$ decay signal.

Neutrino background for p$\rightarrow$ K$^+\nu$ The combined search sensitivity for p$\rightarrow \nu K^+$ is dominated by the prompt gamma method *ii)* for which detection of a 6.3 MeV gamma from the nuclear de-excitation chain is crucial. Assuming this capability will be retained by next-generation underground water Cherenkov detectors, there is but one atmospheric neutrino reaction which may become an irreducible background in the search for this mode, and that is the neutral-current associated strangeness-production reaction (31). That is, in an underground water Cherenkov detector, an atmospheric neutrino of ν_μ or ν_e flavor may interact with a proton bound in an oxygen nucleus, producing a K^+ meson together with a Λ hyperon and an (invisible) outgoing neutrino. Subsequently, the ^{15}N nucleus which is the remnant of the struck ^{16}O, de-excites producing the 6 MeV signature γ. The final state Λ is a target fragment and will most always have low momentum. When it decays into pπ^- as will happen in two-thirds of reaction (31) occurrences, the daughter tracks will usually be below Cherenkov threshold and hence invisible. The final-state K^+ will subsequently decay, usually at rest, to yield a μ^+ or $\pi^+\pi^0$ signature. Consequently the detection sequence in a water Cherenkov experiment indicated above for proton decay (39) is perfectly mimicked:

$$\nu + {}^{16}O \rightarrow \nu + K^+ + \Lambda^0 + {}^{15}N + \gamma(6.3\ \text{MeV})$$

$$\longrightarrow p\pi^- \ (\text{below } \check{C} \text{ threshold})$$

$$\longrightarrow \begin{cases} \mu^+\nu_\mu, \quad \mu^+ \rightarrow e^+\nu\bar{\nu} \\ \pi^+ + \pi^0 \\ \quad \quad \rightarrow \gamma\gamma \\ \rightarrow \mu^+\nu_\mu, \quad \mu^+ \rightarrow e^+\nu\bar{\nu} \end{cases}$$

69
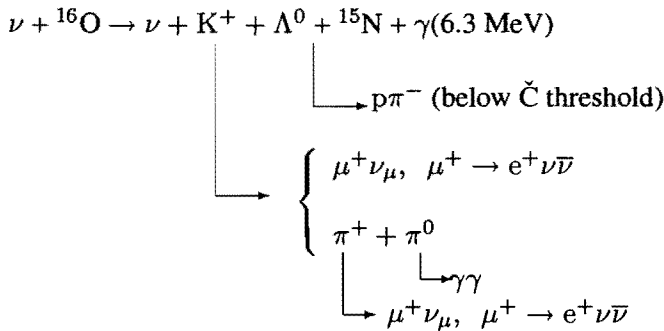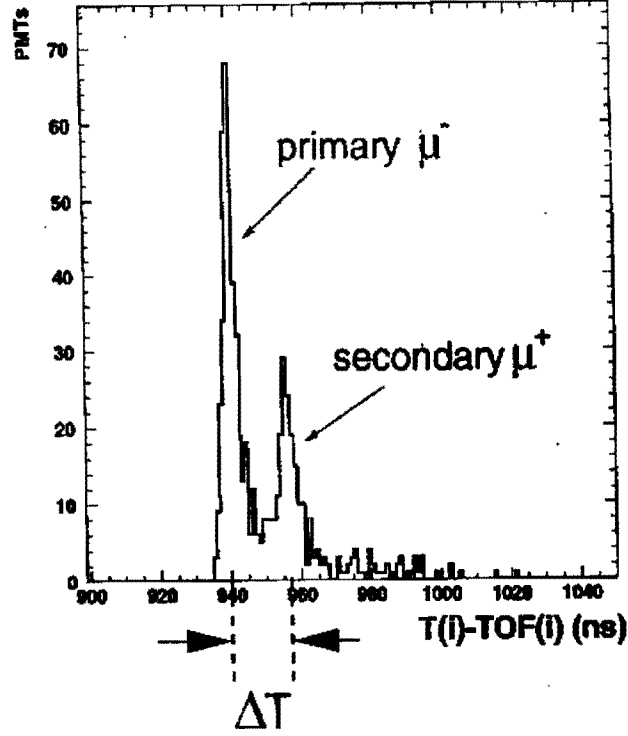
Figure 34: Time distribution from a neutrino interaction candidate for $\nu n \to \mu^- \Lambda K^+$, $K^+ \to \mu^+ \nu$ recorded using the 1 kiloton water Cherenkov detector (1KT) at KEK. Two peaks, separated in time by a few tens of nanoseconds, signal the occurrence of a K^+ decay subsequent to the primary charged-current interaction.

It is crucial for future, and for ongoing proton decay searches as well, that neutrino background posed by (31) and by other neutrino strangeness-production reactions be quantitatively understood. Fortunately, the relevant neutrino strangeness-production cross-sections, including their E_ν dependence, can be precisely measured in MINERνA.

9.4.2 Measurement of $\sigma(\nu \Lambda K^+)$

MINERνAwill measure the exclusive $\Delta S = 0$ neutral-current channel

$$\frac{d\sigma}{dE_\nu}(\nu_\mu N \to \nu_\mu K^+ \Lambda), \tag{43}$$

from its threshold at ≈ 1 GeV through its rise and leveling off to an energy-independent value at E_ν between 10-15 GeV. For purposes of comparison and as a valuable check on systematics[120], the $\Delta S = 0$ companion charged-current reaction will also be measured:

$$\frac{d\sigma}{dE_\nu}(\nu_\mu n \to \mu^- K^+ \Lambda). \tag{44}$$

The off-line selections required to isolate reactions (43) and (44) are straightforward. Assuming the final-state Λ decays into p π^- for these reactions, they share the following topological attributes:

i) The reactions have relatively low charged-particle multiplicities from the primary vertex region. Reaction (43) has three charged prongs, including the two daughter tracks from Λ decay; reaction (44) has four charged prongs.

ii) The proton track of Λ decay will appear as a short, heavily-ionizing track from the vertex region which stops in the scintillator.

iii) The final-state K^+ mesons will decay at rest or nearly at rest, and consequently a large-angle μ^+ track will result.

The most distinctive signature, however, arises with the time sequence for light emission in scintillator elements from these events. For reaction (43) a "prompt" signal arises from the two-body decay of the Λ into charged tracks; in reaction (44) the prompt burst is enhanced by the presence of the charged-current μ^- in the final state. The prompt signal is followed by a second signal, delayed by some few tens of nanoseconds, from two-body decay of the K^+. This timing signature, taken in conjunction with the three topology attributes above, should yield clean samples of reactions (43) and (44).

The feasibility of exploiting the signature afforded by the time profile of these reactions is illustrated in Figure 34. The figure shows the time distribution from Cherenkov light from a candidate event for reaction (44), where the occurrence of two peaks separated by approximately 16 ns is readily seen [118]. At K2K the effective energy reach of the KEK neutrino beam restricts cross-section measurements to $E_\nu \leq 3$ GeV; the atmospheric neutrino flux however extends to higher energies. Thus the NuMI ν_μ beam operated in the "low-energy" configuration will enable a complete picture of $\sigma(E_\nu)$ for reactions (43) and (44) to be obtained, providing an observational basis for future proton-decay searches to discover or set improved lifetime lower limits on decay modes favored by SUSY grand unification models.

9.4.3 Strangeness-changing neutral currents

Notably absent from the interaction categories of the previous paragraphs are neutral-current strangeness-changing reactions. These have never been observed; their occurrence at rates accessible in NuMI would imply new physics beyond the Standard Model. The existing limits on NC $\Delta S = 1$ processes are based upon searches for rare K decays. Although there are experimental difficulties with unambiguous identification of such processes in neutrino reactions, there is nevertheless an opportunity for strangeness-changing NC search in the neutrino sector.

Hints that an unrecognized type of neutral-current processes may exist are to be found in discrepancies involving hyperon weak radiative decays. These strangeness-changing weak decays have a clear disagreements between existing data and a variety of theoretical models - see [121],[122] for recent reviews. A long-standing puzzle concerns the large negative asymmetry coefficient observed in $\Sigma^+ \rightarrow$ $p\gamma$ decay, the measured value of which contradicts accepted notions concerning the size of SU(3)-breaking. To date, all of the assorted models invoked to describe these decays - including pole models, quark models, skyrmion models, vector meson dominance models and chiral models - fail to explain either the asymmetries observed or the decay rates of the various hyperons. Very recently, measurements of asymmetries which are large and negative in the $\Xi^0 \rightarrow \Sigma^0\gamma$ and $\Xi^0 \rightarrow \Lambda^0\gamma$ decays by the KTeV (Fermilab) and NA48 (CERN) experiments ([123] and [124] respectively), run counter to the theoretical predictions for a sizable positive value [125]. According to the comprehensive analysis of Gilman and Wise [126], the hypothesis that all weak radiative hyperon decays in the 56 multiplet of SU(6) are driven by the single-quark short-distance transition $s \rightarrow d\gamma$, is untenable.

71

A search for strangeness-changing neutral-current neutrino interactions can usefully clarify the extent to which new physics parameters may be missing from the analysis of weak radiative hyperon decays. It is plausible that neutrino reactions, in contrast to hyperon weak decays, may provide cleaner signals for a new weak current in as much as the multiloop quark-gluon diagrams which complicate hyperon decay analysis would be absent. To hope for such a circumstance is perhaps not unreasonable; after all, the first clear evidence for existence of the Z^0 in the guise of neutrino NC reactions preceded the direct production of the Z^0 by ten years.

Below we list charged-current neutrino interactions which are examples of hyperon production; included are two-body final states which represent the inverse of hyperon beta-decay. These CC reactions require exposure of MINERνA to an $\bar{\nu}_\mu$ beam. Also listed are "companion" NC neutrino reactions which yield single final-state hyperons. The latter include possible strangeness-changing neutral-current reactions (labeled SCNC), a subset of which could be the focus of a dedicated search. Note that the SCNC reactions are in principle accessible with either ν_μ or $\bar{\nu}_\mu$ beams.

$$\bar{\nu}_\mu + \text{p} \rightarrow \mu^+ + \Lambda^0 \qquad\qquad \nu_\mu + \text{p} \rightarrow \nu + \Sigma^+ \qquad SCNC \qquad (45)$$

$$\rightarrow \mu^+ + \Sigma^0 \qquad\qquad \rightarrow \nu + \pi^0 + \Sigma^+ \quad SCNC \qquad (46)$$

$$\rightarrow \mu^+ + \pi^0 + \Sigma^0 \qquad\qquad \rightarrow \nu + K^0 + \text{p} \quad SCNC \qquad (47)$$

$$\bar{\nu}_\mu + \text{n} \rightarrow \mu^+ + \Sigma^- \qquad\qquad \nu + \text{n} \rightarrow \nu + \Lambda^0 \qquad SCNC \qquad (48)$$

$$\rightarrow \mu^+ + \pi^- + \Lambda^0 \qquad\qquad \rightarrow \nu + \Sigma^0 \qquad SCNC \qquad (49)$$

$$\vdots \qquad\qquad\qquad\qquad \vdots$$

The expected neutrino and anti-neutrino interaction rates for Λ^0 production in the NuMI medium-energy neutrino beam with a 3 ton target detector and 4 years of running through CC reactions would be $\sim 1.5 \times 10^5$ and $\sim 4.5 \times 10^4$. This could translate into search levels of $< 10^{-5}$. for SCNC processes.

To isolate SCNC interactions, it is of course necessary to distinguish them amongst the predominate neutrino CC and NC samples. For certain selected SCNC reactions, this should be feasible. First and foremost on our list to identify SCNC process is the absence of a charged lepton since they are only in the neutral-current reactions in conjunction with only one strange particle being present. Other methods at our disposal is the existence of hyperon resonances without an accompanying meson which requires a highly-segmented detector with excellent containment of neutral mesons. Background estimates under the hyperon resonances can be accurately determined by off-resonance measurement of $\text{p}\pi^-$ states that would then give the accuracy needed for the resonance region. Events above that expectation would yield limits on the SCNC processes. Prerequisite detector requirements are good resonance mass reconstruction, neutral meson containment and a magnetic field, knowledge of the sideband backgrounds not going through resonances to an accuracy $10\times$ better than the resonance search region. All of this is achievable in the current design of MINERνA.

9.4.4 Hyperon beta-decay and inverse neutrino processes

Hyperon beta-decay $A \rightarrow B\ e^-\ \bar{\nu}_e$ provides a window onto weak hadronic current form-factors and their underlying structure. In the V-A formulation the transition amplitude is:

$$M = \frac{G}{\sqrt{2}} < B|J^\lambda|A > \bar{u}_e \gamma_\lambda (1 + \gamma_5) u_\nu \qquad (50)$$

The V-A hadronic current can be written as:

$$< B|J^\lambda|A > = C\, i\, \bar{u}(B) \quad \{ \quad f_1(q^2)\gamma^\lambda + f_2(q^2)\frac{\sigma^{\lambda\upsilon}\gamma_\upsilon}{M_A} + f_3(q^2)\frac{q^\lambda}{M_A} +$$

$$[\quad g_1(q^2)\gamma^\lambda + g_2(q^2)\frac{\sigma^{\lambda\upsilon}\gamma_\upsilon}{M_A} + g_3(q^2)\frac{q^\lambda}{M_A}]\gamma_5 \quad \}u(A)$$

where C is the CKM matrix element and q is the momentum transfer. There are 3 vector form-factors: f_1 (vector), f_2 (weak magnetism) and f_3 (an induced scalar); plus 3 axial-vector form-factors: g_1 (axial-vector), g_2 (weak electricity) and g_3 (an induced pseudo-scalar).

Recent high statistics measurements of these form-factors using KTeV Ξ^0 hyperon beta-decays have been reported[127]; the results show that the level of SU(3) breaking is very small compared to expectations of modern theories[128]. These new results have been used to extract the CKM matrix elements V_{us}[129]. Similar physics studies can be done with anti-neutrino interactions that produce hyperons. The hyperon decays themselves will have the added feature of a self-analyzing power of the polarization vector. Thus the fundamental form-factors and CKM matrix elements will be accessible without the hindrance of double solutions due to the missing neutrino energy. On the other hand, in MINERνA there arises the problem of dealing with the nuclear potentials which comprise the environment for target nucleons. This consideration might motivate running with liquid Hydrogen and Deuterium targets in a future program.

Although the simplest beta-decays and their corresponding inverse processes provide the predominate samples for both hyperon beta-decays and in $\Delta S = 1$ neutrino interactions, there are also interesting albeit more complicated 4-body beta-decay processes listed below along with some corresponding strangeness-producing neutrino interactions:

$$\Lambda \rightarrow p\pi^0 e^- \bar{\nu} \qquad\qquad \bar{\nu}_\mu + p \rightarrow \mu^+\Lambda\pi^0 \qquad (51)$$

$$\Sigma^+ \rightarrow p\pi^- e^+ \nu \qquad\qquad\qquad\qquad\qquad\qquad (52)$$

$$\Sigma^+ \rightarrow p\pi^- \mu^+ \nu \qquad\qquad \nu_\mu + p \rightarrow \mu^-\Sigma^+\pi^+ \qquad (53)$$

$$\qquad\qquad\qquad\qquad\qquad \nu_\mu + p \rightarrow \mu^- pK^+ \qquad (54)$$

$$\Sigma^- \rightarrow p\pi^- e^- \bar{\nu} \qquad\qquad \bar{\nu}_\mu + p \rightarrow \mu^+\Sigma^-\pi^+ \qquad (55)$$

Although none of the 4-body hyperon beta-decays have been officially observed, a handful of Ω^- candidate decays may have been isolated; preliminary results were presented at DPF 2003[130]. The theory behind these decays, [131] and [132], with their more complicated interaction models, were developed in the 60s. With neutrino interactions these processes should be easier to obtain and hence studied for the strength of physics interactions. They would allow for a much more complicated form-factor analysis process that involves 16 variables in the V-A style, but in the Standard Model would be a way to check the scale of the SU(3) breaking. It should also be noted that there are several types of beta-decays in this list that can be studied in neutrino beams before going to anti-neutrinos; these are the types shown in Equations 53 and 54 and others not listed.

There are also forms of 4-body hyperon beta-decays and likewise neutrino interactions that are forbidden by $\Delta S = -\Delta Q$. These too can be extensively searched for in neutrino-beam running before the necessity for anti-neutrino beams. While the existence of the forbidden decays would be exciting in hyperon beams, these interactions in neutrino beams would give information about probing the forms of the interactions.

Study of $\Delta S = 1$ pentaquark states, like those recently announced[133], could be greatly extended here. In regard to these pentaquark states (whether 4-quark and a anti-quark bound combination or a loosely-bound baryon-meson combination similar to mesonic atoms), with the production of hyperons and mesons together a wealth of combinations can be throughly examined for studying the full spectrum of the pentaquark family[134] of particles as well as other exotic quark combinations such as di-baryons.

9.4.5 Charm production physics

Historically, most neutrino scattering experiments found their way into charm-production studies when they investigated opposite or same-sign muon pairs generated by neutrino interactions. This signal arises because many of the charm particles decay with a muon, giving an extra muon along with the one produced by the CC neutrino reaction. The decay muons usually differ substantially from the direct CC neutrino muons in both momentum and angular distribution, but in some cases it is not possible to discern a difference. In MINERνA, with its lower neutrino energy beam, the production of charm particles will be suppressed compared to previous high-energy physics experiments. Hence the reach of MINERνA will be limited, but its large neutrino flux still allows interesting charm physics to be done.

An important contribution MINERνA will provide in charm production is study of the cross-section turn-on at or just a few hundred MeV above threshold. This threshold is very sensitive to the bare charm mass. With the proposed beam running schedule for MINERνA we expect $\sim$ 6500 charm events for a three-ton detector over the first five years, with an additional $\sim$ 3200 from anti-neutrino beam running for $x_F > 0$. Most of these charm events ($\sim$ 65%) will be produced during the HE beam running configuration. As noted, these yields depend strongly on the bare charm mass; varying this parameter by 10% results in expected yield changes of 30%. As discussed earlier, neutrino experiments measure charm-production parameters by studying opposite-sign dimuon production. From preliminary studies, the expected number of dimuons in MINERνA over five years is 530 $\pm$ 50 for a bare charm mass of 1.3 GeV/c^2. For bare charm masses of 1.15 GeV/c^2 or 1.45 GeV/c^2, the expected yields are 680 $\pm$ 60 and 420 $\pm$ 40 respectively. The yield assumes charm produced with $x_F > 0$ and a lower momentum cut on the decay muon of 1.5 GeV/c. The errors on the yields include the error on the average semileptonic branching ratio for charm[136] and the error on subtracting the background rate from pion decay. MINERνA is at an advantage in being able to determine the sign of the muons via magnetic tracking. Background rates can be determined by looking for same-sign dimuons. At MINERνA beam energies the expected number of background events should be approximately equal to the signal values. MINERνA should improve on the charm-quark mass determination currently set by the NuTeV/CCFR data at 1.38 $\pm$ 0.13 GeV/c^2[136].

10 Perturbative/Non-Perturbative Interface

10.1 Parton Distribution Functions

One obvious reason for the importance of neutrino data in the extraction of parton distribution functions is the neutrino's ability to directly resolve the flavor of the nucleon's constituents: ν interacts with d, s, $\bar{u}$ and $\bar{c}$ while the $\bar{\nu}$ interacts with u, c, $\bar{d}$ and $\bar{s}$. This unique ability of the neutrino to "taste" only particular flavors of quarks assists the study of parton distribution functions. A high-statistics measurement of the partonic structure of the nucleon is here proposed, using the neutrino's weak probe, to complement on-going study of this subject with electromagnetic probes at other laboratories.

With the high statistics anticipated in MINERνA, as well as the special attention to minimizing neutrino beam systematics, it should be possible to determine the individual structure functions $F_1^{\nu N}(x, Q^2)$, $F_1^{\bar{\nu} N}(x, Q^2)$, $F_2^{\nu N}(x, Q^2)$, $F_2^{\bar{\nu} N}(x, Q^2)$, $xF_3^{\nu N}(x, Q^2)$ and $xF_3^{\bar{\nu} N}(x, Q^2)$ (where N is an isoscalar target) for the first time.

In leading-order QCD, four of the structure functions are related to the parton distribution functions (PDFs) by:

$$
\begin{aligned}
2F_1^{\nu N}(x, Q^2) &= u(x) + d(x) + s(x) + \bar{u}(x) + \\
& \quad \bar{d}(x) + \bar{c}(x) \\
2F_1^{\bar{\nu} N}(x, Q^2) &= u(x) + d(x) + c(x) + \bar{u}(x) + \\
& \quad \bar{d}(x) + \bar{s}(x) \\
xF_3^{\nu N}(x, Q^2) &= u(x) + d(x) + s(x) - \bar{u}(x) - \\
& \quad \bar{d}(x) - \bar{c}(x) \\
xF_3^{\bar{\nu} N}(x, Q^2) &= u(x) + d(x) + c(x) - \bar{u}(x) - \\
& \quad \bar{d}(x) - \bar{s}(x)
\end{aligned}
$$

Taking differences and sums of these structure functions allows extraction of individual parton distribution functions in each (x, Q^2) bin:

$$
\begin{aligned}
2F_1^{\nu N} - 2F_1^{\bar{\nu} N} &= [s(x) - \bar{s}(x)] + [\bar{c}(x) - c(x)] \\
2F_1^{\nu N} - xF_3^{\nu N} &= 2[\bar{u}(x) + \bar{d}(x) + \bar{c}(x)] \\
2F_1^{\bar{\nu} N} - xF_3^{\bar{\nu} N} &= 2[\bar{u}(x) + \bar{d}(x) + \bar{s}(x)] \\
xF_3^{\nu N} - xF_3^{\bar{\nu} N} &= [\bar{s}(x) + s(x)] - [\bar{c}(x) + c(x)]
\end{aligned}
$$

As the order of QCD increases and gluons are taken into consideration, global fitting techniques must be applied to extract of the parton distribution functions. With the manageable systematic errors expected for the NuMI beam, the ability to isolate individual parton distribution functions will be dramatically improved by measuring the full set of separate ν and $\bar{\nu}$ structure functions with the impressive statistics possible in this experiment.

There are two primary (related) methods for extracting this full set of structure functions. One exploits the varying y behavior of the coefficients of the structure functions in the expression for the cross section:

$$\frac{d^2\sigma^{\nu(\bar{\nu})}}{dxdy} = 2\frac{G_F^2 M_p E_\nu}{\pi}\Big[xy^2 F_1^{\nu(\bar{\nu})}(x,Q^2) +$$
$$\left(1-y-\frac{M_p xy}{2E_\nu}\right) F_2^{\nu(\bar{\nu})}(x,Q^2) \pm$$
$$y\left(1-y/2\right) xF_3^{\nu(\bar{\nu})}(x,Q^2)\Big],$$

the other uses the "helicity representation" of the cross section:

$$\frac{d^2\sigma^\nu}{dxdQ^2} = \frac{G_F^2}{2\pi x}\Big[\frac{1}{2}\left(F_2^\nu(x,Q^2)+xF_3^\nu(x,Q^2)\right)+$$
$$\frac{(1-y)^2}{2}\left(F_2^\nu(x,Q^2)-xF_3^\nu(x,Q^2)\right)-$$
$$2y^2 F_L^\nu x,Q^2)\Big],$$

and

$$\frac{d^2\sigma^{(\bar{\nu})}}{dxdQ^2} = \frac{G_F^2}{2\pi x}\Big[\frac{1}{2}\left(F_2^{\bar{\nu}}(x,Q^2)-xF_3^{\bar{\nu}}(x,Q^2)\right)+$$
$$\frac{(1-y)^2}{2}\left(F_2^{\bar{\nu}}(x,Q^2)+xF_3^{\bar{\nu}}(x,Q^2)\right)-$$
$$2y^2 F_L^{\bar{\nu}}(x,Q^2)\Big],$$

By plotting the data as a function of $(1-y)^2$ in a given $x-Q^2$ bin, it is possible to extract all six structure functions.

For this sort of parton distribution function study, large anti-neutrino samples are an imperative.

10.2 Quark Distributions at Large x

Although a large body of structure function data exists over a wide range of x and Q^2, the region $x > 0.6$ is not well explored. For $x \geq 0.4$ contributions from the $q\bar{q}$ sea become negligible, and the structure functions are dominated by valence quarks.

Knowledge of the valence quark distributions of the nucleon at large x is vital for several reasons. The simplest SU(6) symmetric quark model predicts that the ratio of d to u quark distributions in the proton is 1/2, however, the breaking of this symmetry in nature results in a much smaller ratio. Various mechanisms have been invoked to explain why the $d(x)$ distribution is softer than $u(x)$. If the interaction between spectator quarks is dominated by single-gluon exchange, for instance, the d quark distribution will be suppressed, and the d/u ratio will tend to zero in the limit $x \rightarrow 1$[147]. This assumption has been built into most global analyses of parton distribution functions[148], and has never been tested independently. On the other hand, if the dominant reaction mechanism involves deep-inelastic scattering from a quark with the same spin orientation as the nucleon, as predicted by perturbative QCD counting rules, then d/u tends to $\approx 1/5$ as $x \rightarrow 1$[149].

Measurement of structure functions at large x will yield insights into the mechanisms responsible for spin-flavor symmetry breaking. In addition, quark distributions at large x are a crucial input

for estimating backgrounds in searches for new physics beyond the Standard Model at high energy colliders[150].

The QCD evolution of parton distribution functions takes high-x_{Bj} pdf's at low Q^2 and evolves them down to moderate-and-low x at higher Q^2. This obviously means that one of the larger contributions to background uncertainties at LHC will be the very poorly-known high-x PDF's at the lower Q^2 values accessible to the NuMI beam. The appearance of an anomaly at high x will be discussed below. First note that one problem in studying this problem has been accumulation of sufficient data at high x, off light targets, to extract the PDF's. The NuMI beam will finally yield the necessary statistics to address this important concern.

Uncertainties in current nucleon parton distribution functions at high x are of two types: the ratio of the light quark PDF's, $d(x)/u(x)$, as $x \rightarrow 1$, and the role of leading power corrections (higher twist) in extraction of the high x behavior of the quarks.

Analyses of present leptoproduction data from hydrogen and deuterium targets have been unable to pin down the high-x behavior of $d(x)/u(x)$. Part of the problem is due to the still unknown nuclear corrections involved in extracting the "neutron" results from deuterium [151]. An analysis by Bodek and Yang[152] indicated that the $d(x)/u(x)$ quark ratio approaches 0.2 as $x \rightarrow 1$. However global QCD analyses of experimental results, such as the CTEQ fits[153], do not indicate the need for this higher value of $d(x = 1)/u(x = 1)$. to model nuclear binding effects in the deuterium target could be avoided with high-statistics exposure of an could directly measure the $d(x)/u(x)$ ratio in ratio of neutrino-proton to measurement would require only a contributions at high x.

Measurement of quark densities at high-x_{Bj} is closely related to the question of the leading-power corrections known as "higher twist effects". The nth order higher-twist effects are proportional to $1/Q^{2n}$ and reflect the transverse momentum of the quarks within the nucleon and the larger size of the probe as Q^2 decreases, increasing the probability of multi-quark participation in an interaction. As for the d/u ratio, different analyses of higher-twist corrections in current data leave unresolved issues that new experimental information would clarify. Recent work by Yang and Bodek[154] seems to indicate that what has been measured as "higher-twist" in charged-lepton scattering analyses is essentially accounted for by increasing the order (NNLO) of the perturbative QCD expansion used in the analysis.

The only actual measurements of a higher-twist term in neutrino experiments have been two low-statistics bubble-chamber experiments: in Gargamelle[155] with freon and in BEBC[156] with NeH_2. Both bubble-chamber analyses are complicated by nuclear corrections at high-x. However, both found a twist-4 contribution smaller in magnitude than the charged leptoproduction analysis and, most significantly, negative.

There are several indications that current parameterizations of the PDFs are **not** correct at high x. Figure 35 shows the ratio of measured Drell-Yan pair production[157] compared to the latest CTEQ global fits, CTEQ6[158]. The comparison seems to indicate that the valence distributions are *overestimated* at high-x_{Bj}. This directly contradicts a recent analysis at Jefferson Lab which seems to indicate that the valence distributions are *underestimated* at high x, as shown in Figure 36.

Efforts are underway to understand how the $d(x)/u(x)$ ratio enters into the experimental comparison just discussed, and the large sample of high x events in MINERνA would certainly help clarify these results.

The principal reason that the $d(x)/u(x)$ ratio is not better known is the difficulty of accessing the structure of the neutron, due to the absence of free neutron targets, and the substantial theoretical uncertainties associated with extracting information from neutrons bound in nuclei. To overcome this problem, the BONUS experiment at Jefferson Lab[159] has been approved to measure the inclusive electron
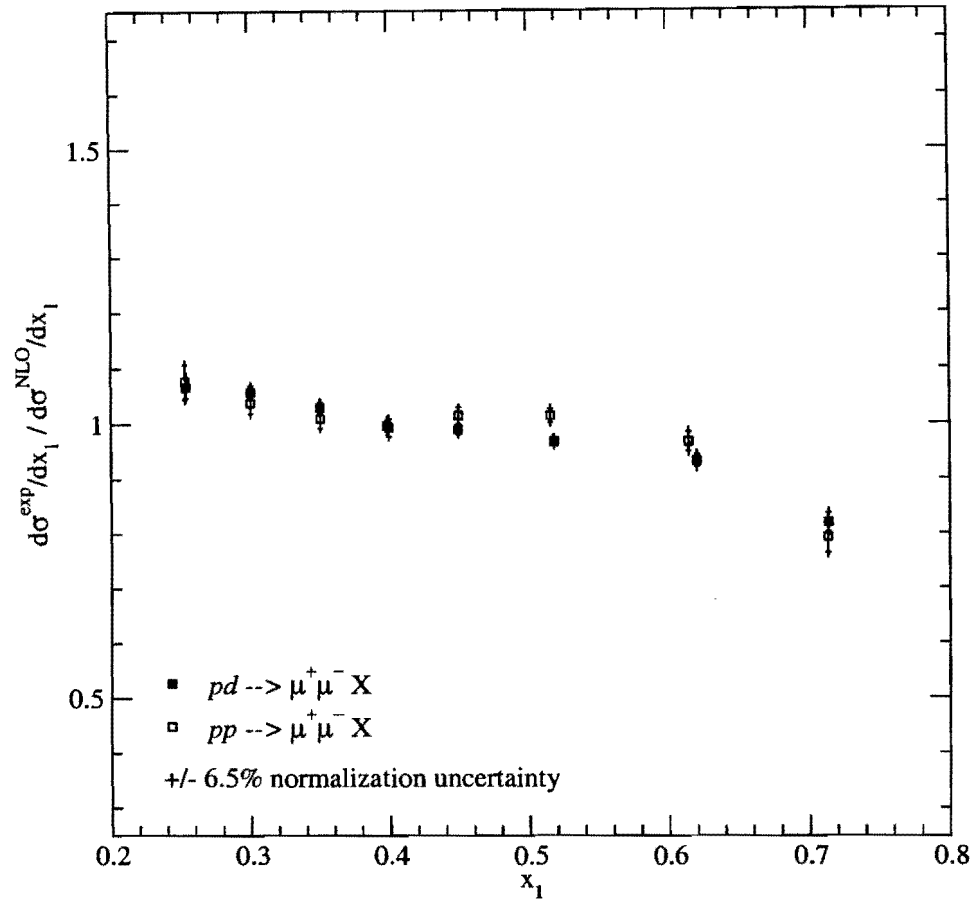
Figure 35: Ratio of data to predictions based on CTEQ6 NLO pdf's vs x_1
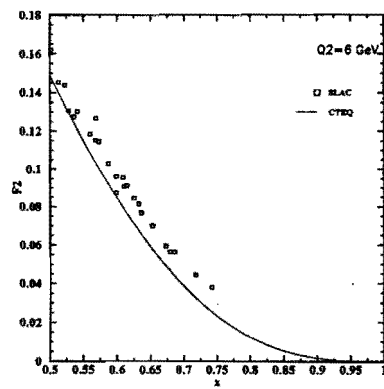
Figure 36: Results from SLAC electron scattering experiments compared to the CTEQ6 NLO prediction at high-x_{Bj}

scattering cross section on an almost-free neutron using the CEBAF Large Acceptance Spectrometer (CLAS) and a novel recoil detector with low momentum threshold for protons and high rate capability. This detector will allow tagging of slow backward-moving spectator protons with momentum as low as 70 MeV/c in coincidence with the scattered electron in the reaction $D(e, e'p_s)X$. This will ensure that the electron scattering took place on an almost free neutron, with its initial four-momentum inferred from the observed spectator proton spectrum. These measurements will unambiguously provide neutron structure measurements, which will thereby also reveal which of the available models best describe for instance, on-shell extrapolation for neutrons in nuclei.

It should be stressed that the BONUS experiment at Jefferson Lab will provide complementary information to MINERνA measurements, overlapping in kinematics, and on a similar time scale. With BONUS and MINERνA combined, most of the questions in large-x nucleon structure, parton distributions, and medium modifications, will be solved in the coming decade. BONUS will provide vital input regarding the extraction of neutron information from nuclei, while MINERνA can uniquely provide flavor decomposition information.

10.3 Quark/Hadron Duality

The description of hadrons in terms of their fundamental quark and gluon constituents is one of the major challenges in nuclear physics today. While at present the quark and gluon degrees of freedom in QCD cannot describe the structure and interactions of hadrons directly, in principle it should be just a matter of convenience whether to describe a process in terms of quark-gluon or hadronic degrees of freedom. This idea is referred to as *quark/hadron duality*, and means that one can use either set of complete basis states to describe physical phenomena. At high energies, where the interactions between quarks and gluons become weak and quarks can be considered asymptotically free, an efficient description of phenomena is afforded in terms of quarks; at low energies, where the effects of confinement make strongly-coupled QCD highly non-perturbative and the final state is guaranteed to consist of hadrons, it is more efficient to work in terms of collective degrees of freedom, the physical mesons and baryons. The duality between quark and hadron descriptions reflects the relationship between confinement and asymptotic freedom, and is intimately related to the nature of the transition from non-perturbative to perturbative QCD. It has been said that (short of the full solution of QCD) understanding and controlling the accuracy of the quark-hadron duality is one of the most important and challenging problems for QCD practitioners today[137].

Although the duality between quark and hadron descriptions is formally exact in principle, how duality is manifest, specifically, in different physical processes and under different kinematical conditions is a key to understanding the consequences of QCD for hadronic structure. The phenomenon of duality is quite general in nature and can be studied in a variety of processes, such as $e^+e^- \rightarrow$ hadrons, or semi-leptonic decays of heavy quarks. Duality in lepton–nucleon scattering, historically called Bloom-Gilman duality, links the physics of resonance production to the physics of deep-inelastic scaling. This duality is illustrated in Figure 10.3, where the nucleon transverse ($2xF_1$) and longitudinal (F_L) structure functions, measured in electron–proton scattering, are plotted as a function of the Bjorken scaling variable x for the indicated Q^2 bins. The curves are a fit to the resonance data by Liang, and the parton distribution function based parameterization of the MRST[138] group at next-to-next-to leading order, corrected for target mass[139]. The data are in the resonance (from Hall C at Jefferson Lab[140]) and deep-inelastic (from SLAC[141]) regimes, as indicated. Duality appears here in the observation that the hadronic (resonance) and quark (scaling) strengths are, on average, equivalent. Moreover, this is true

for all Q^2 bins observed, and thus the perturbative curve (MRST) apparently describes the average Q^2 dependence of the hadronic, non-perturbative, resonance enhancement region.
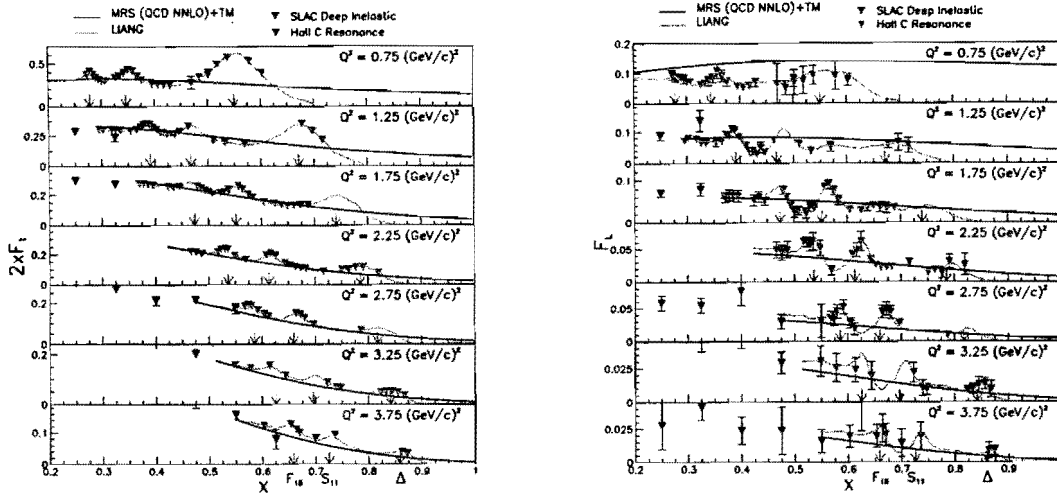
Figure 37: The nucleon transverse $(2xF_1)$ and longitudinal (F_L) structure functions, as measured in electron–proton scattering, are plotted as a function of the Bjorken scaling variable x for the indicated Q^2 bins. The curves are a fit to the resonance data by Liang (light blue), and the parameterization from MRST[138] (dark blue) at next-to-next-to leading order, corrected for target mass[139]. The data are in the resonance (from Hall C at Jefferson Lab[140], purple) and deep-inelastic (from SLAC[141], black) regimes, as indicated.

The proposed MINERνA experiment is uniquely poised to provide a wealth of data to answer where duality works, in what structure functions, in what reactions, and for what kinematics. Duality has been well-verified for the proton F_2 structure function[142], observed recently in the separated longitudinal and transverse unpolarized structure functions[140], on nucleons and in nuclei[161], and in polarized structure functions[143]. While its fundamental cause remains a mystery, duality appears experimentally to be a non-trivial property of nucleon structure. It is, therefore, crucial to test it in a variety of reactions – including neutrino–nucleon and –nucleus scattering and the structure function xF_3. Duality studies of electron–deuteron scattering at low Q^2 found a resemblance to deep-inelastic neutrino–nucleus scattering at much higher Q^2, indicating potential sensitivity of duality to the valence quarks[144]. MINERνA will allow this observation to be verified and tested for the first time, as data from similar kinematic regimes but differing in probe and interaction (from MINERνA and Jefferson Lab) may be compared directly.

It is important to point out that a revolutionary application of duality, if one understands the workings of the resonance–deep-inelastic interplay, would be to open-up the region of very high x, which has not been possible in any other experiment. As discussed above, the region of $x \approx 1$ is an important testing ground for understanding of the valence quark structure of the nucleon, and it will allow us to discriminate between various models for the mechanisms of spin-flavor symmetry breaking in the valence quark distributions of the nucleon. A first attempt at such an application is the recent analysis by Bodek and Yang[8], offering a promising procedure for fitting F_2 in the low Q^2, high x region. Extrapolating their results through the resonance region yields values of F_2 consistent with duality arguments

and the Jefferson Lab results mentioned above. In addition, with nuclear targets, duality extensions to large x would permit measurements of the nuclear-medium modification of the nucleon structure function (nuclear EMC effect) at large x, where deviation of the ratio of nuclear to nucleon structure functions from unity is largest, and sensitivity to different nuclear structure models greatest.

Members of the MINERvA collaboration are currently investigating quark/hadron duality in high-statistics electron scattering at Jefferson Lab with the same or similar nuclear targets as those proposed for MINERvA[160]. This will be followed by a comparison with all existing neutrino data, with the aim of continuing these studies with the higher statistics MINERvA neutrino experiment in the future. Note that investigation of quark/hadron duality in the axial structure functions of nucleons and nuclei with neutrinos also adds a new dimension to the previous electron studies. Many issues, such as nuclear dependencies, should be well understood in advance of the MINERvA data.

10.4 QCD Moments

Figure 38 depicts the substantial enhancement in the kinematic domain of precision data made possible by MINERvA over a range in x and Q^2. This data will serve a variety of purposes, and address long-standing questions regarding structure function behavior at low Q^2. Perhaps most importantly, the range of the data will allow for accurate moments of the structure functions to be obtained. To obtain a structure function moment, it is necessary to integrate over the full range in x at a fixed value of Q^2. The Cornwall-Norton moment of a structure function F, for instance, is expressed as:

$$M_n^{CN}(Q^2) = \int_0^1 dx \, F(x, Q^2) \, x^{n-2}. \tag{56}$$

The moments are fundamental quantities, calculable in QCD and recently calculated in lattice QCD at $Q^2 = 4$ $(\text{GeV/c})^2$ for valence distributions[145]. If duality is shown to hold, the proposed data may provide one of the few available quantities that can be directly compared to lattice QCD calculations.

W2 vs Q2   W2 vs Q2 (contained)
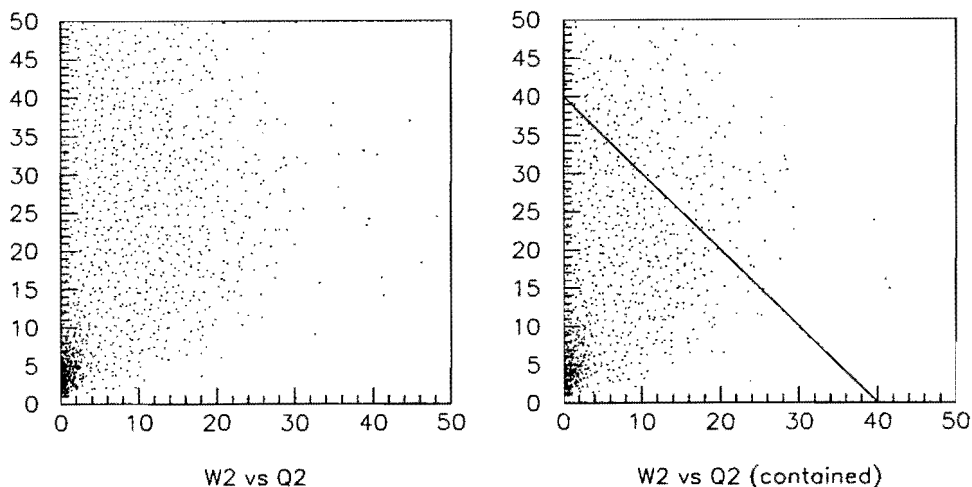
Figure 38: Left: Distribution of DIS events with LE beam in MINERvA Monte Carlo. Right: Events where total hadronic energy is contained by MINERvA. The line is an estimate of the limit where 50% of events do not have containment of hadronic energy.

Bloom-Gilman duality can be formulated in the language of an operator product expansion (OPE) of QCD moments of structure functions, in which contributions are organized according to powers of $1/Q^2$. The leading terms are associated with free quark scattering, and are responsible for the scaling of the structure function. The $1/Q^2$ "higher twist" terms involve interactions between quarks and gluons and hence reflect elements of confinement dynamics. Duality measurements have been explained in terms of a weak Q^2 dependence of the low moments of the structure functions[146]. This is interpreted within the OPE as indicating that non-leading, $1/Q^2$-suppressed, higher-twist interaction terms do not play a major role even at low Q^2 (≈ 1 GeV^2). It is this interpretation that facilitates comparison to lattice calculations, as the latter have no higher twist effects included.

Large-x (resonance region) data become increasingly important for higher-order moments due to the $n - 2$ weighting of the moment. At n=6, for example, the resonance and large x region above $x = 0.7$ make up 70% of the Cornwall-Norton moment of F_2 at $Q^2 = 10$ (GeV/c)^2. The contribution is larger at $Q^2 = 4$ (GeV/c)^2, where lattice calculations are available. As noted above, there currently exist little to no neutrino resonance cross-section data in the resonance region or at larger x, while such data will be easily obtainable with MINERνA.

It is important to reiterate that, regardless of duality or OPE arguments, the experimental values for the moments can be unambiguously obtained with MINERνA. For example, it is straightforward to note, from Figure 38, that even the low-energy beam provides data covering a large range in x (or W^2) for each Q^2 value up to 10 (GeV/c)^2. The higher-energy beams will complement this sensitivity, extending the Q^2 range over which moments can be obtained, and adding statistics to the much of the region covered by the low-energy beam. While comparable coverage can be obtained by combining electron and muon scattering data from a multitude of laboratories, MINERνA will uniquely provide, for instance, the xF_3 structure function, valence sensitivity (necessary to current lattice comparisions), and flavor decomposition.

10.5   Expected Results

The proposed studies of structure function moments and quark/hadron duality are straightforward with the proposed MINERνA experiment. These topics do not have the demanding experimental constraints that many of the other proposed topics do. While it is crucial to understand the projected W^2 or x resolution, for instance, in studying resonance production behavior, duality studies and moment extractions average over these kinematic variables and are therefore virtually insensitive to resolution issues. The expected MINERνA resolutions are more than adequate both to form integrals such as that in Equation 56 and to study duality using data comparison with perturbative predictions, as in Figure 10.3.

Additionally, it is not necessary to isolate specific production processes in these studies. It is only total cross-section averages that are of interest, making MINERνA essential to this effort in neutrino scattering.

It has been observed from studies of quark/hadron duality using nuclear targets that data in the resonance regime scale even more obviously when smeared by the nuclear Fermi momentum[161], as shown in Figure 39. In Hydrogen, the resonance peaks are prominent, while they are much less so in Deuterium, and completely smeared away in Iron. In all cases, however, the resonance region averages to the scaling curves. In Iron, the smearing is such that the resonance data and scaling curves overlap completely; the nucleus performs the duality averaging.

With concerns about nuclear effects removed, then, there remain no impediments to studying duality for the first time in neutrino scattering with MINERνA. Similarly, extractions of higher-twist contribu-
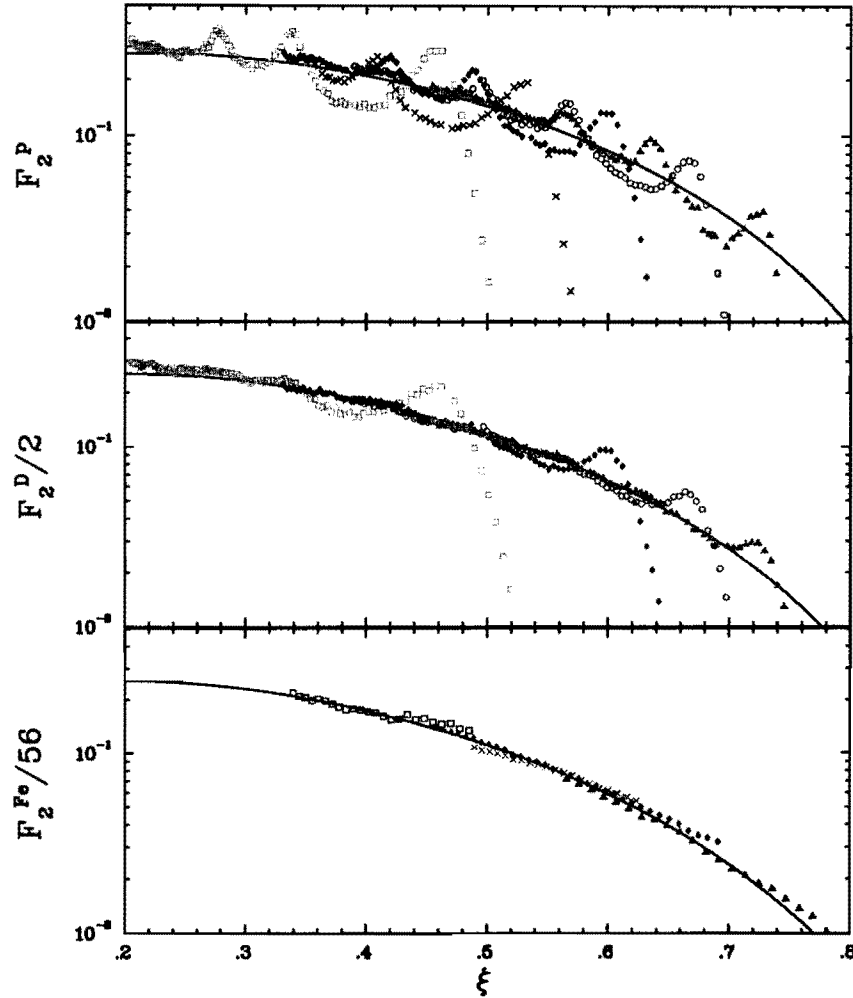
Figure 39: Structure function F_2 data in the resonance region on Hydrogen (top), Deuterium (center), and Iron (bottom) covering a range in $0.8 < Q^2 < 3.3$ $(\text{GeV/c})^2$, and plotted as a function of the Nachtmann scaling variable ξ. The elastic (quasi-elastic) peaks have been removed. The curves are the MRST and NMC parameterizations of the structure function, with a model of the EMC effect applied for Iron.

tions and studies of evolution for parton distribution function extraction through the Q^2 dependence of the structure functions will not be rendered ambiguous through the utilization of nuclear targets.

Most strikingly, it appears that the nuclear effects at large x are the same in the resonance and scaling regimes, as evidenced by Figure 40 from[161], where the cross-section ratios of carbon, iron, and gold to deuterium obtained in the resonance region (red) are the same as those obtained in the deep-inelastic regime (green). Whatever the underlying cause for medium modifications to the structure functions as measured in nuclei, it is the same apparently for both hadronic (resonance) and scaling observables. Since the large x region of the EMC effect is ubiquitously attributed to Fermi motion in the nucleus, MINERνA neutrino data should yield similar A-dependent results as the electron data in the figure. That is, it is expected (and will be tested) that the proposed data in the larger x and resonance regions will have the same EMC effect as data at higher W^2. Therefore, MINERνA data at large x can be used for parton distribution studies, higher twist analyses, and nucleon structure studies with minimal nuclear extraction uncertainties.

The expected numbers of events for the resonance and deep inelastic regimes are tabulated in Section 5.4. These will make possible all of the studies here discussed in the perturbative and non-preturbative transition region of larger x and lower Q^2 values. This is an exciting regime, with many unanswered problems both interesting on their own and of import to other high energy applications.
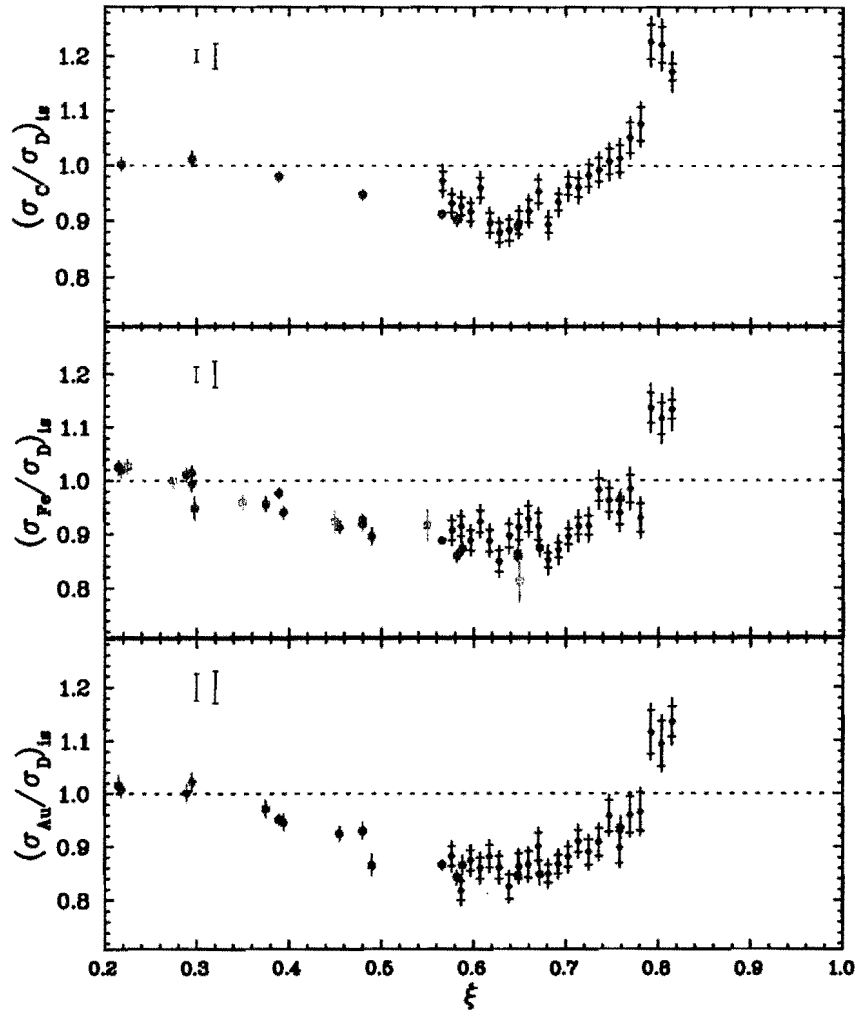
Figure 40: Ratio of electron-nucleus scattering data (from top to bottom, Carbon, Iron, Gold) to that obtained from Deuterium scattering, for data in both the resonance (red) and deep inelastic (green) regimes. The data are plotted as a function of the Nachtmann scaling variable ξ, allowing direct comparison of high W^2, Q^2 DIS data to lower W^2, Q^2 resonance data.

11 Generalized Parton Distributions

One of the main goals of subatomic physics is to understand the structure of hadrons, and in particular the structure of the nucleon. The primary approach to this problem has been through measurement of the nucleon form-factors, with (quasi-)elastic scattering (for Q^2 up to a few $(GeV/c)^2$), parton densities, through inclusive deep-inelastic scattering (DIS), and distribution amplitudes, through exclusive processes. However, the usual parton densities extracted from DIS are only sensitive to the longitudinal component of the parton distributions and do not give information on the transverse component, or other contributions to the nucleon angular momentum.

11.1 The Nucleon Spin Puzzle and GPDs

In the late 1980's, results from polarized DIS showed that a relatively small fraction, about 20%, of the nucleon spin is carried by the valence quarks. The obvious candidates for the missing spin were the quark and gluon orbital momentum and gluon helicity. However, information on those quantities cannot be extracted from DIS.

In 1997, Ji[162, 163] showed that a new class of nucleon observables, which he called "off-forward parton distributions", could be used to determine the spin structure of the nucleon. This work, along with developments by others, especially Radyuskin[164, 165] and Collins[166] showed that these distributions, now called generalized parton distributions (GPDs), had the potential to give a full three-dimensional picture of the nucleon structure. This exciting development has led to an immense amount of theoretical work in the last few years. Short reviews can be found in [167, 168] and a comprehensive review can be found in [169].

Ji showed that in leading twist there are four GPDs, which he called H, $\tilde{H}$, E, and $\bar{E}$, for each quark flavor. H and $\tilde{H}$ are nucleon helicity-conserving amplitudes and E and $\bar{E}$ are helicity-flipping amplitudes. The GPDs are functions of x, ξ (a factor determining the "off-forwardness" of the reaction), and the total momentum-transfer squared, t. The GPDs can be accessed experimentally through reactions proceeding via the "handbag" diagram shown in Figure 41.

11.2 Deeply-virtual Compton Scattering

The most promising reaction to measure GPDs identified so far is deeply-virtual Compton scattering (DVCS). The DVCS reaction is shown in Figure 42a. An interesting feature of DVCS is that it can interfere with the Bethe-Heitler process, Figure 42b, which is completely calculable in terms of the nucleon elastic form-factors. This interference causes an asymmetry in the azimuthal distribution of the scattered proton allowing some quantities to be determined that would otherwise require a polarized target. However, DVCS involves a combination of the four GPD amplitudes, which cannot be separated using DVCS alone. Some complementary information can also be obtained from nucleon form-factor measurements and deep exclusive meson electroproduction.

Neutrino scattering provides a very similar reaction to DVCS. In this case, the virtual exchange is of a $W^{\pm}$ with the production of an energetic photon, a $\mu^{\pm}$, with either a recoiling nucleon or nucleon resonance, as shown in Figure 43. This "weak DVCS" reaction is very promising theoretically because it provides access to different GPDs than DVCS. It will help resolve the individual flavors, e.g. d in neutrino scattering and u in anti-neutrino scattering, and the interference of the V and A currents will give access to C-odd combinations of GPDs.
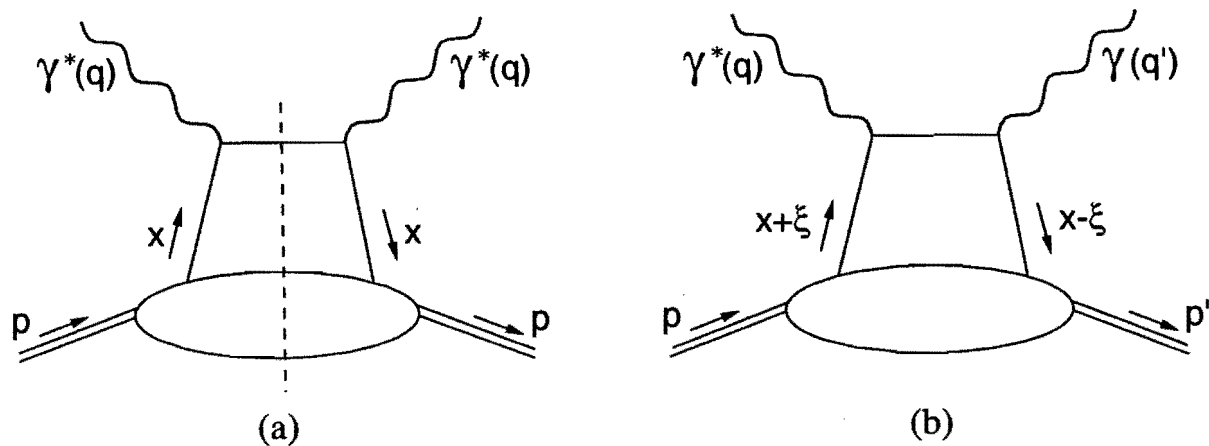
Figure 41: (a) Forward virtual Compton amplitude which describes the DIS *cross-section* via the optical theorem ($x_B = x$); (b) Handbag diagram occurring in the DVCS *amplitude*.
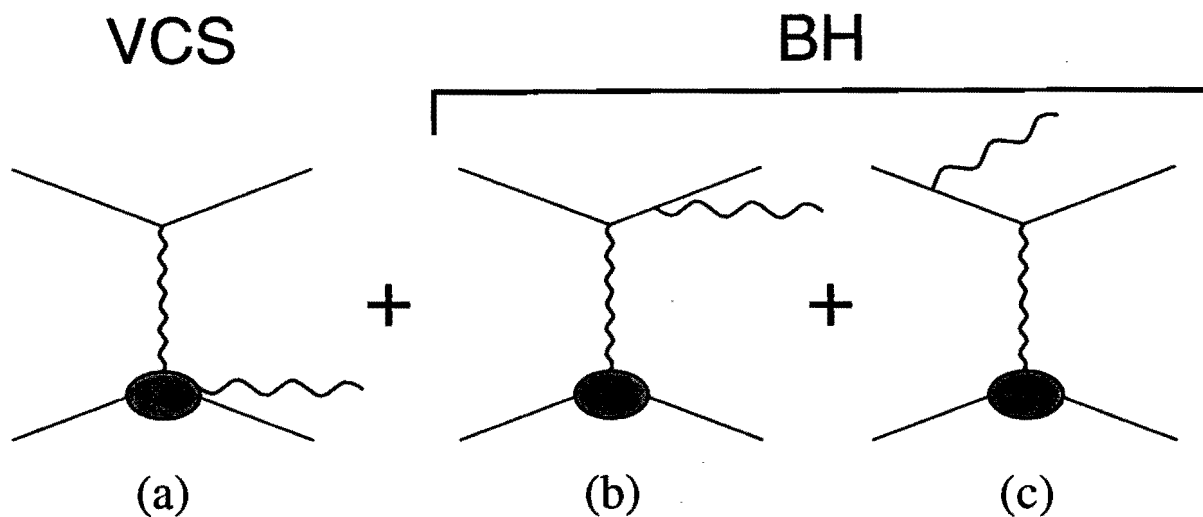
Figure 42: The DVCS process (a) along with the interfering Bethe-Heitler diagrams (b) and (c).
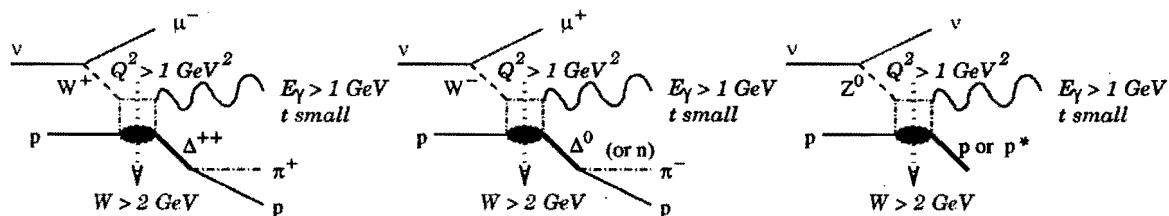
Figure 43: Reactions sensitive to GPDs in neutrino scattering.

11.3 Measurement of GPDs in MINERνA

Studies of the weak DVCS reaction are currently underway by A. Radyuskin, A. Psaker, and W. Melnitchouk. One very encouraging result so far is that the $q\bar{q}$ equivalent of the polarized structure function g_1 can be measured *without* using polarized targets. This would allow separation of the valence and sea parts of the spin-dependent GPDs, and help determine the role of the axial anomaly in the proton spin puzzle. In addition, although the Bethe-Heitler process is suppressed, it is still present and the interference with it would allow measurement of individual GPDs.

The estimated cross-section for weak DVCS is about 10^{-39} cm^2. For neutrino energies in the 5–10 GeV range, this would yield a few hundred events/year for a 1 GeV-wide bin in neutrino energy. Although most of the events will be from nucleons in carbon, any nuclear modifications are expected to be small except at very small or very large x.

At least one other reaction, the hard exclusive production of the D_s has also been proposed[170] as a probe of GPDs. This reaction is sensitive to the gluon structure of the nucleus. Unfortunately, the cross-section for this reaction (estimated at 10^{-5} pb for $Q^2 > 12$ (GeV/c)^2), is too small to be measured with precision in MINERνA. Nevertheless, over the entire run perhaps a few hundred events would be observed over all values of Q^2, which would give some information on the gluon GPDs.

12 Studying Nuclear Effects with Neutrinos

In most neutrino scattering experiments, massive nuclear target/detectors are necessary to obtain useful reaction rates. Neutrino-oscillation experiments, despite the extremely intense beams designed for them, must also use very massive Iron, water or other nuclear target/detectors, since they are located hundreds of kilometers from the production point. Analysis of neutrino reactions within nuclear media requires an understanding of certain processes which are absent in neutrino scattering on free nucleons; these processes involve the so-called "nuclear effects". Two general categories of such effects can be distinguished. Effects comprising a first category include:

- The target nucleon is moving within the nucleus and, when incoming neutrino energies are $\leq$ 2 GeV, the initial target energy and momentum must be accounted for using simulations which include either a target Fermi gas model or, preferably, nucleon spectral functions.

- Certain final states are excluded as a result of Pauli blocking among identical nucleons.

- The resulting final state may undergo final state interactions (FSI), including re-scattering and absorption; these interactions may significantly alter the observed final-state configuration and measured energy.

The first two effects are either already included in Monte Carlos or are currently being examined in collaboration with nuclear theorists and will soon be included. The third effect is perhaps the most troublesome for current and future neutrino experiments. There is a dearth of data for which nuclear effects on specific hadronic final states (the fragmentation functions) have been isolated, whether for neutrino or charged-lepton beams. These effects are likely to be sizable for neutrino energies producing a large fraction of elastic and resonant final states[6].

A second category of nuclear effects are those by which the neutrino interaction probability on nuclei is modified relative to that for free nucleons. These effects occur across a wide range of neutrino energies and are normally categorized by the x_{Bj} of the quark involved in the scattering, and the Q^2 of the intermediate vector boson exchanged. Nuclear effects of this type have been extensively studied in deep-inelastic scattering (DIS) measurements of structure functions using muon and electron beams. For example, Figure 44 shows the ratio of the structure function F_2 measured on a heavy nuclear target to F_2 measured for Deuterium.

With neutrino beams, these nuclear effects have only been studied with low-statistics in bubble-chamber experiments.

12.1 Final-state Interactions

Distortions which result from FSI depend on the particle type and energy. Of primary concern are effects involving final-state nucleons and pions. For nucleons, rescattering is the major effect, resulting in i) change of direction and energy loss, ii) production of secondary nucleons, or iii) neutron or proton pickup leading to deuteron emission. For pions, FSI can also lead to scattering with possible nucleon emission. The pions can charge exchange or be totally absorbed leading to emission of nucleons only. In all of these cases, particles that escape from the nucleus have lower energy than the initial, primary particle, and the redistributed energy information is lost due to detector thresholds.
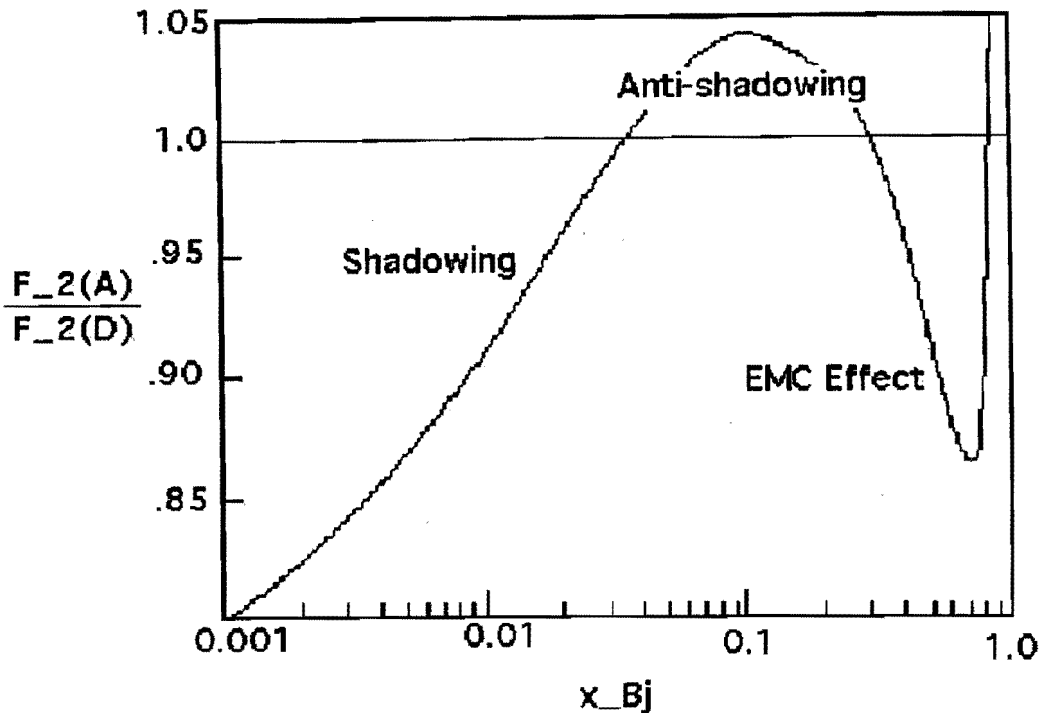
Figure 44: The trend of the ratio of F_2 measured with a heavy nuclear target to F_2 measured using deuterium, for charged-lepton scattering, as a function of x_{Bj}.

The most reliable information on FSI for nucleons comes from transparency measurements in $(e, e'p)$ reactions on nuclei. Transparency, defined as the probability of escaping the nucleus **without** interaction, is measured by detecting the scattered electron and integrating the protons detected within the quasi-elastic peak. The most recent results quoted for protons in the energy range 0.5 to 4 GeV are about 60% for C, to 40% for Pb[171], with very little energy-dependence. The composition and energy distribution of the final-state particles is not well measured. Two-proton and proton-neutron final states should dominate, with each nucleon having about half the total energy of the initial nucleon.

Pion interactions, especially for pions below a few hundred MeV, are dominated by the Δ resonance. The data on FSI can be inferred from reactions of free pions on nuclei. There is little specific data for pions resulting from Δ or other resonant particle production in the nucleus.

The significant feature of pion reactions is the strong absorption component - both inelastic scatters and "true" absorption, when the pion disappears from the final state. The absorption component comprises about two-thirds of the total cross-section. True absoprtion ranges from about 25% of the total cross-section for C to nearly 40% for Pb, for both positive and negative pions in the 100–300 MeV range[172]. Inelastic cross-sections are comparable, although generally smaller for heavier nuclei. Be-

cause of the strong absorption component, pions in this energy range should escape the nucleus only about 50% of the time.

Several experiments have found pion absorption to be a fairly complicated process in complex nuclei[173, 174]. Although the first step is believed to be absorption on an isospin-0 np pair (quasi-deuteron), even in a nucleus as light as carbon the final state is dominated by three-nucleon emission. For heavier nuclei, the final state has a large component of four-nucleon emission. Even π^+ absorption usually includes emission of a neutron, and of course π^- absorption is dominated by neutron emission.

There is very little information on pion reaction cross-sections for energies above about 500 MeV. The total pion–nucleon cross-section drops significantly from the 200 mb resonant peak at 200 MeV to around 30 mb for energies above 500 MeV. Since this is not significantly different than the nucleon-nucleon cross-section, pion transparency should be comparable to proton transparency at higher energies, i.e. approximately half the pions will react through either scattering or absorption.

Interactions of 1–10 GeV neutrinos will produce pions with a wide range of energies. It should be noted that backward decay of the Δ resonance can produce rather low-energy pions, because the decay pions have a velocity in the Δ rest frame comparable to that of the Δ in the lab.

The large absorption cross section (100–200 mb for C, 400–600 mb in Fe) for 100-300 MeV pions means that even pions that escape the nucleus may interact again, with absorption rates of a percent/cm in scintillator.

There are other effects which influence the observed transparency of produced secondaries. As described in the Nuclear Effects section of Chapter 7, the quantum effect of hadron formation length and the QCD effect of color transparency can increase the probability that a secondary escapes the nucleus without undergoing FSI. These effects are proportional to the energy and Q^2 transfer and will not influence the transparency of low momentun secondaries.

12.2 Nuclear Effects and Interaction Probabilities

MINERνA will provide the setting for a systematic, precision study of cross-sections and, with sufficient $\overline{\nu}$, structure functions, on a variety of nuclear targets. Briefly reviewing the nuclear effects on measured structure functions (directly proportional to the cross-sections) as a function of x_{Bj} reveals:

12.2.1 Low-x: Nuclear shadowing

In the shadowing region, $x < 0.1$, there are several areas where neutrino scattering can provide new insights compared to charged-lepton probes. "Shadowing" is a phenomenon which occurs in nuclear targets and is characterized by reduction of the cross-section per nucleon for larger-A nuclei, such as Fe, compared to smaller-A nuclei such as D_2. A recent summary of theoretical interpretation of this effect is presented in [175].

Vector-meson dominance (VMD) is the accepted explanation for shadowing in the scattering of charged leptons off nuclei (i.e. $\mu/e - A$) for $Q^2 \leq\sim 5\,\mathrm{GeV}^2$. In essence, the incoming boson dissociates into a $q\bar{q}$ pair which interacts strongly with the nucleus as a meson. Due to the V-A nature of the weak interaction, neutrino scattering should involve not only a VMD effect but additional contributions from axial-vector mesons such as the a_1. Other sources of nuclear shadowing (mainly in larger nuclei) involve gluon recombination from neighbors of the struck nucleon, shifting the parton distributions toward higher values of x. At higher Q^2, shadowing is dominated by Pomeron exchange in diffractive scattering.

A quantitative analysis of neutrino shadowing effects by Kulagin[176] uses a non-perturbative parton model to predict shadowing effects in ν–A scattering. As illustrated in Figure 45, which predicts the ratio of scattering off Fe to scattering off D_2, shadowing effects with neutrinos should be dramatic at low Q^2 (the kinematic region of the NuMI neutrino beam) and still significant even at large Q^2. Kulagin also attempts to determine the quark-flavor dependence of shadowing effects by separately predicting the shadowing observed in $F_2(x, Q^2)$ (sum of all quarks) and $xF_3(x, Q^2)$ (valance quarks only). These predictions should be testable in MINERνA.
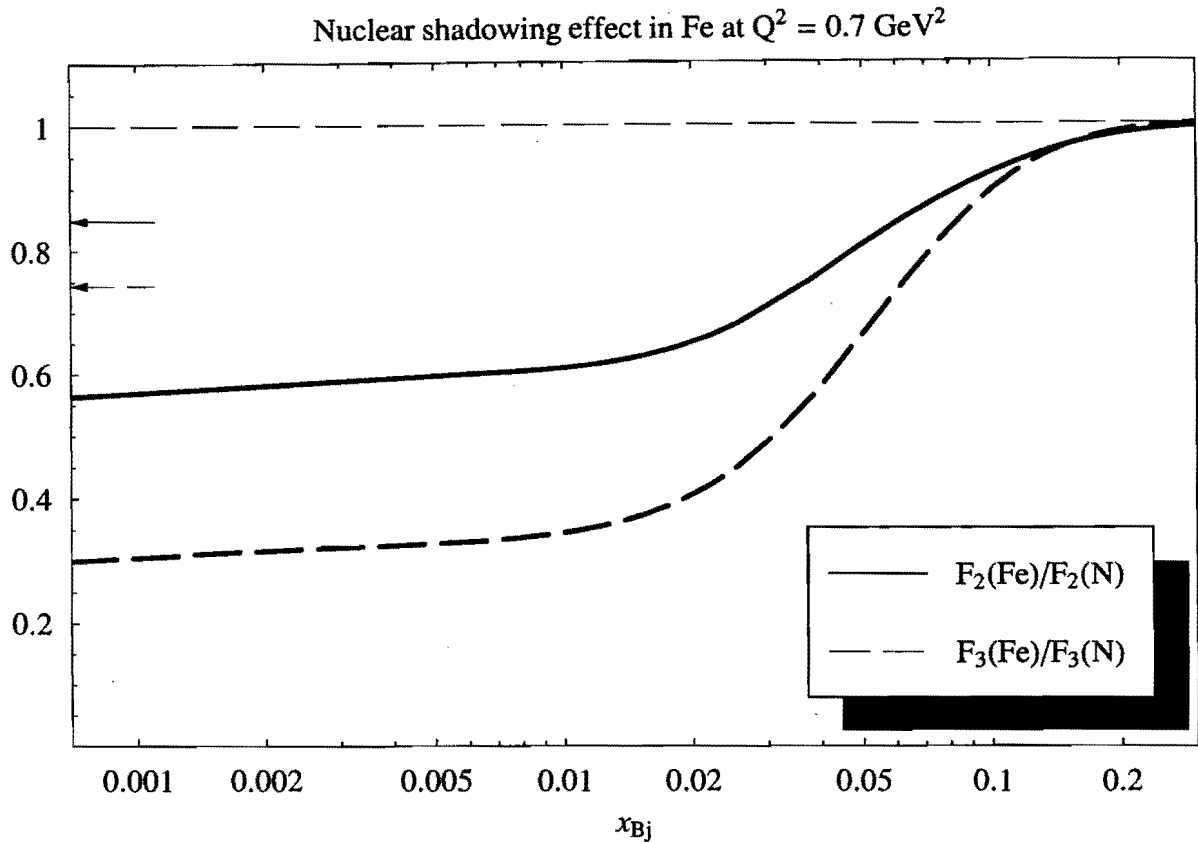
Figure 45: Expected shadowing effects off an Fe target at $Q^2 = 0.7$ $(GeV/c)^2$ with Kulagin's non-perturbative parton model emphasizing the difference in shadowing for F_2 and xF_3. The arrows in the vicinity of R = 0.8 indicate the expected shadowing strength at $Q^2 = 15$ $(GeV/c)^2$.

12.2.2 Mid-x: Anti-shadowing and the EMC effect

Drell-Yan experiments have also measured nuclear effects and their results are quite similar to DIS experiments in the shadowing region. However, in the anti-shadowing region where R_A, the ratio of scattering off a nucleus A to scattering off Deuterium, makes a statistically-significant excursion above 1.0 in DIS, Drell-Yan experiments see no effect. This could indicate a difference in nuclear effects between valence and sea quarks as also predicted by Kulagin.

Eskola et al.[177] have quantified this difference using a model which predicts that the differences between nuclear effects in $xF_3(x, Q^2)$ and $F_2(x, Q^2)$, identified by Kulagin in the shadowing region, should persist through the anti-shadowing region as well. More recent work by Kumano[178] supports these findings using different fitting techniques.

Based on the various theoretical explanations for the anti-shadowing and EMC effects existing today, the measured effects could be considerably different for neutrinos. Neutrino scattering results would help clarify the theoretical understanding of this phenomenon.

12.2.3 High-x: Multi-quark cluster effects

Analyses from DIS experiments of $F_2(x, Q^2)$ in the "Fermi-motion" region $x \geq 0.7$ have used few-nucleon correlation and multi-quark cluster models to fit the data. These models boost the momentum of some quarks, which translates into a high-x tail of $F_2(x, Q^2)$ that should behave as e^{-ax}. However, fits to $\mu - C$[179] and $\nu - Fe$[180] scattering have obtained two different values for the fitted constant a: $a = 16.5 \pm 0.5$ and $a = 8.3 \pm 0.7 \pm 0.7$ (systematic), respectively. This is surprising because any few-nucleon-correlation or multi-quark effects should have already saturated by Carbon. A high-statistics data sample, off several nuclear targets, could go a long way towards resolving the dependence of the value of a on the nucleus and lepton probe.

12.3 Measuring Nuclear Effects in MINERνA

To study nuclear effects in MINERνA, Fe and Pb nuclear targets will be installed upstream of the pure scintillator active detector which, essentially, acts as a carbon target. Two configurations are currently being examined. One would have (upstream to downstream) three 2.5 cm Fe plates, each plate followed by a module of active scintillator detector. Following this would be six 0.8 cm Pb plates (equal radiation thickness to the Fe) again separated by scintillator modules. This would give just over 1 ton of each target. The second possible configuration involves a total of six planes only, with each plane divided transversely into Fe and Pb segments. As one proceeds upstream to downstream, the Fe and Pb exchange sides on each of the six planes. As always, a scintillator module separates each of the six planes. This configuration would also translate to just over 1 ton of each target. For the standard four-year run described in Section 5.3, MINERνA would collect 940 K events on Fe and Pb and 2.8 M events on the C within the fiducial volume of the scintillator.

MINERνA's goals in measuring nuclear effects can be summarized as follows:

- Measure final-state multiplicities, and hence absorption probabilities, as a function of A with incoming ν;

- measure the visible hadron energy distribution as a function of target to determine relative energy loss due to FSI;

- measure $\sigma(x_{Bj})$ for each nuclear target to compare x_{Bj}-dependent nuclear effects with ν and charged lepton.

- With sufficient $\bar{\nu}$, measure the nuclear effects on $F_2(x, Q^2)$ and $xF_3(x, Q^2)$ to determine whether sea and valence quarks are affected differently.

12.3.1 Multiplicities and visible hadron energy

The expected average multiplicity of neutrino events as a function of E_H, with no nuclear effects, is shown in Figure 46. As mentioned earlier, FSI will perturb this distribution via pion absorption and hadron re-scattering in the nuclear medium. FSI will also distort the initial hadron energy, transfered by the intermediate vector boson, yielding less visible energy in the detector. Restricting the study to events where all particles stop within the 2 m of active scintillator downstream of the nuclear targets will permit measurement of the hadron energy by range to within a few percent. The sample of events meeting these criteria is a function of the hadron energy E_H, and is shown in Figure 47. As can be seen, even at higher values of the hadron energy ν, around 20% of the events have all secondary tracks contained within the active scintillator volume. With nearly one million events on each nuclear target in the four-year run, there will be sufficient statistics to determine the nuclear dependence of both multiplicities and visible hadronic energy.
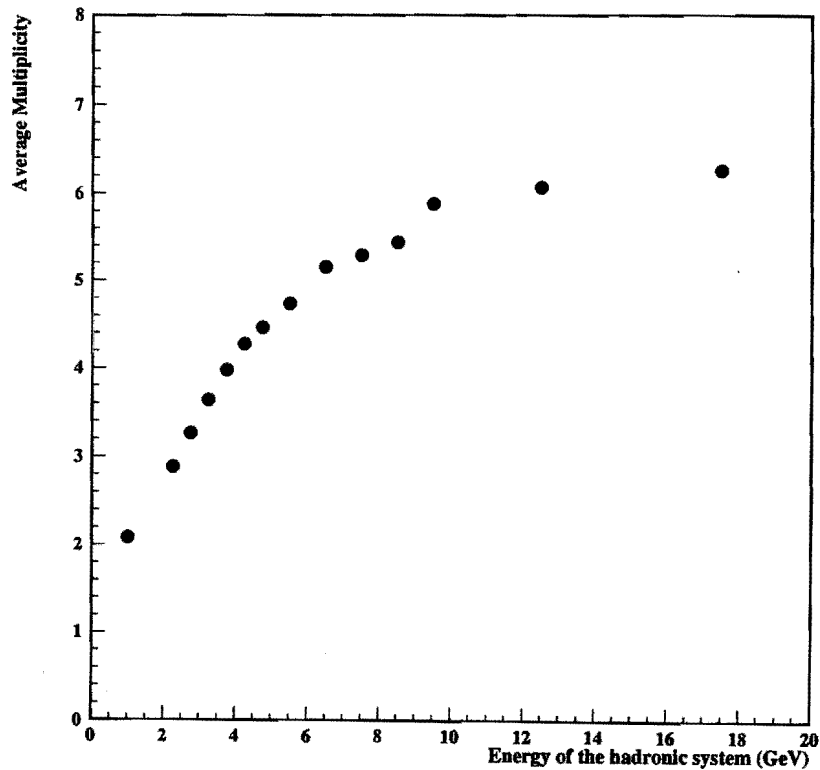
Figure 46: The average multiplicty, excluding neutrons, as a function of the hadron energy of the event. The distribution is predicted by the NEUGEN Monte Carlo without turning on FSI.

12.3.2 x_{Bj}-dependent nuclear effects

Just over 16% of the total event sample has $x_{Bj} \leq 0.10$. The (approximate) statistical accuracy for measurements of the nuclear effects in the ratios of Fe to C events at small x (shadowing region) are summarized in the following table. The columns designated DIS indicate that a cut has been made to retain only events with $W \geq 2.0$ GeV/c^2 and $Q^2 \geq 1.0$ (GeV/c)^2. For the MINERνA DIS analysis,
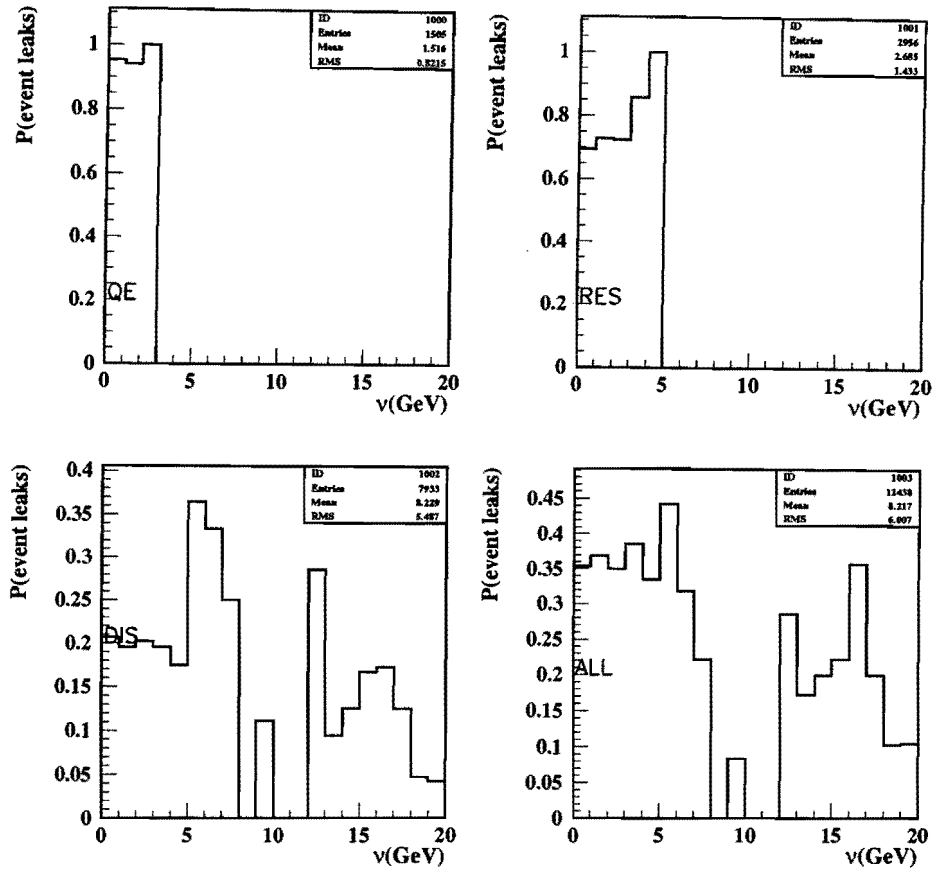
Figure 47: The fraction of events which are fully contained within the active scintillator detector downstream of the nuclear targets as a function of the total energy of the hadronic system. The distributions are for quasi-elastic, resonant, DIS and all reactions, as noted.

the first three bins could be combined into two bins to reduce statistical errors.

Assuming the level of shadowing predicted by Kulagin, the measured ratio of Fe/C and Pb/C, with statistical errors corresponding to the data accumulated during the 4-year run, is shown in Figure 48. The ratios plotted are for all events. The statistical errors would increase, as indicated in Table 9, after making a DIS cut.

The baseline 4-year run would be adequate to achieve the physics goals of the nuclear effects study, although some would be limited by the kinematic reach of the neutrino beam energies used for MINOS running and the minimal $\bar{\nu}$ exposure planned for MINOS.

12.4 Nuclear Effects and Determination of $\sin^2 \theta_W$

There have been many attempts to explain the recent NuTeV [181] measurement of $\sin^2 \theta_W$, which is 3σ away from the Standard Model prediction. Among the most persuasive are the unknown nuclear corrections involving neutrinos[182]. MINERνA will be able to directly measure the ratio NC/CC on various nuclear targets to explore these nuclear effects experimentally.
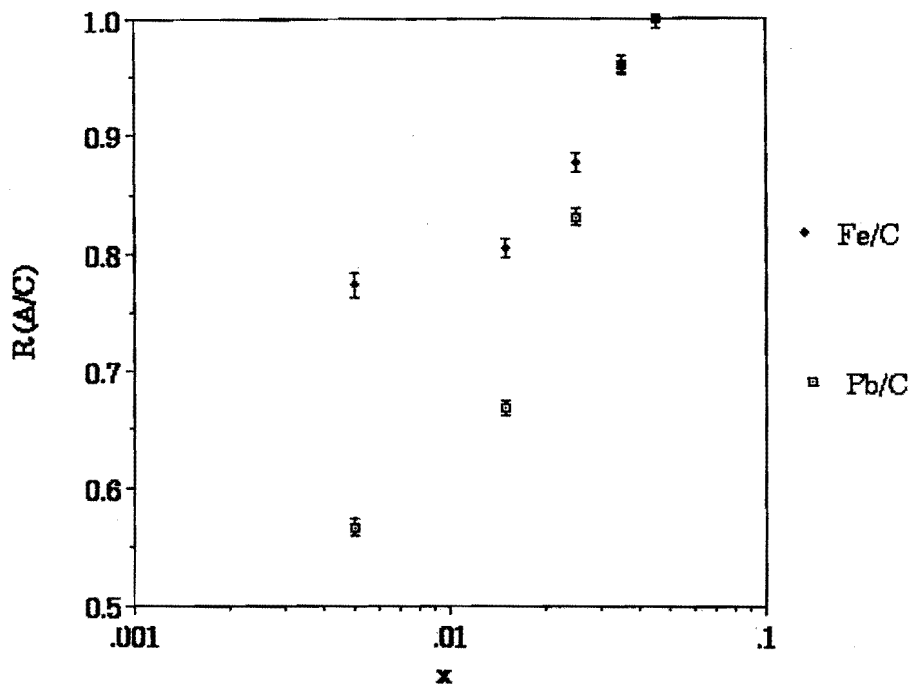
Figure 48: Kulagin's predicted ratio of shadowing effects off Pb, Fe and C targets with the expected errors from all events from the 4-year run.

Ratio Fe/C: $\sim$ Statistical Errors		
x_{Bj}	MINERνA 4-year	MINERνA DIS
0.0 - .01	1.4 %	20 %
.01 - .02	1.1	8
.02 - .03	1.0	5
.03 - .04	1.0	3
.04 - .05	0.9	2.5
.05 - .06	0.9	2.1
.06 - .07	0.8	1.8

Table 9: Statistical errors on the ratio of fully-contained Iron to Carbon events, assuming the level of shadowing predicted by the model of Kulagin, as a function of the x_{Bj} bin.

13 MINERνA and Oscillation Measurements

Over the past decade neutrinos have moved to center stage in the field of particle physics with the discovery of neutrino oscillation. Following on the initial discovery of solar and atmospheric neutrino oscillation are a new generation of high-precision long-baseline experiments dedicated to mapping out the neutrino mixing matrix and mass hierarchy in detail. In this section we address some of the ways in which the measurements made by MINERνA can help these ambitious and expensive experiments achieve maximum senstivity.

13.1 Neutrino Oscillation Landscape

One accelerator-based experiment to explore the atmospheric oscillation sector has already begun, and several more are in the construction phase. The K2K experiment in Japan has seen evidence for ν_μ disappearance, and expects to double its sample of about 50 events over the next year[183]. The MINOS experiment, with a much larger expected event sample, will make the first precision measurement of the atmospheric mass splitting, again through ν_μ disappearance[203]. Finally, the OPERA and ICARUS experiments in Europe will attempt to further confirm the $\nu_\mu \rightarrow \nu_\tau$ oscillation hypothesis by reconstructing actual ν_τ charged-current interactions in a beam produced as ν_μ. The solar sector is being addressed by novel detection techniques of solar neutrinos themselves, and the KamLAND experiment, which uses a number of reactors as its anti-neutrino source[185]. If confirmed by MiniBooNE[184], the LSND anomaly would dramatically affect the lines of inquiry for future experiments, demanding precise oscillation measurements with both long and short baselines, and hence both 1 GeV and several-GeV neutrino beams.

One reason for the flurry of recent activity in neutrino physics is that non-zero neutrino masses and mixing have profound implications not only for the origin of flavor in the universe, but possibly also the origin of the matter-antimatter asymmetry. Because the lepton mixing matrix seems to have large off-diagonal elements, leptonic CP violation could be much larger than observed in the quark sector, and may be large enough to explain the matter/anti-matter asymmetry that we see today.

A three-generation neutrino mixing matrix can be described by three independent mixing angles $(\theta_{12}, \theta_{23}, \theta_{13})$ and a CP-violating phase (δ_{CP}). The standard notation for this matrix, which transforms between the flavor and mass eigenstates is as follows:

$$\begin{pmatrix} \nu_e \\ \nu_\mu \\ \nu_\tau \end{pmatrix} = U \begin{pmatrix} \nu_1 \\ \nu_2 \\ \nu_3 \end{pmatrix} \tag{57}$$

where if $s_{ij} = \sin\theta_{ij}$, $c_{ij} = \cos\theta_{ij}$, then U can be expressed as three rotation matrices:

$$U = \begin{pmatrix} 1 & 0 & 0 \\ 0 & c_{23} & s_{23} \\ 0 & -s_{23} & c_{23} \end{pmatrix} \begin{pmatrix} c_{13} & 0 & s_{13}e^{i\delta} \\ 0 & 1 & 0 \\ -s_{13}e^{-i\delta} & 0 & c_{13} \end{pmatrix} \begin{pmatrix} c_{12} & s_{12} & 0 \\ -s_{12} & c_{12} & 0 \\ 0 & 0 & 1 \end{pmatrix}$$

In this parameterization, the $\nu_\mu \rightarrow \nu_\tau$ oscillation probability, which describes atmospheric neutrino disappearance, can be expressed:

$$P(\nu_\mu \rightarrow \nu_\mu) = 1 - \cos^4\theta_{13} \sin^2 2\theta_{23} \sin^2\left(\frac{\Delta m_{23}^2 L}{4E}\right) \tag{58}$$

The solar (electron) neutrino disappearance, which has been further confirmed by the KamLand reactor (electron anti-)neutrino experiment (with average baseline 100 km), can be expressed as:

$$P(\nu_e \to \nu_e) = 1 - \sin^2 2\theta_{12} \sin^2 \left(\frac{\Delta m_{12}^2 L}{4E} \right) \tag{59}$$

The measurements in the solar and atmospheric sectors have shown that the mixing angles θ_{12} and θ_{23} are large, but there remains one mixing angle which has not been determined, θ_{13}. This angle would be manifest by electron neutrino disappearance a few kilometers from a reactor, or electron neutrino appearance in a few-GeV ν_μ beam a several hundred kilometers from an accelerator. In the latter case the oscillation probability in vacuum is

$$P(\nu_\mu \to \nu_e) = \sin^2 \theta_{23} \sin^2 2\theta_{13} \sin^2 \left(\frac{\Delta m_{32}^2 L}{4E} \right) + \dots \tag{60}$$

where the missing terms are suppressed by at least one factor of $\Delta m_{12}^2 / \Delta m_{23}^2$.

Although reactors can play an important role in discovering non-zero θ_{13}, this field will rely on accelerator experiments to eventually search for CP violation and determine the mass hierarchy. For example, the asymmetry in neutrino and anti-neutrino oscillation probabilities, in the absence of matter effects, is (to first order):

$$\frac{P(\nu_\mu \to \nu_e) - P(\bar\nu_\mu \to \bar\nu_e)}{P(\nu_\mu \to \nu_e) + P(\bar\nu_\mu \to \bar\nu_e)} \approx \frac{\Delta m_{12}^2 L}{E} \frac{\sin \delta}{\sin \theta_{13}} < 1 \tag{61}$$

When electron neutrinos pass through the earth they can scatter off electrons, which creates an additional potential not present for muon or tau neutrinos[186]. This additional potential means the effective mixing angle and oscillation length is changed from equation 60, and is changed differently for neutrinos and antineutrinos. Moreover, the sign of the asymmetry is determined by whether Δm_{23}^2 is positive or negative. The asymmetry in $\nu_\mu \to \nu_e$ oscillation probabilities due to matter effects, in the limit of Δm_{12}^2 being zero, is (to first order, when $E < E_R$)

$$\frac{P(\nu_\mu \to \nu_e) - P(\bar\nu_\mu \to \bar\nu_e)}{P(\nu_\mu \to \nu_e) + P(\bar\nu_\mu \to \bar\nu_e)} = \frac{2E}{E_R} \left(1 - \left[\frac{\pi}{2} \right]^2 \frac{E - E_{om}}{E} \right) \tag{62}$$

$$E_R = \frac{\Delta m_{23}^2}{2\sqrt{2} G_F \rho_e} \approx 11 GeV$$

$$E_{om} = \frac{\Delta m^2 L}{2\pi}$$

To measure this asymmetry, oscillation experiments will need to search for electron neutrino appearance in muon neutrino (and anti-neutrino) beams, and to measure the atmospheric Δm^2 precisely, future (and current) experiments will need to measure the muon neutrino survival probability with corresponding precision. Both kinds of experiments will require extremely long baselines, as well as near and far detectors to make the actual probability measurements. Even with an identical near detector, oscillation measurements will require reliable neutrino interaction models. For ν_μ disappearance measurements, these models will be used to determine the mixing parameters from measured distributions in near and far detectors. For ν_e appearance measurements, these models will be used to predict the far detector backgrounds based on data from a near detector. In both cases, the measurements are complicated by the fact that the far detector's ν_μ charged-current event spectrum is dramatically different from the near detector's, due to the large, energy-dependent ν_μ disappearance probability.

102

13.2 Benefits of MINERνA to Oscillation Experiments

With its fine grained, fully-active inner detector, electromagnetic and hadronic calorimetry, and excellent muon measurement capabilities, MINERνA will have superb pattern recognition, energy resolution, and efficiency. These abilities, coupled with the high flux of the NuMI beam make possible a host of improvements that will directly assist oscillation experiments. Indeed, most of the physics areas discussed in this proposal, from the precision measurement of quasi-elastic form factors, to exclusive channel studies, to coherent production, to nuclear physics, have the potential to improve oscillation measurements in one way or another. In particular, improving our knowledge in these areas may help avoid problems in the analysis of oscillation data that are difficult to foresee at this point.

In practice, this benefit will be realized in the development of improved neutrino event generators that encapsulate the information learned from MINERνA and provide a powerful and portable resource for all future neutrino experiments. The primary authors of two of the most widely-used, publicly available event generators are actively involved in MINERνA and see the development of such a 'next generation' generator as one of the principal tangible benefits of this experiment.

The remainder of this chapter will focus on two specific areas where MINERνA can aid oscillation experiments. One is determination of the "neutrino energy calibration", important for Δm^2_{23} measurements, and the second is measurement of backgrounds to ν_e appearance, in a search for θ_{13}.

While this section focuses on MINOS and the proposed NuMI off-axis experiment, MINERνA will undoubtedly benefit other future oscillation experiments as well, including the proposed J-PARCnu project in Japan. The J-PARCnu beam energy is matched to its shorter baseline (and is therefore lower), but neutrino energy calibration and neutral-current π^0 backgrounds are as essential to J-PARCnu as they are at NuMI. Neutrino energy reconstruction in J-PARCnu (as in K2K) is limited by knowledge of the non quasi-elastic background induced by inelastic reactions which feed down from higher neutrino energies. Similarly, most neutral-current background to ν_e appearance in J-PARCnu originates from the high-energy tail of the beam. Although MINERνA obviously cannot directly measure the J-PARCnu beam (as it can for NuMI), its somewhat higher energy reach arguably makes it better-suited for minimizing J-PARCnu systematic uncertainties from neutrino-interaction physics than the J-PARCnu beam itself.

13.3 Δm^2_{23} Measurements

As an example of the importance of neutrino interaction physics to oscillation experiments, consider a measurement of the "atmospheric" mass splitting, which is the primary (but not only) goal of the MINOS experiment.

In a long-baseline experiment there are two limiting cases: a far detector without a near detector (and maximum systematic uncertainties) and a far detector with a perfect near detector (and negligible systematic uncertainties). For a far detector without a near detector, the predicted "no oscillation" distributions are determined by integrating the flux and cross section over a smearing function with takes into account detector acceptance, reconstruction inefficiencies and measurement resolution. In this case the determination of oscillation parameters can only be as good as the understanding of the beam, neutrino interaction cross-sections, detector performance, and reconstruction. In the other idealized extreme, identical near and far detectors see an identical spectrum. In this case, allsources of systematic uncertainty cancel in the near/far comparison.

For MINOS, the near detector will help reduce many of the important systematic errors, but the situation is not quite as perfect as ideal case. The beams (oscillated vs. unoscillated and point source

vs. line source), detector shapes (octagon vs. "squashed octagon"), photodetectors (Hammamatsu M16 vs. M64), electronics (IDE vs. QIE), reconstruction (single neutrino event per readout vs. multiple neutrino events per readout), and beam-related backgrounds all differ between far and near. Great effort in the areas of calibration, reconstruction, and analysis is invested to understand and correct for these small near-far differences. In addition, dedicated measurements of hadron production on the NuMI target by the MIPP experiment should reduce the uncertainties on the near to far flux ratio to the few percent level.

13.4 Neutrino Energy Calibration

Analysis of near detector data aims to predict expected rates and spectra in the far detector in the absence of oscillation, and for different values of θ_{23} and Δm_{23}^2. Differences between these predictions and real data will be used to fit the oscillation parameters. A crucial link in this prodcedure is the translation between measured energy and the neutrino energy, as this quantity is directly related to the oscillation probability. Even the most elaborate suite of near- and far-detector calibrations can at best characterize the response of the detector to known incoming *charged* particles. There is no equivalent test beam for "neutrino calibration"; this final step requires appeal to a model. A reliable understanding of the spectrum and multiplicity of particles produced in neutrino interactions is indispensible for reconstructing the true neutrino energy from the visible energy measured in a calorimeter. There are several areas where these models have large uncertainties, which MINERνA could help to reduce:

13.4.1 Charged and neutral pion production

As MINOS responds differently to electromagnetic and hadronic showers, it will be essential to estimate the relative abundances of charged and neutral particles. These abundances are determined by isospin amplitudes at each point in phase space. As explained in Section 15.1, these amplitudes necessarily include a resonant component from the low invariant mass region where specific exclusive channels are produced, and the deep-inelastic regime where scattering is described by quark transitions in the framework of the parton model. The predictions therefore depend on the resonance model adopted, the model for fragmentation of inclusive quark final-states (particularly at low invariant mass where standard models like the JETSET string model are not applicable), and the treatment of the deep-inelastic/resonant overlap region.

13.4.2 Charged particle multiplicities

Neutrino energy reconstruction also depends on the charged particle multiplicity, as the rest energy of pions disappears via nuclear absorption and the neutrinos produced in π and μ decays. Correction for these losses is therefore also related to the model(s) of charged pion production.

13.4.3 Intra-nuclear scattering

At NuMI energies, intra-nuclear scattering can result in large distortions of the hadronic multiplicities, angular distributions and total energies. A feeling for the variation of intranuclear rescattering can be gleaned from Figure 49, which shows the π^+ spectra from 3 GeV neutrino interactions on three different target nuclei: Carbon, Iron, and Lead. Little data is available to constrain or validate models

of these effects. Measurement of these processes requires a 4π detector, hence electron scattering data has limited utility.
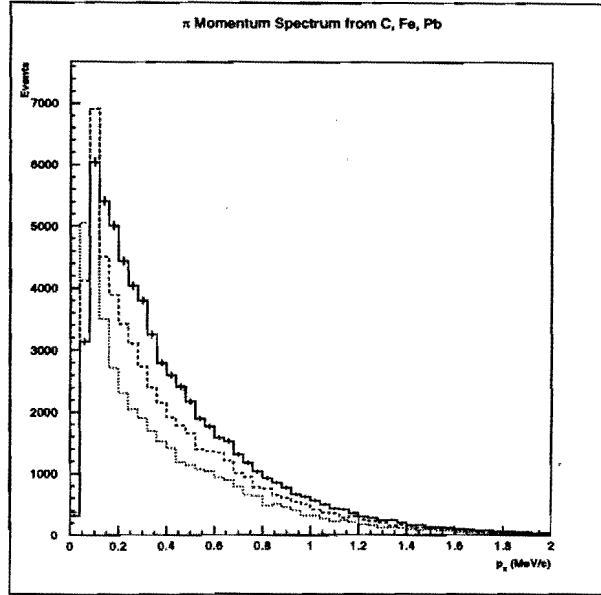
Figure 49: Simulated π^+ momenta for 100,000 3 GeV ν_μ charged-current interactions on Carbon, Iron, and Lead.

13.4.4 Expected results

Figure 50(a) shows the "neutrino energy resolution" for 1 GeV and 2 GeV charged-current interactions in a perfect calorimeter that measures the *kinetic* energy of charged pions and baryons but the *total* energy of photons and electrons. The structure in the distribution results from production of one or more charged pions, and with corresponding amounts of lost rest energy. Figure 50(b) shows the average ratio of visible to true neutrino energy versus neutrino energy for the same detector. For the solid lines there is no intranuclear rescattering, while for the dashed lines rescattering in a carbon target is assumed. Both models show that a correction as large as 10% is required, which translates into a Δm_{23}^2 uncertainty equivalent to the statistical error of MINOS[187].

MINERνA can play an important role in the MINOS Δm^2 analysis by measuring the charged-pion multiplicity as a function of visible neutrino energy. Data from a variety of nuclear targets (including Iron) will strongly constrain and redundantly validate rescattering models. Figure 51(a) shows the charged paticle multiplicity for ν_μ charged-current interactions in the NuMI low-energy beam, for the two models described in Figure 50(b). Finally, Figure 51(b) shows the difference between the oscillated and unoscillated ν_μ interaction spectra for the two models of nuclear rescattering. Note that the differences below 1 GeV are enormous, but even at 3 or 4 GeV they are sizeable.

13.5 θ_{13} Measurements

A longer-term goal in oscillation physics is to probe leptonic CP violation and the neutrino mass hierarchy by comparing measurements of $\nu_\mu \rightarrow \nu_e$ and $\bar\nu_\mu \rightarrow \bar\nu_e$ oscillation. These measurements
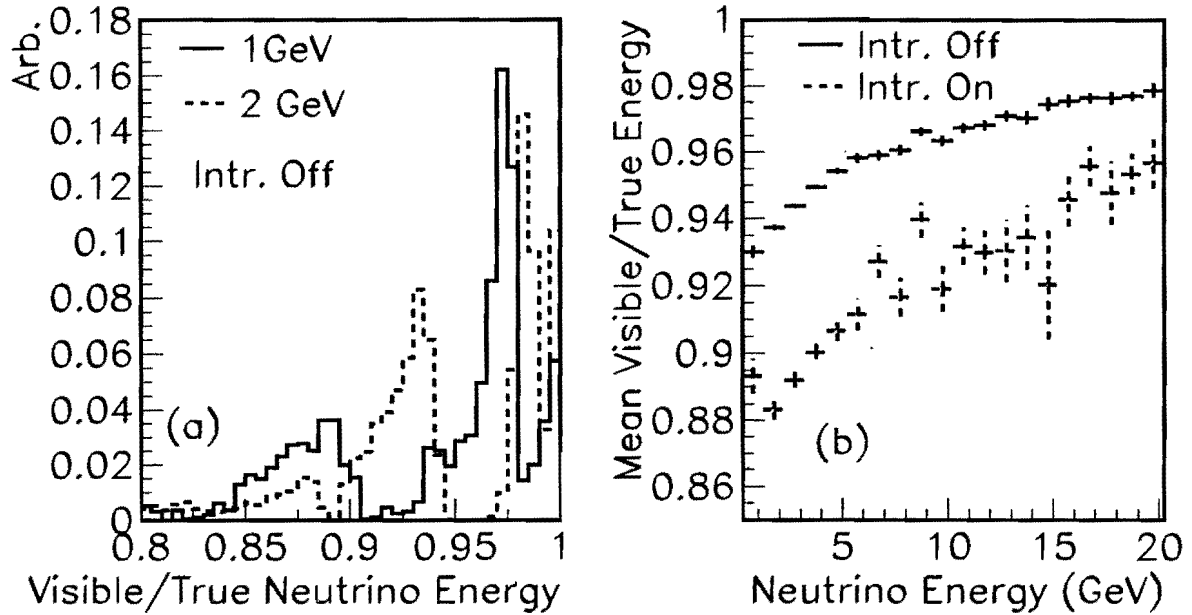
Figure 50: (a) Distribution of the ratio of visible to true neutrino energy for 1 GeV and 2 GeV charged-current neutrino interactions (b) the average of that ratio versus true neutrino energy, for two different models: one withoug intra-nuclear rescattering, and one where rescattering in Carbon is simulated.

are particularly challenging because of backgrounds. Conventional neutrino beams always include ν_e contamination from muon and kaon decays in the beamline. In addition, neutral-current interactions produce π^0 which can be mistaken for electron appearance in the far detector.

In MINOS, neutral-current backgrounds should be several times the intrinsic ν_e contamination, and θ_{13} sensitivity depends strongly on the assumed systematic uncertainties, as shown in Figure 52. MINOS is not optimized to separate neutral-current interactions from ν_e charged-current interactions, and the background for this search is roughly 75% deep-inelastic π^0 production, 15% intrinsic ν_e, and 10% ν_μ charged-current interactions[188].

Because MINOS can only hope to achieve, at best, a factor two improvement in $\sin^2 \theta_{13}$ sensitivity over existing limits, other experiments better suited to this search have been proposed. One proposed experiment would use a much finer-grained detector off-axis from the NuMI beamline, where the neutrino spectrum is much narrower and thus the signal to background ratio is higher. In this off-axis experiment, the dominant background would be intrinsic ν_e, although neutral-current background is comparable, and the ν_μ charged-currents are considerably smaller[189].

Since both MINOS and the off-axis experiment need to measure the intrinsic ν_e and neutral-current background rates, they each require near detectors similar to their respective far detectors. Measuring neutral-current backgrounds directly is difficult at a near detector location, as ν_μ charged-current interactions are far more abundant in the unoscillated beam.
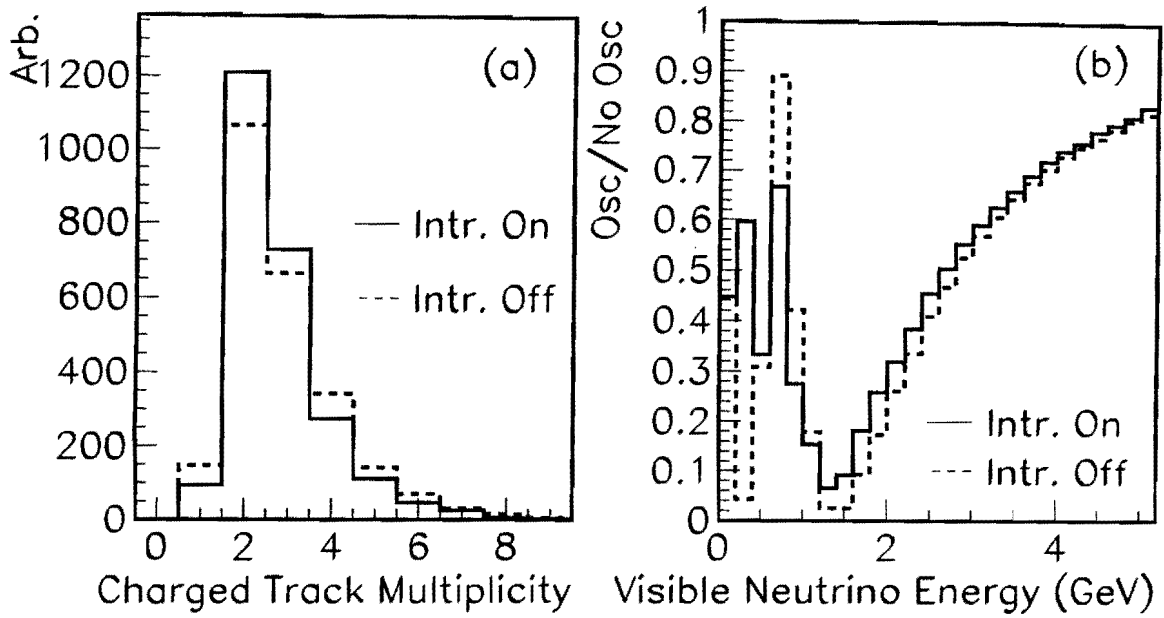
Figure 51: (a) Charged particle multiplicity for the two models of nuclear rescattering discussed in the text, (b) Ratio of oscillated and unoscillated event spectra for those two models, assuming $\Delta m^2 23 = 2.5 \times 10^{-3}$ eV^2
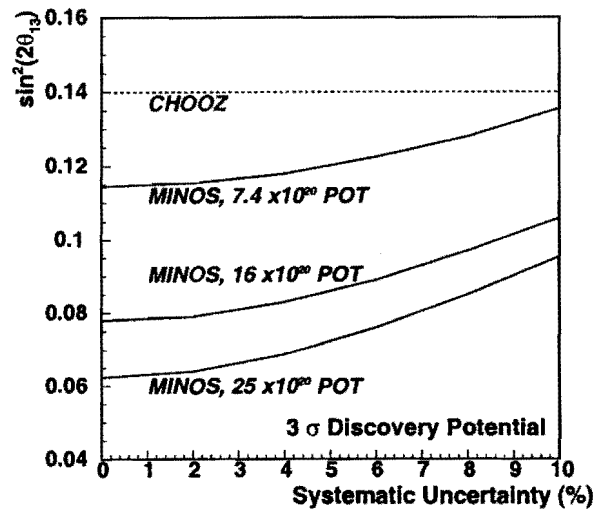
Figure 52: MINOS 3σ sensitivity to non-zero θ_{13} (assuming $\Delta m^2_{23} = 2.5 \times 10^{-3}$ eV^2), as a function of the systematic uncertainty on the background, for several possible integrated proton luminosities.

13.6 ν_e Appearance Backgrounds

MINERνA can measure all three types of ν_e appearance backgrounds. Thanks to superior segmentation, MINERνA can isolate a very clean ν_e charged-current sample and directly measure the ν_e flux. Similarly, with its excellent π^0 identification, energy ($\sigma_E = 6\%/\sqrt{E}$), and angular resolution, MINERνA can map out all the processes that produce neutral pions. Finally, with a fully active detector and good timing resolution, ν_μ charged-current backgrounds can also be identified in MINERνA by exploiting the delayed muon-decay signature that is unavailable to oscillation detectors. The remainder of this section sketches two possible analyses illustrating both MINERνA's potentially decisive ability to isolate appearance backgrounds, and its impressive resolution.

13.6.1 Beam ν_e

The cleanest signature for ν_e charged-current interactions in MINERνA will be the presence of an electromagnetic shower originating near a proton track. Figure 53 shows the distance between the electromagnetic shower origin and the true primary vertex for charged-current ν_e interactions and π^0 production. The figure also shows the length of the showers, measured in MINERνA scintillator planes, or 1.75 cm of polystyrene. For neutral pions the length is from the beginning of the first showering photon to the end of the second one.
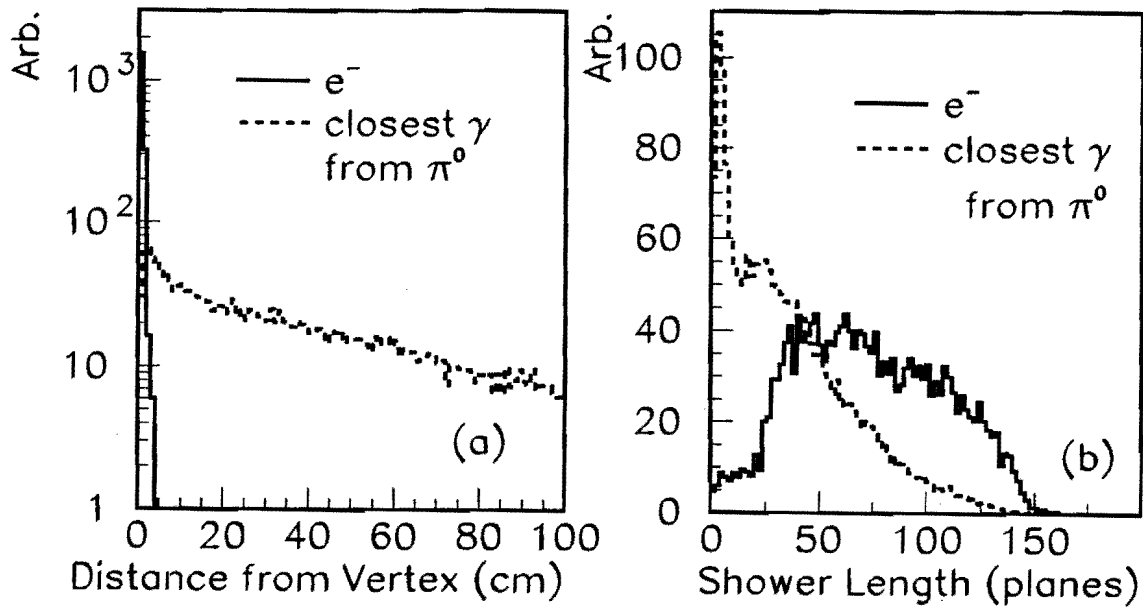
Figure 53: (a) The distance in centimeters between the neutrino vertex, which can be determined from a proton track, and the start of the most upstream electromagnetic shower, for both electrons and photons from neutral pions. (b) The shower length in units of scintillator planes, for electrons and neutral pions.

The MIPP experiment[11] will reduce the uncertainty on the ν_e/ν_μ flux ratio to roughly 5%, but to determine the true intrinsic ν_e background, the uncertainty on the quasi-elastic (Section 6) and resonant (Section 7) cross-sections must also be taken into account.

With a simple analysis that requires a proton track and an electromagnetic shower depositing over 0.5 GeV in the detector and starting within 2 planes of the proton track, MINERνA would collect roughly 1500 charged-current ν_e events per year in a 3-ton fiducial volume, with a neutral-current background about a third the size of the ν_e signal. Figure 54 shows the resulting energy spectra for the ν_e signal and neutral-current background. Further cuts to remove events with an identifiable second photon cluster from π^0 decay could reduce this background even further.

13.6.2 Neutral-current π^0 production

Neutral-current π^0 production can occur through a number of mechanisms - resonant production, coherent production, and deep-inelastic scattering. Figure 55 shows a striking example of MINERνA's response to coherent π^0 production.

Coherent π^0 production is a dangerous ν_e appearance background, because the neutral pion is produced along the direction of the incoming neutrino, and carries away most of the neutrino's energy. See Section 8 for a complete discussion of this process. Its cross-section uncertainty is $\pm 50\%$ or worse, and it has not been measured accurately at 2 GeV, the relevant energy for the NuMI off-axis experiment.

Production of Δ (and other nucleon resonances) is another mechanism for faking a ν_e signal, since their decay products often include π^0. Neutral pions from resonance decay are not as energetic or collinear as those produced coherently, but their angular distribution mimics that of the signal. Resonant π^0 are particularly susceptible to final-state nuclear interaction and rescattering, which will be studied in detail by MINERνA using charged-current reactions (see Sections 7 and 12).

As a proof-of-concept, a sample of neutral-current single-π^0 events has been selected using simple cuts. For events with two well-separated electromagnetic clusters ($E_\pi \equiv E_1 + E_2$), each passing through at least six planes of the fully-active region, requiring $E_\pi/E_{tot} > 90\%$ and $E_{tot} - E_\pi < 100$ MeV efficiently isolates a neutral-current π^0 sample, as shown in Figure 56. After these cuts, the contamination of ν_e and ν_μ charged-current interactions (combined) is less than 1%. The resulting sample contains about 2400 neutral-current π^0 events per 3 ton-yr, of which half are resonant and half coherent.

Coherent and resonant interactions can be cleanly separated by cutting on the π^0 angle to the beam direction, as shown in Figure 57, which also highlights MINERνA's excellent π^0 angular resolution. The overall efficiency for selecting coherent neutral-current π^0 is about 40%.

Finally, some $\nu_\mu \rightarrow \nu_e$ backgrounds in oscillation experiments will come from deep-inelastic scattering, although that sample is easily isolated from the other two processes in MINERνA because of the high multiplicity. Since the mean hadron multiplicity in deep-inelastic scattering is large, and the π^0 angular distribution rather flat, this channel is less likely to contribute background to a ν_e search than the other two. On the other hand the cross-section for deep-inelastic scattering is larger, even at $E_\nu = 2$ GeV than for either resonant or coherent production, and most deep-inelastic interactions in MINOS or the NuMI off-axis experiment will fall into the poorly-understood $W \sim 2$ GeV/c^2 transition region at the border of resonant production (see Sections 10), and fragmentation of low-W hadronic systems is not well-modeled by existing simulations like PYTHIA.
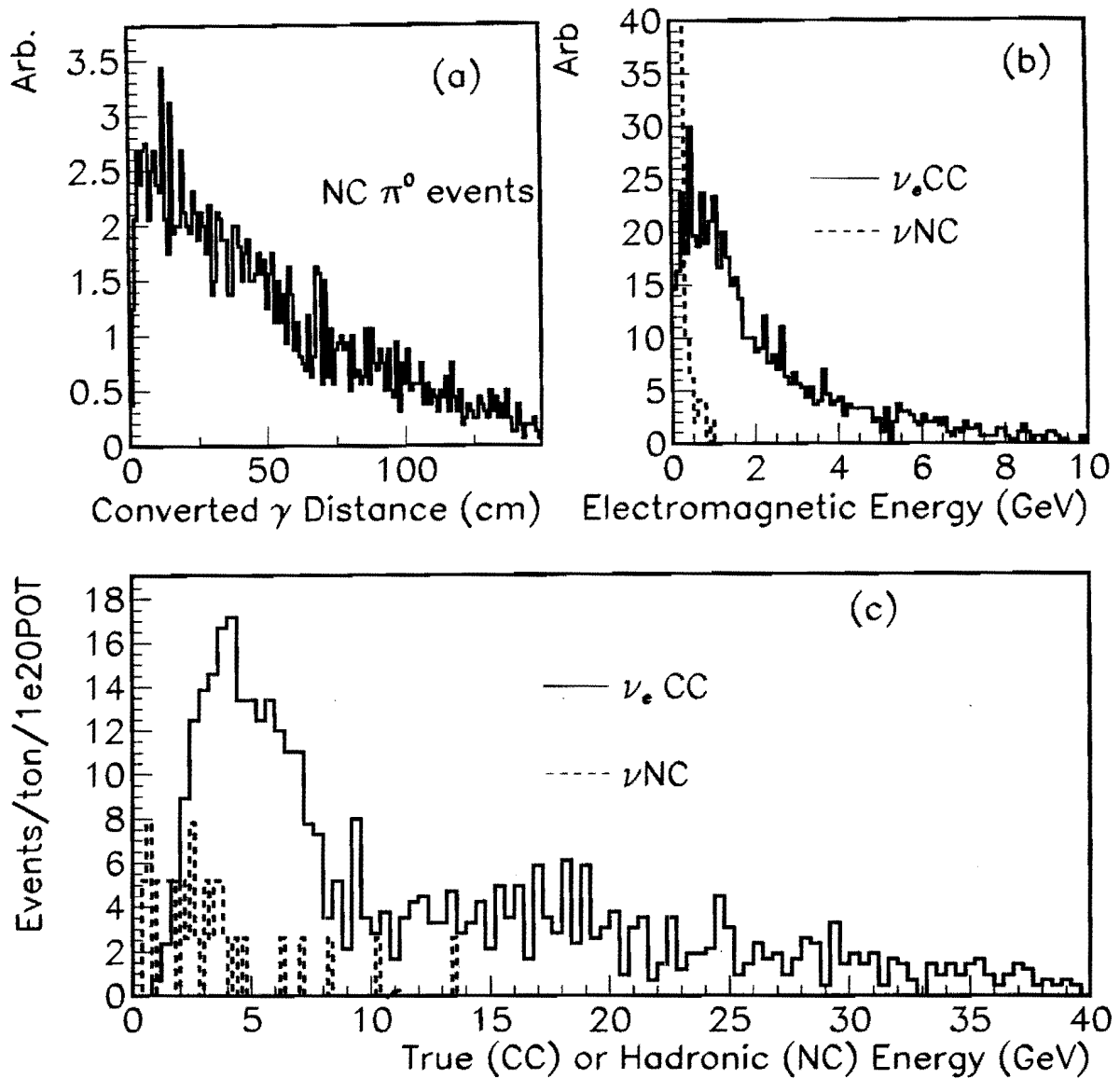
Figure 54: Variables to identify ν_e charged current events in MINERνA : (a)Distance between vertex (determined by proton track) and most upstream converted photon from π^0 decay, and (b)Energy in electromagnetic cluster, for ν_e charged-current and all neutral-current events. (c) True (hadronic) energy for ν_e charged-current (all neutral-current) events, after applying the simple cuts described in the text.

MINERVA TOP VIEW

Run   0 Event   16 Int Type COH
         CC/NC   2 Mech. nu—p
        Vertex (0.0,   0.0,1336.3)
PNEU 14 (0.0000,0.0000,2.3821,2.3821)
PLEP *** (−.0670,−.0650,0.0488,******)
      x 0.000 q2 0.000 y 0.000 w2 0.0000
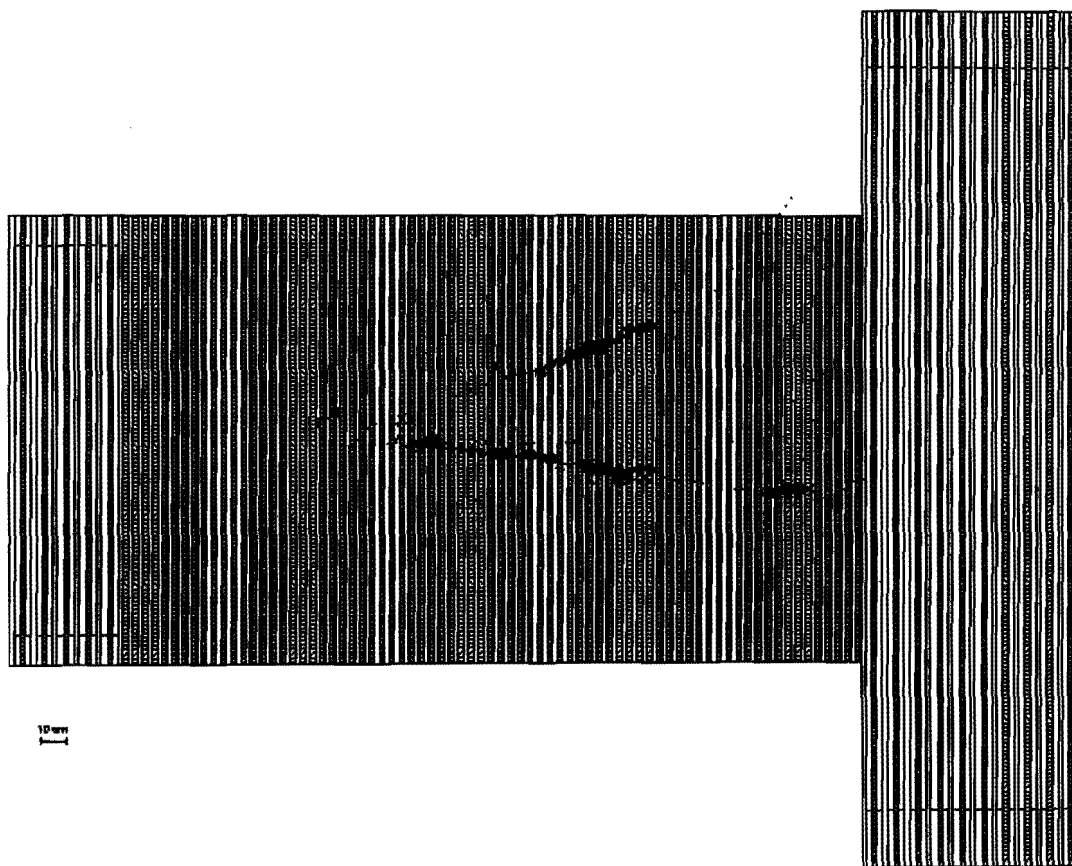
Figure 55: A simulated neutral-current coherent π^0 production event in MINERνA. The position of the $\pi0$ decay vertex can be determined accurately by extrapolating the two photons backward. Notice that both photons pass through a number of planes before beginning to shower, distinguishing them from electrons.
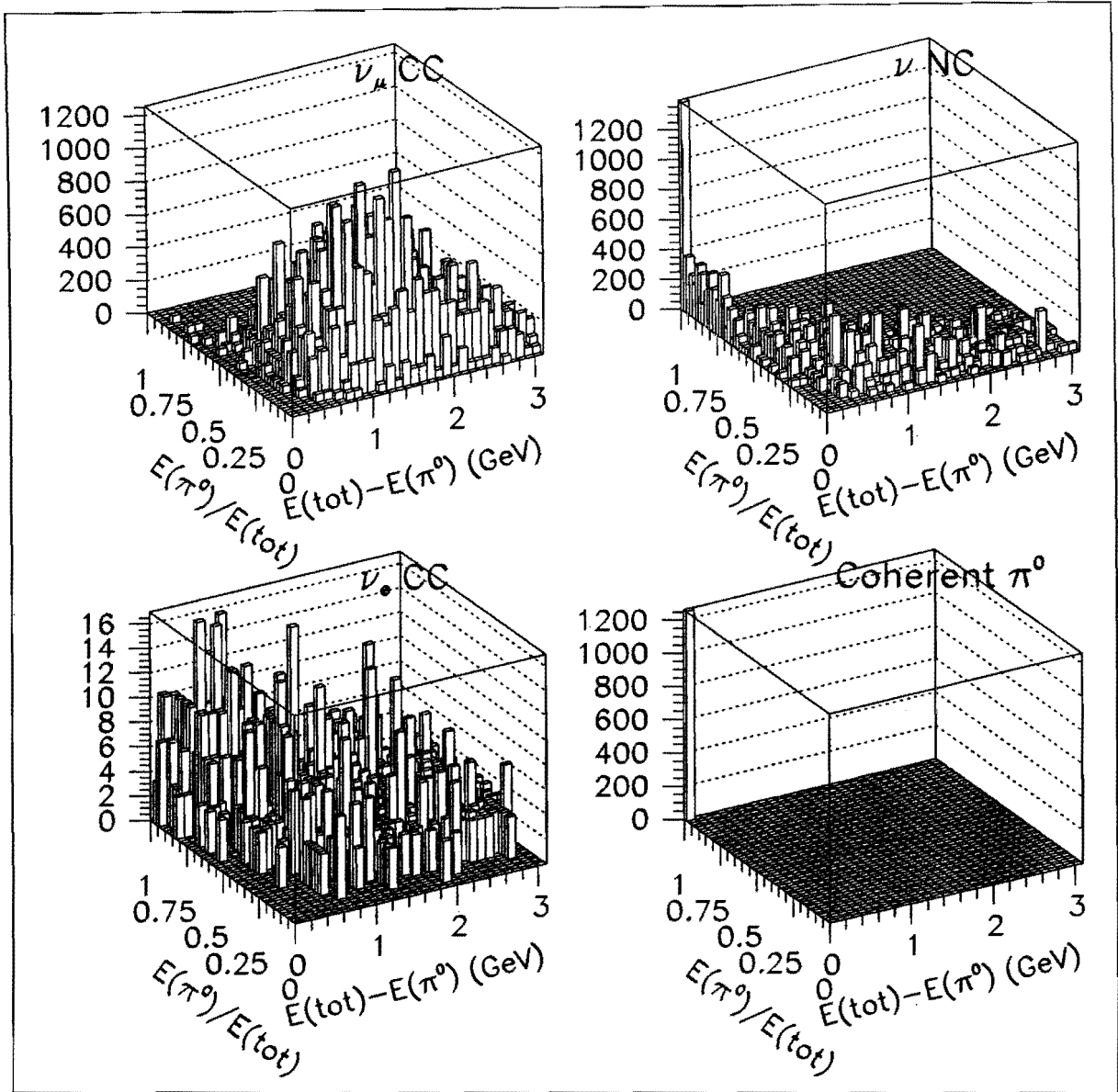
Figure 56: Selection of neutral-current single-π^0 production. The variables plotted are the fraction of visible energy carried by the π^0 candidate (E_π/E_{tot}) and the residual energy $E_{tot} - E_\pi$. The left-hand plots show the backgrounds from ν_μ(top) and ν_e(bottom). The plot at top right shows the same distribution for true neutral-current π^0 production, and the lower right shows the subset from coherent scattering. In the neutral-current plots, notice the dramatic concentration of the coherent π^0 signal in a single bin, in the left-most corner of the graph. All samples shown are normalized to a 3 ton-yr exposure of MINERνA.
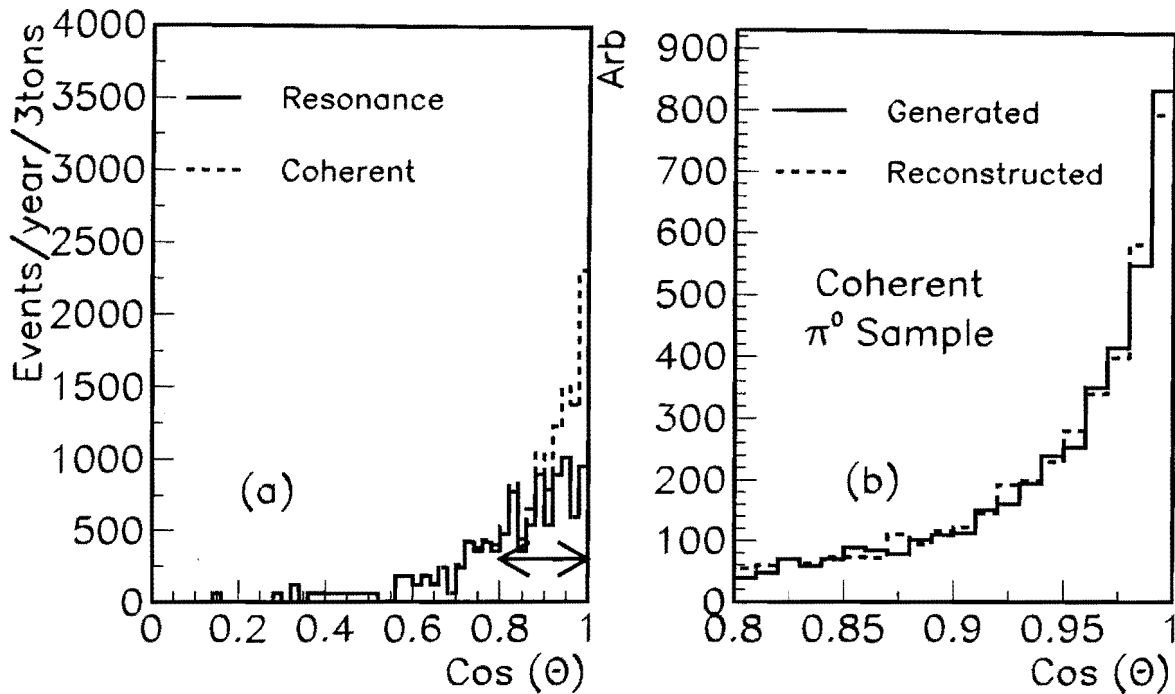
Figure 57: Angular distribution of neutral-current single-π^0 sample. The plot at left shows all events passing the cuts on E_π / E_{tot} and $E_{tot} - E_\pi$ described in the text, broken down into coherent and resonant reactions. The coherent sample is strongly forward-peaked. The plot at right is a close-up of the forward region comparing the true and reconstructed π^0 angular distributions from the beam direction. The distributions are nearly identical, highlighting the MINERνA's excellent angular resolution.

Part III
Project Description

14 The NuMI Near Experimental Hall

The MINOS Near Detector Hall[190] is a fully-outfitted experimental facility that can accomodate the MINERνA experiment with a limited number of additions to the infrastructure.

The detector hall is 45 m long, 9.5 m wide, 9.6 m high, with its upstream end just over 1 km from the NuMI target, at a depth of 106 m below grade. The MINOS detector will be installed towards the downstream end of the hall, leaving a free space upstream amounting to, roughly, a cylinder 26 m in length and 3 m in radius. The neutrino beam centerline will descend at a slope of 3.3°, and enter the MINOS detector at a height of 3 m from the hall floor. The hall has been excavated, and is currently being outfitted for the MINOS near detector, with beneficial occupancy expected in late January, 2004.

Ground water is pumped from the NuMI/MINOS complex at a rate of approximately 320–400 gallons (1300–1600 l) per minute. The hall floors and walls may be damp in places, and a drip ceiling will need to be extended upstream of the MINOS detector to protect MINERνA. The air will be held at a temperature of between 60° F and 70° F (15° C and 21° C), and 60% relative humidity.

14.1 Utilities

The MINOS Service Building on the surface houses the access shaft to the Near Detector Hall, and is the entry point for electrical, cooling, and data services to the hall. A 15-ton capacity crane, with a hook height of 18.5 feet (5.66 m), will be used to lower the 3.47 T MINOS detector planes to the hall. MINOS Detector planes will be moved within the hall using an overhead 15-ton crane, with 22 foot (6.7 m) hook height and a coverage along the beam axis of approximately 40 m.

Quiet power to the hall is provided by a 750 KVA transformer at the surface, which branches to a 45 KVA transformer for the muon monitoring alcoves, and two 75 KVA transformers for the Near Detector hall. The power needs of the MINOS detector account for the capacity of the 4 panelboards served by the two 75 KVA transformers, so additional panelboards for MINERνA will likely be needed. The current estimate for MINERνA electronics and high voltage power is less than 5000 W. It appears that overall capacity for the additional load exists within the MINOS hall, but this needs to be verified in detail.

MINERνA's main non-quiet power need is for the magnet coils, with an estimated ohmic power loss of 30 kW. The MINOS magnet coil power supply will be served by a 480 V line with 400 A capacity, but will require less than 80 kW of power. This will leave ample capacity for the addition of a power supply for the MINERνA coil on the same line.

The heat sink for the MINOS LCW cooling circuit is the flux of ground water collected in the MINOS sump. The cooling is adequate for MINOS, with an output water temperature of 70°F. This should be sufficient to absorb the heat load of the MINERνA magnet, but would likely be too warm to effectively cool the front end electronics. The relatively low heat load of the MINERνA electronics would likely be absorbed without problems by the MINOS hall air conditioning.

14.2 Detector Placement

MINERνA will be placed with its downstream end 1.75 m upstream of MINOS. This will leave sufficient work space between the two detectors, and avoid interfering with the MINOS coil, which extends approximately 1.5 m upstream of MINOS, to the lower right in the view of Figure 58. To have the beam axis intersect the detector axis close to the center of the active plastic target, the lower vertex of

117

MINERνA would be placed 1.10 m off the hall floor. The beam centerline would enter the detector at an elevation of 3.4 m from the floor (Figures 59 and 60).

MINERνA will impinge slightly on a "stay clear" egress space for the lower MINOS detector electronics racks. This could be resolved by either raising MINERνA by less than 10 cm, or by rearranging the layout of the upstream part of the MINOS electronics platform and stairs.

14.3   Impact on MINOS

The impact on MINOS of the heat load and power consumption of the MINERνA detector can be made negligible through relatively minor additions to the hall infrastructure. The presence of the detector in the neutrino beam will cause an increase in the rate of activity in the MINOS detector, particularly in the first 20 planes forming the MINOS veto region. With the current design of the MINERνA detector, the expected event rate in the detector is $\approx$ 1.4 CC events / 10^{13} POT. For a spill of 2.5 x 10^{13} POT this is 3.4 CC events plus an additional 1.0 NC event. Since, in addition, the vectors of all particles leaving MINERνA , with a trajectory heading towards MINOS, will be made available to MINOS, this should be a managable situation.

14.4   MARS Simulation of Radiation Flux

The intense neutrino beam will create a fluence of other particles due to neutrino interactions in the rock surrounding the experimental hall. Several physics topics are sensitive to background interactions caused, particularly, by neutrons. A MARS14-based model[191] has been created to estimate non-neutrino background in the detector. The model includes the rock surrounding the experimental hall, and the MINERνA detector located upstream of MINOS. Both the detectors are positioned on the NuMI axis. The MINERνA detector is simulated as described in Section 16, but with the magnetic field ignored.

The muon neutrino energy distributions used in this simulation for the Low, Medium, and High Energy beam configurations are shown in Figures 61–63. There is an admixture of the other types of neutrinos from π^-, kaon and muon decays (Figure 64).

The MARS14 neutrino interaction model tracks the energy and angle of final state neutrinos, hadrons, $e^{\pm}$, and $\mu^{\pm}$ from neutrino interactions. These particles, along with the showers they initiate, are transported through the user-defined geometry, and energy deposition and dose are estimated. MARS distinguishes four types of neutrinos: ν_μ, $\overline{\nu}_\mu$, ν_e and $\overline{\nu}_e$, all of which are present in the NuMI beam (Figure 64). The interactions included in the model are listed in Table 10.

The model is described in detail in [195]. Some notable features of the model include:

• Recoil of the target is simulated only for elastic interactions.

• The model does not include inelastic neutrino interactions which produce pions via resonances. The cross sections for such processes are relatively small however compared to ones for the deep-inelastic (DIS) and coherent elastic scattering (process 8 in Table 10).

• For charged-current DIS (process 1 in Table 10), the process of hadronization is simplified. Once the momentum of lepton is decided, the total momentum is balanced by a single pion, which is forced to undergo a deep-inelastic interaction in the same nucleus. This coarse "hadronization" is justifiable since we are interested in certain gross averages over the showers.

118
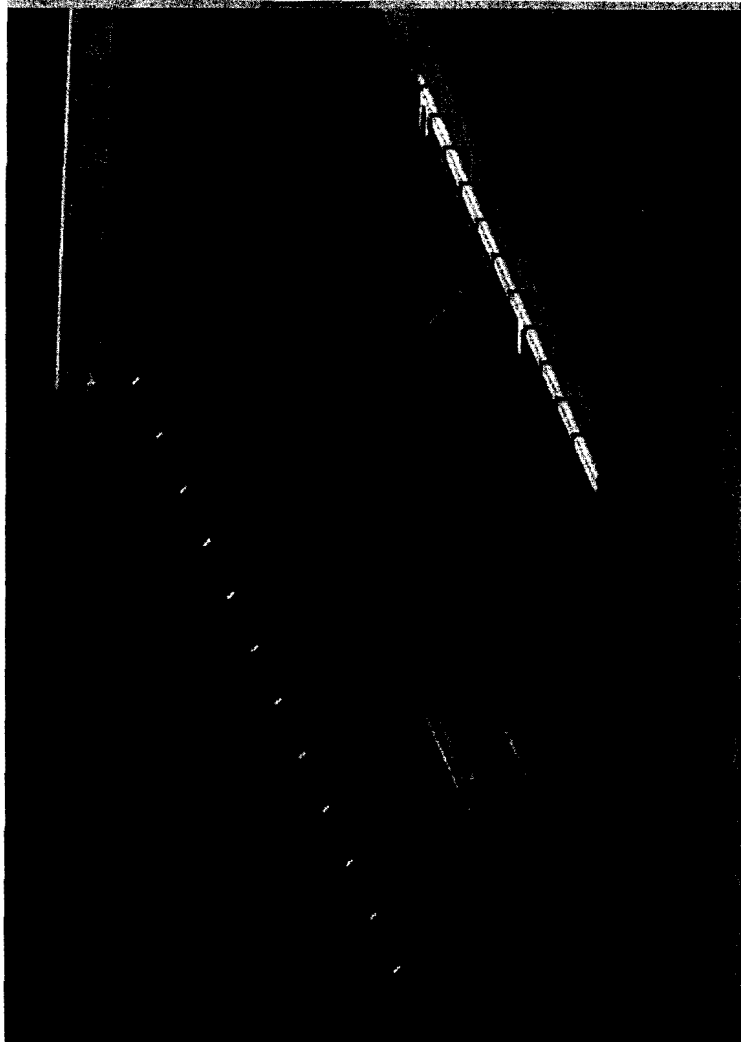
Figure 58: View of the proposed MINERνA detector, and the MINOS detector, looking dowstream.

119
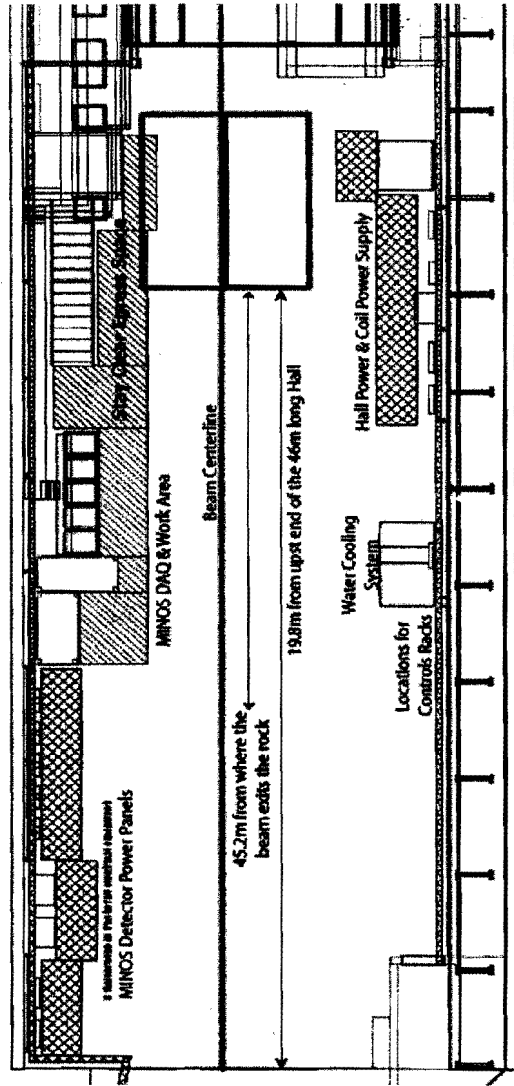
Figure 59: Plan view of the MINERνA detector (purple outline near top of figure).
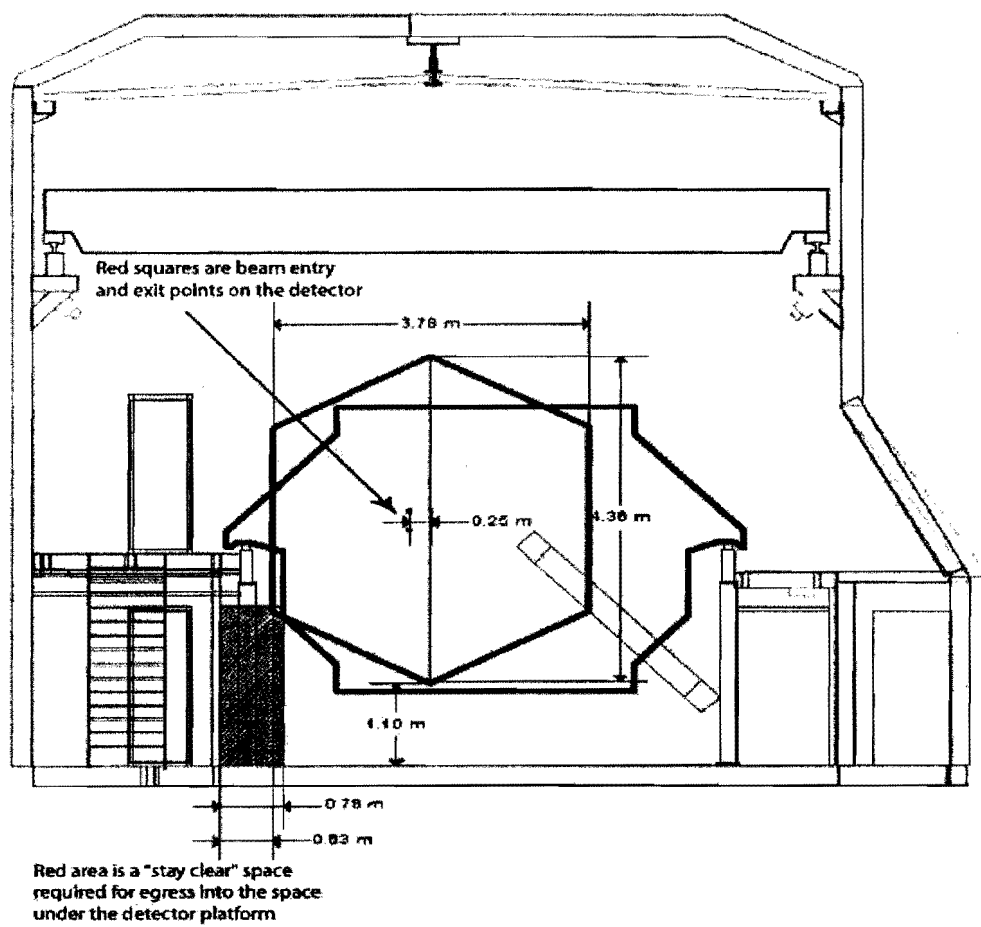
Figure 60: Front view of the MINERνA detector.

121
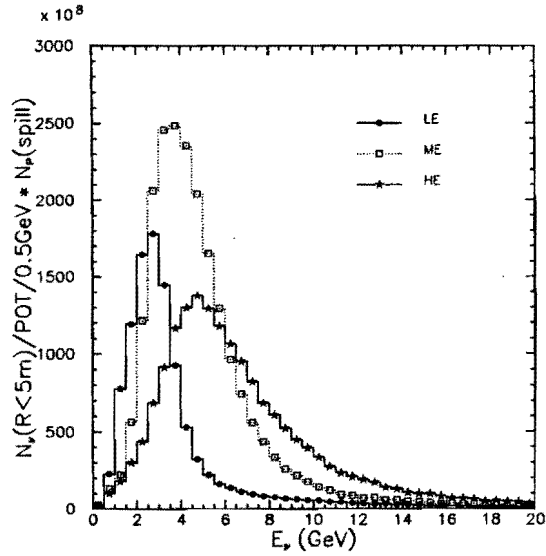
Figure 61: Muon neutrino energy distributions at the near detector hall within a distance of 5 m around the axis of NuMI.
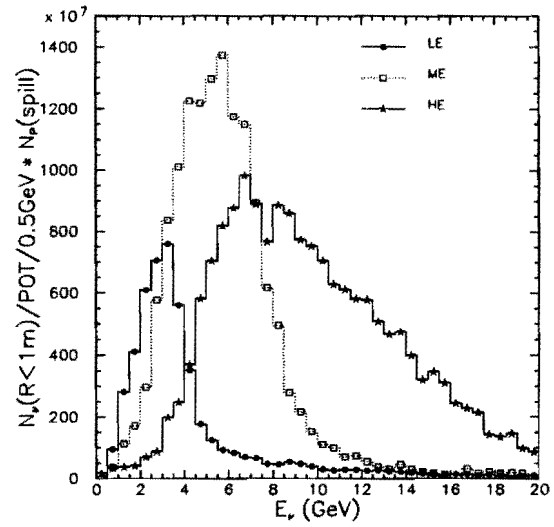
Figure 62: Muon neutrino energy distributions at the near detector hall within a distance of 1 m around the axis of NuMI.
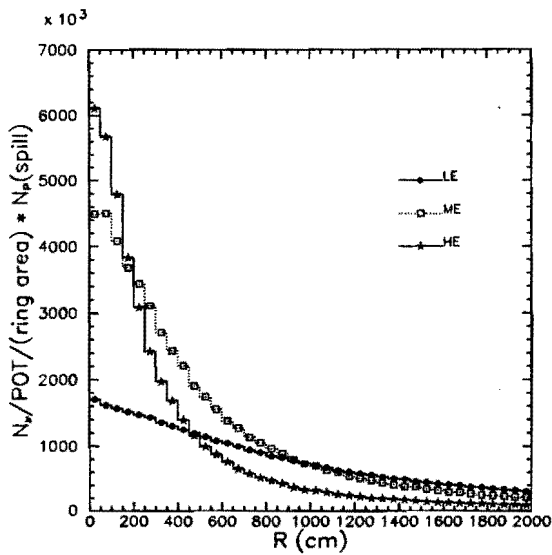
Figure 63: Muon neutrino radial distributions at the near detector hall. The origin corresponds to the NuMI axis.
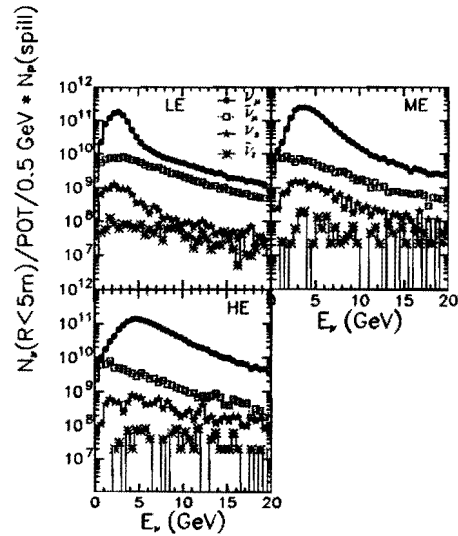
Figure 64: Neutrino beam components.

14.5 Fluxes in MINERνA

Particle fluxes in the scintillator part of detector were calculated for three beam configurations and various threshold energies (Table 11). All the fluxes are given for one spill with the beam intensity of

1)	$\nu_\ell N \to \ell^+ X$	$\overline{\nu}_\ell N \to \ell^- X$
2)	$\nu_\ell N \to \nu_\ell X$	$\overline{\nu}_\ell N \to \overline{\nu}_\ell X$
3)	$\nu_\ell p \to \ell^+ n$	$\overline{\nu}_\ell n \to \ell^- p$
4)	$\nu_\ell p \to \nu_\ell p$	$\overline{\nu}_\ell p \to \overline{\nu}_\ell p$
5)	$\nu_\ell n \to \nu_\ell n$	$\overline{\nu}_\ell n \to \overline{\nu}_\ell n$
6)	$\nu_\ell e^- \to \nu_\ell e^-$	$\overline{\nu}_\ell e^- \to \overline{\nu}_\ell e^-$
7)	$\nu_\ell e^- \to \nu_e \ell^-$	
8)	$\nu_\ell A \to \nu_\ell A$	$\overline{\nu}_\ell A \to \overline{\nu}_\ell A$

Table 10: MARS model interactions for ν_ℓ and $\overline{\nu}_\ell$, where $\ell = \{e, \mu\}$.

2×10^{13} protons on target/spill. The units are 10^{-5}cm^{-2}. The total integrated path-length of a given type of particle is obtained by multiplying the flux by the fiducial volume of the detector.

The neutron background can be dramatically reduced with an appropriate trigger. For example, neutrons entering the detector through the side surface may interact in the barrel calorimeter. A simulation with the following trigger conditions was made. An event was rejected in case of any energy deposited in at least one of four outer scintillator layers of the barrel. For the LE beam configuration and no cut on the threshold energy, the neutron flux dropped to $0.71 \times 10^{-5} cm^{-2}$.

Particle	E_{th} (MeV)	flux (10^{-5} cm^{-2}/2 × 10^{13} P.O.T.)		
		LE	ME	HE
n	0	4.18	4.99	27.86
	20	1.25	1.76	9.93
	50	0.73	1.33	7.61
	100	0.65	0.64	4.15
Charged hadrons	0	1.53	1.21	7.46
	20	0.77	0.98	6.57
	50	0.62	1.59	7.03
	100	0.73	0.80	6.03
γ	0	40.37	27.91	187.89
	20	1.34	1.12	10.23
	50	0.41	1.00	5.27
	100	0.29	0.21	2.34
$e^{\pm}$	0	3.03	2.13	12.03
	20	0.86	0.81	4.49
	50	0.24	0.54	2.65
	100	0.16	0.11	1.94
μ	0	1.71	2.81	8.17
	20	1.64	2.74	8.40
	50	1.53	2.72	8.13
	100	1.67	2.69	7.66

Table 11: Particle fluxes averaged over the scintillator target. E_{th} is a threshold kinetic energy used in the simulations.

15 Monte Carlo Studies and Performance

This section outlines the event simulation and reconstruction software used to optimize the detector's design and quantify its physics capabilities. Much of this software has been borrowed from other experiments, where it has been thoroughly validated. The detector simulation and reconstruction software has been developed specifically for MINERνA, but is based on widely-used libraries and algorithms.

15.1 Event Generators

The MINERνA simulation software interfaces with two event generators that model neutrino interactions with matter: NEUGEN[119] and NUANCE[58]. NEUGEN was originally designed for the Soudan 2 experiment and is now the primary neutrino generator for the MINOS experiment. NU-ANCE was developed for the IMB experiment and is currently used by the Super-Kamiokande, K2K, MiniBooNE and SNO collaborations. Both have evolved from "proprietary" programs designed for atmospheric neutrino studies into freely-available, general-purpose utilities that aim to model neutrino scattering over a wide range of energies and for different nuclear targets. Total charged-current cross-sections calculated by NUANCE (Figure 2) and NEUGEN (Figure 3) appear elsewhere in this proposal. As the results of the two generators agree with each other (to within the depressingly large range of uncertainties in available data)[108], they have been used interchangeably for the present studies.

As in the past, future studies of neutrino oscillation and searches for nucleon decay will rely heavily on the best possible description of neutrino interactions with matter. Neutrino event generators are tools which encapsulate our understanding of this physics in an easily usable and portable form. Practically, they serve two related functions: to allow the rates of different reactions with the experimental target to be calculated, by providing total exclusive and inclusive cross-sections, and to simulate the dynamics of individual scattering events, by sampling the differential cross-sections. Many comparable packages are available to the collider physics community, and have been incrementally improved for decades, forming a common basis for discussion of different models and phenomena. One important goal of MINERνA is to improve the quality of neutrino Monte Carlo event generators, and thereby enhance the physics reach of many future experiments.

MINERνA will attack this problem from both experimental and theoretical directions. Experimentally, MINERνA will make definitive measurements of dozens of exclusive and inclusive cross-sections, across the range of energies most important for future oscillation and nucleon-decay experiments, with a well-controlled flux, and on a variety of nuclear targets. The era of 25% uncertainties and marginally-consistent cross-section data for even the simplest neutrino reactions will end with MINERνA; for the first time it will be possible to validate the details, and not merely the gross features, of competing models.

At the same time, MINERνA will be a natural focus of attention for theorists and phenomenologists developing these models. NEUGEN and NUANCE are two of the most sophisticated neutrino-physics simulations in the world, but NUANCE models quasi-elastic scattering with the 1972 calculation of Smith and Moniz[57], and both programs use the Rein–Sehgal[4] resonant production model which dates from 1981. That no other widely-accepted models for these, the most fundamental neutrino–nucleon reactions, have emerged in the last quarter century is sobering evidence that an experiment like MINERνA is long overdue. New, high-quality data is the surest way to catalyze theoretical ingenuity, and MINERνA will provide the former in abundance. Through our contacts with these theorists, and ability to translate well-tested, state-of-the-art models into universally-available and widely-adopted

software, MINERνA will serve as a conduit for expertise from a diverse collection of disciplines into the high-energy neutrino physics community.[2]

15.2 Beam Simulation

The neutrino fluxes used in the simulation are derived from the GNuMI[192] program developed for the MINOS experiment. GNuMI is a full GEANT[193]-based simulation of the NuMI beamline. As with all current neutrino beams, neutrinos arise from decay of π, K and μ mesons that originate in collisions of a proton beam on a production target. GNuMI simulates all aspects of the neutrino beamline. Protons are fired into the target and the interaction products are transported through the focusing and filtering elements of the beam. Appropriate care is taken to ensure that the description of the beamline's geometry is as complete as possible, and that meson decays proceed with the correct kinematics and branching ratios. For this proposal, all fluxes in MINERνA are taken from the official tables used by the MINOS collaboration.

15.3 Detector Simulation

The simulation of neutrino interactions in the MINERvA detector is carried out by a GEANT-based Monte Carlo program. This program combines a flexible description of the detector geometry, the NuMI neutrino beam flux from the beam simulation, neutrino interaction physics from either of the two generators and simulation of the scintillator response with the standard tracking and particle interaction routines available in GEANT.

15.3.1 Interface to the GNuMI flux

The output of the GNuMI simulation of the beamline is a set of files recording the neutrino flux in 0.5 GeV bins for a nominal number of protons on target. The flux files are in a standard format and hence can be interchanged with no additional modifications to the code. In this way different beam configurations can be easily studied. An option exists to generate interactions with a flat energy spectrum. In this case, beam weights are stored in an output ntuple. This is particularly useful if one wishes to study the effect of different beam configurations without furthur Monte Carlo running.

15.3.2 Interface to the event generators

The Monte Carlo simulation program can be configured to accept neutrino interactions from either NEUGEN3 or NUANCE. The results of a neutrino interaction can be passed to the simulation in a number of ways. By default, the event generation routines in NEUGEN3 are usually called from within the simulation itself. In this mode, the code chooses a neutrino energy from the flux files, samples the density of material along the neutrino path; chooses a vertex and nucleus type, calls the kinematics generator and inserts the list of particles thus obtained into the GEANT data structures. This is not the only mode of generation. As a stand-alone generator, NUANCE provides events in either a text or ntuple format and so provision is made to read in events from a standard external format. NEUGEN3

---

[2]This trend is already beginning, thanks to collaborative work sparked by the NUINT series of workshops. The BBA–2003 quasi-elastic form-factor fits (see Chapter 6) and Bodek–Yang duality-inspired model of deep-inelastic scattering (Section 10.3) have recently been implemented in NUANCE, and NEUGEN is exploring Benhar's spectral-function approach[196] to nuclear binding effects.

has been modified to write out events in the same format, so that the results of both generators may be compared in a consistent manner.

15.3.3 Geometry

Flexibility drives the design of the detector geometry code. The size, segmentation, material and shape of all components of the detector can be set and altered almost entirely from the input datacards. The detector is logically divided into longitudinal sections. Each section can have different dimensions, strip sizes and absorber widths. In addition the absorbers in each section can be be constructed from segments of differing material and widths. The geometry description is sufficiently abstract that minor changes in detector design may be accommodated merely by changing the datacard, allowing for fast detector reconfiguration and easy bookkeeping.

15.3.4 Hits and digitizations

Particles are tracked through the GEANT geometry in the standard manner. When a particle traverses a sensitive detector volume the particle type, volume identifier, entrance and exit points and energy deposition (including Landau and other fluctuations) are recorded as a hit. When GEANT has finished tracking the event, the hits are considered and converted to digitizations. There are as many digitizations as there are strips hit. Multiple hits on a single strip are condensed into one digitization, although information on which tracks contributed to the digitization is stored. These digitizations are then passed to the event reconstruction program.

15.4 Photon Transport Simulations

The MINERνA detector simulation assumes "ideal" light collection, and records the raw energy deposited in each channel. During event reconstruction, the energy deposit is converted to a number of detected photo-electrons. The scale factor between energy deposited and expected photo-electrons detected is determined by a standalone optical simulation validated for the MINOS experiment; the expected number of photo-electrons is smeared by Poisson statistics, and a 10% channel-to-channel Gaussian smearing reflecting a conservative estimate of remaining systematics after calibration and attenuation corrections.

In addition to the GEANT Monte Carlo, a photon transport Monte Carlo written by Keith Ruddick[197] for the MINOS experiment was used to optimize the strip and fiber dimensions. The average light yield from a MINOS scintillator module is 4.25 photo-electrons/MIP at a distance of 4 meters, and attenuation in the fiber is well described in terms of a double exponential [198]:

$$N(x) = A(e^{-x/90 \text{ cm}} + e^{-x/700 \text{ cm}}) \qquad (63)$$

The photon transport Monte Carlo (LITEYLDX) is used to calculate the number of photons trapped in the fiber for a MIP entering at a particular position and for a given configuration of strip geometry, fiber diameter, and fiber placement. This information is then used to determine a relative light collection efficiency for a particular configuration compared to MINOS strips. With the overall normalization and attenuation curve from MINOS one can then calculate the amount of light for any particular configuration. Figure 66, for instance, shows the relative light output for triangular extrusions when the strip thickness, fiber diameter and fiber placement are varied. As expected, light output is nearly proportional
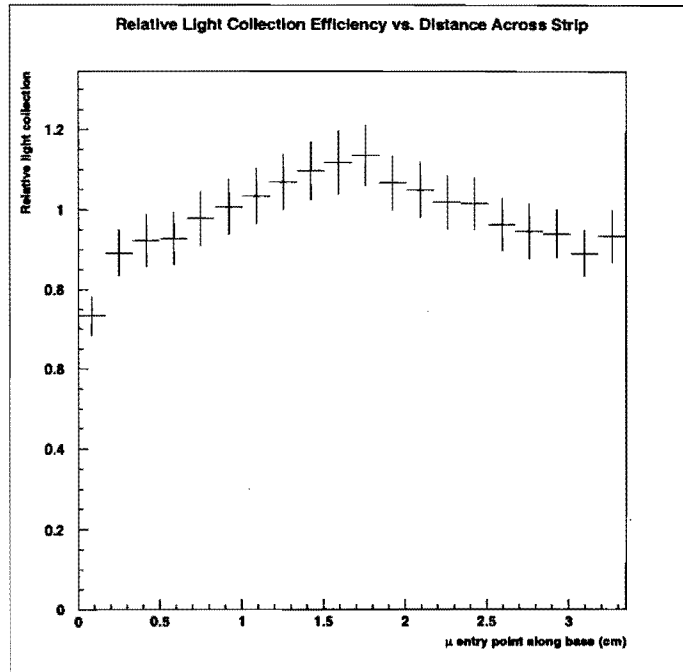
Figure 65: Relative light collection efficiency across the 3.35 cm triangular width of the scintillator extrusion.

to the strip thickness, and is greatest when the fiber is placed at the center of gravity of the strip. Having a fiber in a groove at the edge only results in a 9% drop in the light level. Figure 65 shows the relative light collection efficiency for a triangular extrusion where the entry point of the minimum ionizing particle is varied across the strip width, and indicates that the collection efficiency varies by ±10% over the strip width.

15.5 Event Reconstruction

The output of the detector simulation comprises a list of digitizations for each strip. We have developed a basic reconstruction program to take this list and reconstruct the tracks and vertices in an event.

15.5.1 Pattern recognition

Development of a fully-realistic pattern-recognition algorithm to associate hits to track candidates was not undertaken, in view of the manpower and time available. We are confident that the three-dimensional XUXV modular design of the detector, and its relatively modest occupancy, will allow highly-efficient pattern recognition and track identification. Visual inspection of events through the graphical interface of the detector simulation program reinforces this conclusion. For our design studies, we have adopted "omniscient" pattern recognition based on Monte Carlo truth information. All hits generated by a given track (ignoring channels with overlap) are used to reconstruct it.
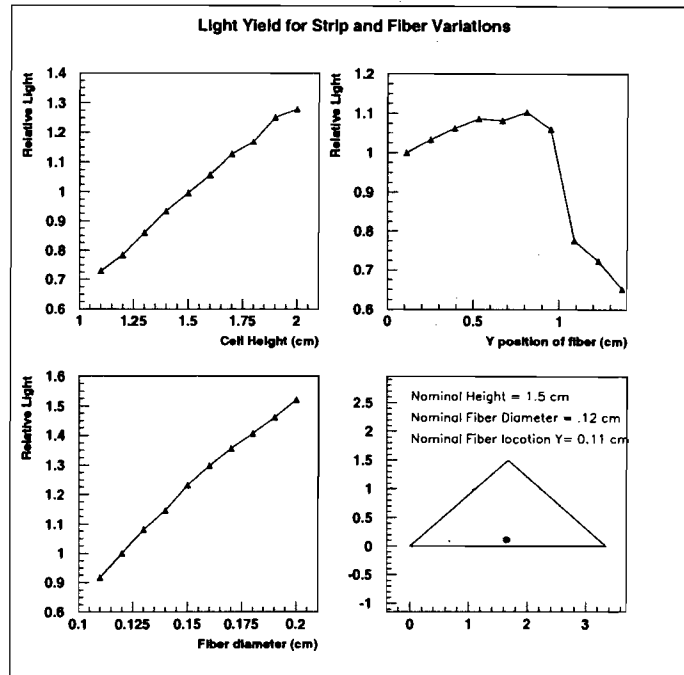
Figure 66: Relative light yield for different strip widths and fiber diameters.

15.5.2 Coordinate reconstruction

Tracks generating hits in at least six scintillator planes of the inner detector, including three planes of the X view, are reconstructed. Coordinates are estimated from the raw, smeared digitizations, using only planes which have one or two strips hit. Tracks at high angles to the detector axis may pass through more than two strips in a single plane, and it should be possible to recover these higher-multiplicity hits with a more sophisticated algorithm. For single hits, the coordinate is taken as the center of the strip. For dual hits, the position is interpolated using the charge-sharing between between strips, with a small geometrical correction based on the estimated crossing angle.

The coordinate resolution for a large test sample of single and double hits can be measured directly using the residuals obtained when each coordinate is excluded, in turn, from the track's fit. This coordinate resolution is parameterized as a function of the track's crossing angle, and used to assign errors to coordinates in the fitter.

15.5.3 Track reconstruction

Reconstructed coordinates are used to fit each track using a Kalman filter algorithm[199]. For this proposal, tracking performance has only been studied in the non-magnetic region of the detector; the track model is perforce a strictly linear one. Neglect of the magnetic field is justified because mission-critical resolutions are determined by performance of the fully-active (non-magnetized) volume, and since coordinate resolution for the strips should not depend on the presence of a magnetic field. The momentum resolution for charged tracks in a magnetic field can be reliably estimated from the coordinate resolution, momentum and field strength[48]. As long tracks may pass through many radiation lengths of

129

scintillator and absorbing material, the Kalman filter's ability to correctly account for multiple Coulomb scattering ("process noise") is essential. The algorithm can optionally be used to exclude outliers from the fit.

Figure 67 shows the expected hit residuals, impact parameter and angular resolution for muons from a sample of quasi-elastic interactions, assuming triangular strips of 3 cm width and 1.5 cm thickness (close to the final design values). Hit resolutions of $\sim$ 3 mm and angular resolutions of $< 0.5°$ are expected. The coordinate resolution is degraded to approximately 1.5 cm if rectangular strips are employed instead of triangular ones, since interpolation based on charge is no longer possible.

Tracking Performance
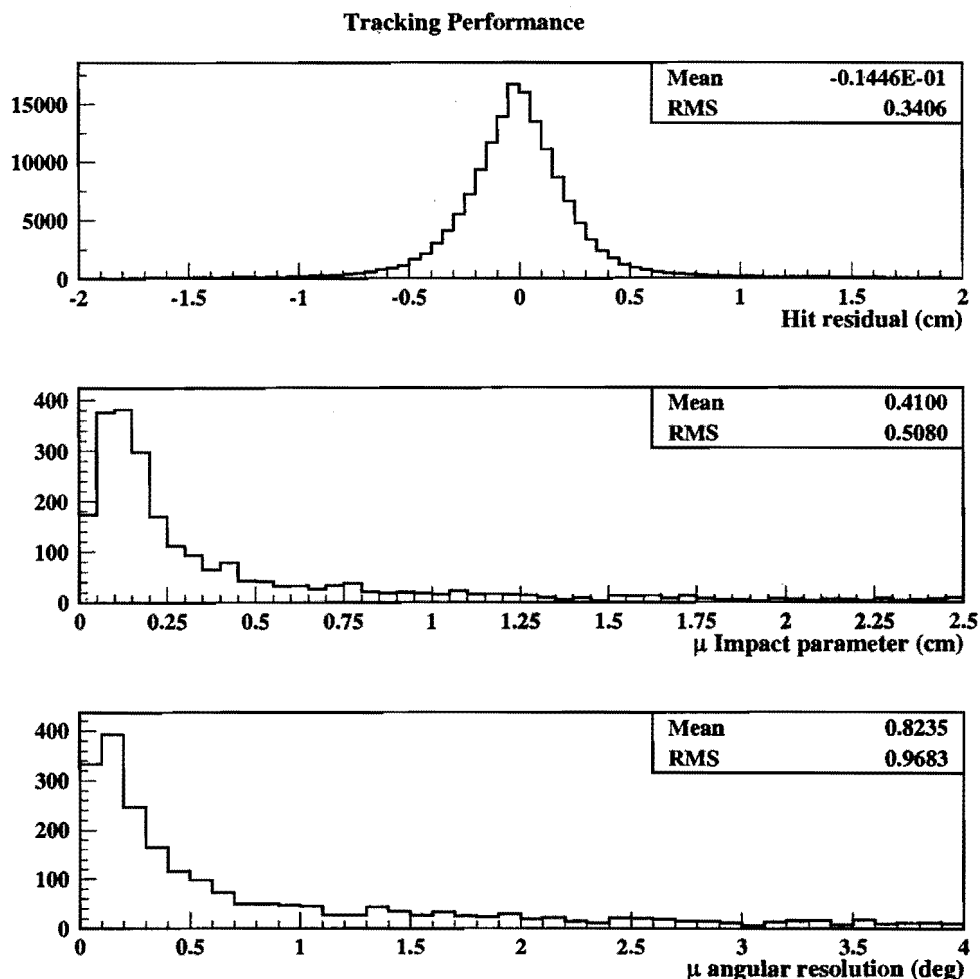
Figure 67: Performance of the tracking algorithm on muons from from a sample of simulated charged-current quasi-elastic interactions. Shown are (top) the hit residuals, (middle) the impact parameter of the muon with the vertex and (bottom) the muon angular resolution.

15.5.4 Vertex reconstruction

In this study, reconstructed tracks are associated to vertices using Monte Carlo truth information. The vertex positions are then fit using a Kalman filter algorithm. Track directions at the vertex are updated

130

taking account of the constraint. This is equivalent to a least squares fit, but mathematically more tractable since it does not involve inversion of large matrices and can be easily extended to a helical track model. The primary vertex resolution for a sample of simulated quasi-elastic interactions with two visible tracks is shown in Figure 68. The vertex postion can be measured to a precision of better than a centimeter.
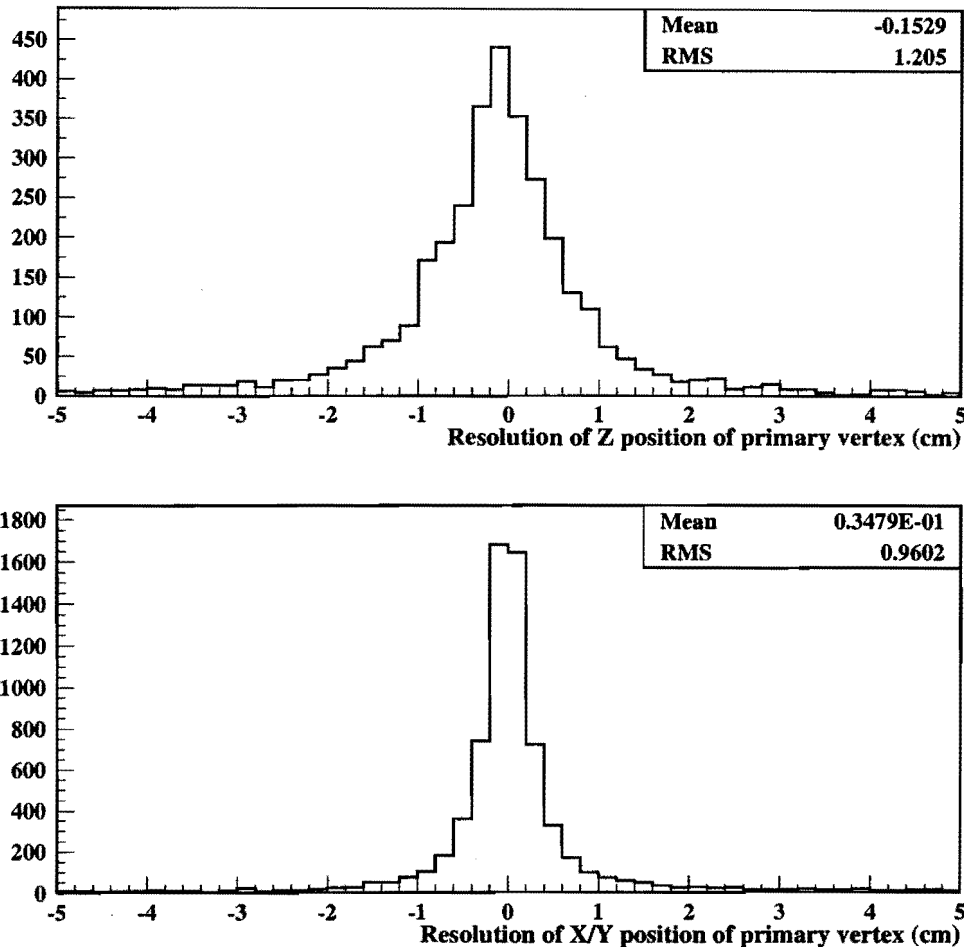
Figure 68: Reconstructed vertex resolution for two track charged current quasielastic events. Shown are (top) the resolution in the longitudinal position of the vertex (Z) and (bottom) the resolution of the transverse position of the vertex (X and Y).

15.5.5 Particle identification

Particle identification in MINERνA will rely on measuring specific energy loss (dE/dx) as well as topology (hadron and electromagnetic showers, decay signatures).

Electromagnetic showers Electromagnetic showers are easily identifiable by their diffuse track and characteristic dE/dx profile in the fully-active central detector and energy deposition in the electromag-

131

netic calorimeters. Section 13.6.1 describes a preliminary technique to separate electrons and photons, when the primary vertex is known, using distance to shower onset and shower length (Figure 53).

Muons Energetic muons can be identified by their penetration of material in the calorimeters and/or MINOS near detector. Muons with a momentum measurement in the magnetic field, or which stop inside the detector can be distinguished from protons and kaons by dE/dx. In addition, the delayed $\mu \rightarrow e$ decay signature can be detected.

Hadrons Hadrons can be identified as such by their interactions in the inner detector and/or hadron calorimeters. Hadrons which stop without interacting or have their momentum measured by the magnetic field can also be distinguished as π, K or p with good efficiency using dE/dx.

dE/dx analysis Specific energy loss (dE/dx) will be an important tool for particle identification in MINERvA. For tracks which stop in the inner detector, the charge deposited near the end of the track (corrected for sample length) can be compared with expected curves for, e.g., the $\pi^{\pm}$, $K^{\pm}$ and proton hypotheses. This technique does not require an independent momentum measurement, since the range (x_{stop}, in g/cm^2) from the stopping point to a given sampling point is closely correlated with the momentum at the sampling point. The algorithm is calibrated by fitting the expected dE/dx vs. x_{stop}, and the standard deviation of this quantity, $\sigma_{dE/dx}$, as a function of x_{stop} for the three different particle types (see Figure 69). The measured dE/dx for a track is compared to the expected value at each sample, to form χ^2 estimators reflecting the goodness of fit to each of the three particle identification hypotheses:

$$
\chi^2(\alpha) = \sum_{i=1}^{N_{sample}} \left[\frac{\left(\frac{dE}{dx}\right)_i^{obs} - \left(\frac{dE_\alpha}{dx}\right)_i^{exp}}{\sigma_i^\alpha} \right]^2 ,
$$

where the sum runs over all measured samples, and $\alpha = \{\pi, K, p\}$. The hypothesis α with the minimum χ^2 is assigned to the track. The frequency of misidentification can be visualized most easily by plotting the difference $\Delta\chi^2$ between the correct χ^2 (for the particle's true type) and the smallest of the two (incorrect) others (Figure 70). With this naïve dE/dx analysis, MINERvA correctly identifies 85% of stopping kaons, 90% of stopping pions, and $> 95\%$ of stopping protons. A similar analysis can be applied to tracks with momenta measured in the magnetic regions of the detector.

15.5.6 Energy reconstruction and containment

The energy of muons from charged-current interactions will be measured using range and/or curvature in the magnetized regions of the detector and the MINOS spectrometer. For muons stopping in the detector, the momentum resolution will be $\frac{\Delta p}{p} \sim 5\%$. If the MINOS detector is used, the momentum resolution will be 13%[190]. Preliminary work on hadronic energy reconstruction suggests that the energy of hadrons which rangeout in the detector will also be measured to a precision of 5% whereas the resolution for isolated showering hadrons will be $35\%/\sqrt{E(\text{GeV})}$. The resolution for hadronic showers in deep-inelastic scattering will be approximately $55\%/\sqrt{E}$ assuming the "ideal" light collection and smearing effects described in section 15.4. For electromagnetic showers, the estimated energy resolution is $6\%/\sqrt{E}$.
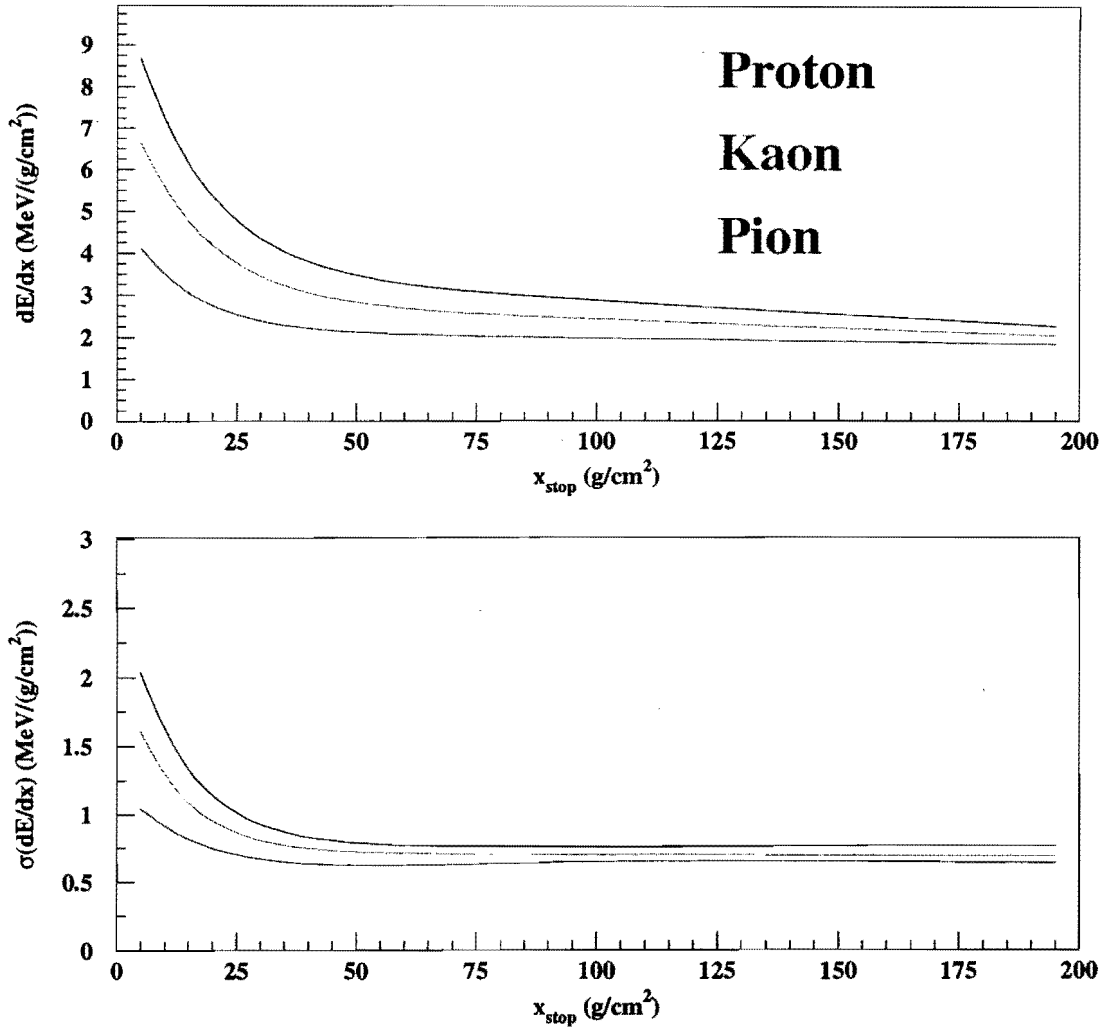
Figure 69: The top figure shows the average specific energy loss dE/dx for stopping $\pi^{\pm}$, kaons and protons, vs. range from the stopping point (in g/cm^2), for the simulated MINERνA inner detector. The bottom figure shows the estimated standard deviation of the energy loss, which is used to form a χ^2 estimator for particle identification.
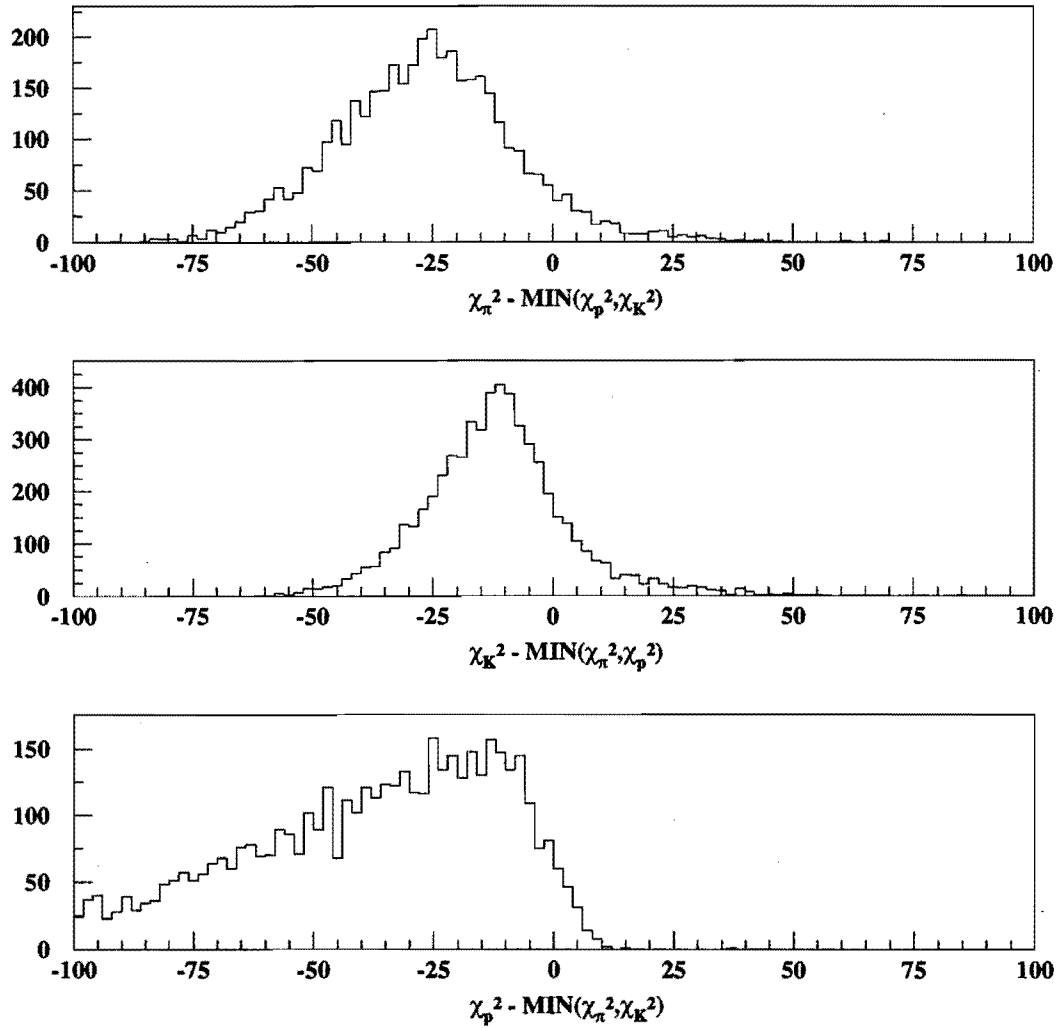
Figure 70: The three plots show the $\Delta\chi^2$ dE/dx estimator for simulated and reconstructed charged pions(top), kaons(middle) and protons(bottom) stopping in the inner detector. Tracks with $\Delta\chi^2 < 0$ are correctly identified.

Containment of hadronic energy is a significant design consideration, as it assists in meeting many of the experiment's physics goals. Studies show that the visible hadronic component of quasi-elastic and resonant events in the fully-active central region of the detector are completely contained, apart from secondary neutrinos and low-energy neutrons. Figure 71 shows the fraction of escaping visible hadronic energy for deep-inelastic reactions in several hadronic energy ranges, and figure 72 shows the probability that a deep-inelastic event will leak visible energy as a function of the true hadronic energy. Only for hadronic energies greater than 8 GeV is there any significant probability of leakage and only above 15 GeV is the average fraction of escaping energy greater than 10%. The fraction of deep-inelastic interactions with hadronic energies over 15 GeV in the low-energy, semi-medium or semi-high energy beams is $< 1\%$, and so visible energy leakage should be insignificant. These estimates ignore downstream components beyond the forward hadron calorimeter, such as a muon ranger and/or the MINOS detector, and are therefore conservative.

Energy Leakage for DIS events
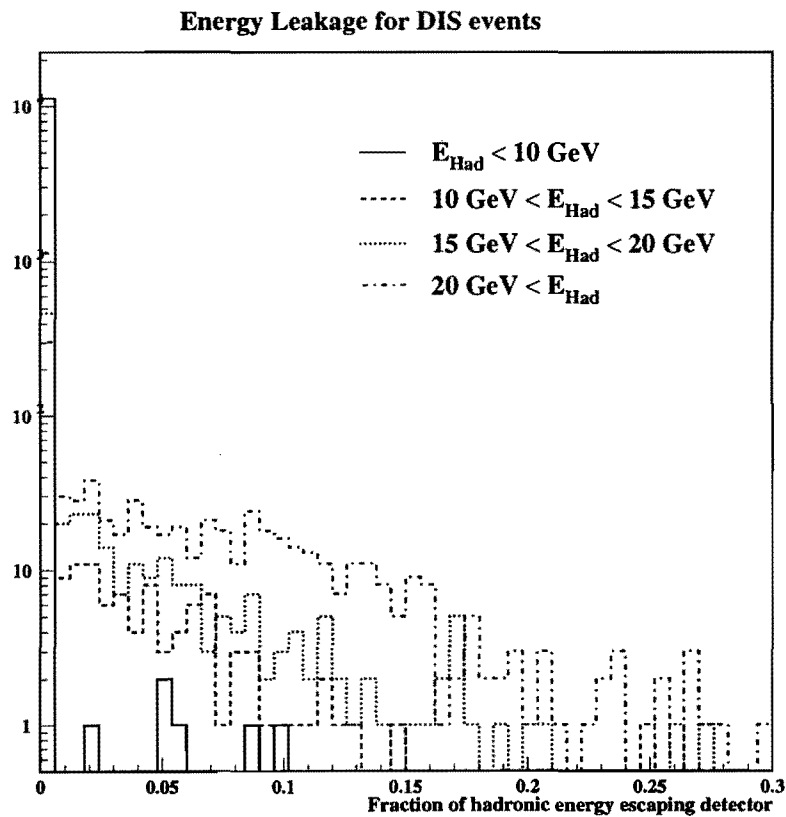
Figure 71: Fraction of hadronic energy escaping the detector for deep-inelastic scattering in the fully-active central region.

15.6 Event Categorisation

Particle identification and event classification will play a central role in the analysis of data from MINERνA. One possible method of event classification is use of artificial neural network (ANN) techniques.

135

Probability of hadronic energy leakage for DIS events
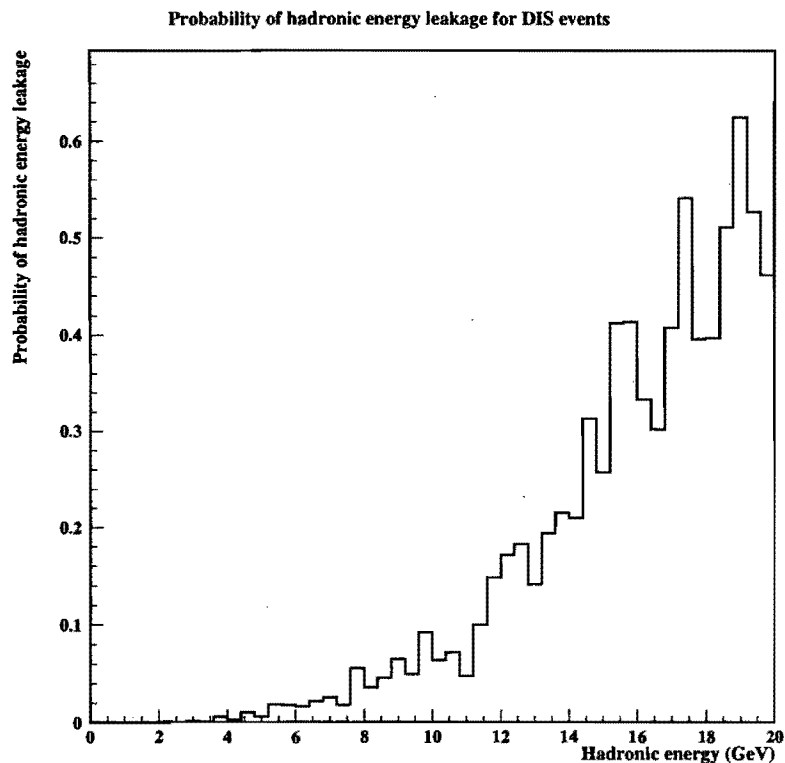
Figure 72: Probability that visible hadronic energy from a deep-inelastic event escapes undetected vs. total hadronic energy.

Event classification will be based on on topological characteristics as well as on particle ID. Separation of CC from NC interactions will be based on muon identification. Detection of muon decays for low energy muons stopping in the carbon gives the potential for accurate CC identification even at high y_{Bj}. In each such class further event identification will be based on other particle ID, energy/momentum measurements and kinematics. Neural networks are designed for such categorisation and have been frequently used in the analysis of data from high energy physics experiments (see, for example, the DONUT[200] experiment).

16 Detector Design

This section describes the basic elements of the MINERνA detector, including the arrangement of active elements and absorber, photosensors and scintillator strip details, and the electronics. A summary of detector parameters along with an estimate of costs and construction schedule are provided in Section 17.

Muon Ranger (MR) **Outer Detector (OD)** **Veto**
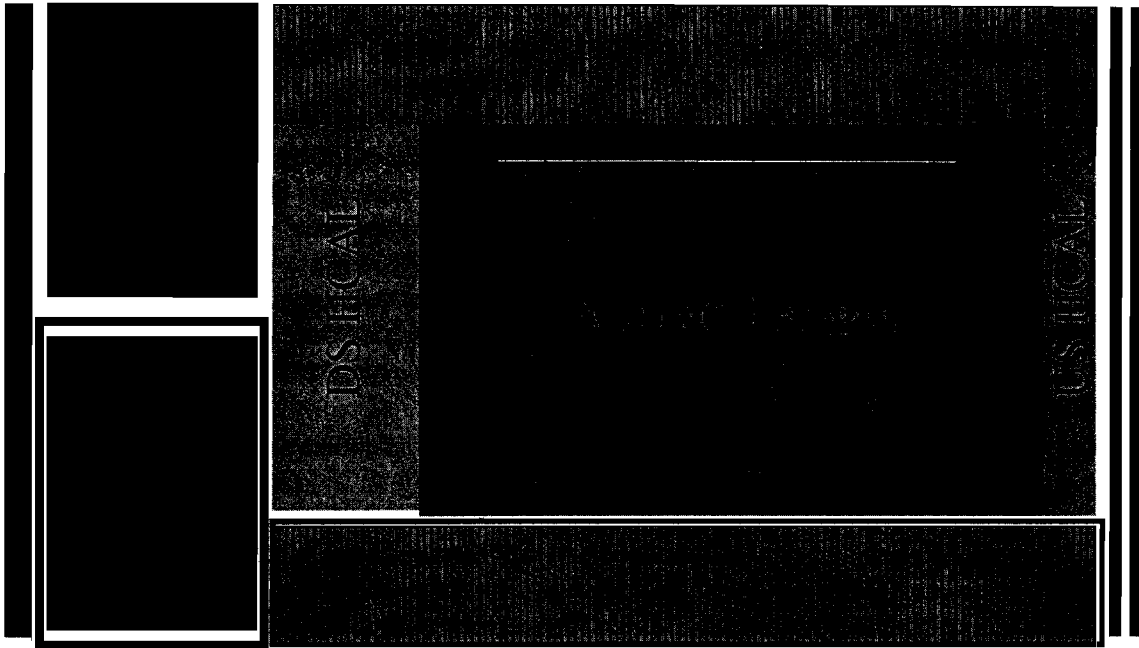
Figure 73: A schematic side view of the MINERνA detector with sub-detectors labeled. The neutrino beam enters from the right.

The MINERνA detector is made up of a number of sub-detectors with distinct functions in reconstructing neutrino interactions. The fiducial volume for most analyses is the inner "Active Target" shown in Figure 73, where all the material of the detector is the scintillator strips themselves. In other regions of the detector, the strips are intermixed with absorbers. For example, the side, upstream (US) and downstream (DS) electromagnetic calorimeters (ECALs) have lead foil absorbers. Surrounding the ECALs are the US and DS hadronic calorimeter (HCAL) where the absorbers are steel plates. On the side of the detector, it is the outer detector (OD) that plays the role of the HCAL; however, note also that the OD is a magnetized toroid which will focus and bend muons, thus allowing a momentum measurement for muons which exit the detector. Upstream of the detector is a veto of steel and scintillator strips to shield MINERνA from incoming soft particles produced upstream in the hall. Finally, the most downstream element, the muon range detector/toroid (MR) gives MINERνA the capability to fully reconstruct even high energy muons without the use of the MINOS near detector as an external muon spectrometer. The presence or absence of the MR in the final design will depend upon the location chosen for MINERνA.

137

16.1 Overview of MINERνA Detector Design

For MINERνA to meet its physics goals, detector must break new ground in the design of high-rate neutrino experiments. With final states as varied as high-multiplicity deep-inelastic reactions, coherent single-π^0 production and quasi-elastic neutrino scattering, the detector is a hybrid of a fully-active fine-grained detector and a traditional calorimeter.

At the core of the MINERνA design is a solid scintillator-strip detector, similar in principle to the recently commissioned K2K SciBar[201]. The plastic inner detector serves as the primary fiducial volume, where the precise tracking, low density of material and fine sampling ensures that some of the most difficult measurements can be performed. These include multiplicity counting in deep-inelastic scattering, tracking of photons, detection of recoil protons in low-Q^2 quasi-elastic events, and particle identification by dE/dx.

The scintillator detector cannot contain events due to its low density and low Z, and therefore, the MINERνA design surrounds the scintillator fiducial volume with sampling detectors. At the low energies needed to study cross-sections of interest to neutrino-oscillation studies, many of the events contain sideways-going and backward-going particles, and therefore these sampling detectors extend to the sides, and even to the back of the detector where they also serve as high A targets for studies of nuclear dependence in cross-sections. Finally, it is important to contain or measure the final-state muon in charged-current events, and for this purpose, the outer side detector and downstream muon ranger of MINERνA are magnetized toroids. A side view of the complete MINERνA design is shown in Figure 74.

The sensitive elements of MINERνA are extruded triangular scintillator strips, 1.7 cm height with a 3.3 cm base, embedded with WLS fibers as detailed in Section 16.4. To improve coordinate resolution while maintaining reasonably large strips, these elements are triangular in shape and assembled into planes as shown in Figure 75; this allows charge-sharing between neighboring strips in a single plane to interpolate the coordinate position. Calorimetric detectors and nuclear targets in the central region of the detector are constructed by inserting absorber between adjacent planes as illustrated in Figure 76. In the outer detector (OD), strips of steel absorber and scintillator are assembled in a picture frame around the inner detector. In the case of the triangle, the scintillator strips are not the full size, but rather half (right) triangles, 1.7 cm in height with a 1.65 cm base and are assembled in doublets between steel absorber strips.

For construction and handling convenience, a single plane of MINERνA, shown in cross-section in Figure 77, incorporates both the inner detector and OD "picture frame" as well as an outer picture frame support structure. Groups of four planes (occasionally two planes only in the upstream veto and downstream muon ranger components) are ganged together into modules, again as illustrated in cross-section in Figure 77. There are three distinct orientations of strips in the inner detector, muon ranger and veto, separated by 60°, and labelled X, U, V. A single module of MINERνA has two X layers to seed two-dimensional track reconstruction, and one each of the U and V layers to reconstruct three-dimensional tracks. The 60° offset makes the hexagon a natural transverse cross-section for the detector, and the size and shape of MINERνA are illustrated in Figure 78.

Except for the upstream veto and downstream muon range (MR) detector, the entire MINERνA detector is segmented transversely into an inner detector with planes of solid strips and an outer picture frame magnetized toroid (OD). In Figure 74, the upsteam and downstream most detectors, the veto and muon range toroid, respectively, are shown in Figure 79. As shown, the scintillator strips extend the full length of the hexagon and range between 205 and 400 cm in length. The toroid steel/absorber is 15 cm

Figure 74: A side view of the MINERνA detector (landscape). A schematic view of the same with labelled detectors is shown in Figure 73.

Basic element: 1.7x3.3cm triangular strips.
1.2mm WLS fiber readout in groove at bottom

Assemble
into planes
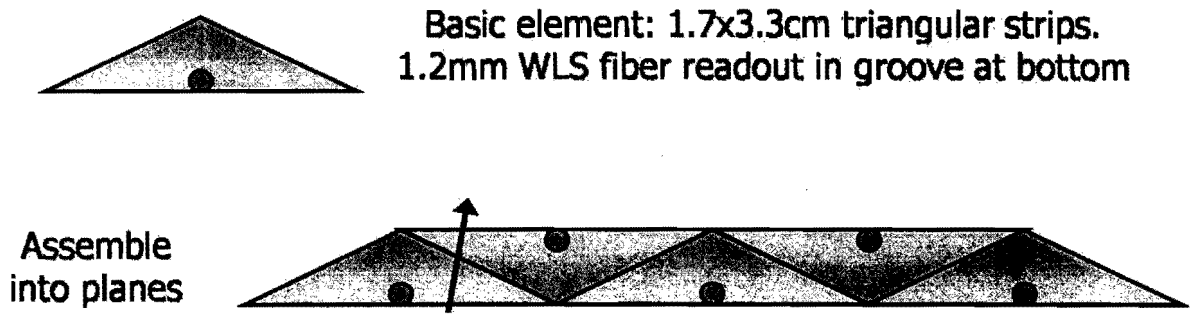
Figure 75: Assembly of scintillator strips into planes.

Absorbers
between planes
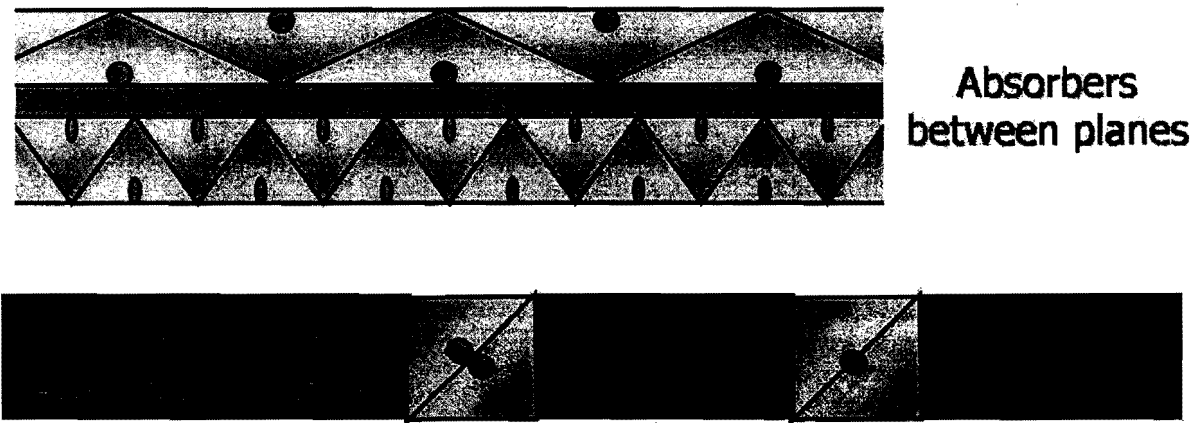
Figure 76: Integration of planes with absorbers in calorimeters or nuclear targets in the inner (above) and outer (below) detectors.
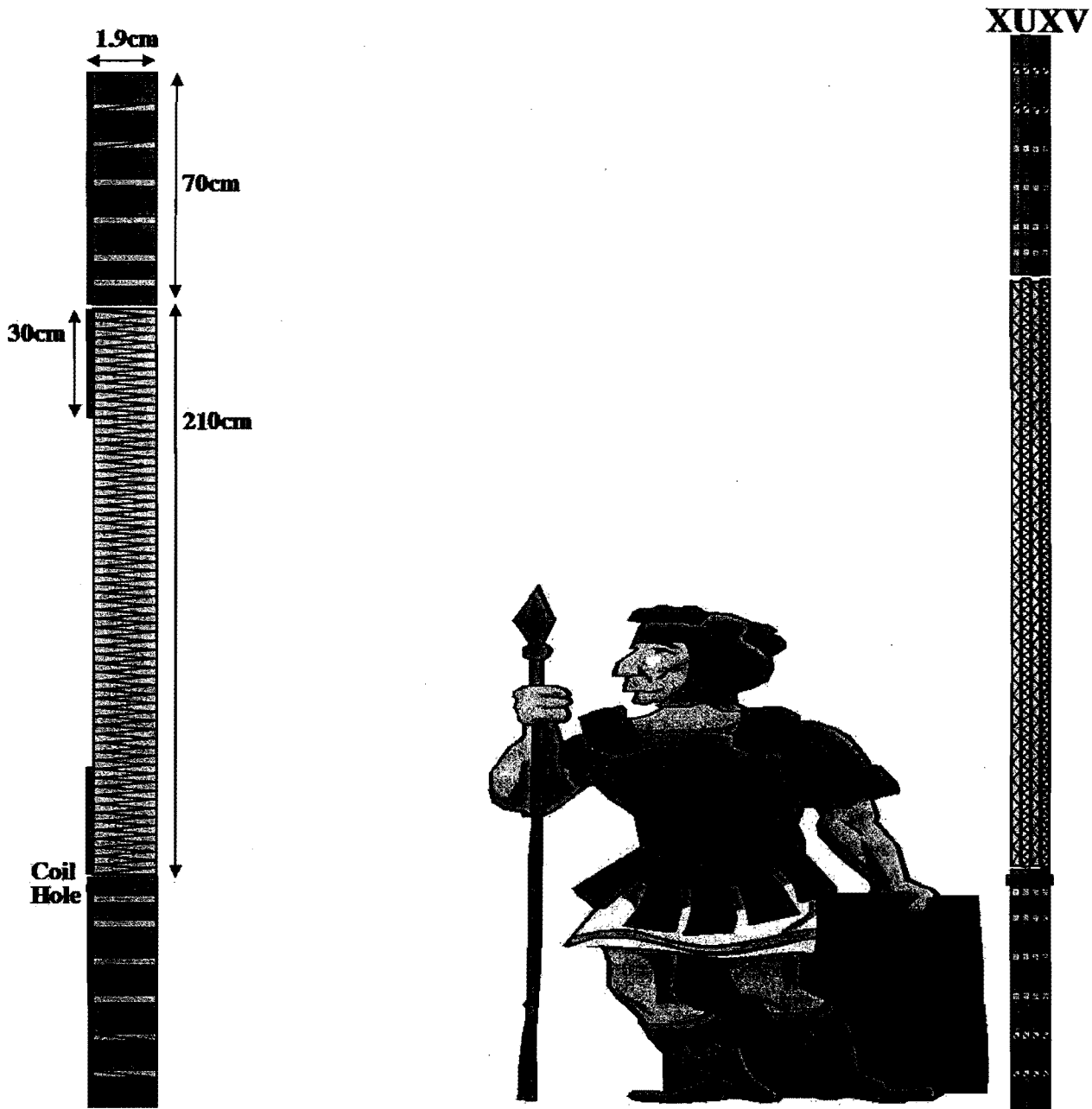
Figure 77: Plane assembly (left) and module assembly (right) in the active target region for MINERνA. On each drawing, the scale is exaggerated in the horizontal direction to show details.
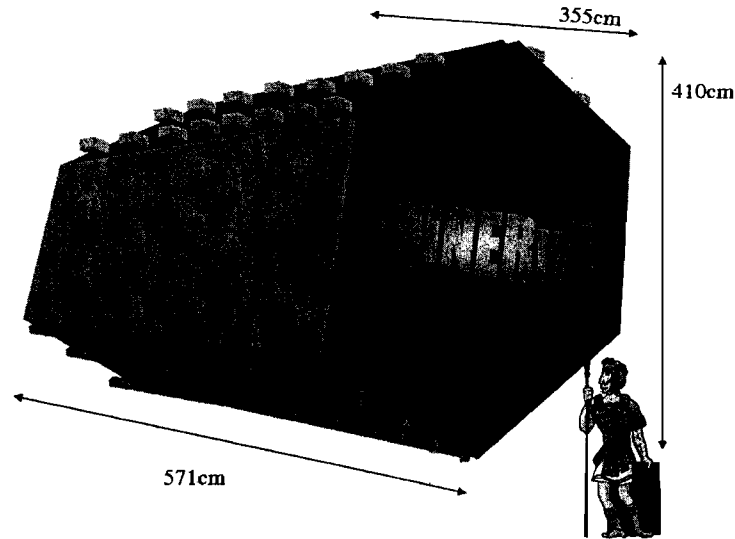
Figure 78: Outline of MINERνA detector to illustrate shape and scale. Note the locations of the PMT readout boxes on top of the detector, coils on the bottom, and the support stands.

thick in the muon ranger and 10 cm thick in the veto; note also that the final module in the muon ranger is constructed without steel to ensure one final three dimensional spatial point free of local multiple scattering. The magnetic properties of the OD and the MR detectors are discussed in Section 16.2.

Moving towards the center of the detector from each end, the next detectors are the downstream and upstream hadronic calorimeters (HCALs), shown in Figure 80, with 2.5 cm absorbers, one per plane downstream and one per module upstream. This detector is surrounded by the picture frames of absorber and scintillator strips that make up the outer detector (OD). Note that the strips in the OD run only in one direction, in the bend plane of the magnetic field. Three-dimensional tracks must therefore be matched from the inner detector and extrapolated outwards for an energy measurement or muon momentum measurement. A complication of the design is illustrated by the fact that the inner detector strips, which range in length from 120 to 240 cm, end inside the OD, and therefore the WLS fibers from must be routed out to the detector edge through a grooved plastic guide plate through the region of the OD. Note also the holes for the OD muon toroid coil in the lower region of the detector. Magnetic flux will be isolated in each region frame of the OD, and will be prevented from leaking into the inner detector by a guard ring of stainless steel as part of the HCAL absorber.

Moving in again from upstream and downstream, the next detector module elements are the electromagnetic calorimeters (ECALs), which have 0.2 cm Pb/Stainless absorbers downstream, one per plane, and 0.8 cm Pb absorbers upstream, one per module. Their design is shown in Figure 81. Note that the absorber only overlaps the inner detector and not the outer detector where it would represent a negligible fraction of the absorber material. The fine granularity of the ECAL ensures excellent photon and electron energy resolution as well as a direction measurement for each.

Finally, we reach the center of the detector, the fully-active inner detector (ID), whose plastic core represents the fiducial volume for most analyses in MINERνA. A plane of the active target is shown in Figure 82. In the center region, there is no absorber at all; however, 30 cm from the edge of the

142
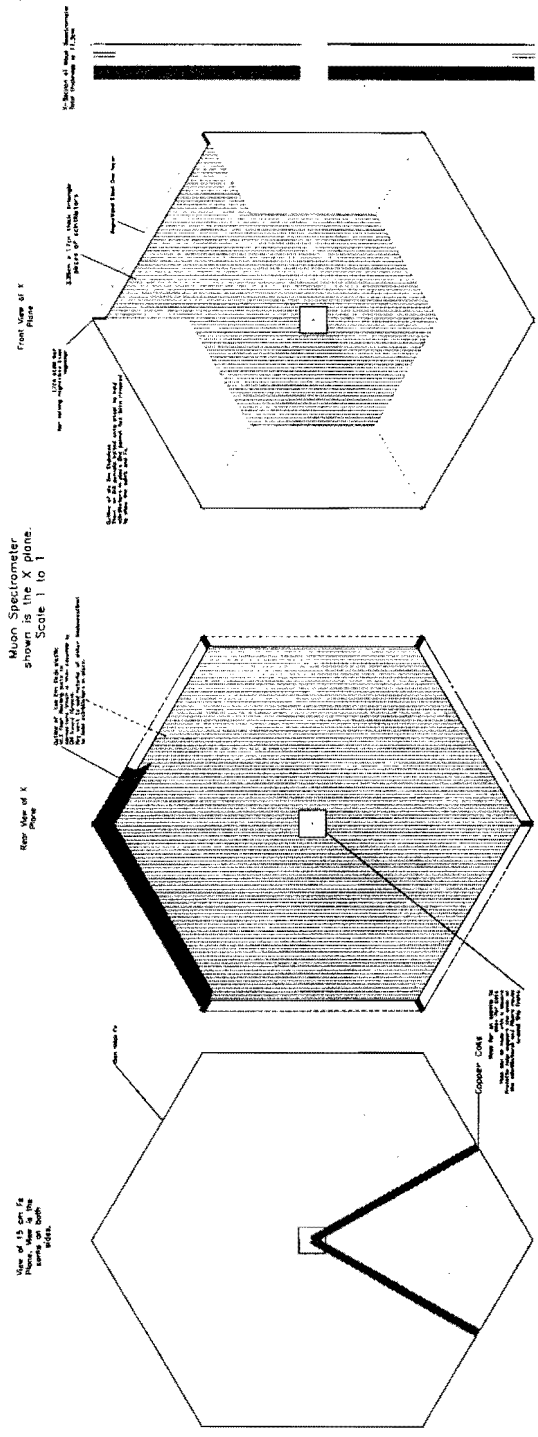
Figure 79: Muon range/toroid and upstream veto plane design (landscape).

143

Figure 80: The Hadronic Calorimeter Plane Design (landscape).

144

Figure 81: Electromagnetic calorimeter plane design (landscape).

145

Figure 82: Active target plane design (landscape).

146

ID, there are lead/stainless absorbers identical in thickness to the downstream ECAL, which act as a side electromagnetic calorimeter. This part represents the bulk of the detector in length, and the outer calorimeter surrounding the fully active planes are the largest part of the detector in mass.

Note that MINERνA is, by design, entirely modular along the beam direction. Individual elements may be easily lengthened or shortened by omitting modules from the design or adding new modules. One configuration that would be attractive is to forgo installation of the muon ranger and perhaps a portion of the downstream HCAL in order to move as close as possible to the front face of the MINOS near detector, thus allowing MINOS to serve as a calorimeter and muon detector. For the purposes of cost and schedule, however, we proceed to make estimates under the assumption that the full stand-alone detector will be built.

16.2 Muon Toroid Performance

The MINERνA design calls for toroidal muon spectrometers in the outer detector (OD) and downstream of the HCALs in the muon range (MR) detector. (Again, however, it should be noted that if MINERνA were situated immediately upstream of MINOS, the downstream muon toroid may be omitted.) This section describes the momentum reconstruction and range capabilities of these detectors for μ produced in the inner plastic fiducial volume.

The OD has a total of 50 cm of magnetized steel sampled by active planes that are traversed by muons in a direction perpendicular to the beam. It is magnetized by a 48 turn coil with 700 Amp current. The average magnitude of H in the OD is therefore about 30 Gauss. We plan to use Armco specialty steel [202] for the OD absorber which would give a magnetic field of about 16 kGauss. For muons which exit the side of the OD, the fractional momentum resolution measured from the bend angle varies from 22% to 30% for muons with an angles of 30° to 90° with respect to the beam. In practice, of course, the resolution will be better because of the loss of momentum with dE/dx in the OD. The OD will run to focus muons forward with a transverse momentum kick of 0.5 GeV (0.25 GeV) 30° (90°) angle. Focusing will serve to lengthen the path length through the OD and to direct the muons into a downstream muon range detector, be it the MINERνA MR or the MINOS near detector.

The downstream MR toroid has a total thickness of 1.2 m of magnetized steel with a 48 turn coil and 1200 Amp current, resulting again in an average field of 16 KGauss. This yields a typical p_T kick of 0.6 GeV and a momentum resolution of 20% from the bend, which is, again, improved by the muon's energy loss in passing through the steel.

In summary, the MINERνA detector has, on its own, excellent acceptance and momentum resolution for muons. This resolution can be improved, especially for forward-going high-energy muons, by use of the MINOS near detector as a downstream muon toroid.

16.3 Photosensors for MINERνA

With an inexpensive active detector technology, the dominant equipment costs for MINERνA are photosensors and their associated readout electronics. The path through the parameter space of available technologies is determined by the answers to three questions. First, is the light output of the detector for a MIP signal sufficient to support a low quantum-efficiency detector such as photomultiplier tubes (PMTs) or image intensifier tubes (IITs)? For MINERνA there is sufficient light to use a 1/6 quantum efficiency photocathode with a WLS fiber diameter of at least 1.2 mm as demonstrated in 16.4. Second, is timing within the spill important or can a technology that only integrates over a long spill, such as

IITs be used? We concluded that timing within the spill, both to flag overlapping events and measure time of flight and decay times at rest was important for our physics goals. Third, what level of technical risk, R&D time and cost is acceptable? We concluded that to allow MINERνA to operate as early as possible in the NUMI beamline and given the modest size of our collaboration and expected detector costs, we should choose low technical risk over lengthy R&D programs designed to reduce those costs or improve performance.

In our design exercise, we considered four technologies for photosensors: multi-anode photomultiplier tubes (MAPMTs), IITs, avalanche photodiodes (APDs) and visible light photon counters (VLPCs). Ultimately, we chose to pursue a solution based on MAPMTs which results in a sensor+electronics cost (including EDIA and overhead but without contingency) of approximately $40 per channel, which breaks down approximately as $15 per channel for the sensor, $15 for the electronics and $10 for EDIA and testing. To defend this important decision, we discuss the alternative technologies mentioned above.

Image intensifying tubes coupled to CCDs as a readout device are an extremely appealing low cost solution for reading out bundles of fibers, in part because the CCD itself is the final stage photosensor and readout device. This device is well-matched to the pulsed structure of the neutrino beam with one readout corresponding to one beam pulse. Costs per channel are largely proportional to the total photocathode surface required, which is set by the number of channels and fiber diameter. Crosstalk in adjacent channels is a non-trivial issue, but can be addressed because of the high density of CCD channels relative to fiber granularity, even with intermediate spatially demagnifying stages. We were driven to relatively expensive CCD cameras because of the need maintain reasonable linearity. Our candidate system, based on Hamamatsu C8600 2-stage multi-channel plate (MCP) intensifiers and C7190 bombardment CCDs, was approximately $15 per channel, including photosensor and CCD readout but not including required demagnification optics. Nevertheless, a complete IIT/CCD system would still likely be half the cost of the chosen MAPMT solution. Our concerns about the system were the smaller effective dynamic range, even with relatively costly IIT/CCD systems, and the relatively low mean time to failure per device reported in other large systems (4 years per two stages in the CHORUS experiment). However, the missing capability of timing within a single main injector spill was enough for us to discard this otherwise promising option.

Avalanche photodiodes (APDs) were also considered because of their recent successful application in the CMS ECAL and their proposed use in the NUMI off-axis far detector. APDs are low gain (~ 100), high quantum efficiency (85% for Y11 WLS fibers) devices which offer significant cost savings in the photodetector. Complications of operation include the need to cool the sensors below room temperature to reduce noise, but this is a fairly easily solved problem as cryogenic temperatures are not required. The primary problem we identified with APDs for MINERνA was the need for significant electronics R&D to develop a relatively low-cost system capable of controlling noise over the long NUMI spill. For MINERνA we set a requirement of keeping the photosensor and electronics noise well below 10 delivered photon equivalents to maintain good sensitivity to a MIP (typically 70 photons in a doublet of triangular scintillators) and a low rate of detector noise. Over a 12 μsec gate (the NUMI spill plus $2\tau_\mu$) at -10°C with an operating gain of 100 (optimal), the signal from 10 photons is 850 electrons and the noise on the best existing candidate electronics, the MASDA chip, is 900 electrons. To achieve the better signal to noise that is the goal of the proposed NuMI off-axis R&D program requires design of a new ASIC, which would imply at least a one-year development project. In short, although the APD is a potentially promising technology, we were not convinced it could be in production on the timescale required for MINERνA.

The final option we considered was the VLPC. These have the advantage of successful past deploy-

148

ment and electronics design in the D0 fiber tracker and preshower detectors. However, the costs for just the VLPCs themselves, even with optimistic assumptions about the outcome of future R&D, are expected to exceed $50 per channel, and are thus significantly more expensive than the MAPMT solution. Given that the low quantum-efficiency solution gives sufficient resolution, it is difficult therefore to justify VLPCs.

The MAPMT we have tentatively selected as our default photosensor is the Hamamatsu R7600U-00-M64. These are an incremental design improvement from the R5900-00-M64 MAPMTs used in the MINOS near detector, and we expect much of the experience gained by the MINOS collaboration with these detectors to be applicable. In particular, we have confidence in costing the testing, housing for and optical connectors to the PMTs because of our ability to scale costs from the MINOS experience.

Having chosen MAPMTs, a low quantum-efficiency device with good timing, low noise and a large dynamic range, the following two sections address the issues of the photoelectron yield from the strips married to the MAPMTs and the electronics to readout these MAPMTs, respectively.

16.4 Scintillator Strips

The MINOS experiment has successfully demonstrated that co-extruded solid scintillator with embedded wavelength shifting fibers and PMT readout produces adequate light for MIP tracking and can be manufactured with excellent quality control and uniformity in an industrial setting. The performance characteristics of the MINOS scintillator modules produced at the three 'module factories' are now well known, both through measurements taken with radioactive sources post-fabrication at the factories and through measurements of cosmic rays at Soudan. We intend to use the same technology for the active elements of MINERνA.

The basic active element in MINERνA is a co-extruded triangular scintillator strip with a wavelength-shifting fiber glued into a groove. Like MINOS, the scintillator strips are polystyrene (Dow 663) doped with PPO (1% by weight) and POPOP (0.03% by weight), co-extruded with a reflective coating of TiO_2 loaded polystyrene[203]. The strip cross-sections have width 3.35 cm and height 1.7 cm. Strip lengths vary throughout the detector and range from 1.4 meters to 2.2 meters in the inner tracking detector to 4 meters for the veto and muon ranger sections. The WLS fiber (Kurrary Y11, 175ppm dopant) is 1.2 mm in diameter, glued into an extruded groove and covered with aluminized mylar tape in the same fashion as MINOS. The WLS fibers are brought to optical connectors at the edge of the modules, and clear optical cables bring the light to a PMT box. Single-ended readout is used, and the far strip/fiber ends are mirrored.

Physics simulation studies indicate that for a triangular extrusion, average [3] light levels above 3.9 photo-electrons("PE")/MeV of dE/dx for a minimum-ionizing particle (MIP) are required in the inner detector in order to obtain good particle identification as described in Section 15.5.5. Coordinate resolution, vertex finding, and track pointing are also affected by light levels, but to a lesser extent. For this design we have targeted an average light level of 7.8 PE/MIP on average through the strips. This allows for losses expected to be 25% in the clear fiber and connectors and possible effects from the degradation of the scintillator over time, the latter of which was measured to be as large as 20% over 10 years for MINOS[204].

The overall light levels from 3 lengths of strips, as calculated using the photon transport Monte

---

[3]Note that this is an not only an average over photostatistical fluctuations, but also an average over all locations for normally incident tracks to enter the strip. The average light through the full thickness of scintillator in a plane, a doublet of triangles, is twice this average.
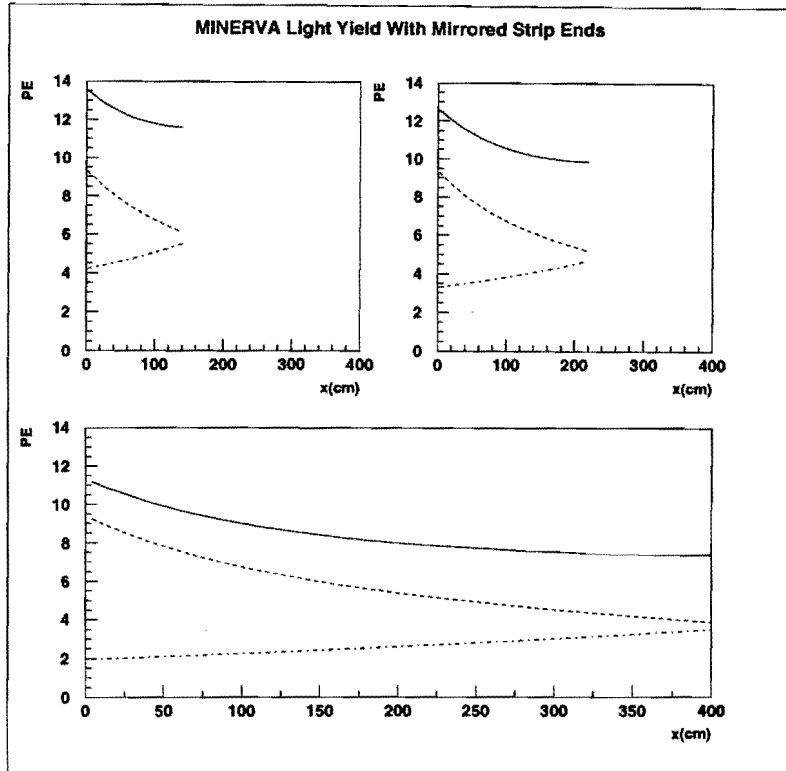
Figure 83: Light yield vs. distance along strip for MINERνA scintillator strips with one-ended readout and a mirrored end. Dot-dashed line is light collected from reflections off the mirrored end, dashed line is light travelling directly to the readout end; solid line is the sum. The top plots correspond to the shortest and longest strips used in the fully-active inner detector, and the bottom plot is for the longest strips in the veto and muon ranger.

Carlo described in Section 15.4, are shown in Figure 83. Here we have assumed a 90% reflectivity from the mirror end of the fiber, and in all cases a 1 meter WLS 'pigtail' from the end of the near end of the strip to the PMT face. Clear fiber lengths and connectors are not included. In the MINOS near detector, the far strip end was not mirrored; here we assume the strip ends are mirrored with 100% reflectivity. Because the light produced in the scintillator is generally collected within a few cm of the MIP crossing location, this approximation only affects the calculation of collection efficiency at the very far end of the strip. Shown are the light levels predicted for three strip lengths. In each plot, the lowest curve corresponds to light collected from reflections off the mirrored end, the middle line corresponds to light travelling directly from the MIP to the readout end, and the upper line is the sum. As the figure shows, the light level in the inner tracking detector, with a maximum length of 2.2 m, exceeds the design requirement of 7.8 PE/MIP over the entire length by about 25%. In the longer strips (only used in the downstream muon range detector and upstream veto counters), the light falls slightly short of this target at the far ends of the strips; however, because these detectors are not used for particle identification by dE/dx, this is still acceptable.

150

16.5 Electronics

The requirements for the MINERνA electronics are summarized in Table 12. To minimize technical risks, we studied a number of existing solutions, including those used for the MINOS design. Major components of the electronics system include the front-end boards, the PMT and electronics housing and the slow controls and readout systems.

16.5.1 Front-end boards

For the front-end digitization and timing, the best performing system with the least required R&D is a scheme based on D0 TRiP ASIC. The TRiP chip is a redesign of the readout ASIC for the D0 fiber tracker and preshower originally motivated by the need to run at 132 ns bunch crossings in the TeVatron. A production run of one version of TRiP with 7000 produced chips has been completed; however, since the TeVatron run plans do not now call for 132 ns operation, these chips will not see their original use. These existing chips, however, could be recycled into use in MINERνA.

TRiP was designed by Abder Mekkaoui of the Fermilab ASIC group and successfully met the specs in its first submission and has undergone extensive testing by D0 [205]. Its analog readout is based on the SVX4 chip design, and each TRiP chip supports 32 channels for digitization, but only half that number of channels for timing. A simplified schematic of the TRiP ASIC is shown in Figure 84. The preamp gain is controlled by SW2 and has two settings which differ by a factor of four. The gain of the second amplifier stage is controlled by SW3-SW5. We will set the chip to the lowest gain setting for the preamp and largest integration capacitor. This gives a linear range with a maximum charge readout of 5 pC. The "ANALOG_OUT" goes into a analog pipeline, which is identical to the one used on the SVX4 chip and 48 cells deep. The SVX4 chip can read out four of these 48 buffers, and although the TRiP chip was also designed to read out four buffers, it can empirically only read out one buffer. It is not known why only one buffer can be read out; however, this is not an issue in MINERνA as shown by the per channel per spill occupancy illustrated in Figure 85. To gain dynamic range, MINERνA will increase the input range of the electronics by using a passive divider to divide charge among two TRiP channels with a ratio of a factor of 10. This "high range" channel, then, will give a equivalent total readout charge of 50 pC. Each TRiP channel will be digitized by a 12 bit ADC.

In MINERνA the integration time for the ADC will be 10–12 μs, much less than the hold time for

Parameter	Value	Comments
Active Spill Width	12μsec	Spill plus $2\tau_\mu$
Repetition Time	> 1.9 sec	
Number of Channels	37478	
Occupancy per Spill	0.02	LE beam, 2.5E13 POT/spill
Front-end noise RMS	< 1 PE	
Photodetector gain variation	4.5 dB	extremes of pixel-to-pixel variation
Minimum Saturation	500 PE	proton range-out or DIS event
Maximum Guaranteed Charge/PE	50 fC	lowest possible charge at highest gain
Time Resolution	3ns	Identify backwards tracks by TOF Identify decay-at-rest $K^\pm$

Table 12: Electronics design requirements and parameters for MINERνA
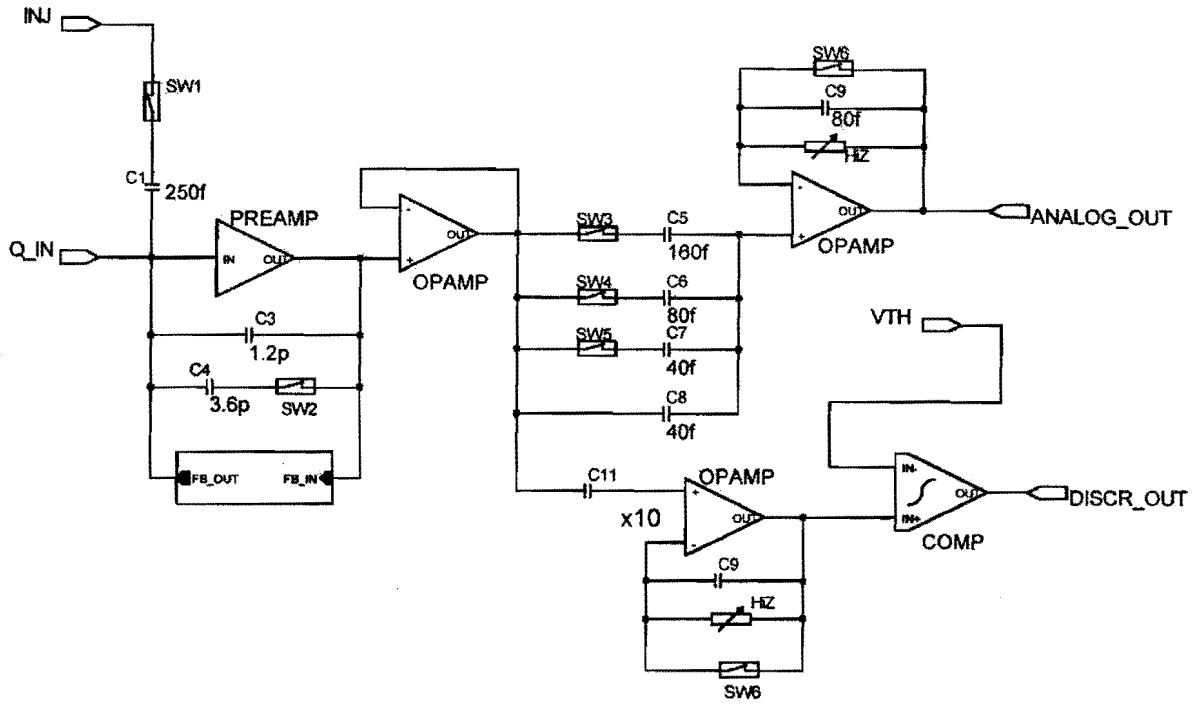
Figure 84: A simplified schematic of the front end electronics of the TRiP chip
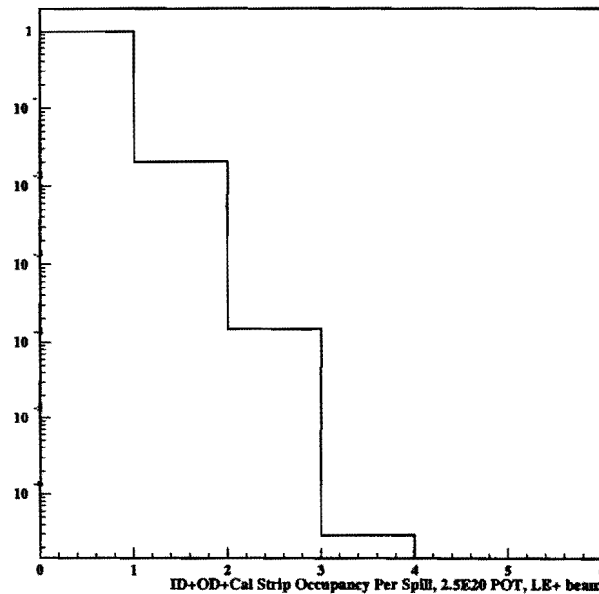
Figure 85: The mean number of neutrino interactions in which a strip is hit per 2.5E13 POT spill, NUMI LE neutrino beam

Histogram of measured signal w/ 5fC injected
10us gate
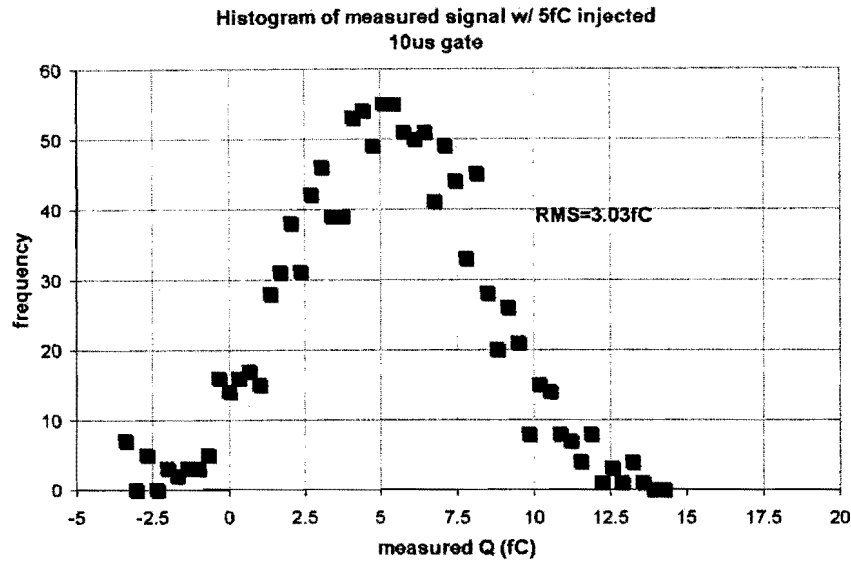
Figure 86: Response of the TRiP chip to 5 fC injected with a 10 μs gate.

the charge in the capacitor of 100 μs. The TRiP chip has been tested explicitly with a 10 μs gate, and Figure 86 shows pedestal RMS of 3 fC for the estimated MINERνA input capacitance of 36 pF. The MINERνA design requires no saturation below 500 photoelectron (PE) and RMS noise well below 1 PE. Matching this to the 5 pC charge limit, the highest gain anodes in a tube would be set at 100 fC/PE and therefore the lowest gain anodes would be run at 33 fC/PE. Since the RMS of the noise is about 3.0 fC, this will put a single photoelectron approximately a factor of 10 above the pedestal RMS, well within our design spec. The maximum PMT gain for the lowest gain anode will be 50 fC/PE, safely within the desired parameters above.

Only one of every two input channels to the TRiP chip have a latched discriminator output (latch) which can be used for timing information. Hence, only the lower range channels will feed the latch whose output will then go into an FPGA. The internal clock of the FPGA can be used to get timing with a granularity of 5 ns, and with a delay line scheme this can be improved to below 3 ns. The reset for the latch is only 15 ns, so inside the spill the latch will be in the ready state by default. When the signal exceeds a threshold of 1.5 PE, the latch will fire. After storing the time, the latch is reset, incurring minimal deadtime. Figure 87 shows result of the D0 timing test of the TRiP chip using their fiber tracker and VLPCs. They get a timing RMS of 3ns for signals with ≥8 PE. Y-11 (the waveshifter in the MINERνA fibers) has an equivalent decay time to 3HF (the dye used in D0's fiber tracker), and hence in a doublet of triangles in the scintillator, we can reasonable expect similar timing resolution.

Note in the MINERνA scheme, there is no trigger. Two charges are read from all channels along with all latched times at the end of each spill.

Although individual parts of this system have been tested by D0, the system described above has not been tested. Ray Yarema's group at FNAL has begun layout of a board for a vertical slice test of this system, and we expect a proof of principle from this test by early summer 2004.

153

Time from D0 Test Fiber Tracker > 4 pe

RMS 4.143

Time from D0 Test Fiber Tracker > 8 pe

RMS 3.125
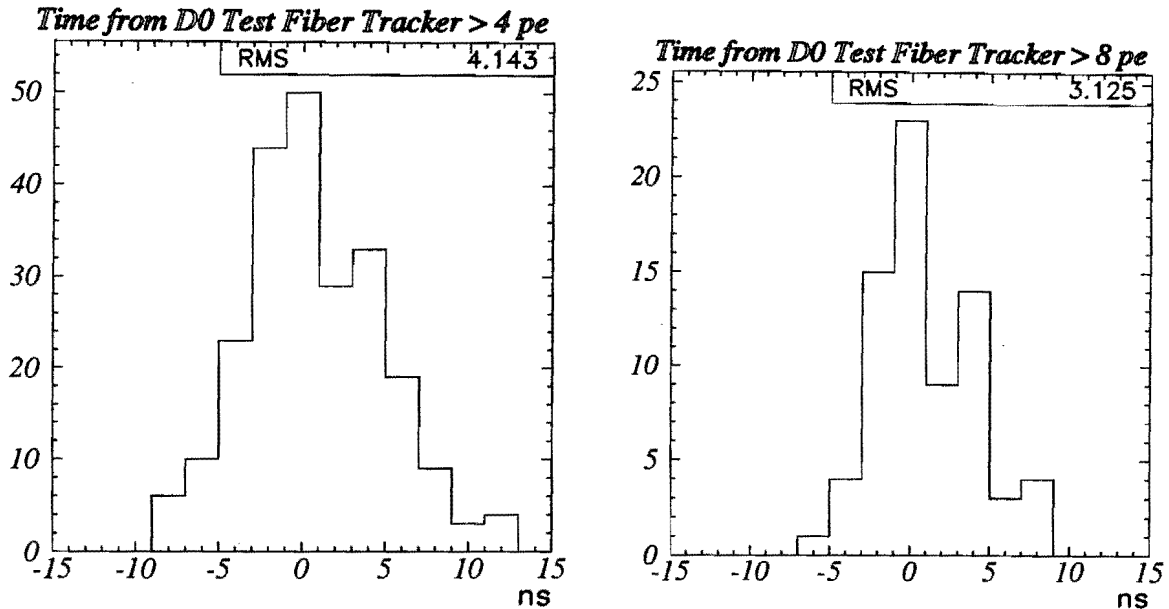
Figure 87: Results of the D0 test of timing of TRiP using the Test Fiber Tracker with signals > 4pe and signals > 8pe

16.5.2 PMT boxes, readout electronics and controls

The MAPMTs will be mounted directly on the front-end boards to reduce input capacitance. Therefore, the front-end board and PMT need to reside in a single light-tight box with optical cables from the detector as input. In our preliminary design, each PMT box will have a single PMT and front-end electronics for its 64 channels, along with a Cockcroft-Walton HV generator.

In addition to the optical input cable, each PMT box has three electrical cables. The slow-control cable and the low-voltage cable will travel from box-to-box in a daisy chain. The digitial readout LDVS cables will arranged in 16-box 'Token Rings', and will connect to a VME card at the first and last box in the ring. In addition to reading out the data after each spill, the token ring will supply the timing synchronization signal. The low-voltage cable will likely run at an intermediate DC voltage and step down at each box to minimize the role of resisitive losses in the chain. The slow-control cable will be a MIL 1553b bus which is in wide use at FNAL. An existing VME card (the 1553 controller) will drive the slow control system. Table 13 shows the number of parts needed for the complete electronics system.

To minimize the length of the clear fiber cables from the WLS fibers to the PMT boxes, we plan to mount the PMT boxes directly on the upper parts of the MINERνA detector, on the two highest sides of the hexagon to avoid conflict with the coils or side clearance of the detector. This will require magnetic shielding of the MAPMTs.

The DAQ requirements for this system are trivial as the data rate is expected to be under 100 kByte/second. A VME-resident PVIC interface in each of the four VME crates will be readout with a single Linux PC. Data will be buffered in a local RAID system and transferred over the network to FCC for permanant storage.

154

16.5.3 Whither the TRiP chip?

D0 is likely to redesign the TRiP chip as part of the fiber tracker front end upgrade. As part of that upgrade, features desirable for MINERvA, including individual channel discriminator threshold and front end buffer gain could be added. A major goal for this submission, independent of MINERvA, would be to get the multi-buffer readout mode, which would be a useful safety valve if rates in portions of the detector were higher than we now predict. The MINERvA readout board would be able to use either chip without any modification to the board; hence, development of the front-end board and a new TRiP submission could occur in parallel minimizing the scheduling impact. This upgrade is not essential for MINERvA, but could provide enhanced performance.

We also note that if the new submission fails, D0 might need to use the existing chips. If the yield is 90%, as was found in a sampling of 100 chips, we would have about 2460 chips after satisfying the D0 requirements, which is enough for 39000 channels. Hence, in the "worst-case" scenario of both D0 needing the existing TRiP chips and also a lower yield than the sampling to date would suggest, we might have to make more TRiP chips with the existing design and masks.

16.6 Parameters of the MINERvA Detector

MINERvA combines the fine granularity of an electronic bubble chamber with the final state analyzing power of more traditional (but very fine grained) sampling calorimeter and muon magnetic spectrometers. To maintain the segmentation required to identify each final state particle in a low energy neutrino interaction and to accurately track final state photons for π^0 reconstruction, the number of channels in MINERvA must be large. To contain the produced final state particles, the mass of MINERvA must be large. We attempt to break down the contributions to mass and channels by sub-detector in this section.

Table 14 lists the total number of channels by sub-detector. Predictably, it is the granuarlity required in the plastic, Pb and Fe targets that dominates the channel count, with the downstream calorimeters, side calorimeters, the muon and the veto systems contributing 19%, 17%, 7% and 1% of the channels, respectively. As shown in Table 15, the situation is very different with the mass apportionment among the detectors where the OD and MR dominate the mass.

The scintillator and optical system system of MINERvA, though it pales in comparison to long baseline neutrino experiments like MINOS, is impressive on the scale of the CDF Plug calorimeter or CMS HCAL. MINERvA will use 19.2 metric tons of extruded polystyrene scintillator, 93 km of

Component	Number	Comments
Channel	37478	WLS Fibers
PMT boxes	587	includes 90 empty M-64 anodes
Readout Token Rings	37	16 PMTs/ring
VME Readout Cards	10	4 rings/card
VME Slow Control Cards	20	30 PMTs/card
VME Crates	4	
VME PVIC Interface	4	one per crate
DAQ PCs with PVIC, RAID system	1	data rate is 120kB/spill

Table 13: Parts count for MINERvA Electronics Design

Sub-Detector	Channels in Inner Detector	Channels in Outer Detector
Active Target and Side ECAL	15360	5760
US ECAL (Pb Target)	3072	1152
US HCAL (Fe Target)	1536	576
DS ECAL	2560	960
DS HCAL	2560	960
Veto	426	n/a
MR/Toroid	2556	n/a
Totals	28070	8408

Table 14: Channel count by sub-detector

Sub-Detector	Mass (metric tons)
Active Target	4.2
Side ECAL	8.5
US ECAL (Pb Target)	3.5
US HCAL (Fe Target)	7.0
OD Framing the Target Regions	126.5
DS ECAL	19.8
DS HCAL	26.4
Veto	15.1
MR/Toroid	90.8
Total	302.1

Table 15: Mass by sub-detector

wavelength-shifting fiber and another 46 km of clear fiber in optical cables between the detector and the 587 M-64 multi-anode photomultipliers.

17 Cost and Schedule

This section describes the cost and schedule associated with the construction of the MINERνA detector.

Given the relatively modest cost of the detector, we plan to largely fund the construction of the MINERνA detector from a combination of university program research funds and special program funds indepedendent of the Fermilab budget.

Portions of the project that would be, by necessity, managed and funded by Fermilab would include site outfitting and utilities (e.g., magnet and quiet power, cooling), crucial safety items for the NUMI hall that must be designed at Fermilab (e.g., low voltage distribution to the electronics, the magnet coils), and installation costs associated with bringing modules to the NUMI near hall. At the time of the submission of this proposal, we do not have complete evaluations of these costs. As discussed in Section 14.1, these costs have *not* been estimated. We are encouraged, however, to note that the utilities requirements of MINERνA appear to be within the capacity of the NUMI near hall, and do not appear to require major infrastructure upgrades. We expect to update this document with a good estimate of these costs by the time of oral presentation to the PAC on December 12, 2003.

17.1 Description and Summary of Costs

The cost of MINERνA is dominated by three major categories of expenses: external materials purchases, craft durable items and labor to assemble the active elements and absorber into modules. Each of these has its own appropriate costing methodology.

For the large external equipment costs, the MAPMTs, the clear and WLS fiber and the metal plate to construct absorbers, we have contacted our preferred vendors directly to obtain quotes. For the photosensors, we have shown that the stock specifications of the R7600U-00-M64 PMTs are adequate for our application. Similar phototubes are in wide use throughout the lab, and have performed reliably. Hamamatsu has provided a quote on our quantity with a three month delivery time, and we are investigating cost savings that can be realized through a more efficient custom packaging suitable for our Cockcroft-Walton supplies. It is worth noting that another manufacturer, Burle Technologies, manufactures a product which would likely meet our specifications with better channel gain uniformity, the Planacon 85011-501, and we plan to pursue this possibility as well. The clear and WLS fiber vendor, Kurary, again is a vendor with a long history at Fermilab, and they have provided similar fiber to MINOS, CMS, CDF, etc. We have also secured a quote on our quantities independent of the concentration of WLS dopant should we chose to reoptimze the dopant for our strip lengths. Finally, the costs of the absorber were provided by suppliers who have established relationships with the Rutgers Physics Department machine shop, and variations here would likely result only from movement in the bulk prices of the relevant materials. The machining costs have been estimated through the Rutgers shop which is ready to perform the work as needed. Because of the relative certainly of these costs, we allow relatively low contingencies for these items, ranging from 20% (MAPMT and fibers) to 30% (absorbers). We have not yet included F&A costs on most of our equipment purchases since we anticipate most of these purchases will be made through University fully-costed shops which will try to negotiate low F&A costs on these large, bulk purchases.

The second category of costs come from the craft items which must be constructed to assemble the detector, including the front-end electronics and associated auxiliary systems, parts for the PMT/front-end housing and the extruded scintillator strips. Here the strategy was to identify similar components from the construction of the MINOS far or near detectors, or from the CMS HCAL or CDF Plug con-

struction, and to attempt to scale the actual project costs. For example, the clear fiber cable costs were scaled from the CMS HCAL project which was of similar scope with similar fiber and connector scheme. These costs already include actual labor and EDIA costs. Following this approach is very useful because one learns interesting and relevant facts about hidden cost drivers. For example, the front-end boards require approximately 5 kWatts of power over the entire system, and surprisingly, scaling from the MINOS far front-end costs, one calculates a low voltage power supply system cost in excess of $135,000, excluding cables. The reason turned out to be the special fire protection requirements imposed by underground operation of power supplies, so at least in this case, we found a cost that would otherwise have been missed. For these projects, we assigned contingencies between 40–50% of total sub-project cost, based on our scaled estimates. In the case of the electronics, there is an additional contingency cost of $70,000 for the case where we have to re-submit the TRiP ASIC due to unexpected demand for these chips from D0.

The final item is technical labor for component assembly and testing for procedures that have not yet been prototyped. These have been estimated based on assembly models from the CMS HCAL and MINOS far detector projects, and are generally more uncertain than other estimates because of differences in construction between CMS HCAL, MINOS and what we proposed in MINERνA. We have assigned contingencies of 50% for these projects. Labor and EDIA costs which dominate here are based on FY2005 projected costs for technician and engineering staff on the CMS HCAL project at the University of Rochester.

A summary of the costs is shown in Table 16. The total project construction cost is estimated to be $3.96M, excluding the installation and hall utilities costs. Our calculated contingency, $1.54M, is 39% of the total cost. As previously noted, the M&S costs do not include F&A.

A brief summary of what is included in each sub-project category follows.

Extruded Scintillator: prototype and production extrusion dies; purchase of plastics; extrusion in the Lab 5 facility; Q/C and monitoring.

Fiber and Glue: WLS and clear fiber (1.2mm, Y11 0-400 ppm, J-type, S-35), BC-600 epoxy.

WLS Fiber Prep.: Design and construct gluing assembly; cut fibers, mirror one end and glue into scintillator, prepare fiber pigtail for connector.

Optical Cables: Purchase connectors and test equipment; EDIA for fiber termination procedure and cable layout; bundle fibers into conduit; insert WLS and clear fibers into two pairs of connectors; polish ends; test for transmission and light tight.

Absorbers: ECAL: purchase and machine Pb and stainless sheets, epoxy, stainless to Pb, ship to assembly site; OD: order strips pre-cut from vendor and ship to assembly site; HCAL: order partial plates pre-cut from vendor, weld and ship to assembly site; Coil: purchase Cu AWG4 wire for coil and fabricate bus bars; Plastic fiber router plate for OD: purchase polypropylene sheets, program and route groves on CNC router and ship to assembly site.

Module Assembly: prototype procedures; laminate sub-planes of ID strips; connect inner OD frame; connect stainless stop to frame and attach to strongback; construct OD in layers; attach plastic routing plates; lay in ID strips and route fiber; add stainless retainer; layer in additional planes; join OD at outside layer; attach WLS bundle connector; prepare for delivery to experimental hall

Photosensors: purchase R7600U-00-M64 PMTs.

MAMPT Testing: design and assemble test stand; test for specs.

PMT Box and Optics: design and prototype PMT box; design and assemble testing station; construct box; add connectors; assemble internal optical system; mount front-end board and PMT socket; add PMT; add fiber bundle from connector to cookie and attach; attach internal cables to board; light tight and Q/C.

Electronics and DAQ: prototype front-end TRiP design; design front-end board; design VME data board; purchase VME crates, controllers, PVIC interfaces and DAQ PC; TRiP checkout; produce, assemble and checkout front-end, VME data and slow controls boards; purchase LV system; purchase LDVS, slow controls and LV power cables.

17.2 Schedule

The MINERνA collaboration has not yet produced a resource-loaded schedule for the experiment capable of reliably predicting the schedule. We plan to present such a schedule at the PAC meeting on December 12, and to update this section when it is available.

This having been said, the schedule driving elements for the experiment to be ready to be installed are three: construction of the front-end electronics, assembly of the detector modules, and construction of the PMT boxes. We will discuss each of these in turn. With the possible exception of the PMT boxes, we have high confidence that the result of the resource-loaded schedule will be to produce detector modules ready to install in the NUMI near hall approximately two years from the project start, assuming that the bulk of the project funds for M&S items can be expended at the front end of the project.

Construction of custom electronics with an ASIC would usually be an overriding concern in such an aggressive schedule. However, as Section 16.5 explains, both the ASIC and the bulk of the front-end designs are being recycled from the D0 fiber tracker upgrade to 132 ns bunch crossings. Design for a vertical slice test of a prototype front-end system has already begun, and we are confident that we can demonstrate success of this prototype front-end by 2004. The VME data board will require only minor modifications from existing designs, and the slow controls board is a stock design which will require no modification. Even with the earliest project start date of summer 2004, we would have a completed design of all boards by the end of 2004, and be finishing production in the middle of 2005.

The assembly of the modules is a very complicated task because of the large number of channels in the detector, the complicated routing of fibers in the detector and the need to reduce support mass in the inner region of the detector. Furthermore, assembly of modules cannot begin until scintillator production, WLS fiber installation and absorber production are well underway. We have developed an assembly procedure and manpower assessment based on that procedure and the University of Rochester CMS HCAL experience that suggests that seven technician-years would be required to assemble the 53 MINERνA modules. It is aggressive, but perhaps plausible to attempt to fit those seven technician years into twelve or fifteen months, after completing a prototyping Q/C development phase of six months. Of the prerequisites for beginning module construction, it is most likely the start of significant scintillator production will most severely limit our ability to prototype and construct modules. We would expect to be able to begin scintillator production approximately four months after the project start, and therefore we conclude module production could be complete 22 – 25 months after project start. Installation of the modules in the near hall could proceed in parallel with the completion of the last modules.

Finally, we are working to develop a complete model of the construction of the PMT box and associated optical components. With over 550 boxes to construct and assembly of complicated optical

connectors and a fiber bundle in a tight space, the quality control concerns are very non-trivial. We have sufficient experience within the collaboration from the design and construction of the MINOS "MUX boxes" and the CMS HCAL to address this problem and expect to have a confident assessment of the schedule and schedule risks associated with the PMT box by the time of the PAC presentation.

Sub-Project	Cost (kUSD)			
	M&S (no F&A)	SWF (w/ F&A)	EDIA (w/ F&A)	Contingency (%)
Extruded Scintillator	151	12	30	78 (40%)
Fiber and Glue	262	n/a	n/a	52 (20%)
WLS Fiber Prep.	50	104	16	85 (50%)
Optical Cables	77	162	11	100 (40%)
Absorbers	310	67	32	122 (30%)
Module Assembly	11	473	53	268 (50%)
Photosensors	772	n/a	25	159 (20%)
MAPMT Testing	6	45	n/a	26 (50%)
PMT Box and Optics	278	95	51	212 (50%)
Electronics and DAQ	628	33	206	435 (50%)
Totals	2545	990	423	1537 (39%)

Table 16: Summary of MINERνA detector costs in exclusive sub-project categories

Part IV
Appendices

A Cryogenic LH$_2$ and LD$_2$ Targets

Some of the nuclear and fundamental particle physics described in this document may be dramatically improved by the inclusion of cryogenic liquid Hydrogen and/or Deuterium targets. The data from such targets would allow a detailed comparison with Jefferson lab experiments that are currently using Liquid Hydrogen and Deuterium as targets in electron and photon scattering experiments. A comparison with these experiments in a similar momentum transfer range with the high precision neutrino cross section measurements made possible by MINERνA would provide for unprecedented studies of nucleon structure, particularly at large x where it has heretofore been very difficult. It is, for example, clear that the substantial uncertainties on parton distribution functions at large x, which are dominated by nuclear corrections and uncertainties involved in the flavor decomposition, would be removed.

Those measurements described in this proposal which may become limited by resolution would benefit greatly from the inclusion of a cryogenic target system. The interpretation of resonance data, for example, would no longer be complicated by uncertainties in nuclear binding and on shell extrapolation. This would allow direct comparison with the Sato and Lee pion cloud predictions without additional model systematics. The availability of a clean nucleon target would remove the complexity of the nuclear potential in heavy targets allowing the underlying physics of strange particle production, for instance, to be probed without interference and quasielastic studies would be greatly helped by the lack of intra-nuclear proton scattering. Furthur, comparison of the data from the liquid Hydrogen/Deuterium target with data gathered from interactions in the MINERνA nuclear targets would be of great use in the determination of nuclear effects in neutrino interactions and would help to limit even furthur systematic effects in the oscillation experiments.

The cryogenic target itself would be small and compact. It could be installed upstream of the detector proper and would only require that the veto array be moved to cover it. There exists the possibility that the cryogenic target could be converted from a passive to an active target with the inclusion of CCD cameras to view the interactions; however, even considered only as a passive target, a high-statistics sample of neutrino interactions on liquid Hydrogen or Deuterium would be of a great benefit in the understanding of neutrino interactions in this relatively complicated few-GeV region.

B Off-Axis Running

When the MINERνA detector is located on the beamline axis of the NuMI beamline, it is exposed to a broad band of neutrino energies with a peak energy dependent on the momenta of the pions being focused by the horns. Because there are high energy mesons that travel through the holes of both horns, there is also a long tail of neutrino events with energies well above the peak energy. However, as the detector moves off the axis, the peak neutrino beam energy spectrum decreases and becomes much more narrowly distributed in energy, and the highest energy mesons are no longer pointing at the detector, essentially removing the "high energy tail", as shown in Figure 88. Note that at 10mrad away from the beamline axis the ν_μ event rate is peaked at 2GeV. This is solely a result of the 2-body kinematics of the $\pi \rightarrow \nu_\mu \mu$ decay. Although the event rates are highest when the MINERνA detector is on axis, the energy of the incoming neutrino is not known *a priori* and so by moving the MINERνA detector off axis for a given running period the experiment can make measurements of cross sections in a more narrowband beam. This is particularly useful for neutral current measurements, where the total incoming neutrino energy cannot be reconstructed because of the loss of the outgoing neutrino. Due to the intensity of the NuMI beamline, MINERνA can collect appreciable statistics for precision measurements of low energy neutral current processes when running for short periods of time off the beam axis.
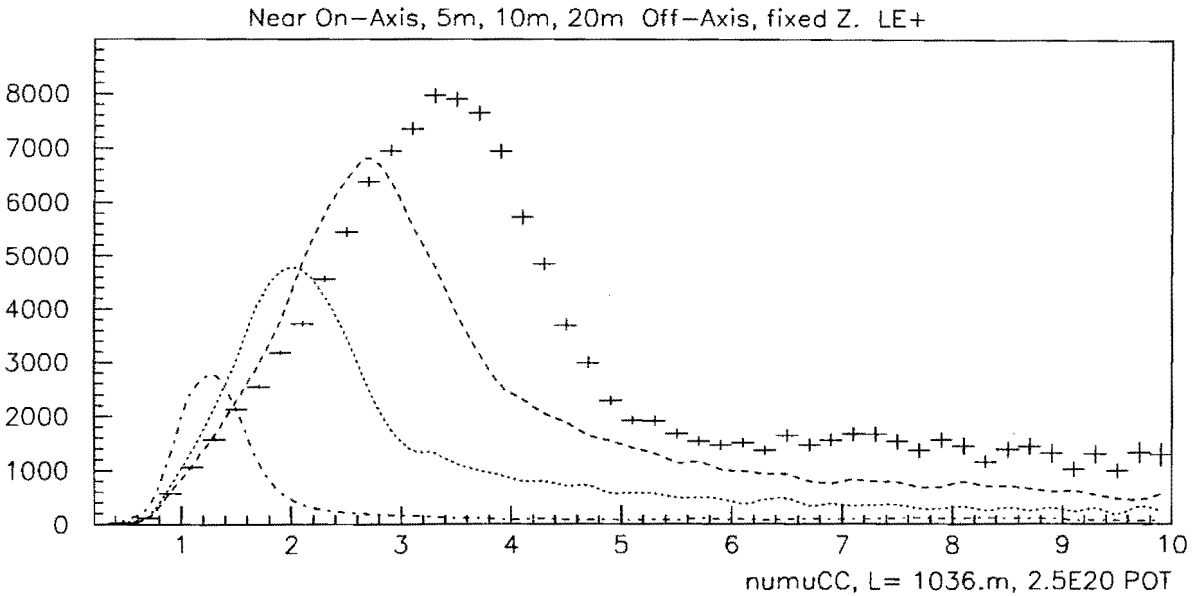

Figure 88: Distribution of off-axis events that are available at different distances off-axis at the distance from the target of the MINOS near detector in the LE beam. In order of the peak from left to right, the curves represent event rates 20 m off-axis, 10 m off-axis, 5 m off-axis and on-axis, for comparison.

The NuMI underground complex itself was excavated primarily by a 21.5 foot diameter tunnel boring machine (TBM), and because of this there are large sections of excavated regions underground which will be unused once the MINOS near detector is in place. These regions are located anywhere from 0 to 20mrad off the NuMI beamline axis, and could house a future off axis near detector. The Off Axis experiment is likely to place a near detector in these drifts to be able to predict the ν_e appearance

backgrounds at a far off axis detector.

Figure 89 shows three possible locations for the MINERνA detector to be placed for off axis running. We discuss from downstream to upstream, the advantages and disadvantages of each location, keeping in mind that none of these locations would require any additional excavation.
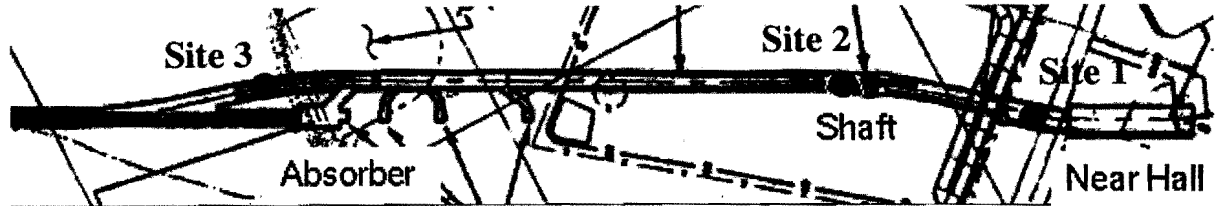

Figure 89: Possible sites for off axis running in the NuMI Underground area

The most downstream site, site 1 in figure 89, is the easiest site to use, as it is the closest to the MINOS near hall. It is just downstream of the shaft, and the floor is flat between the base of the MINOS shaft and the MINOS near hall. This location views off axis beams anywhere from 5 to 10mrad off the NuMI Axis. The drift itself has an access tunnel on the east side for emergency personnel egress, and some cable tray and utilities on the west side, but there is a region in the middle of the drift which measures 4.5m wide by 6m tall which is currently vacant, as shown in figure 90. The neutrino energy spectrum in this hall would be anywhere from 1.5 to 3 GeV, depending on the location, since at the downstream end of the access tunnel the tunnel is nearly on axis, and at the upstream end of the tunnel, near the shaft, the tunnel is about 10m off axis.
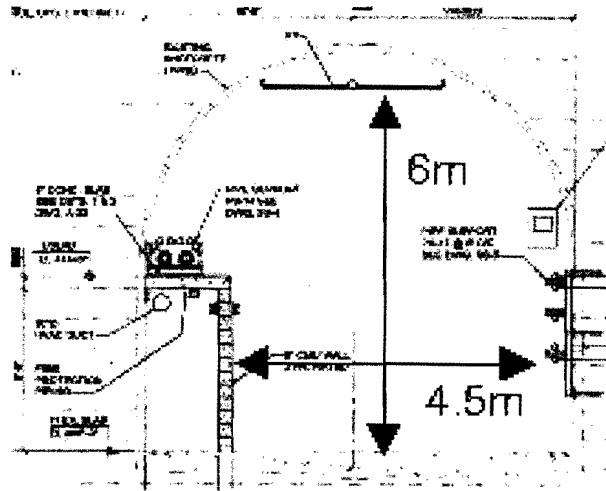
Figure 90: Off-axis drift cross-section for site 1.

Moving upstream, the next site is just upstream of the MINOS shaft (called site 2 in figure 89). This location is also relatively easy to get to since it is near the MINOS shaft and therefore close to utilities, but the floor in this region has a 9% slope. The available cross section in this area is also wide, at least as wide as the area for site 1, but some space must be left for access to points upstream, since there is no longer an independent egress tunnel as with site 1. Here the mean neutrino energy is about 1.5GeV. Finally, the most remote site is located in a drift that was created when the tunnel boring machine had

170

to change angles between excavating for the decay volume itself and excavating for the access tunnel to the downstream areas. This site is substantially closer to the decay pipe, located about 725m from the NuMI target. This site has the widest cross cross section available since it is located in a "dead end", and would allow off axis distances from 5 to 15m off axis, which correspond to between 8 and 20mrad off axis angles. To run in this location the detector would have to be moved up the 9% sloped floor about 200m from the base of the MINOS shaft, and then re-assembled in this new hall, which also has a floor with a 9% slope. There are always several meters of earth between the NuMI hadron absorber and the detector, but neutron radiation issues would be worse here than in the other two sites. However, this site's weakness is also its strength, in that a detector in this location would have the least amount of interference with the MINOS experiment during construction. The closer location would also provide a significantly higher event rate. The downstream portion of this site has utilities for the NuMI absorber, but there are about 10 meters of cleared space upstream of those utilities where the MINERνA detector could be placed.

References

[1] The EOIs from the groups that combined to form the MINERνAcollaboration, the NuMI "On-axis" and NuMI "Off-axis" groups, can be found on the MINERνA home page at: http://www.pas.rochester.edu/minerva/

[2] A. Vovenko, "Total cross sections and structure functions for neutrino interactions in 3-30 GeV energy range and near plans for 1-5 GeV energy range", submitted to the Proceedings of NuInt01 : Proceedings of The First International Workshop on Neutrino-Nucleus Interactions in the Few GeV Region, pg 116. (2002).

[3] A recently-formed working group coordinated by Hugh Gallagher, Costas Andreopoulos and Sam Zeller is attempting to gather all existing neutrino scattering data for the Durham and PDG data bases.

[4] D. Rein and L. M. Sehgal, Annals Phys. **133**, 79 (1981).

[5] T. S. Lee and T. Sato Few Body Syst. Suppl. **15**, 183 (2003).

[6] E. A. Paschos, L. Pasquali and J. Y. Yu, Nucl. Phys. B **588**, 263 (2000) and E. A. Paschos, J. Y. Yu and M. Sakuda [arXiv:hep-ph/0308130].

[7] S. Wood, "Resonance Region to DIS, Quark-Hadron Duality", submitted to the Proceedings of NuInt01 : The First International Workshop on Neutrino-Nucleus Interactions in the Few GeV Region, (2002).

[8] A. Bodek and U. K. Yang, [arXiv:hep-ex/0203009.]

[9] R. Shrock, Phys. Rev. **D12**, 2049 (1975); A. A. Amer, Phys. Rev. **D18**, 2290 (1978); H.K. Dewan, Phys. Rev. **D24**, 2369 (1981).

[10] N. Solomey, "Physics prospects with an intense neutrino experiment," [arXiv:hep-ex/0006021] and "Neutrino Interactions-Strange Particle Production", contribution to the Workshop on New Initiatives for the NuMI Neutrino Beam, Fermilab, 2002.

[11] P-907: Proposal to Measure Particle Production in the Meson Area Using Main Injector Primary and Secondary Beams, May 2000

(http://ppd.fnal.gov/experiments/e907/Proposal/E907_Propsal.html)

[12] NuMI Technical Design Handbook

(http://www-numi.fnal.gov/numiwork/tdh/tdh_index.html)

[13] D. MacFarlane *et al.*, Z. Phys. **C26**, 1 (1984).

[14] J. P. Berge *et al.*, Z. Phys. **C35**, 443 (1987).

[15] J. G. Morfin *et al.*, Phys. Lett. **B104**, 235 (1981).

[16] D. C. Colley *et al.*, Zeit. Phys. **C2**, 187 (1979).

[17] A. I. Mukhin *et al.*, Sov. J. Nucl. Phys. **30**, 528 (1979).

[18] D. S. Baranov *et al.*, Phys. Lett. **B81**, 255 (1979).

[19] C. Baltay *et al.*, Phys. Rev. Lett. **44**, 916 (1980).

[20] S. J. Barish *et al.*, Phys. Rev. **D19**, 2521 (1979).

[21] N. J. Baker *et al.*, Phys. Rev. **D25**, 617 (1982).

[22] S. Ciampolillo *et al.*, Phys. Lett. **B84**, 281 (1979).

[23] S. J. Barish *et al.*, Phys. Rev. **D16**, 3103 (1977).

[24] N. J. Baker *et al.*, Phys. Rev. **D23**, 2499 (1981).

[25] H. Kluttig, J. G. Morfin, and W. Van Doninck, Phys. Lett. **B71**, 446 (1977).

[26] O. Erriquez *et al.*, Phys. Lett. **B73**, 350 (1978).

[27] W. Krenz *et al.*, Nucl. Phys. **B135**, 45 (1978).

[28] M. Pohl *et al.*, Phys. Lett. **B82**, 461 (1979).

[29] W.-Y. Lee *et al.*, Phys. Rev. Lett. **38**, 202 (1977).

[30] S. J. Barish *et al.*, Phys. Rev. Lett. **33**, 448 (1974).

[31] M. Derrick *et al.*, Phys. Lett. **B92**, 363 (1980).

[32] M. Derrick *et al.*, Phys. Rev. **D23**, 569 (1981).

[33] N. J. Baker *et al.*, Phys. Rev. **D23**, 2495 (1981).

[34] J. Campbell *et al.*, Phys. Rev. Lett. **30**, 335 (1973).

[35] T. Kitagaki *et al.*, Phys. Rev. **D34**, 2554 (1986).

[36] J. Bell *et al.*, Phys. Rev. Lett. **41**, 1008 (1978).

[37] P. Allen *et al.*, Nucl. Phys. **B264**, 221 (1986).

[38] Y. Fukada *et al.*, Phys. Rev. Lett. **81** 1562 (1998).

[39] H. Budd, A. Bodek and J. Arrington, [arXiv:hep-ex/0308005]; A. Bodek, H. Budd and J. Arrington, [arXiv:hep-ex/0309024] (to be published in Proceedings of CIPANP2003, New York City, NY 2003.)

[40] C.H. Llewellyn Smith, Phys. Rep. **3C** (1972).

[41] V. Bernard, L. Elouadrhiri, U.G. Meissner, J. Phys. **G28** (2002).

[42] J. Arrington, nucl-ex/0305009.

[43] M. Paschos, (private communication).

[44] M. K. Jones *et al.*, Phys. Rev. Lett **84**, 1398 (2000); O. Gayou *et al.*, Phys. Rev. Lett **88**, 092301 (2002).

[45] A. F. Krutov, V. E. Troitsky, Eur. Phys. J. **A16**, 285 (2003).

[46] K. L. Miller *et al.*, Phys. Rev. **D26**, 537 (1982).

[47] T. Kitagaki *et al.*, Phys. Rev. **D26**, 436 (1983).

[48] Particle Data Group, Eur. Phys. J **C15**, 1 (2000).

[49] W.A. Mann *et al.*, Phys. Rev. Lett. **31**, 844 (1973).

[50] J. Brunner *et al.*, Z. Phys. **C45**, 551 (1990).

[51] M. Pohl *et al.*, Lett. Nuovo Cimento **26**, 332 (1979).

[52] L.B. Auerbach *et al.*, Phys. Rev. **C66**, 015501 (2002).

[53] S.V. Belikov *et al.*, Z. Phys. **A320**, 625 (1985).

[54] S. Bonetti *et al.*, Nuovo Cimento **38**, 260 (1977).

[55] N. Armenise *et al.*, Nucl. Phys. **B152**, 365 (1979).

[56] G. Zeller (private communication).

[57] R. A. Smith and E. J. Moniz, Nucl. Phys. **B43**, 605 (1972) ; E. J. Moniz *et al.*, Phys. Rev. Lett. **26**, 445 (1971); E. J. Moniz, Phys. Rev. **184**, 1154 (1969).

[58] D. Casper, Nucl. Phys. Proc. Suppl. **112**, 161 (2002).

[59] K. Tsushima, Hungchong Kim, K. Saito, nucl-th[0307013].

[60] Ghent Theory group in Belgium, Jan Ryckebusch (jan@inwpent5.UGent.be).

[61] JLab hydrogen experiment 94-110, C.E. Keppel spokesperson.

(http://www.jlab.org/exp_prog/proposals/94/PR94-110.pdf)

[62] JLab deuterium experiment 02-109, C.E. Keppel, M.E. Christy, spokespersons.

(http://www.jlab.org/exp_prog/proposals/02/PR02-109.ps)

[63] JLab experiment 99-118 on the nuclear dependence of R at low Q^2, A. Brull, C.E. Keppel spokespersons.

[64] W. K. Brooks, NUINT02 proceedings.

175

[65] M. Ripani, Nucl. Phys. **A699**, 270 (2002), V. D. Burkert, Proceedings of the 9th International Conference on the Structure of Baryons, Baryons 2002, p. 29.

[66] S. A. Wood, To be published in *Proceedings of the Second Workshop on Neutrino-Nucleus Interactions in the Few-GeV Region (NUINT02)*, Irvine, California (2002).

[67] T. Sato and T.-S. Lee, Phys. Rev. **C54**, 2660 (1996); T. Sato and T.-S. Lee, Phys. Rev.**C63**, 055201 (2001).

[68] T. Sato, D. Uno and T.-S. Lee, Phys. Rev. **C67**, 065201 (2003).

[69] P. A. Schreiner and F. Von Hippel, Nucl. Phys. **B58**, 333 (1973).

[70] D. Rein and L. Seghal, Nucl. Phys. **B223**, 29 (1983); D. Rein, Z. Phys. **C35**, 43 (1987).

[71] C.E. Carlson, Phys. Rev. **D 34**, 2704 (1986).

[72] P. Stoler, Phys. Reports, **226 3**, 103-171 (1993).

[73] P. Stoler, Phys. Rev. Lett. **66**, 1003 (1991).

[74] M. Gari and N.G. Stephanis, Phys. Lett. **B175**, 462 (1986).

[75] M. Gari and W. Krupelmann, Phys. Lett. **B173**, 10 (1986).

[76] R.M. Davidson *et al.*, Phys. Rev. **D43**, 71 (1991).

[77] E.P. Wigner, Proc. Cambridge Philosophical Soc. **47**, 790 (1951).

[78] J.P. Ralston and B. Pire, Univ. of Kansas preprint 5/92.

[79] G.R. Farrar and D.R. Jackson, Phys. Rev. Lett. **35**, 21 (1975).

[80] C.E. Carlson and J.L. Poor, Phys. Rev. **D 38**, 2758 (1988).

[81] G.P. Lepage and S.J. Brodsky, Phys. Rev. **D 22**, 2180 (1980).

[82] A.I. Vainshtein and A.V. Zakharov, Phys. Lett. **B72**, 368 (1978).

[83] C. Becchi and G. Morpurgo, Phys. Lett. **17**, 352 (1969).

[84] V. V. Frolov *et al.*, Phys. Rev. Lett. **82**, 45 (1999).

[85] S.J. Brodsky and A.H. Mueller, Phys. Lett. **B 206**, 685 (1988).

[86] N.C.R. Makins *et al.*, Phys. Rev. Lett. **72**, 1986 (1994); T.G. O'Neill *et al.*, Phys. Lett. **351**, 87 (1995).

[87] K. Garrow *et al.*, Phys. Rev. C **66**, 044613 (2002).

[88] A.S. Carroll *et al*, Phys. Rev. Lett. **61**, 1698 (1988).

[89] Y. Mardor *et al*, Phys. Rev. Lett. **81**, 5085 (1998); A. Leksanov *et al*, Phys. Rev. Lett. **87**, 212301 (2001).

[90] D. Dutta, R. Ent, K. Garrow, *et al*, Jefferson Lab Hall C Experiment E-01-107, approved with A-priority and expected to run in 2004.

[91] D. Gaskell, To be published in *Proceedings of the Second Workshop on Neutrino-Nucleus Interactions in the Few-GeV Region (NUINT02)*, Irvine, California (2002).

[92] B. Z. Kopeliovich and P. Marage, Int. J. Mod. Phys. **A8**, 1513 (1993).

[93] D. Rein and L. M. Sehgal, Nucl. Phys. **B223**, 29 (1983).

[94] A. A. Belkov and B. Z. Kopeliovich, Sov. J. Nucl. Phys. **46**, 499 (1987).

[95] C. A. Piketty and L. Stodolsky, Nucl. Phys. **B15**, 571 (1970).

[96] E. A. Paschos and A. V. Kartavtsev, (2003), [arXiv:hep-ph/0309148].

[97] H. Faissner *et al.*, Phys. Lett. **B125**, 230 (1983).

[98] E. Isiksal, D. Rein, and J. G. Morfin, Phys. Rev. Lett. **52**, 1096 (1984).

[99] CHARM, F. Bergsma *et al.*, Phys. Lett. **B157**, 469 (1985).

[100] CHARM-II, P. Vilain *et al.*, Phys. Lett. **B313**, 267 (1993).

[101] BEBC WA59, P. P. Allport *et al.*, Z. Phys. **C43**, 523 (1989).

[102] BEBC WA59, P. Marage *et al.*, Z. Phys. **C31**, 191 (1986).

[103] SKAT, H. J. Grabosch *et al.*, Zeit. Phys. **C31**, 203 (1986).

[104] C. Baltay *et al.*, Phys. Rev. Lett. **57**, 2629 (1986).

[105] V. V. Ammosov *et al.*, Yad. Fiz. **45**, 1662 (1987).

[106] E632, S. Willocq *et al.*, Phys. Rev. **D47**, 2661 (1993).

[107] E. Paschos and A. Kartavtsev (private communication).

[108] G. Zeller, To be published in *Proceedings of the Second Workshop on Neutrino-Nucleus Interactions in the Few-GeV Region (NUINT02)*, Irvine, California (2002).

[109] H. Deden *et al.*, Phys. Lett. **58B**, 361 (1975).

[110] O. Erriques *et al.*, Phys. Lett. **B70**, 385 (1977); Nucl. Phys. **B140**, 123 (1978).

[111] S.J. Barish *et al.*, Phys. Rev. Lett. **33**, 1446 (1974)

[112] N.J. Baker *et al.*, Phys. Rev. **D24**, 2779 (1981).

[113] E. G. Cazzoli *et al.*, Phys. Rev. Lett. **34**, 1125 (1975).

[114] P. Astier *et al.*, Nucl. Phys. **B611**, 3-39 (2001).

[115] A. A. Amer, Phys. Rev. **D18**, 2290 (1978).

[116] H. K. Dewan, Phys. Rev. **D24**, 2369 (1981).

[117] K. Nakamura in proceedings of *Neutrinos and Implications for Physics Beyond the Standard Model*, SUNY at Stony Brook, October 2002, pp. 307-317. *Physics Potential and Feasibility of UNO*, (http://nngroup.physics.sunysb.edu/uno/), report SBHEP-01-03 (2000).

[118] SuperKamiokande Collaboration, S. Mine, presented at *Neutrino Interactions at Few GeV Energies NUINT02*, (http://nuint.ps.uci.edu/) UC Irvine, California, December 2002; see also, S. Mine, Nucl. Phys. B (Proc. Suppl.) **112**, 154 (2002).

[119] H. Gallagher, Nucl. Phys. B (Proc. Suppl.) **112**, 188 (2002).

[120] For the cross section excitation of Equation (43), measurements at ANL (Table 4.5 in D.L. Day, Ph.D. thesis, University of Kansas, 1977) agree with those reported by BNL [24] to within large errors, however the $\sigma(E_\nu)$ nominal values are higher by factors 1.5 to 2.0.

[121] J. Lach and P. Zenczykowski, Int. J. Mod. Phys. **A10**, 3817 (1995).

[122] P. Singer, Nucl. Phys. B (Proc. Suppl.) **50**, 202 (1996).

[123] A. Alavi-Harati *et al.*, Phys. Rev. **86**, 3239 (2001).

[124] S.A. Schmidth, Ph.D. Thesis, Univ. Mainz, D-55099 Mainz (November 2001).

[125] P. Zenczykowski, [arXiv:hep-ph/0205311] (October 2002).

[126] F.J. Gilman and M.B. Wise, Phys. Rev. **D19**, 976 (1979).

[127] A. Alavi-Harati *et al.*, Phys. Rev. **87** 132001 (2001).

[128] P.G. Ratcliffe, Phys. Rev. **D59**, 014038 (1999).

[129] N. Cabibbo *et al.*, Semileptonic Hyperon Decay and CKM Unitarity, [arXiv:hep-ph/0307214] (July 2003).

[130] N. Solomey, Recent Rare Ω Decay Results from the HyperCP Experiment, talk at DPF 2003, Philadelphia.

[131] A. Pais and S.B. Treiman, Phys. Rev. **178**, 2365 (1969).

[132] Y. Singh, Phys. Rev. **161**, 1497 (1967).

[133] T. Nakano *et al.*, [arXiv:hep-ex/0301020]; V.V. Barmin *et al.*, [arXiv:hep-ex0304040]; S. Stepanyan [arXiv:hep-ex/0307018].

[134] R. Jaffe and F. Wilczek, Di-quarks and Exotic Spectroscopy, [arXiv:hep-ph/0307341] (July 2003).

[135] B. Saghai, Nuclear Physics **A639**, 217-226 (1998).

[136] M. Goncharov *et al.*, Phys. Rev. **D64**, 112006 (2001).

[137] M. Shifman, Handbook of QCD, Volume 3, 1451, World Scientific (2001).

[138] A.D. Martin, R.G. Roberts, and W.J. Stirling, Phys. Rev. **D50** (1994) 6734.

[139] R. Barbieri, J. Ellis, M.K. Gaillard, G. Ross, Nucl. Phys. **B117**, 50 (1976).

[140] C. E. Keppel, "Quark hadron duality studies at Jefferson Lab: An overview of new and existing results," *Prepared for Exclusive Processes at High Momentum Transfer, Newport News, Virginia, 15-18 May 2002.*

[141] L.W. Whitlow, E.M. Riordan, S. Dasu, S. Rock and A. Bodek, Phys. Lett. B **282**, 475 (1992).

[142] I. Niculescu *et al.*, Phys. Rev. Lett. **85**, 1186 (2000).

[143] A. Fantoni [HERMES Collaboration], Eur. Phys. J. **A17**, 385 (2003).

[144] I. Niculescu *et al.*, Phys. Rev. Lett. **85**, 1182 (2000).

[145] D. Dolgov *et al.* [LHPC collaboration], Phys. Rev. **D66**, 034506 (2002) [arXiv:hep-lat/0201021].

[146] A. De Rujula, H. Georgi, and H.D. Politzer, Ann. Phys. **103** 315 (1977).

[147] R. P. Feynman, *Photon Hadron Interactions* (Benjamin, Reading, Massachusetts, 1972); F. E. Close, Phys. Lett. **B43**, 422 (1973); Nucl. Phys. **B80**, 269 (1973); R. D. Carlitz, Phys. Lett. **B58**, 345 (1975); N. Isgur, Phys. Rev. **D59**, 034013 (1999).

[148] A. D. Martin, R. G. Roberts, W. J. Stirling and R. S. Thorne, Eur. Phys. J. **C14**, 133 (2000); H. L. Lai *et al.*, Eur. Phys. J. **C12**, 375 (2000); M. Glück, E. Reya and A. Vogt, Eur. Phys. J. **C5**, 461 (1998).

[149] G. R. Farrar and D. R. Jackson, Phys. Rev. Lett. **35**, 1416 (1975).

[150] S. Kuhlmann *et al.*, Phys. Lett. **B476**, 291 (2000).

[151] W. Melnitchouk and A. W. Thomas Phys. Lett. **B377**, 11 (1996).

[152] U. K. Yang and A. Bodek, Phys. Rev. Lett. **82**, 2467 (1999). [arXiv:hep-ph/9809480]

[153] H. L. Lai *et al.*, Phys. Rev. **D51**, 4763 (1995) [arXiv:hep-ph/9410404].

[154] U. K. Yang and A. Bodek, Eur. Phys. J. **C13**, 241 (2000) [arXiv:hep-ex/9908058].

[155] H. Deden *et al.*, Nucl. Phys. **B85**, 269 (1975).

[156] K. Varvell *et al.*, Z. Phys. **C36**, 1 (1987).

[157] J. Webb, Thesis "Measurement of Continuum Dimuon Production in 800-GeV/c Proton-Necleon Collisions" (New Mexico State Univ., Sept 2002), unpublished.

[158] J. Pumplin, D. R. Stump, J. Huston, H. L. Lai, P. Nadolsky and W. K. Tung, JHEP **0207**, 012 (2002) [arXiv:hep-ph/0201195].

[159] Jefferson Lab Experiment E03-012 Proposal (approved).

[160] A. Bodek, C. Keppel, et al, E93-110 Collaboration Proposal to Jefferson Lab Hall C (2003).

[161] J. Arrington, R. Ent, C. E. Keppel, J. Mammei and I. Niculescu, arXiv:nucl-ex/0307012 (submitted to *Phys. Rev. Lett.*).

[162] X. Ji, Phys. Rev. Lett. **78**, 610 (1997).

[163] X. Ji, Phys. Rev. **D55**, 7114 (1997).

[164] A. V. Radyushkin, Phys. Lett. **B380**, 417 (1996).

[165] A. V. Radyushkin, Phys. Lett. **B385**, 333 (1996).

[166] J.C. Collins, L. Frankfurt, and M. Strikman, Phys. Rev. **D56**, 2982 (1997).

[167] A. V. Radyushkin, Nucl. Phys. **A711**, 99 (2002).

[168] M. Vanderhaeghen, Nucl. Phys. **A711**, 109 (2002).

[169] M. Diehl, hep-ph/0307382 (2003).

[170] B. Lehmann-Dronke and A. Schafer, Phys. Lett. **B521**, 55 (2001).

[171] K. Garrow *et al.*, Phys. Rev. **C66**, 044613 (2002).

[172] D. Ashery *et al.*, Phys. Rev. **C23**, 2173 (1981).

[173] M.K. Jones *et al.*, Phys. Rev. **C48**, 2800 (1993); R.D. Ransome *et al.*, Phys. Rev. **C46**, 273 (1992); R.D. Ransome *et al.*, Phys. Rev. **C45**, R509 (1992).

[174] D. Rowntree *et al.*, Phys. Rev. **C60**, 054610 (1999); B. Kotlinksi *et al.*, Eur. Phys. J. **A9**, 537 (2000).

[175] L. Frankfurt, V. Guzey, M. McDermott and M. Strikman, JHEP **0202**, 027 (2002), [arXiv:hep-ph/0201230].

[176] S. A. Kulagin, [arXiv:hep-ph/9812532].

[177] K. J. Eskola, V. J. Kolhinen, P. V. Ruuskanen and C. A. Salgado, Nucl. Phys. **A661**, 645 (1999), [arXiv:hep-ph/9906484].

[178] S. Kumano, [arXiv:hep-ph/0109152].

[179] A. C. Benvenuti *et al.*, Z. Phys. **C63**, 29 (1994).

[180] M. Vakili *et al.*, Phys. Rev. **D61**, 052003 (2000), [arXiv:hep-ex/9905052].
[181]

[181] G. P. Zeller *et al.*, Phys. Rev. Lett. **88**, 091802 (2002), [arXiv:hep-ex/0110059] and references therein.

[182] S. Kovalenko, I. Schmidt and J. J. Yang, [arXiv:hep-ph/0207158].

[183] M.H.Ahn *et al*, Phys. Rev. Lett. **90** 041801 (2003).

[184] G. McGregor [MiniBooNE Collaboration], AIP Conf. Proc. **655**, 58 (2003).

[185] K. Eguchi *et al*, Phys. Rev. Lett. **90**, 021802 (2003).

[186] L. Wolfenstein, Phys. Rev. **D 17** (1978) 2369; Phys. Rev. **D 20** (1979) 2634; S. P. Mikheyev and A. Yu. Smirnov, Sov. J. Nucl. Phys. **42** (1986) 913.

[187] "Proposal for a Five Year Run Plan for MINOS", The MINOS Collaboration, NuMI-930, May 2003, submitted to the Fermilab Directorate, see `http://hep.caltech.edu/~michael/minos/fiveyear.ps`.

[188] M.Diwan, M.Messier, B.Viren, L.Wai, "A Study of $\nu_\mu \to \nu_e$ Sensitivity in MINOS" NUMI-L-714, February 2001.

[189] D. Ayres *et al*, `hep-ex/0210005` and `http://www-off-axis.fnal.gov`.

[190] MINOS Collaboration, "MINOS Technical Design Report" ,NuMI-NOTE-GEN-0337 (1998).

[191] N. V. Mokhov, "The MARS Monte Carlo", FERMILAB FN-628 (1995); N. V. Mokhov and O. E. Krivosheev, "MARS Code Status", FERMILAB-Conf-00/181 (2000); http://www-ap.fnal.gov/MARS/.

[192] M. Messier (private communication)

[193] GEANT Manual, CERN Program Library Long Writeup W5013.

[194] M. Kostin et al., "Proposal for Continuously-Variable Beam Energy", NuMI-B-783.

[195] Nikolai Mokhov and Andreas Van Ginneken, "Neutrino Radiation at Muon Colliders and Storage Rings", FERMILAB-Conf-00/065.

[196] O. Benhar, [arXiv:nucl-th/0307061].

[197] K. Ruddick (private communication).

[198] L. Mualem (private communication).

[199] R. Fruhwirth, Nucl. Inst. Meth. **A262**, 444 (1987).

[200] K. Kodama *et al.*, Nucl. Phys. Proc. Suppl **98**, 43-47 (2001)

[201] Y. Hayato, To be published in *Proceedings of the Second Workshop on Neutrino-Nucleus Interactions in the Few-GeV Region (NUINT02)*, Irvine, California (2002).

[202] J.F. Ostiguy, FNAL-MI-0127.

[203] MINOS, P. Adamson *et al.*, IEEE Trans. Nucl. Sci. **49**, 861 (2002).

[204] P. Border *et al.*, Nucl. Instrum. Meth. **A463**, 194 (2001).

[205] P. Rubinov, FNAL-TM-2226. P. Rubinov, FNAL-TM-2227. P. Rubinov, FNAL-TM-2228.